The Role of Artificial Intelligence In Predicting Potentially Harmful Element Behaviour During Flooding Using Physicochemistry

Michael McGlade

July 2024

A Thesis Submitted for the Degree of Doctor of Philosophy,

Biological and Environmental Sciences,
Faculty of Natural Sciences,
University of Stirling

Declaration of Authorship

I, Michael Alistair McGlade, declare that this thesis has been composed by me and it embodies the results of my own research. Where appropriate I have acknowledged the nature and extent of work carried out in collaboration with others.

……………………………………………Michael A McGlade [15th July, 2024]

Abstract

Anthropogenic contamination from the extensive use of potentially harmful elements (PHEs) in industrial, commercial, and agricultural activities is a significant public health concern. PHEs, such as lead, can become immobilised within soils, but are remobilised during flooding, which erodes soil and transports these elements downstream, depositing them on floodplains - often densely populated areas. Flooding alters porewater physicochemistry (e.g., pH), affecting PHE solid-phase distribution and bioaccessibility. Understanding these changes is crucial for managing the risks of increased exposure to remobilised PHEs during flooding.

This thesis developed a machine-learning predictive tool to monitor changes in PHE porewater solubility, solid-phase distribution, and bioaccessibility during flooding. The tool was trained on physicochemical data from microcosm and mesocosm flood experiments and demonstrated the critical influence of soil particle size, redox potential, pH, and dissolved organic carbon on PHE dynamics. Decision tree models, particularly random forests, provided highly accurate predictions for PHE behaviour during flooding. When integrated with geographical information systems (GIS), these models enabled rapid, large-scale estimations of PHE changes, reducing the need for resource-intensive laboratory analyses.

The findings suggest that machine-learning, informed by physicochemical data, offers a scalable and reliable method for predicting PHE dynamics during flooding. This approach may significantly support policymakers in identifying areas at risk of contamination under future flood scenarios. Future research should validate the random forest predictions across diverse catchments with varying physicochemical conditions.

Acknowledgements

I want to give recognition to David Copplestone, who has quite honestly been the dream supervisor anyone could wish for. His attention to detail, encouragement and his willingness to always find time for myself is something I will not forget. His patience, especially when I provide him on a Monday morning with a list of tough and thought-inducing questions, is a testimony of his character. I now recognise why so many students like myself want David as a supervisor because of his unique ability to set aside his tasks, as difficult as they are, and always provide an immense level of encouragement and support.

As a self-funded student, it was not easy initially to find contacts who could additionally support me throughout my studies. This was quickly dismissed when Joanna Wragg decided to go out of her way and provide continual support beyond any expectations. I am truly grateful Jo for your support and your detail, especially around the “why” question, and like David, I regard you as my friend not just a colleague.

I would love to recognise Clare Wilson, who was another supervisor. I remember Clare eight years ago when I was a first-year student coming out of high school. I never knew when Clare was teaching all those students; I would have the pleasure of working alongside a truly kind warm-hearted individual. Thank you Clare for all your support. I also have forgotten a lot about what Clare has taught me (I did not get an A in her class); I sincerely hope that after reading this thesis, Clare does not find myself misusing terms or definitions, or I may find myself shortly back in her class.

I would also like to recognise the support technicians Ian Washbourne, Pauline Monteith, James Wier, Peter Smith, Lorna English, Isabelle Jones and Scott Jackson. Thank you also, Martina Tully, for your lab work assistance; I wish you all the best in your new career.

I want to thank my extensive support family network, including my mum, dad and brother. I am incredibly grateful for all the opportunities you have given me, the support, the encouragement and, most challengingly, putting up with me, which requires a PhD in itself. I want to thank my very close family friend, who I call family anyways, Eoin Rennie, for your utmost support with this work, your proof-

reading, motivation, but also your means of challenging my reasoning with this research.

I want to thank my friend group (my family), with many of them graphic and product designers, for your help in creating illustrations for this thesis; the support you have all given me throughout my life I truly cannot pay back. Thank you to my close Aunt and Uncle Audrey and Gordon for your support with my local church, prayer groups and bible studies, which has given me so much peace and encouragement throughout my studies.

There are many others I have not recognised, but I would love to express my deepest appreciation for your support in my life and for facilitating getting me where I am today.

Table of Contents

List of Terminology

Terminology	Definition
Anthropogenic	Man-made and non-naturally occurring (Ponting et al 2021).
Aerobic	Conditions in the presence of available oxygen molecules (McLaren 2017).
Anoxic	Ambient conditions in the absence of oxygen (Laurent et al 2017).
Bagging	Acronym for **B**ootstrap **Agg**regat**ing** which combines multiple decision tree predictions to formulate a single prediction (Tyralis et al 2019).
BARGE	The Unified Bioaccessibility Research Group of Europe (BARGE) method is an extraction laboratory test investigating bioaccessible concentrations (Swartjes 2010, Wragg 2011).
Bioaccessibility	PHE concentration solubilised within the gastric fluid (Bindal and Singh 2019).
Bioavailability	The proportion of a solubilised gastrointestinal bioaccessible PHE as a concentration, diffusing through the intestinal epithelium, and entering systemic circulation (Bindal and Singh 2019).
Boosting	Iteratively train weak learners to formulate a strong learner (Shaheen and Iqbal 2018).
Bootstrap Aggregation	Parallel processing of decision trees splitting and organising data. The decision tree outputs are collected using a majority voting classifier either by averaging the results (regression) or calculating the mode (classification) (Brieman 2001).
Porewater Solubility	The mobilisation of a PHE that is solubilised and not bound, complexing, or coprecipitating with any soil, sediment, or organic particulate matter (McLaren 2017).

Solid Phase Distribution	Reference to the soil mineral phase a PHE associates (Laurent et al 2017).
CISED	Chemometric identification of substrates and element distributions is a laboratory extraction test aiming to investigate PHE solid phase distribution (Cave et al 2015).
Cross-validation	Partition the training data into testing and training subsets (Tyralis et al 2019).
Coprecipitation	The simultaneous precipitation of more than one compound from a solution (Ponting et al 2021).
Decision Tree	Splits a dataset from a high order entropy to a lower entropy to finalise a prediction (Brieman 2001).
Deep Learning	Form of AI modelling referring to calculating a prediction by reconfiguring wights and bias values. An example of this refers to a neural network (Brieman 2001).
Dissolution	The chemical release of contaminants from mineral phases whereby the ionic bonding is broken and the contaminant eventually becomes solubilised (Ponting et al 2021).
Entropy	The order of the data (e.g., how structured is data) (Tyralis et al 2019).
Fulvic Acids	These acids are a group of organic acids that result and are created from organic matter decomposition. Fulvic acids are a component of humic substances (Ponting et al 2021).
Grid-Searching	Systematic exploration of hyperparameter combinations (e.g., n_tree and mtry) to identify the optimal combination to maximise the model performance (Tyralis et al 2019).
Gini Impurity	This refers the quality of the final decision tree output. This impurity assesses the number of misclassified variables within the decision tree final output (Brieman 2001).
Generalisation Error	Refers to when the model overfits the data within the training dataset too well it cannot predict well outside its training data (Brieman 2001).

Geogenic	Naturally occurring and non-man made, opposite from anthropogenic (Ponting et al 2021).
Humic Substances	Products resulting from the decomposition of organic materials, omnipresent within soil and sediment systems, and are complex organic compounds (Ponting et al 2021).
Hyperparameter	Set to control the performance and behaviour of the predictive model (Genuer et al 2010).
Hyperplane	Decision boundary dividing the input space into two or more regions each responding to different classes (Brieman 2001).
Mean Square Error	Metric used to assess the predictive model accuracy (Brieman 2001).
Model Accuracy	Defines the model "accuracy" as the prediction closeness value to the microcosm results. In classification problems, the model "accuracy" defines the ability of the model to correctly classify the different target variable classes (Genuer et al 2010).
Model Sensitivity	The proportion of true positives correctly predicted by the model (Genuer et al 2010).
Model Specificity	The proportion of true negatives correctly predicted by the model (Genuer et al 2010).
Neural Network	Predictive network mimicking the structure of the brain containing neurons linked by interconnecting layers (Schubach et al 2017).
Occluded	Refers to the blockage, trapping or incorporation of a solid, liquid or gas within soil and sediment minerals (Schubach et al 2017).
Overfitting	Model is too complex and fits the training data too well (Schubach et al 2017).
Physical Remobilisation	The erosion of sediment beds from flood water, resuspending contaminated material, and through high water velocities, physically remobilising these

	contaminated insoluble sediments downstream, eventually depositing on floodplains (McLaren 2019).
Physicochemistry	Defines a physical, chemical, biotic or abiotic substrate within water or soil (Ponting et al 2021).
Potentially Harmful Element	A type of element, whether anthropogenic or geogenic, whereby exposure may cause health consequences (Ponting et al 2021).
Predictive Robustness	Defines whether the predictive model results from the training dataset remain accurate, irrespective of altering variables and assumptions (Breiman 2001).
Random Forest	Combination of decision trees used to formulate a prediction which adds feature randomisation and sampling with replacement (Breiman 2001).
Recursively Partitioning	Decision tree splitting assigning variables in common groupings aiming to reduce the dataset entropy (Breiman 2001).
Regularisation	Technique used to address overfitting or underfitting which adds a penalty function (Tyralis et al 2019).
Solid-Phase Distribution	Determines the specific soil mineral a PHE complexes (Ponting et al 2021).
Soil	A particle containing mineral fractions, organic carbon, air and water (Breiman 2001).
Sediment	A particle containing primarily mineral fractions (Tyralis et al 2019).
Underfitting	Model is too simple and does not fir training dataset well (Tyralis et al 2019).
Weight	How strong (statistically significant) is such neural connections Tyralis et al 2019).

Project Rationale

Anthropogenic climate change is increasing the frequency and magnitude of flooding worldwide, which, along with rising temperatures that alter soil's biogeochemical cycling processes, is significantly increasing PHE solubility, and thus their bioaccessibility and solid phase distribution (Sarhadi et al 2024). Understanding such changes is limited because of the complex interactions between physical, physicochemical, biological, and thermodynamic variables. Estimates indicate that 52% of the worldwide population will be at risk of flooding by 2100 (Kirezci et al 2020).

The effect of flooding on soil/sediment PHE solubility may lead to greater contamination of food crops, drinking water supplies, and household allotments, potentially exposing humans and wildlife. The medical effects of PHE exposure include various conditions such as kidney failure, autism and autoimmune disease, which can vary in severity (Neuwirth et al 2024). Research is needed to investigate flooding’s impact on soil/sediment PHE solubility, bioaccessibility, and solid phase distribution, and to develop novel research methods that reliably predict such changes, particularly under a climate warming scenario.

The research in this thesis investigates the potential of machine learning, trained on porewater physicochemical data, to predict PHE porewater solubility, solid-phase distribution, and bioaccessibility changes during flooding. This approach enables predictions of PHE dynamics across micro, meso, and macro spatial scales, utilising microcosm, mesocosm, and GIS experiments, respectively.

The work is structured as follows:

- **Chapter 1**: A literature review exploring how flooding alters porewater physicochemistry, examining the potential of machine learning, trained using this physicochemical data, to predict PHE changes during flooding.
- **Chapter 2**: A meta-analysis synthesising the findings from 327 peer-reviewed studies to quantify flooding’s impact on PHE porewater solubility and bioaccessibility across different soil textures. This chapter identifies the key physicochemical variables driving PHE changes during flooding.

- **Chapter 3**: Microcosm experiments investigating the correlations between physicochemical changes during flooding and their influence on PHE porewater solubility, bioaccessibility, and solid-phase distribution.
- **Chapter 4**: Evaluation of various machine learning models, trained on physicochemical data, to predict PHE porewater solubility, solid-phase distribution, and bioaccessibility during flooding.
- **Chapter 5**: A mesocosm experiment testing the random forest ability to predict PHE dynamics under varying flood severities (e.g., 1 in 100 and 1 in 10,000-year events) in larger-scale laboratory setups.
- **Chapter 6**: Integrating the random forest model with geographical information systems (GIS) to predict PHE changes rapidly and reliably across large macro spatial scales.

Thesis Structure

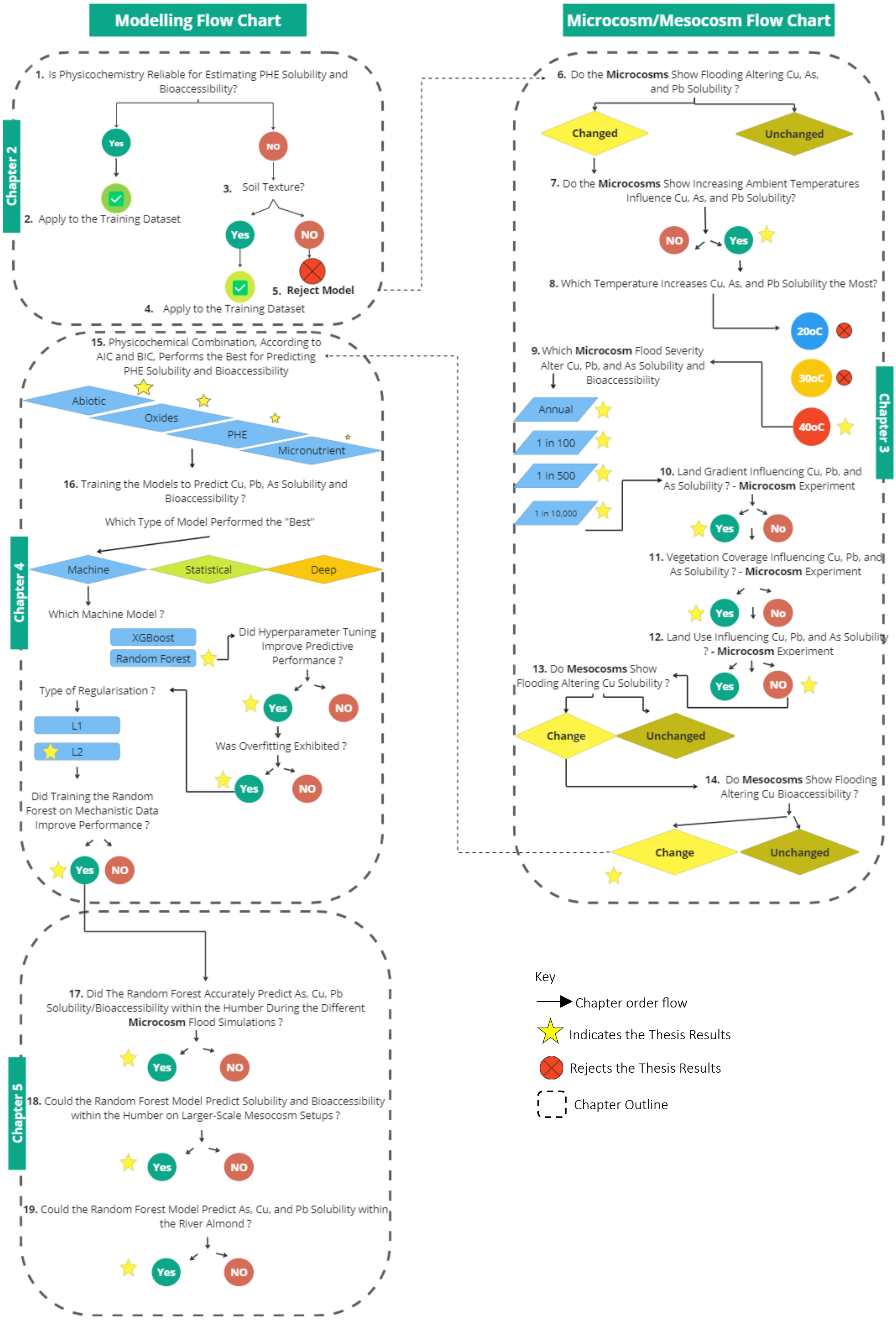

Chapter 1: Thesis Literature Review

1.1 The Origins of Environmental Contamination

A "PHE" refers to any chemical, physical, biological, or radiological substance or matter in water or any solid medium that could harm ecosystems and human health (USEPA 2022). By "harms," this may involve growth, reproduction, and overall health status (McLaren 2019). Geogenic PHE sources originate from weathered mineral fractions (e.g., lead atoms embedded within galena minerals) through geological processes, such as erosion and acid precipitate dissolution (Foroutan et al 2021). The slight acidity of precipitation (sulfur dioxide and nitrogen oxide) erodes acid-sensitive mineral phases, such as carbonates, dissolving and releasing geogenic lead mineral fractions into the surrounding environment (Ponting et al 2021). The proportion of geogenic PHE depends principally on a location's geology (Foroutan et al 2021). Areas with abundant arsenopyrite geological formations (e.g., Cornwall) contain higher geogenic arsenic sources than locations with significantly fewer arsenopyrite minerals (Kilunga et al 2017).

The Industrial Revolution significantly increased the availability and release of these geogenic PHE through mining, production, and industrial waste release (Szuskiewicz et al 2021). Such industrial processes may include tanneries, mineral smelters, and fossil fuel combustion (McLaren 2019). Specific geogenic PHE, such as lead, zinc, and chromium, are used for these industrial activities, such as casting and ore processing (Table 1.1; Koh et al 2021).

Table 1.1. *Example of industries and the associated industrial processes producing different PHE and potentially releasing such PHE into the environment (Koh et al 2021).*

Industry Type	Industrial Process	PHE Released	Human Health Effects
Metalworking	Smelting and casting	Lead and zinc	ADHD and autism (Goodland 2013)
Agriculture	Pesticide application	Copper and arsenic	Convulsions (Xie et al 2022)
Tanning	Leather tanning	Chromium	Respiratory inflammation (Bidstrup 1983)
Mining	Extracting	Gold and lead	Kidney damage (Mohamed et al 2016)

Human or wildlife exposure to PHE may occur through inhalation, dermal contact, or ingestion of soil (Driver et al 1989, Nigg 2016, Table 1.1). Children exhibiting pica behavioural disorders by deliberately consuming large quantities of such contaminated soil may become subject to significant long-term health risks (Table 1.1; Koh et al 2021). These health burdens can range from neurotoxic, hepatotoxic, dermatoxic, and carcinogenic complications (Table 1.1) (Coro et al 2021). There is extensive evidence of statistically significant correlations between lead exposure and neurological complications, such as attention deficit hyperactivity disorder (ADHD), autism, and attention deficit disorder (ADD) (Coro et al 2021, Goodland 2013, Nigg 2016).

Direct exposure to specific PHE, such as copper and zinc, may not cause adverse health effects compared to lead and arsenic, which are known to have more severe and deleterious toxicological impacts (Ponting et al 2021). Copper and zinc are essential micronutrients for regulating metabolic enzymatic processes within the human system (McLaren 2019). However, serious health problems following sub-chronic oral exposure to copper and zinc may promote hepatic oxidative stress and inflammation (liver damage) (Tang et al 2019). Arsenic and lead, however, serve no beneficial purpose within human or wildlife biological systems; exposure to such PHE may create significant health consequences (Goodland 2013). The specific concentration of exposure to such elements within soil and sediment systems creating health consequences is challenging to quantify (McLaren 2019). Specific variables, such as the receptor's weight, food intake, age, and exposure (acute or chronic), must be considered when assessing the risks of exposure to such PHE (Goodland 2013).

These PHE can be sequestered by soil and sediment beds (BGS 2024). The main difference between soil and sediment particles is that soil comprises a mixture of mineral particles, organic matter, air, and water, while sediment particles mainly consist of mineral particles with low organic matter fractions and limited air pockets (Figure 1.1; data extracted from Zhang et al 2004). Riverine sediment beds sequester PHE through inorganic and organic constituents. Examples of inorganic constituents include clay minerals, silica, iron and aluminium oxides and calcium carbonate (Rossi et al 2009). Organic constituents include humic substances, microbial biomass, and organic matter (Devi and Khatua 2017). These constituents have high affinities for co-precipitating PHE through chemical interactions, such as ion exchanges and complexation (Peck et al 2004). Environmental concentrations of such PHE, for example, lead, within the soil across the UK are significantly high and, in many cases, may exceed many of the minimum threshold concentrations imposed under Part 2A of the Environmental Protection Act 1990 and soil guideline values (SGVs) (Figure 1.2, BGS 2024).

The total soil lead concentrations presented in Figure 1.2 are derived from the G-BASE (Geochemical Baseline Survey for the Environment) model. While the model provides valuable predictions of spatial trends, it does not account for sub-grid resolution or variability within grid cells. Addressing such spatial heterogeneity is critical when scaling from micro to macro models to ensure accurate and reliable predictions based on soil parameter estimates.

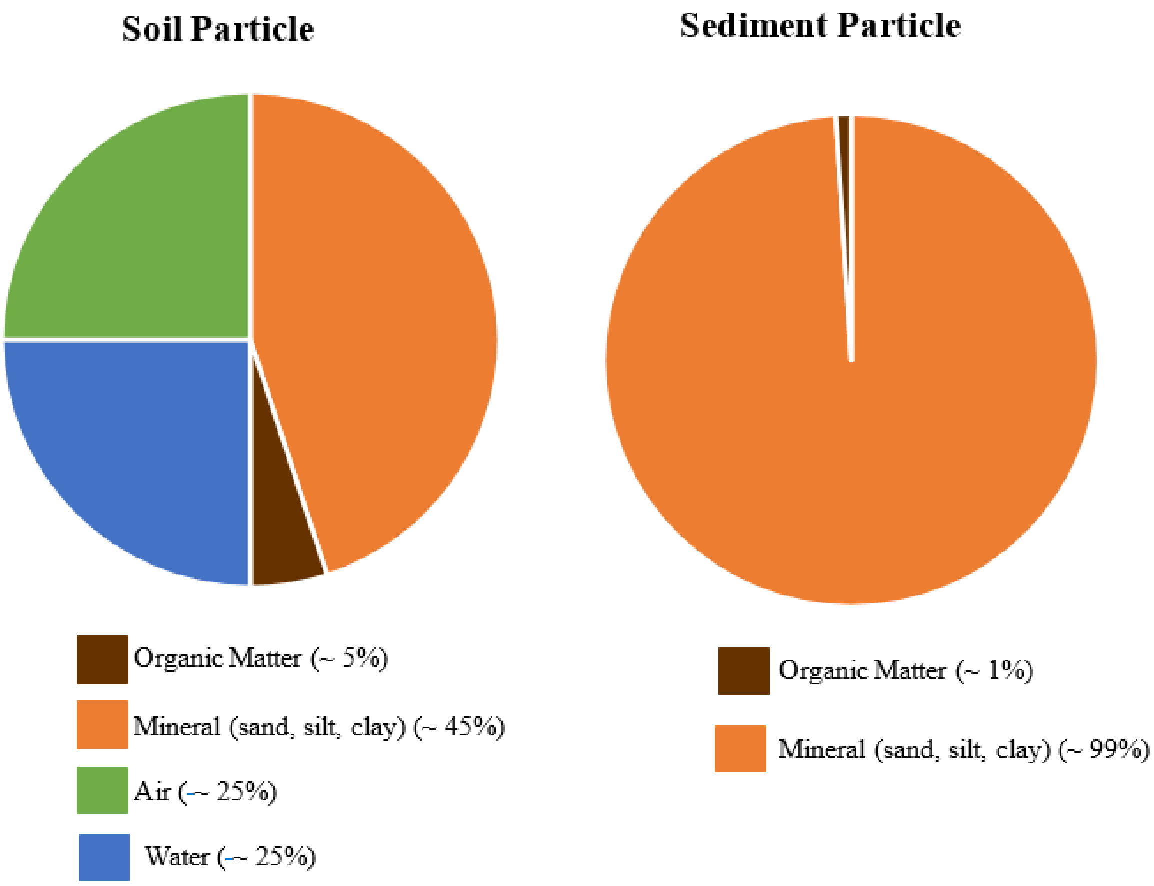

Figure 1.1. *Outlines the structural difference between a soil and sediment particle, illustrating the main difference being the mineral phase, air, and water composition (data sourced from Zhang et al 2004).*

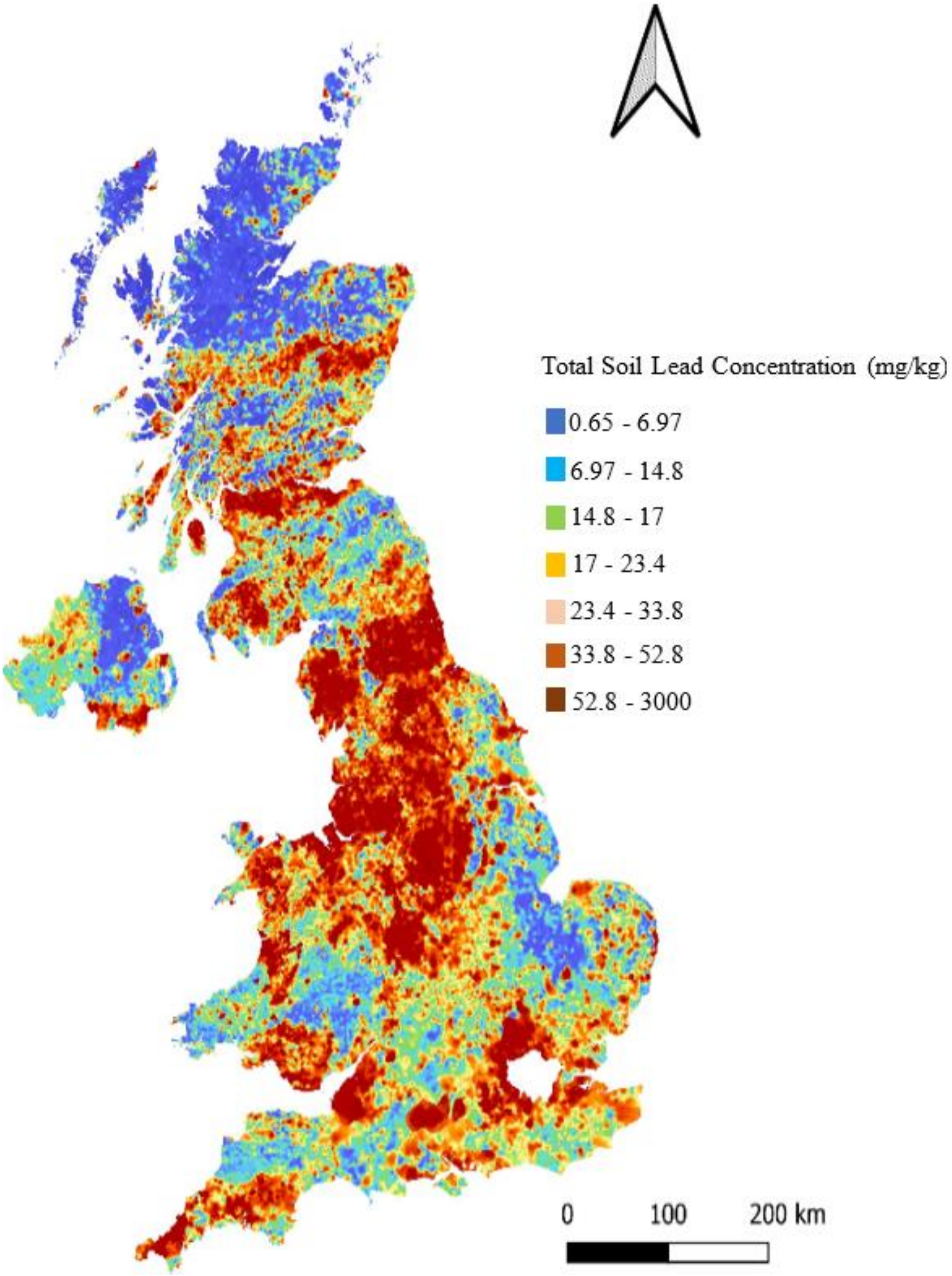

Figure 1.2. *Outlines the total soil lead concentration throughout the UK, indicating the different concentration gradients within 500-metre x 500-metre grid cells (BGS 2024). The predictions shown are generated by the G-BASE model, not from direct high-resolution sampling. The figure illustrates that the total soil lead concentrations vary significantly across the UK, with high concentrations predominately in the middle of the country and the lowest concentrations in northwest Scotland.*

1.2 Ion Exchange and Adsorption of PHE - Organic and Inorganic Constituents

The term “adsorption” refers to the adherence of a PHE to the surface of inorganic and organic constituents (e.g., organic materials, iron and manganese oxides, and clay minerals) (Kilunga et al 2017). Ion exchange involves the movement of anions or cations through the soil, where cations or anions that are adsorbed on soil surfaces are exchanged or replaced by other cations or anions in the soil solution (Mclaren 2019). For example, organic constituents on clay surface minerals are negatively charged through isomorphic substitutions, which electrochemically attract positively charged Pb cations; these cations may outcompete other cations originally coprecipitating with clay, leading to ion exchanges (Kilunga et al 2017).

These exchanges can be “competitive,” whereby two or more ions compete for ligand binding exchanges on such constituents (Devi and Khatua 2017, Kilunga et al 2017). This ion exchange competition is driven by the ionic charge (Schmidt et al 2010). Ions with higher ionic charges (i.e., greater than one elementary positive or negative charge), such as divalent and trivalent ions, have greater electrostatic forces for adsorbing PHE (Tyler 2004). The differences in ionic charges mean that PHE adsorption is more competitive for trivalent ions, exerting a greater ionic charge than monovalent ions, which have much weaker ionic changes (Schmidt et al 2010).

Several studies suggest that the sequestration of PHE by organic and inorganic constituents within rivers renders them effective buffering sinks for absorbing water-soluble contamination (Kilunga et al 2017, Nel et al 2018, Peck et al 2004, Roussiez et al 2006, Walling et al 2003). This buffering capacity is poorly understood and not definitively established (Roussiez et al 2006, Walling et al 2003). By not fully understanding this buffering capacity, it remains unclear to what extent certain rivers, based on their sediment composition, may adsorb more contamination than others.

However, it is understood that the process of PHE coprecipitation to organic and inorganic constituents plays a significant role in immobilising PHE soluble transport (Peck et al 2004). The PHE adsorption onto constituents means less

PHE concentrations are soluble and free-flowing within riverine water and, instead, are bound to these constituents, which are less susceptible to mobilisation downstream (Peck et al 2004). These constituents have vital roles in reducing PHE mobility by reducing PHE solubility (Walling et al 2003) .

These riverine sediment beds can sequester and accumulate significant PHE concentrations, forming potential PHE “hotspots” (Nel et al 2018). These “hotspots” are not uniform throughout the river sediment beds; however, they are more prominent within slack areas or the outer meanders, exhibiting higher sediment deposition and accumulation (Kilunga et al 2017). These slack areas have lower kinetic energy conditions, favouring sediment deposition and potentially accumulating PHE-contaminated sediments (Nel et al 2018). These lower energy environments reduce sediment resuspension and transport, increasing deposition (Wu et al 2024). The low-energy environments particularly increase the deposition of large sediment particles, which require higher energy for resuspension and transport, giving rise to PHE sediment deposition of large particles within these slack areas (Nel et al 2018). The study by Iwuoha et al (2016) shows that these low-energy slacks significantly accumulate large sediment particles contaminated with PHE, often requiring dredging to remove such sediments.

1.3 Economic and Legislative Mechanisms for Reducing Soil PHE

To understand why there is extensive anthropogenic contamination released within soil, it is important to appreciate the existing economic and legislative challenges that have contributed to this issue. Understanding these economic and legislative challenges emphasises the need for environmental science interventions to address soil contamination which overcomes these economic and legislative barriers.

Several economic strategies have been applied to reduce the release of PHE from industry into the environment. Market-based economic mechanisms, such as cap-and-trade schemes, carbon taxation, and habitat offsetting, aim to reduce PHE concentrations within these “hotspots” (Haites 2018). These economic approaches reduce the anthropogenic release of PHE (e.g., lead, chromium and arsenic) in two ways. Firstly, placing a tariff or carbon taxation on polluting industries that emit carbon may deter such industries from polluting by investing in cleaner technologies to reduce emissions (Table 1.1). Secondly, these mechanisms attempt to internalise the negative externalities created by producing these PHE “hotspots,” increasing an industry’s marginal abatement cost and making it cheaper to use “cleaner” technologies, which use and release less PHE (Shi et al 2018). Such investment in technologies because of these market-driven approaches, including the use of nanofiltration, reduces chromium release by 98.8% (Giagnorio et al 2018). The purpose of this discussion is to outline the challenges and complexities, but also the opportunities of addressing PHE release in the environment using economic approaches.

European environmental law attempts to address these “missing markets” by implementing regulations to reduce environmental contamination, such as the legally binding Water Framework Directive (2000/60/EC) (Conrad and Perzanowski 2019). Much of environmental law faces enforcement and compliance challenges through “game theory” concepts, with many countries unwilling to commit to such laws to reduce the production and release of many PHE due to fears of economic disadvantages (Conrad and Perzanowski 2019). The economic and legislative shortcomings of reducing environmental contamination underpin the urgency for scientific intervention (Ponting et al 2021).

1.4 Overview of PHE Behaviour in Soil and Sediment

Less than 1% of soil and sediment PHE, such as lead, arsenic, and zinc, are soluble within the riverine water, whereas over 99% of PHE are insoluble and coprecipitate with soil and sediment particles (Section 1.2; Filgueiras et al 2004). Many PHE are metals (e.g., lead, copper, zinc) and are positively charged cations (Wilson et al 2010). Some PHE, such as arsenic, are metalloids, which can exist as negatively charged anions (e.g., As^{3-}) (Wilson et al 2010). The chemical form and source of PHE (cationic or anionic) and the availability and type of soil organic and inorganic constituents, which coprecipitate with PHE, make understanding the behaviour of PHE within soil systems highly complex (Simmler et al 2017).

Understanding the relationship and complex interactions between soil chemistry and PHE may provide a deep understanding around the behaviour of PHE within soil systems. By “behaviour,” this means PHE coprecipitation and dissolution with different soil mineral phases (Izaditame et al 2022). Understanding PHE interactions with different soil mineral phases provides an understanding of PHE chemical speciation, which influences PHE solubility and is essential for predictive purposes.

Individual PHE interact with soil and sediment differently; however, this literature review will mainly discuss lead, copper, arsenic, zinc, chromium, and nickel because chronic exposure to all these PHE can cause severe health consequences (Table 1.1).

1.4.1 Arsenic

Arsenic is a metalloid, biochemically similar to phosphorus, which can either form cations (e.g., As^{3+}) or anions (e.g., $AsO^{3-}{}_4$) (Wilson et al 2010). Arsenic combines with elements such as oxygen, chlorine, and sulfur, referred to as inorganic arsenic (e.g., As_2O_3), and with hydrogen and carbon, referred to as organic arsenic (e.g., $C_5H_{11}AsO_2$) (Izaditame et al 2022). Geogenic arsenic sources derive from sulfide minerals and iron oxides, and also anthropogenically, for example, from glass and dye industries which use arsenic in industrial processing (Bindal and Singh 2019). The worldwide average soil arsenic concentration is 32 mg/kg^{-1} in non-mineralised areas and ~290mg/kg^{-1} in mineralised locations (Moldes et al 2011).

Arsenic’s remobilisation, bioaccessibility, and toxicity depend on its solid phase distribution (Bindal and Singh 2019). Arsenic’s predominant speciation within oxidising redox (E_h) conditions (+0mV) is As(V), and under reducing redox conditions (< 0mV) is As(III) (Simmler et al 2017). The toxicity between these arsenic species significantly differs, with As(V) being significantly less toxic than As(III), which is more lipophilic (fat-soluble) by having a greater affinity for binding with thiol groups, increasing the ability of As(III) to cross cellular membranes, thereby increasing the toxicity (Jinadasa et al 2024). Such As(V) species coprecipitate with Fe oxyhydroxides (e.g., $FeAsO_4 . 2H_2O$) (Izaditame et al 2022). Flooding reductively dissolves iron oxyhydroxides, causing As(V) species to coprecipitate with clay minerals through surface ligand exchanges and organic matter (Roe et al 2015).

1.4.2 Copper

Copper is a soft, malleable, ductile metal derived from geogenic sources, including chalcopyrite, and is also released in various forms through anthropogenic activities, such as mining and refineries, for use in products (Lair et al 2007). Copper exists in two oxidation states (Cu^+ and Cu^{2+}) as free ions, exchangeable, organic, precipitated, and residual forms (Kah et al 2022). Naturally occurring copper in the soil varies between 1-55mg/kg^{-1} in non-mineralised areas and ~340mg/kg^{-1} in mineralised areas (McLaren 2019). Exposure to excessive copper concentrations (i.e., > 180 mg/dL) exerts detrimental health consequences, including neurodegenerative disorder (e.g., Wilson's Disease); however, at lower concentrations (0.7 - 1.6 mg/dL), copper is an essential micronutrient involved in carbohydrate metabolism (Kumar et al 2021).

The soil pH influences copper solid phase distribution, porewater solubility, and bioaccessibility by influencing the stability of copper compounds and complexes and copper's adsorption capacity (McLaren 2019). Increasing soil pH alkalinity increases copper's adsorption capacity and affinity, particularly with organic matter through chelate complex formation (Kumar et al 2021). Copper forms complexes, given the appropriate pH conditions (pH > 7), with both organic (amino acids, peptides, and chelating agents) and inorganic ligands (carbonates, hydroxides, cyanides) (Kah et al 2022; Lair et al 2007). These organic and ligand complexes alter copper mobility by influencing copper solubility fraction and chemical speciation (Kumar et al 2021).

1.4.3 Lead

Lead is a soft and malleable heavy metal derived from geogenic sources, including galena minerals (e.g., PbS); however, it is also anthropogenically derived from mineral extraction, coal mining, and fossil fuel combustion (McLaren 2019). Naturally occurring lead in soil varies between 1-27mg/kg^{-1} in non-mineralised areas and ~ 2,400 mg/kg^{-1} in mineralised areas worldwide (Nigg 2016).

Lead’s solid phase distribution and remobilisation are strongly influenced by the soil pH, ion exchanges, adsorption and desorption reactions, biological immobilisation, and aqueous complexation (Nigg 2016). Lead’s chemical form strongly influences its mobility, where lead compounds, such as lead acetate, are relatively soluble compared to insoluble compounds, such as metallic lead phosphate (Goodland 2013). Many physicochemical parameters influence lead porewater solubility, including the soil pH, texture, organic matter content, and cation exchange capacity (Goodland 2013).

1.4.4 Zinc

Zinc’s primary anthropogenic sources include mining and metallurgic operations, which release zinc through smelter slag discharges, mine tailings, and the use of fertilisers containing zinc compounds (Goodland 2013). Zinc is naturally found within the Earth’s crust and upper and lower mantle layers, predominately in the form of sphalerite minerals (Coro et al 2021). The background zinc concentrations in surface waters are typically < 500µg/L and in soils between 5 - 2900mg/kg worldwide (Nigg 2016).

Zinc occurs primarily in the +2 oxidation state and complexes with inorganic and organic ligands (McLaren 2019). Under aerobic conditions, such ligands include organic matter, clay minerals, hydrous iron, and manganese oxides (Lair et al 2007). During anaerobic conditions, zinc may form complexes with organic matter and sulfide. Sorption by such ligands highly depends on the ligand’s cation exchange capacity, zinc concentration, soil redox and pH conditions (Roe et al 2015). At lower soil pH conditions, zinc remains as free ions within the soil and water matrix (McLaren 2019). Under anaerobic flooding conditions, zinc primarily coprecipitates with sulfide ions (e.g., ZnS) (Coro et al 2021).

1.4.5 Chromium

Chromium is used extensively within industrial processing, such as electroplating industries using anti-biofouling and anticorrosive agents, steel production, and automobile manufacturing (Kumar et al 2021). Chromium exists in the trivalent or hexavalent state (Coro et al 2021). The chromium element occurs naturally within soils and sediments from the geochemical weathering of chromium minerals (e.g., chromite) or is released into the soil anthropogenically through the industrial extraction of chromium for products. Aqueous hexavalent chromium is a public health concern, with acute exposure leading to cancer, skin irritation, liver diseases, and neurotoxicological complications, such as the association with dementia and chronic chromium exposure (Lair et al 2007). Chromium reduction transformation from Cr(VI) to Cr(III), facilitated by organic matter acting as a reductant, as well as the soil pH, redox status, and available electron donors, can effectively immobilise chromium (McLaren 2019). Once reductively transformed, Cr(III) precipitates as chromium hydroxide, forming stable complexes with organic materials, therefore immobilising chromium (Kumar et al 2021).

The soil composition (i.e., texture and electron donor availability) and conditions (i.e., pH and vegetation coverage) can influence chromium porewater solubility and mobility (Roe et al 2015). Such mobility is enhanced under neutral soil pH conditions, particularly in the presence of competing oxyanions (Roe et al 2015). Irrespective of the soil composition and conditions, trivalent chromium is less mobile, precipitating as Cr(OH)3 or $Fe_xCr_{1-x}Cr1\text{-}X(OH)_3$ under slightly acidic environments (pH 5.5 - 6.8 (Kumar et al 2021).

1.4.6 Nickel

The element nickel is the 24th most abundant metal within the Earth's crust (Naggar et al 2021). Natural sources of nickel minerals (e.g., Pentlandite) include forest fires and volcanic emissions (McLaren 2019). Anthropogenic nickel releases derive from coal and oil combustion, waste incineration, and phosphate fertilisers (Ponting et al 2021). The concentration of soil nickel ranges between 5 - 500mg/kg worldwide (Ponting et al 2021). Nickel is essential for regulating organismal metabolic and digestive processes; however, excessive exposure and intake of nickel may cause severe allergies, cancer, and reduced lung functions (McLaren 2019).

Nickel exists in several elemental forms (e.g., nickel oxides, nickel sulfate and nickel sulfide) that depend on the adsorption or complexation with organic surfaces, inorganic cation exchanges, free-ions, or chelated metal complexes (Naggar et al 2021). This complexation depends highly on nickel's oxidation state (+1, +2, +3, +4) (Naggar et al 2021). The soil pH significantly influences nickel's oxidation state and adsorption capacity with organic and inorganic ligands

(Naggar et al 2021). Nickel has high affinities under optimal pH conditions (pH 4 - 9) with metallic sulfur, iron, and fulvic acids and humic substances within organic matter (Naggar et al 2021).

1.4.7. Contaminant Interaction Effects

Such relationships between different PHE and soil chemical properties do not act in isolation, rather, PHE mobility, bioaccessibility, and solid-phase distribution are often influenced by interactions with other contaminants and environmental factors. Many PHE, such as zinc and lead, have similar geochemical pathways, where they both precipitate as sulfides, for example. The competitive sorption between PHE can lead to displacement effects, where one metal (e.g., Zn^{2+}) outcompetes another (e.g., Pb^{2+}) for available ligand binding sites on mineral surfaces. Such interactions occur between metals (e.g., Pb) and metalloids (e.g., As), where during reducing redox conditions, the reductive dissolution or iron and manganese oxides, sulfide and dissolved organic carbon formation, changes the availability and competition of redox-sensitive arsenic and lead binding with surface minerals.

1.5 Anthropogenic Climate Change and Future Flooding

Anthropogenic climate change is predicted to increase the frequency and magnitude of severe storm events (Dube et al 2021). Such changes are attributed to warmer temperatures, increasing evaporation and atmospheric moisture, rising sea levels causing coastal flooding, and urbanisation and industrialisation degrading natural flood buffers, such as wetlands, riparian zones, and forests (Dube et al 2021).

The last decade has witnessed several category 3+ storms globally, including hurricanes Harvey (2017), Irma (2017), Florence (2018), Barry (2019), Hanna (2020), Delta (2020), and Ida (2021) (Met Office 2020). Storm events are associated with high-magnitude flooding (e.g., 1 in 500-year flooding) (Dube et al 2021). Estimates predict that 52% of the worldwide population will be at risk of high-magnitude flooding by 2100 (Kirezci et al 2020).

Like many countries, the UK is not immune to such flood challenges and is experiencing a significant increase in flood severity, frequency, and economic costs associated with flood defence (Met Office 2020). In 2018, the cost of flood defence amounted to £777 million; in 2021, it was £1.1 billion, and in 2050, it is projected to be £5 billion (Office for National Statistics, 2023). The UK has approximately 1.9 million housing developments on floodplains susceptible to regular flooding (Environment Agency 2021). Despite these flood forecasts, many local authorities approve housing development within such flood-prone locations; for example, in 2020, approximately 5,000 household developments occurred within floodplain zones (Richardson Jr 2021). Such developments are driven by land scarcity, the economic ease of building on floodplains, and the demand for new housing development (Environment Agency 2021).

1.5.1 Flood Types

A flood occurs when heavy precipitation exceeds the soil absorption capacity, leading to a water saturation surplus and an infiltration deficit within the soil (Ponting et al 2021). Several factors influence the balance between this surplus and infiltration capacity, including the level of urbanisation, vegetation coverage, land gradient and soil texture (Zhu et al 2022). The level of urbanisation reduces soil infiltration through increasing surface runoff from concrete foundations and soil sealing (Miller and Hutchins 2017). Nature-based solutions, such as peatlands, forestry, and wetlands, can adsorb and reduce flood water's flow, velocity, and volume (Bogdzevic 2023). The topographical gradient influences flooding velocity, with steeper gradients increasing surface runoff and reducing infiltration (Flesch and Reuter 2012). Soil particle sizes influence floodwater absorption, with finer-grained particles reducing infiltration compared to larger particle sizes (Chen et al 2019).

1.5.2 Riverine Flooding

The saturated and overlying floodwater flows downstream into these river systems (surface runoff) (Mladenovic et al 2017). The absorbed water underground may also enter river systems from the processes of "throughflow" and "baseflow" (Mladenovic et al 2017). Such river runoff increases a river's volume, flow, and velocity (Xu et al 2022). The excess river water will eventually overflow from the riverbanks, inundating the surrounding floodplain (Viji et al 2020). For an illustration denoting the basic concepts around riverine flooding, see Figure 1.3 (Yorkshire Dales River Trust 2021).

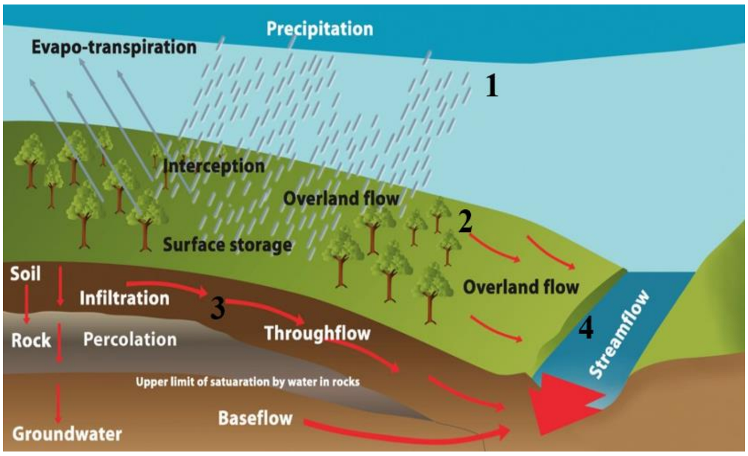

Order:

1. A storm usually characterises extreme precipitation events.
2. Precipitation reaching ground level exceeds soil and sediment absorption capacity, leading to surface runoff.
3. The absorbed precipitation infiltrates underground, and through deep water channels, eventually flows into the river (throughflow).
4. The river's flow and velocity can increase by adding surface water and throughflow inputs from extreme precipitation events.

Figure 1.3. *Outlines the process of how a riverine flood is created. The illustration indicates a significant precipitation event saturating the overland, potentially infiltrating the ground, eventually entering the river system, and increasing the river's flow and velocity (Yorkshire Dales River Trust, 2021).*

1.5.3 Coastal Flooding

The effects of coastal flooding may result from several events, including sea level rise, high tides, storms, or the depletion of natural flood buffers (Zhang et al 2004). The land's topography, such as bays, estuaries, and inlets, influences the frequency and magnitude of coastal flooding (Zhang et al 2004). The storm surge of sea water can eventually reach inland, flooding low-lying areas (Lee et al 2017). Approximately 200 million individuals worldwide are vulnerable to coastal flooding (Lee et al 2017). The average sea levels are predicted to rise between 0.28-0.98 metres, exacerbating coastal flooding (Lee et al 2017). Riverine and coastal flooding differ regarding the floodwater chemistry, with coastal floodwater having significantly higher saline concentrations (~3% - 3.5%) than riverine (0.1% - 0.5%) (Zhang et al 2004). For an overview of how coastal flooding forms, see Figure 1.4 (MacDonnell 2019).

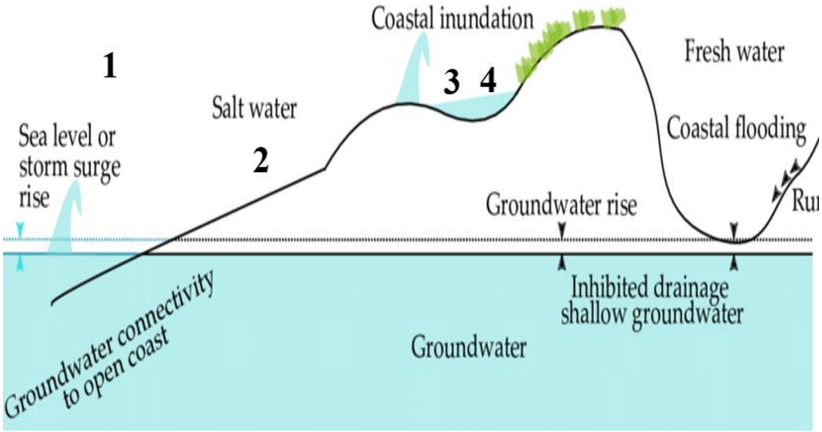

Order:

1. Sea level rise or storm surge from meteorological events create large waves.
2. The large waves and currents reach inland.
3. Locations which are low-lying become inundated with coastal flood water.
4. The flooded water is highly saline in concentration.

Figure 1.4. *Indicates the process of how coastal flooding works. The figure illustrates that a storm surge brings lots of coastal seawater inland on low-lying topographies (taken from MacDonnell 2019).*

1.6 Flooding and PHE Remobilisation

1.6.1 Physical Remobilisation

The effects of flooding increasing a river water's volume and velocity (Section 1.5.2) may influence PHE physical remobilisation (Viji et al 2020). Devi and Khatua (2017) show that flooding's high-velocity and hydraulic turbulences have the kinetic energy to physically erode riverine banks, which act as a store for sequestered PHE (Viji et al 2020). The floodwater then resuspends the eroded sediments and soil particles, transporting them downstream and eventually depositing them onto floodplains, where the water velocity and kinetic energy decrease (Mendez et al 2017, Sun et al 2007). People who reside on floodplains could become exposed to physically remobilised PHE from the floodwater (Viji et al 2020).

Quantifying PHE physical remobilisation during flooding is poorly understood, particularly under a climate change scenario that may increase the risk of flooding (Viji et al 2020, Wang et al 2020, Wragg et al 2011, Xu et al 2022). The different soil textures, land gradients, vegetation coverage, and flood magnitude, to name a few parameters, make quantifying the effects of flooding increasing PHE physical remobilisation significantly challenging (Xu et al 2022). In other words, the heterogeneous environmental conditions, like the vegetation coverage, can make the severity of flooding variable.

Research has established the physical drivers influencing PHE remobilisation, such as increased flow velocity, currents, and turbulences (Ciszewski and Grygar 2016, Ding et al 2019). However, there are significant limitations in quantifying PHE remobilisation during flooding (Kelly et al 2020, Kilunga et al 2017). Research on quantifying PHE physical remobilisation during flooding must encompass multiple high-quality studies, analysing PHE remobilisation within different soil textures, riverine systems, and flood types (Biswas et al 2020, Ciszewski and Grygar 2016, Ding et al 2019, Devi and Khatua 2017, Eggleton and Thomas 2004, Kelly et al 2020, Kilunga et al 2017).

1.6.2 Chemical Remobilisation (Porewater Solubility)

Flooding alters water and soil physicochemistry (e.g., redox status and pH), creating anaerobic conditions by restricting the input of atmospheric oxygen (Ponting et al 2021). In certain circumstances during flooding, particularly under fast-flowing water conditions, water can rapidly flow over rocks and debris, trapping air bubbles and reoxygenating, and therefore, creating aerobic conditions (Xu et al 2022). “Physicochemistry” defines soil and water interacting with physical and chemical properties (e.g., organic matter, iron, manganese) (Ponting et al 2021). Such physicochemistry changes influence PHE porewater solubility, defined as the soluble fraction of a PHE mobilised within an aqueous matrix (McCauley et al 2009). In other words, the changing physicochemical conditions during flooding, such as soil pH, may influence the binding properties of PHE within different soil mineral phases, such as carbonates and organic materials (Xu et al 2022).

Flooding alters the physicochemistry, which influences the binding properties of PHE with different mineral phases, impacting PHE porewater solubility or chemical mobility (Kelly et al 2020). For example, the lower redox conditions during flooding promote As(V) mobility and solubility, by enhancing the reductive dissolution of arsenic from iron and manganese oxides, influencing arsenic porewater solubility (Mendez et al 2017). As physicochemistry is inherently correlated with PHE porewater solubility, exploring the literature on how individual physicochemical changes influence PHE porewater solubility is necessary (McCauley et al 2009). The data presented in this thesis identifies major physicochemistry variables. By "variables," this refers to different physicochemical properties, such as the pH, organic carbon, and calcium, which primarily influence PHE dynamics according to literature searches. The physicochemistry variables selected cover abiotic (e.g., pH), anionic (e.g., organic carbon), cationic (e.g., potassium) or both cationic and anionic (e.g., iron and manganese) types.

1.7 Flooding and PHE Solid Phase Distribution

Physicochemical changes during flooding alter PHE solid phase distribution with soil mineral phases (Laurent et al 2017). The term "solid phase distribution" describes the PHE solubility or immobility, depending on its complexation, with soil mineral phases (e.g., soluble within the exchangeable phase or immobilised by sulfide etc) (Fan et al 2014) (Figure 1.5, amended from Laurent et al 2017). For example, Cu^{2+} may speciate with sulfate, forming copper sulfate ($CuSO_4$); however, redox physicochemistry changes from flooding can change copper solid phase distribution, forming copper sulfide (Cu_2S) (Xu et al 2022). In the example above, the reducing redox conditions reductively dissolve sulfate, forming sulfide.

Soil and sediment particles contain mineral fractions (Fan et al 2014). These fractions comprise organic materials, clays, sulfide, and carbonates (Xu et al 2022). The organic and inorganic constituents (Section 1.1) coprecipitate with PHE (e.g., iron oxides, zinc sulfide, and organolead compounds) (Laurent et al 2017). The term "PHE solid phase distribution," refers to the concentration, proportion, and abundance of a PHE complexing, coprecipitating, or being adsorbed to either one of these organic and inorganic constituents (see Figure 1.5, Laurent et al 2017).

As an example, flooding significantly impacts arsenic, copper, and lead solid phase distribution (Figure 1.6, amended from Kelly et al 2020, McCauley et al 2009, Mendez et al 2017). The lower redox conditions from flooding reduce As(V) to the more toxic and mobile As(III), Pb(II) to the more soluble Pb(I), and Cu(II) to Cu(I) (Figure 1.6A, 1.6D and 1.6F, respectively). This lowering redox state during flooding does not always increase PHE mobility and toxicity (Ponting et al 2021). The introduction of organic materials during flooding (e.g., organic carbon allochthonous inputs) may form complexes with arsenic (methylarsonic acid) and copper (ethylenediaminetetraacetate) (Figure 1.6B and 1.6G, respectively). The pH changes influence lead coprecipitation with available hydrogen ions, influencing lead complexation with iron particles (Figure 1.6E). The reducing redox conditions also created during flooding promote sulfide cluster complex formation, influencing arsenic's solid phase distribution with sulfide minerals (Figure 1.6C).

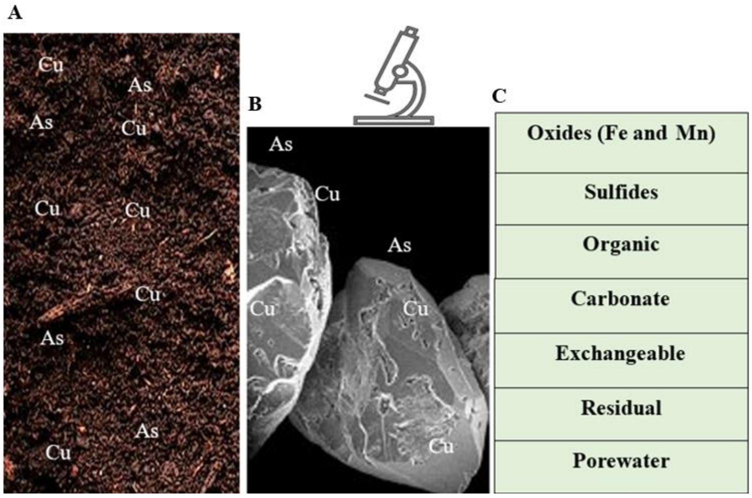

Figure 1.5A. *Indicates contaminated soil.* ***Figure 1.5B*** *shows a microscopic image of the soil particles with coprecipitated PHE.* ***Figure 1.5C*** *shows a zoomed-in version of a soil particle, showing the different soil particle mineral phases, both soluble and insoluble (Laurent et al 2017).*

Multiple studies have quantitatively shown physicochemistry changes during flooding that influence PHE solid phase distribution (Doherty et al 2022, Izaditame et al 2022, Kelly et al 2020, McCauley et al 2009, Mendez et al 2017, Sun et al 2007). For example, Sun et al (2007) indicate that the higher soil pH levels (> pH 7) during flooding promote cadmium coprecipitation with exchangeable hydrogen ions. Doherty et al (2022) demonstrates antimony and arsenic solid phase distribution can alter through coprecipitating with sulfide cluster complexes during reducing redox conditions. Izaditame et al (2022) indicate that reducing redox conditions increase dissolved As(III) concentrations. These are just a few examples of solid phase distribution alterations; however, such changes emphasise the complexity of understanding PHE solid phase distribution alterations with just a few physicochemistry changes during flooding (McCauley et al 2009). The current mechanisms for evaluating PHE solid phase distribution changes are poorly understood due to changing physicochemical parameters, the costs and resources required for speciation testing, and the spatial scale of testing needed (Ponting et al 2021).

Arsenic

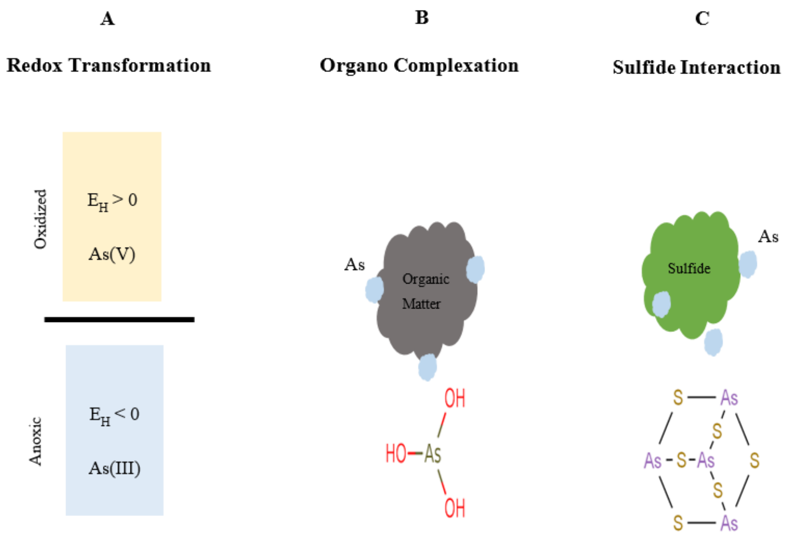

Legend

A. Indicates changes in arsenic solid phase distribution under reducing redox potentials (Eh < 0), which form (As) III, and under oxidising redox potentials (Eh > 0), forming As(V). The colour yellow denotes arsenic speciation during drying periods and blue colour during flooding.

B. Organo-complexation refers to how arsenic, for example, can bind with organic matter through humic substances and fulvic acids.

C. Sulfide interaction indicates that arsenic can bind with sulfide ions, forming metal sulfide complexes.

Lead

Redox Transformation

D

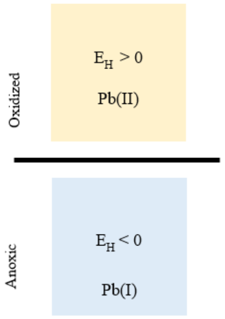

pH Effects

E

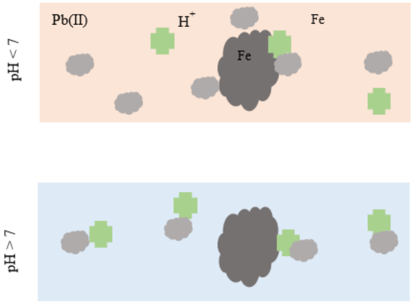

Legend

D. Indicates that redox changes can influence lead’s solid phase distribution. The figure in yellow highlights non-flooding conditions, showing that lead solid phase distribution is typically Pb(II) during oxidising redox conditions. Flooding (highlighted in blue) creates reducing redox conditions, changing lead’s solid phase distribution from Pb(II) to Pb(I).

E. Illustrates how changing soil and water pH conditions influence iron complexation with lead. The grey circular dots represent iron molecules, the green crosses denote the positive hydrogen ions, and the smaller grey dots denote lead ions. During drying, lead ions coprecipitate with iron molecules because of these hydrogen ions. Flooding (denoted by a blue background) causes the hydrogen ions to be consumed by raising the soil and water pH conditions.

Copper

Redox Transformation

F

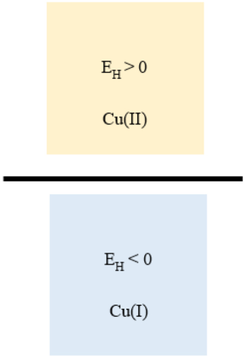

Organo Complexation

G

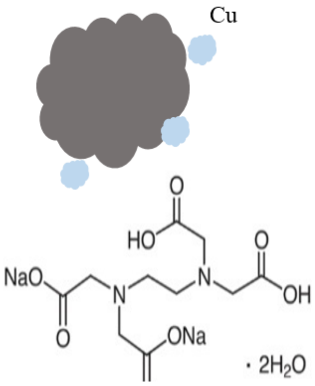

Legend

F. Indicates how changing redox conditions influence copper solid-phase distribution. The figure shows that during drying conditions under oxidative redox conditions, copper solid phase distribution is Cu(II). However, during flooding and reductive redox conditions (indicated in blue), the copper ions change from Cu(II) to Cu(I).

G. Shows copper ions (blue dots) coprecipitating with organic matter (grey dot). The chemical formula illustrates the chemical process of copper complexation with organic matter.

Figure 1.6. *Outlines how changing redox potentials, organic carbon concentrations, and sulfide cluster formations alter arsenic, lead, and copper solid phase distribution. Figures 1.6A, 1.6D and 1.6F indicate a solid-phase distribution change of As(V) to As(III), Pb(II) to Pb(I), and Cu(II) to Cu(I) under oxidising to reducing redox potentials. The effects of organic carbon materials introduced to the riverine system from flooding can cause coprecipitation with arsenic and copper compounds (Figure 1.6B and 1.6G). The reductive dissolution of sulfate ions increases sulfide concentrations, which complex with arsenic, forming insoluble metalloid arsenic sulfide cluster complexes (Figure 1.6C). Increasing pH alkalinities during flooding alter lead's complexation with hydrogen ions (Figure 1.6E). Under low pH conditions (pH < 7), lead ions compete with hydrogen ions for ligand exchanges on oxides, such as iron and manganese (Figure 1.6E). However, increasing the pH alkalinity facilitates lead's complexation with hydrogen ions, altering lead solid phase distribution (Figure 1.6E, McCauley et al 2009, Kelly et al 2020 and Mendez et al 2017).*

1.8 The Relationship Between Soil and Porewater Physicochemistry Influencing PHE Solubility, Bioaccessibility, and Solid-Phase Distribution

The influence of flooding altering the ambient soil and porewater physicochemistry can significantly influence PHE behaviour. Soil and water physicochemistry can refer to several things, such as cationic, anionic, biotic, and abiotic properties, which will all be discussed in Sections 1.8.1 to 1.8.11. Investigating how a single physicochemical property can change during flooding can allow detailed insight into how physicochemistry influences PHE behaviour. This literature review qualitatively explores the different physicochemical parameters that influence PHE dynamics. Chapter 4 quantitatively examines the reliability of these physicochemical parameters to predict PHE porewater solubility, bioaccessibility, and solid-phase distribution during flooding.

1.8.1 Soil and Water pH

The pH is the negative logarithm of potential hydrogen ion concentrations (i.e., $pH = -log[H^+]$) (McCauley et al 2009). Flooding alters the soil and water pH, typically increasing the pH between pH 0.5-1, through the Eh changes and allochthonous inputs of organic material (Ding et al 2019, McCauley et al 2009, Sun et al 2007, Wang et al 2020).

There are well-established correlations between the pH and Eh fluctuations; as the soil becomes flooded, hydrogen ions (H^+) are consumed mainly through the reductive dissolution of iron oxides, increasing the pH alkalinity (Ponting et al 2021; Seo et al 2017; Simsek 2016). Significant amounts of allochthonous inputs enter fluvial systems through bank overflows (Ding et al 2019). Base-forming cations, such as calcium, magnesium, and potassium, typically increase pH alkalinity, whereas acid-forming cations, including aluminium and iron, decrease pH alkalinity (McCauley et al 2009). Whether the allochthonous inputs are either base or acid-forming determines whether the pH increases or decreases during flooding (McCauley et al 2009).

As the flooding recedes, the oxidising Eh produces protons, decreasing pH alkalinity (Ponting et al 2021). Soil and sediments oxidise in the air post-flooding, converting dissolved organic carbon (DOC) into CO_2, which then solubilises as carbonic acid, decreasing pH alkalinity (Ponting et al 2021). Such pH fluctuations may influence PHE porewater solubility. The pH is a significant physicochemical parameter regulating PHE coprecipitation and dissolution reactions with soil mineral phases (Boer et al 2012, Chen et al 2020).

Acidifying pH conditions enhance PHE porewater solubility by dissolving pH-sensitive soil mineral phases, thereby solubilising PHE. Guo et al (2005) show significant solubilisation of chalcophile PHE (e.g., silver, arsenic, copper, mercury, and lead) from the carbonate soil mineral phase during acidifying pH conditions. Flooding increases the soil and water pH alkalinity, meaning PHE dissolution from the carbonate phase is upon soil drainage.

The consumption of protons (increasing pH/alkalinity) often releases dissolved organic carbon (DOC). The DOC forms organo-metal complexes with PHE. Such DOC and PHE coprecipitation reactions reduce soluble PHE concentrations. The increasing pH alkalinity during flooding may reduce PHE porewater solubility. The findings from Kelly et al (2020) show statistically strong relationships between DOC coprecipitation with nickel and chromium ions ($R^2 = 0.78$, $R^2 = 0.52$, respectively). These findings from Kelly et al (2020) could be attributed to the pH altering the partition coefficients with humic and fulvic acids on DOC (Ponting et al 2021). In other words, Kelly et al (2020) findings suggest that soil pH changes can impact how humic and fulvic acids interact with DOC. Paolis and Kukkonen (1997) demonstrate that the partitioning coefficient of pentachlorophenol with humic acids decreased significantly with a pH increase from pH 5 to pH 8. Decreasing protons under alkaline pH conditions reduces PHE competition for binding with DOC and Fe-Mn oxides. As such, more alkaline conditions may alter the binding associations with DOC, highlighting the interconnectedness between different physicochemical variables (pH and DOC) and influencing PHE porewater solubility (Ponting et al 2021).

1.8.2 Redox Potential

The redox potential (Eh) is the equilibrium between oxidative and reducing conditions (Mendez et al 2017). Flooding decreases oxygen concentrations, transitioning from oxic ($[O_2] > 30$ µmol L^{-1}) to anoxic or reducing conditions ($[O_2] < 14$ µmol L^{-1}) (Huang et al 2021). These reducing conditions can chemically transform soluble sulfate into insoluble metal sulfide and, eventually, into sulfide cluster complexes with PHE, thereby immobilising PHE and decreasing their porewater solubility (Mendez et al 2017).

During reducing redox conditions, sulfate ions gain electrons, transforming sulfate into sulfide (see Figure 1.7; Huang et al 2021). Figure 1.7 shows that during the drying process, there is sulfide oxidation, and during flooding, there is sulfate reduction. In Figure 1.7, during flooding (denoted by a blue background), it illustrates that, in some instances, multiple sulfide metal cluster complexes immobilise PHE. During drying, the oxidative conditions mean that such cluster complexes no longer exist, and the PHE is dissociated from the sulfide complex (arrows pointing away).

Reducing redox conditions also chemically transform redox-sensitive iron and manganese oxides. These oxides often coprecipitate with PHE due to their high surface reactivity; however, during these reducing redox conditions, the electrons are transferred to these metal oxides, weakening the structural integrity of these oxides and eventually releasing PHE (Fan et al 2014). The transition from reducing to oxidising redox conditions, when floods recede, can oxidatively transform insoluble sulfide back into soluble sulfate, resolubilising PHE coprecipitated with such sulfide cluster complexes (Figure 1.7, amended from Huang et al 2021).

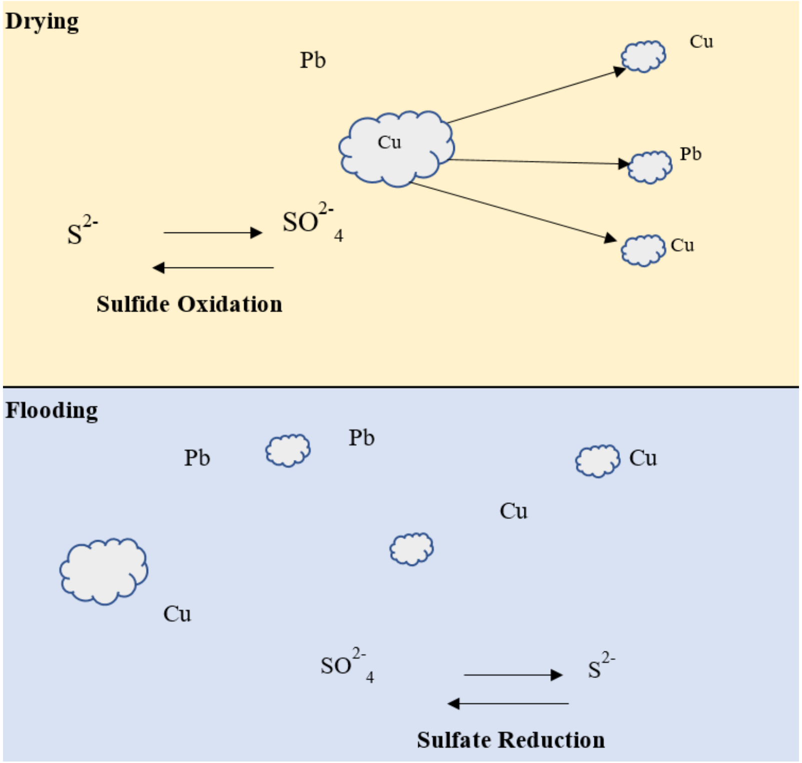

Figure 1.7. *Outlines the sulfide oxidation process upon flood drainage and sulfate reduction during flooding. Such transitions alter PHE porewater solubility and remobilisation (Huang et al 2021).*

1.8.3 Organic Carbon

Organic carbon derives from residual plant and animal materials, synthesised by microorganisms, and subsequently biologically decomposed under abiotic controls (i.e., temperature) (Hao et al 2023). Organic carbon influences PHE porewater solubility by forming stable organic complexes (Hao et al 2023). Fulvic substances within organic matter are the complexants (Li et al 2023, Lodygin and Abakumov 2022). Organic carbon "arranges" into aqueous micelle-like formations containing hydrophobic interior domains, protected by hydrophilic exteriors (Figure 1.8, by Fu et al 2018). By “arranges,” the organic carbon molecules are structured into micelle-like formations (Hao et al 2023).

These micelle-like formations optimise surface complexation with PHE by increasing the surface area and enhancing the formation of organic ligands (Fu et al 2018). The organic carbon’s hydrophobic interiors and hydrophilic exteriors have high affinities for complexing with hydrophobic organic PHE (e.g., polycyclic aromatic hydrocarbons) (Lodygin and Abakumov, 2022). Fu et al (2018) suggest that the organic carbon’s aliphatic chains, comprising of organic compounds with branched or straight chains, optimise this complexation with hydrophobic organic PHE. This organic complexation with organic PHE also happens with inorganic PHE (Deonarine et al 2011). Buschmann et al (2006) show that arsenite and arsenate partition with organic ligands, specifically humic substances. Deonarine et al (2011) indicate zinc sulfide nanoparticles are partitioning with humic substances. Whitby and Berg (2015) show that organic humic substances within organic carbon reduce soluble copper.

Several physicochemical parameters control the partitioning and complexation of organic and inorganic PHE with organic carbon, such as soil pH and calcium concentrations (Lodygin and Abakumov 2022). Calcium ions can modulate organic carbon complexation with PHE, with calcium ions competing for organic carbon binding sites and altering organic carbon’s charge density, influencing PHE partitioning and complexation with organic carbon (Lodygin and Abakumov 2022). Oste et al (2002) demonstrate how pH and calcium ions influence organic carbon, showing increasing organic carbon concentrations under increasing alkalinity and, conversely, decreasing organic carbon concentrations under increasing calcium concentrations (Hao et al 2023). Increasing the alkalinity increases organic carbon's surface negativity, increasing the affinity for complexing with negatively charged ions (Ponting et al 2020). Increasing calcium concentrations create higher negative electrostatic potentials, increasing the organic carbon’s electrostatic repulsion and reducing its attraction for complexing with positively charged PHE (Whitby and Berg 2015).

For this thesis, investigating how organic carbon influences PHE porewater solubility, bioaccessibility, and solid-phase distribution may provide insight into reliably predicting how flooding influences such changes (Hao et al 2023). For example, understanding a soil's organic carbon content may provide reliable predictive insights into estimating PHE behaviour before flooding (Lodygin and Abakumov 2022). An example of understanding soil organic carbon content and organic carbon species could be using online platforms that record the total soil organic carbon contents and species across the UK (e.g., James Hutton Institute, BGS, and the Environment Agency). If organic carbon strongly influences PHE dynamics during flooding, understanding the soil carbon of a given location before flooding, with the information derived from these digital platforms, may provide valuable information about how flooding may influence PHE dynamics (Lodygin and Abakumov 2022). Such analysis directly impacts the thesis’s aims by exploring how incorporating physicochemical data (e.g., organic carbon) into predictive models may reliably estimate PHE mobility, bioaccessibility, and solid-phase distribution changes during flooding (Lodygin and Abakumov 2022).

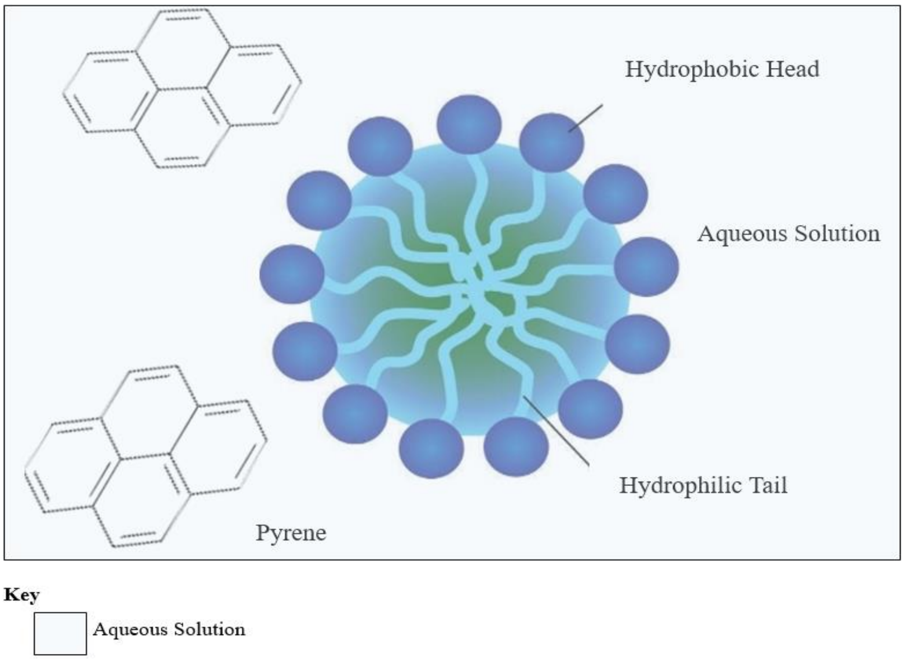

Figure 1.8. *Outlines the binding of hydrophobic PHE to hydrophilic and hydrophobic constituents of organic carbon. The outer hydrophobic head are denoted by the blue circles, and the hydrophobic tails (thin blue strips) represent the hydrophilic section (Fu et al 2018).*

1.8.4 Potassium

Depending on the total soil potassium concentration, potassium may increase or decrease the soil and water oxidative redox potential during flooding (Hosaka et al 2021). Soil potassium concentrations ranging between 150-250mg/kg optimally regulate plant cellular electrolyte metabolism, giving rise to vegetation growth, reproduction and survival (Khaledian et al 2017; Moustafa and Shedid 2018). Increased vegetation coverage increases oxygen production and diffusion within soil systems, increasing soil oxidative redox potentials (Hosaka et al 2021). Excessive potassium levels exceeding 500mg/kg may create toxicity (e.g., nutrient imbalance, salt stress, hyperkalaemia), reducing plant growth (Hosaka et al 2021). This reduction in plant growth may restrict oxygen production in soil systems, lowering the oxidative redox conditions (Khaledian et al 2017).

1.8.5 Calcium

Calcium is an alkaline, reactive metal cation (Zhang et al 2004). Studies report that calcium ions influence PHE porewater solubility by complexing with PHE, altering soil and water pH conditions, and stabilising soil organic carbon (Bashir et al 2019, Huang et al 2021, Pinheiro et al 1999, Zhang et al 2004). Calcium ions coprecipitate with PHE through electrostatic interactions (Huang et al 2021). Additionally, the calcium ion is highly alkaline (pH > 7), meaning excess calcium concentrations can increase soil and water pH levels (Huang et al 2021). Increasing soil and water pH conditions may alter PHE dissolution and porewater solubility from the acid-sensitive carbonate soil mineral phase (Huang et al 2021; Pinheiro et al 1999). Calcium ions also stabilise soil organic carbon, an essential mineral phase for complexing PHE (Section 1.8.3) (Ponting et al 2021). Rowley et al (2018) show the calcium ions hydration shell forming an inner-sphere complex with organic carbon, stabilising organic carbon molecules from microbial degradation (Figure 1.9, amended from Rowley et al 2018).

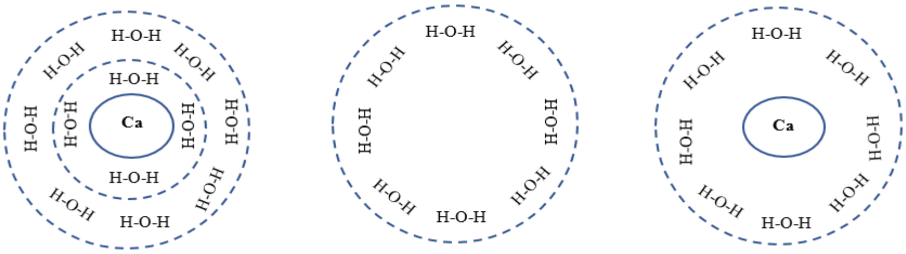

Figure 1.9. *Outlines the effects of calcium in providing a protective layer (hydration shell) around organic matter (amended from Rowley et al 2018).*

1.8.6 Salinity

The salinity of a solution or particulate matter refers to the sodium ion concentration (Peng et al 2022). Soil salinity concentrations exceeding 35,000mg/kg can increase water conductivity above 50 millisiemens per centimetre (Paz et al 2020). High water conductivity levels influence water electrical currents, with more sodium ions conducting electricity (Peng et al 2022). These electrical currents and sodium ion alterations may displace calcium and magnesium ions on soil exchange sites, influencing a soil's cation exchange capacity (CEC) (Asselman et al 2021). Altering soil CEC may influence PHE coprecipitation with different soil mineral phases by altering the availability of soil binding exchange sites (Ponting et al 2021). Sodium ions may also compete with PHE for available ligand exchange sites on soil mineral phases, influencing PHE porewater solubility (Asselman et al 2021). Investigating how soil salinity alterations influence PHE porewater solubility during flooding is important given the increasing frequency and magnitude of coastal flooding, erosion, and wave overtopping events (Paz et al 2020).

1.8.7 Iron

Iron is a lustrous metal ion and the most abundant transition element in the Earth's crust (Heyden and Roychoudhury 2015). Iron influences PHE porewater solubility through inner-sphere monodentate and outer-sphere complexation bonding, ligand-exchange reactions, and the formation of ternary complexes (Cundy et al 2008). Inner-sphere complexation occurs when PHE directly coordinate with iron (Zhang et al 2004). Outer-sphere complexation occurs when the PHE do not coordinate directly but rather indirectly through non-covalent interactions, such as hydrogen bonding (Cundy et al 2008). This unique inner and outer-sphere complexation between iron and PHE has resulted in the development of several environmental clean-up technologies, such as injected zero-valent iron nanoparticles, to adsorb and remove soil PHE (McCauley et al 2009). Iron also forms ternary complexes with PHE, reducing PHE solubility and mobility (McCauley et al 2009). A bridging ligand (i.e., ethylenediaminetetraacetic acid) interacts with the iron species and PHE, forming these ternary complexes (McCauley et al 2009).

1.8.8 Manganese

Manganese is the second most abundant metal in the Earth's crust (Das et al 2011). Manganese influences PHE porewater solubility through its large microporous surface area and ionic charge (Han et al 2006). The surface area of manganese consists of layered octahedral sheets with hydrated interlayers (Flynn and Catalano 2019). These octahedral sheets have negative ionic charges that promote the attraction of positively charged PHE (Das et al 2011). The octahedral sheets also contain vacancy sites with ligand exchange receptors for PHE binding (Flynn and Catalano 2019). Brandao and Galembeck (1990) show that these vacancy sites adsorb and remove significant quantities of lead, copper, and zinc ions. Suda and Makino (2016) indicate that the total average proportion of arsenic, cadmium, cobalt, copper, nickel, lead, and zinc occluded onto manganese oxides is 60, 38, 55, 58, 55, 43, and 57%, respectively, emphasising the role of manganese in reducing PHE porewater solubility.

1.8.9 Magnesium

Magnesium is an essential Earth metal, serving as a vital microelement for plant and mammalian physiological development (Gransee and Fuhrs 2012). Previous studies show that magnesium ions contain multiple available PHE sorption sites (Mao et al 2021; Pinto et al 2019; Shi et al 2018). Allochthonous inputs during flooding, rich in magnesium, may change PHE porewater solubility, affecting the availability of these magnesium sorption sites (Anyanwu et al 2023). Shi et al (2018) demonstrate the capabilities of magnesium ions in reducing PHE porewater solubility by incorporating magnesium ions with eucalyptus biochar and significantly reducing soil lead and copper by 99.9%. Pinto et al (2019) show that biochar impregnated with magnesium ions has a high removal efficiency for phosphorus compounds. Suzuki et al (2013) indicate that magnesium treatment for lead-contaminated kaolinite also successfully coprecipitates and immobilises lead PHE. Soil magnesium concentrations also influence the soil pH (Pinto et al 2019). Excessive soil magnesium concentrations, exceeding 500-1000mg/kg, typically increase soil pH levels (Gransee and Fuhrs 2012). Magnesium can react with water molecules during flooding, forming brucite (Equation 1). The presence of brucite neutralises the soil acidity through brucite, by producing and increasing the concentration of available soil hydroxyl ions (Sanderson et al 2015).

$MgO + H_2O \longrightarrow Mg(2)(OH)_2$ **Eq. 1**

1.8.10 Fluorine

Fluorine is the 13th most abundant element in the Earth's crust (Dec et al 2017). Empirical observations show that flooding can significantly remobilise fluorine, such as along the Dwarka River Basin (Thapa et al 2017). Fluorine has a high electron affinity of -322kj/mol, meaning fluorine atoms have a strong tendency to gain electrons (Dec et al 2017). The fluoride ion is small, with a radius of 1.33 nanometres (Dehnen et al 2021). Fluoride is also the least polarisable anion, meaning its electron cloud is highly resilient to changing ambient electrical charges, making the fluoride ion highly stable (Dec et al 2017). The high electron affinity and stability of fluoride also make this ion significantly effective for ionic bonding with transition metals (e.g., manganese (IV) fluoride and chromium (V) fluoride), influencing PHE porewater solubility (Dehnen et al 2021).

1.8.11 Chloride

Chloride is an ion that regulates plant photosynthesis, fertilisation, and transpiration (Li et al 2023). The chloride ion can stimulate iron's oxidation process by acting as an electron acceptor (Lytle et al 2020). This iron oxidation can solubilise iron minerals, influencing iron complexation with PHE (Peng et al 2022). However, research investigating PHE porewater solubility in relation to chloride is scarce, and therefore, associations between chloride, iron, and PHE porewater solubility are limited and speculative in the context of flooding (Lytle et al 2020, Peng et al 2022).

1.9 Physicochemistry and Bioaccessibility

The term "bioaccessibility" defines the PHE fraction as soluble within the gastrointestinal tract, and readily available for adsorption through the intestinal epithelium (Thakur et al 2020). Frequently confused with the term "bioaccessibility," "bioavailability" relates to the movement of PHE across the cell wall (Figure 1.10, amended from McLaren 2019).

Bioavailability testing uses *in vivo* studies, typically involving rats and monkeys as host organisms (Thakur et al 2020). These *in vivo* experiments are costly, time-consuming, and ethically challenging (Mehta et al 2020). Bioaccessibility testing (*in vitro*) of PHE in soil has been developed over the last 30 years to overcome some issues associated with using animals (Cave et al 2011).

To this end, a suite of *in vitro* bioaccessibility tests has been developed that simulate the physicochemical conditions (e.g., stomach pH, bodily temperature, simulated body fluids, time) in the gastrointestinal tract of “at risk” receptors (e.g., children) (Cave et al 2011). To gain acceptance by regulatory bodies, some of these *in vitro* methods have been validated against animal studies, including the method of the Bioaccessibility Research Group of Europe (BARGE), known as the Unified BARGE Method (UBM) (Denys et al 2012). This method has now been adopted by the International Standards Organisation (ISO) for determining PHE bioaccessibility in soil (ISO 17025) (Juhasz et al 2009).

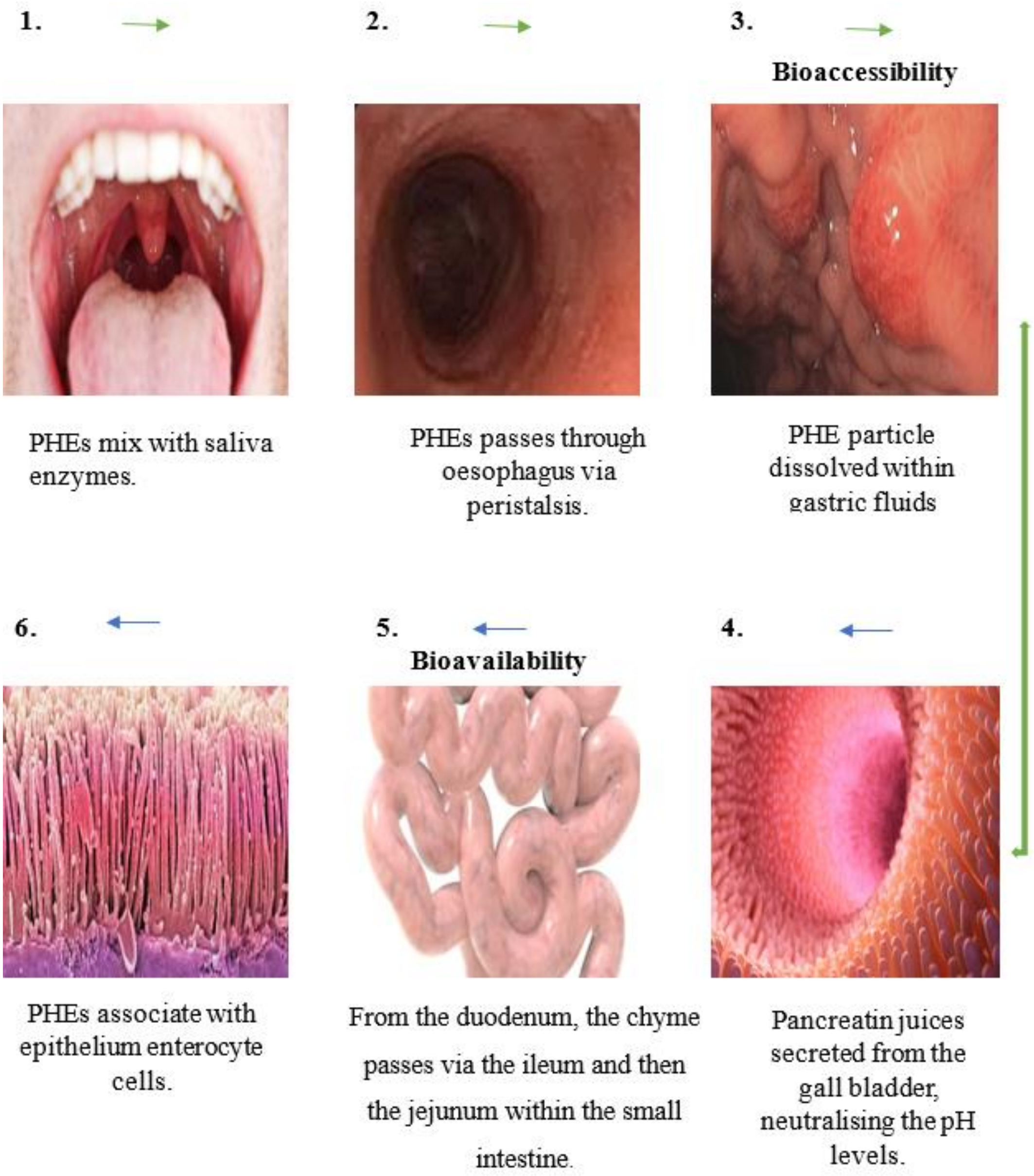

Figure 1.10. Illustrates the *biological processes where contaminated soil or sediment enters the human system, is solubilised within gastric fluids (bioaccessibility), and becomes available for adsorption into the intestinal epithelium (bioavailability) (amended from Ng et al 2015).*

Physicochemical changes during flooding alter PHE porewater solubility (Section 1.8) by influencing PHE coprecipitation with different soil mineral phases (Rastegari et al 2021; Trukhina et al 2022). This relationship between physicochemical changes during flooding and PHE bioaccessibility is understood as linear (Table 1.2) (Trukhina et al 2022). By “Linearly,” this means one physicochemical change directly influences PHE bioaccessibility (Juhasz et al 2009). An example of “linearly” includes how soil pH alkalinity influences PHE bioaccessibility, how increasing soil calcium concentrations influence bioaccessibility, or how reducing redox conditions alter bioaccessibility (Trukhina et al 2022). The above examples have direct causes (physicochemical change) and effects (PHE bioaccessibility increase or decrease).

As observed for PHE porewater solubility, many physicochemical parameters interconnect and operate “non-linearly” (Chen et al 2022). For example, "non-linearly," under a hypothetical, may involve flooding lowering the redox potential, increasing metal sulfide cluster complexes, and reducing PHE bioaccessibility (Juhasz et al 2009). This "non-linearity" example may result in the opposite effect, with the lowering redox conditions promoting oxide dissolution, solubilising PHE and increasing bioaccessibility (Trukhina et al 2022). In this hypothetical scenario, the lower redox conditions during flooding could either increase or decrease PHE bioaccessibility (Juhasz et al 2009).

Predicting PHE bioaccessibility changes during flooding is significantly limited because these interconnecting physicochemical changes affecting PHE bioaccessibility (Juhasz et al 2009). Understanding the dynamic interconnectedness among various physicochemical parameters that influence PHE bioaccessibility is fundamental for identifying locations susceptible to higher PHE bioaccessible concentrations after flooding (Camba et al 2024). Using information based on the soil’s physicochemical properties may help pre-emptively predict locations susceptible to high and low PHE bioaccessibility concentrations before, during, and after flooding (Chen et al 2022, Gu and Wong 2004, Rastegari et al 2021, Trukhina et al 2022).

Table 1.2. *Shows the different soil and porewater physicochemical changes during flooding. The table outlines the main physicochemical components, the physicochemical interactions, and how such interconnectedness influences PHE bioaccessibility.*

Physicochemical Parameter	Flooding	Physicochemical Interaction	Influence on PHE Bioaccessibility
pH	More Alkaline Conditions	Eh, Potassium, Calcium, Magnesium oxide, Iron	**Decreases** by reducing the solubilisation of the carbonate phase and promoting organo-ligand formation, decreasing PHE bioaccessibility (Ponting et al 2021).
Eh	Creation of Reducing Conditions	pH, salinity, Organic Carbon	**Decreases,** promoting sulfide complex formation, and **increases** solubilisation, stimulating the reductive dissolution of Fe-Mn hydroxides (Huang et al 2021).
Salinity	Unknown, dependent on the allochthonous input types	Eh and pH	**Unknown** effect of flooding depended on allochthonous inputs. **Decreases** PHE bioaccessibility by promoting PHE coprecipitation with DOC carboxylic groups; however, **increases** as salinity may compete for ligand binding sites (Asselman et al 2021).
Potassium	Increases	pH	**Increases**, alleviates the reducing conditions during flooding, decreasing sulfide formation; however, **decreases** as this may reduce the reducing dissolution of Fe-Mn hydroxides (Kelly et al 2020).
Iron	Unknown, dependent on the allochthonous input types	Potassium, pH, Eh, Chloride	**Decreases**, through irons binding capabilities via inner sphere monodentate bonding (Cundy et al 2008).

Calcium	Increases	pH, Fluorine	**Decreases**, calcium may increase solution pH and protect soil organic carbon (Bashir et al 2019).
Manganese	Unknown, dependent on the allochthonous input types	pH, Eh	**Decreases,** manganese oxides may bind with PHE within the vacancy sites (Flynn and Catalano 2019).
Magnesium	Unknown, dependent on the allochthonous input types	pH	**Decreases,** effective immobilisation agent, evidence within the literature (Mao et al 2021).
Organic Carbon	Increases	pH, Eh, Fe	**Decreases** through the chemical binding of humic and fulvic acids; **however**, such an effect is highly dependent on other physicochemical controls (Li et al 2023).

1.10 Physicochemical Interconnectedness - PHE Porewater Solubility, Solid Phase Distribution and Bioaccessibility

Soil and water physicochemical changes during flooding strongly influence PHE solid phase distribution, porewater solubility, and bioaccessibility; however, most work has focused on linear relationships (e.g., increasing soil pH influencing copper porewater solubility or decreasing iron concentrations influencing arsenic solubility) (Mendez et al 2017). In reality, physicochemical parameters influencing PHE solid phase distribution, porewater solubility, and bioaccessibility are dynamic, nonlinear, and highly interconnected (Figure 1.11, Gu and Wong 2004). For example, flooding can create reducing redox conditions, promote iron oxide reductive dissolution, and potentially increase the lead, copper, and arsenic porewater solubility from iron oxides (Xiong et al 2008). These reducing redox conditions also promote sulfide formation, eventually forming metal sulfide complexes and reducing PHE porewater solubility (Rastegari et al 2021). The example above concerning the redox conditions

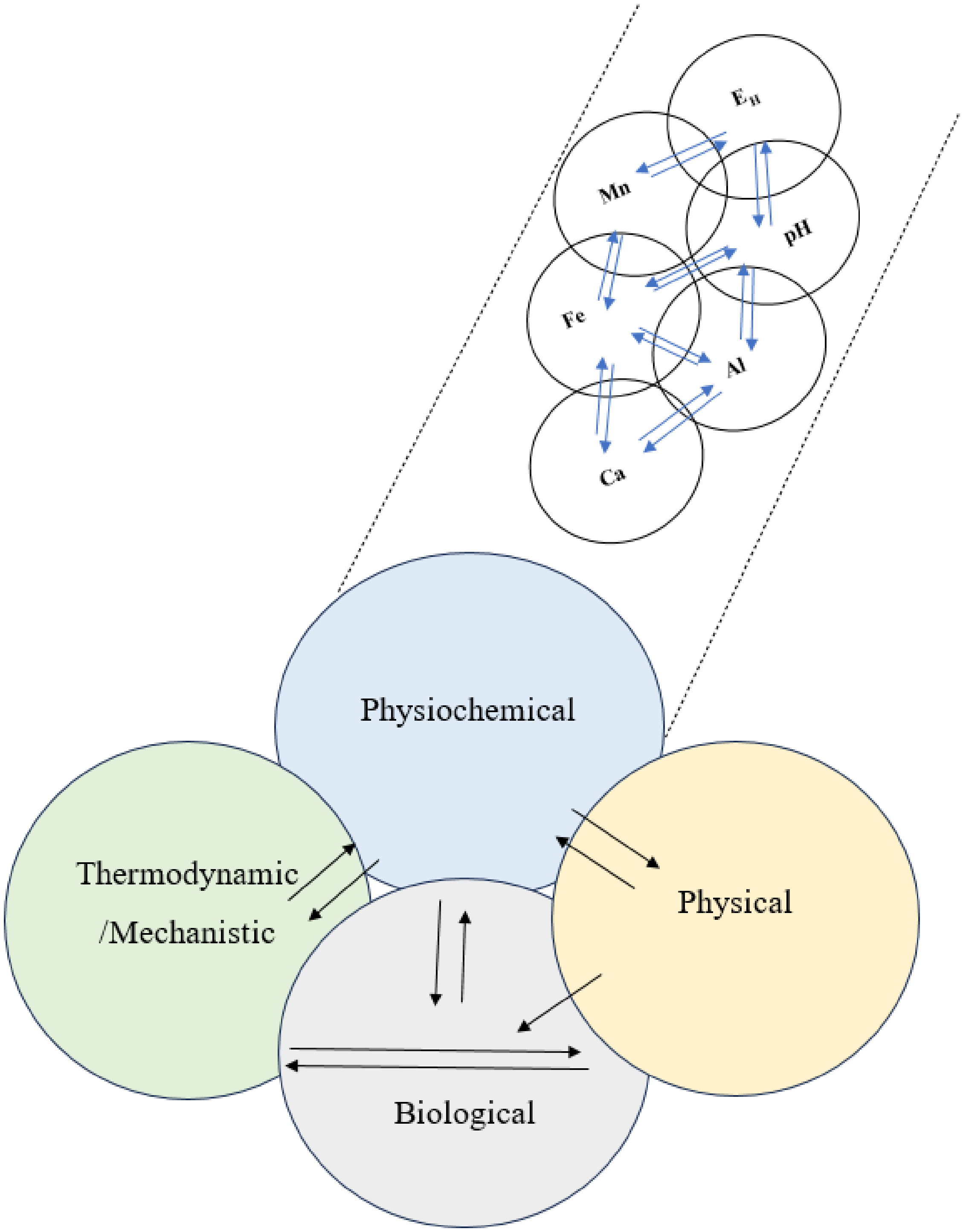

Figure 1.11. *Outlines the complexity between different variables (physicochemical, thermodynamic, physical, and biological) that influence PHE porewater solubility. The figure illustrates complex interactions within such variables (Gu and Wong 2004).*

The example above concerning the redox conditions highlight the inaccuracies of assuming reducing redox conditions can only increase or decrease PHE porewater solubility (Trukhina et al 2022). The issue with assuming linear correlations (i.e., one variable influencing another) is that these relationships can significantly oversimplify complex non-linear reactions (Rastegari et al 2021).

Another example of this “non-linear” relationship assumes that increasing soil and water pH alkalinity decreases PHE porewater solubility by reducing PHE dissolution from the acid-sensitive soil carbonate mineral phase (Chen et al 2022). However, increasing pH conditions also increase the concentration of hydroxide ions competing for available sorption sites with soil mineral phases, which may outcompete PHE for these ligand exchange sites, increasing PHE porewater solubility (McLaren 2019). These examples highlight that physicochemistry influences PHE porewater solubility non-linearly, which can both increase and decrease PHE porewater solubility (Ponting et al 2021).

Understanding these non-linear relationships is essential for predictive modelling using physicochemistry to estimate PHE dynamics (Gu and Wong 2004). However, it is not fully understood how these non-linear relationships influence PHE porewater solubility, and how to incorporate these complex interactions into predictive models (Chen et al 2022, Gu and Wong 2004, Rastegari et al 2021, Trukhina et al 2022).

Thermodynamic variables (e.g., water temperature and ambient water pressure) also influence this non-linear relationship between physicochemical changes and PHE dynamics (Huang et al 2021). For example, higher ambient water pressures increase soil porewater saturation (Trukhina et al 2022). Increased soil saturation alters physicochemical properties (principally the redox conditions) by restricting the diffusion of oxygen molecules (McLaren 2019; Xiong et al 2008).

The atmospheric ambient temperature strongly correlates with soil physicochemistry, particularly soil microbial communities and organic carbon concentrations, by promoting microbial respiration (Gu and Wong 2004; Li et al 2023). Such respiration rates increase because higher temperatures stimulate the enzymatic breakdown of organic compounds by increasing microbial enzymatic kinetic energy (McCauley et al 2009). This relationship between temperature and microbial respiration rate does not increase consistently with temperature increases, with the respiration rates generally decreasing when the ambient temperatures exceed 50ºC, which causes soil microbial enzymes to denature (Flynn and Catalano 2019).

The effects of rising ambient temperatures can increase soil microbial respiration rates, which accelerate organic carbon degradation, and decrease soil organic carbon concentrations, directly increasing PHE porewater solubility (Ponting et al 2021). This increasing PHE mobility is attributed to the strong relationship organic carbon has with binding and immobilising PHE through humic substances and fulvic acids (Hao et al 2023). Such correlations indicate a nexus relationship between thermodynamic variables (i.e., temperature), biological communities, and physicochemistry (organic carbon), all influencing PHE porewater solubility (Huang et al 2021; Ponting et al 2021).

Increasing ambient temperatures and soil microbial respiration may increase microbial oxygen demands because the higher temperatures accelerate microbial metabolism (Rastegari et al 2021). Increasing microbial oxygen demands reduce soil and water oxygen concentrations (Trukhina et al 2022). This oxygen concentration decrease may also decrease the redox potential; the term for this is called “oxidation-reduction potential” (Trukhina et al 2022). As discussed in Section 1.8.2, lowering redox potentials may influence sulfide formation, altering PHE porewater solubility by potentially increasing the formation of metal-sulfide cluster complexes and immobilising PHE (Rastegari et al 2021). This interconnectedness makes predicting PHE porewater solubility in soils highly complex because of the multilayered linkages between thermodynamic changes, biological community responses, and soil’s physicochemical changes (Li et al 2023).

These interlinked changes also vary depending on the physical elements, such as the land gradient, land use type, and vegetation coverage, all affecting soil surfaces (Lodygin and Abakumov 2022). Locations with steeper soil gradients influence flood water's physical velocity, impacting water's erosional ability on contaminated soils (Das et al 2011). The abundance of vegetation affects soil oxygen concentrations, with more vegetation coverage decreasing soil oxygen concentrations (Xiong et al 2008). As previously discussed, lowering soil oxygen concentrations influences soil microbial biological communities and alters soil physicochemical variables (McLaren 2019).

The land use type, underlying geology, and soil depth may influence the availability of minerals, soil compression, and surface runoff (Flynn and Catalano 2019). For example, if flooding occurs within agricultural land, the availability of fertilisers may alter soil biological community responses, impacting such soil enzymatic production (Lodygin and Abakumov 2022). Flooding can lead to the widespread dispersal and dilution of these fertilisers, which are typically concentrated within specific locations. If locations that are not originally fertilised receive this diluted fertiliser from floodwater, this can alter soil microbial communities, providing food sources to these microbes because these fertilisers contain several proteins, carbohydrates and fats (Flynn and Catalano 2019). Bohme et al (2005) show that organic fertilisation alters the activities of many soil microbial nutrient-cycling enzymes, particularly alkaline phosphatases, β-glucosidases, and proteases. Bohme et al (2005) also showed that these enzymes increase by providing rich organic materials that serve as a food source for many soil microbes.

Soil compression from agriculture may alter porewater absorption within soils, influencing hydrodynamic pressures (Lodygin and Abakumov 2022). Conversely, urbanised concrete locations reduce water infiltration, increasing surface runoff, which may change the water velocity and oxygen concentrations, and indirectly impact thermodynamic forces and biological communities, strongly influencing PHE porewater solubility (Shi et al 2018). The central message from this section is that complex interactions between physical variables, thermodynamics, soil microbial communities, and physicochemistry influence PHE dynamics.

1.11 Applying Statistical and AI Modelling to Interpret Physicochemical Interconnectedness and Predict PHE Dynamics

The soil and water physicochemistry strongly correlates with PHE solid-phase distribution, porewater solubility, and bioaccessibility during flooding (Ponting et al 2021) (Sections 1.7, 1.8, and 1.9, respectively). The complex non-linear relationships between physicochemical parameters influencing PHE dynamics pose significant challenges in understanding the changing physicochemistry impact during flooding on PHE porewater solubility, bioaccessibility, and solid-phase distribution (Flynn and Catalano 2019; Lodygin and Abakumov 2022; Ponting et al 2021; Rastegari et al 2021).

There are opportunities to explore the role of numerical modelling in identifying complex relationships, correlations, and patterns between physicochemistry and PHE dynamics (Gall et al 2018; Giesselman and Catran 2020). Such numerical models could include statistical methods like linear regression and mixed models, machine learning methods like random forests and extreme gradient boosting (XGBoost), and deep learning approaches like neural networks (Tyralis et al 2019). The fundamental difference between machine learning and deep learning approaches lies in the model's architectural decision-making (Sorenson et al 2019). Machine learning methods apply decision-tree approaches for predicting, whereas deep learning mimics how the human brain processes information (Brieman 1990).

This review will specifically analyse statistical mixed modelling. The purpose of selecting mixed models is that these models specifically address pseudo-replication within the dataset (Tyralis et al 2019). Addressing pseudo-replication is necessary because soil and water physicochemistry influencing PHE dynamics are likely interrelated rather than truly independent (Kuhn and Johnson 2013). The machine learning models selected include random forests and XGBoost for handling non-linear interactions, assessing feature variable importance, and their versatility in performing well on classification and regression tasks (Genuer et al 2010; Hastie et al 2009; Sorenson et al 2019). The deep learning approach selected is a feedforward neural network to compare different artificial intelligence architectures between machine and deep learning methods (Shaheen and Iqbal 2018).

1.11.1 Statistical Models

Mixed modelling is a form of regression analysis that incorporates fixed and random effects (Sorenson et al 2019). Fixed effects refer to the constant overall impact of physicochemical parameters influencing PHE dynamics (Gall et al 2018). Random effects denote the variation in PHE responses to physicochemical changes across land use types, time points, and experimental conditions (Gall et al 2018). Distinguishing between fixed and random effects is challenging, especially when the problem to predict is complex and highly dynamic (Shaver 2019).

1.11.2 Machine Learning Random Forests

Among the various artificial intelligence methods, the use of a multi-decision tree approach, such as random forests, has gained considerable attention and use for predicting PHE dynamics during flooding (Feng et al 2015; Lopez et al 2021; Sorenson et al 2019; Sun et al 2019). Random forests are supervised machine learning algorithms that combine the concepts of classification and regression trees using bootstrap aggregation (bagging) (Tyralis et al 2019). Supervised machine learning involves training random forests with known labelled datasets (Sun et al 2019). In other words, it is like giving a student a practice exam with the answers next to the questions to prepare the student for the exam with similar questions, representing the concepts of supervised learning. The principle of “bagging” in random forests involves averaging or calculating the mode output of the decision tree predictions (Sun et al 2019).

A random forest model consists of independent decision trees that split data to identify patterns and calculate the prediction, which is then averaged (bagging) across the decision trees (Sorenson et al 2019). The bagging process within random forests significantly reduces the bias within machine learning because multiple decision trees are attempting to calculate the prediction, reducing the model variance (Sun et al 2019). For an outline illustrating the design and processes of random forest modelling, see Figure 1.12 (Galiano et al 2014). Figure 1.12 shows the dataset (randomly coloured circles), highlighting each decision tree having a subset sample from the original dataset. The bottom of Figure 1.12 depicts the decision tree leaf (leaf node), the final predictor, with the coloured dot representing each decision tree prediction. The results are calculated using a voting classifier, with Figure 1.12 showing the most common prediction output from the different decision trees, which is the colour blue. Some random forests may produce unreliable predictions because poor-performing decision trees are averaged into the final prediction (Sorenson et al 2019).

By leveraging random forest models, it is possible, for the first time, to significantly upscale the analysis of PHE dynamics, deepening the understanding of how flooding influences PHE transport, fate, and behaviour (Genuer et al 2010). These random forests' popularity has grown considerably in computing science, ecology, and medicine since their introduction by Breiman in 2001 (Couronne et al 2018). Such popularity results from the random forests' unique ability to address the bias-variance trade-off in machine learning, handle high-dimensional datasets, and their hyperparameter tuning capabilities (Genuer et al 2010). In 1999, Breiman and Cutler introduced the random forest algorithm. For a historical timeline of the random forest model's development, see Figure 1.13 (Tyralis et al 2019). Extensive literature, including works by Breiman (2001), Biau and Scornet (2016), and the textbooks by Hastie et al (2009), Kuhn and Johnson (2013), and James et al (2013) elucidates the computational nature of random forest models.

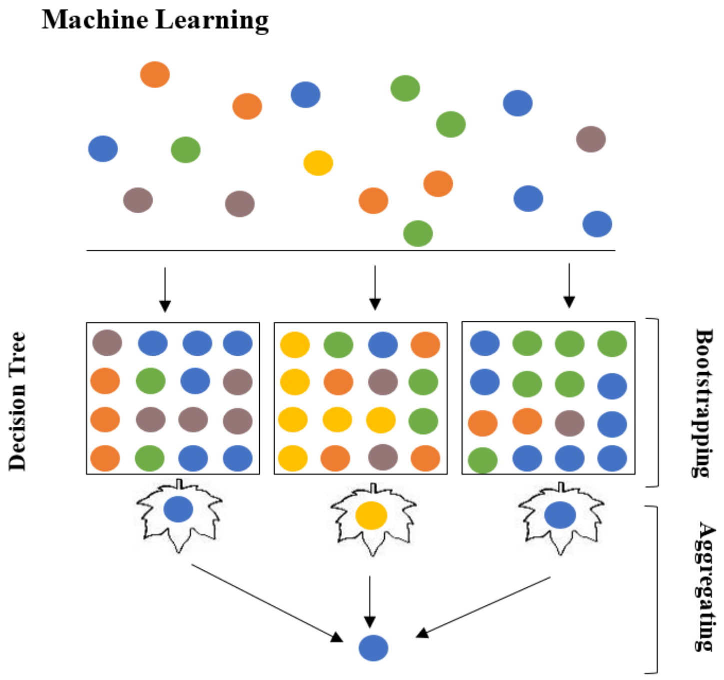

Figure 1.12. *Illustrates the random forest computational process, which involves splitting the data, classifying, and averaging the results using a voting classifier (Galiano et al 2014). The random coloured dots at the top of the figure denote the dataset. The three square boxes represent the different decision trees. The leaf symbol represents each decision tree's final prediction, and the single blue dot represents the random forest model's final decision.*

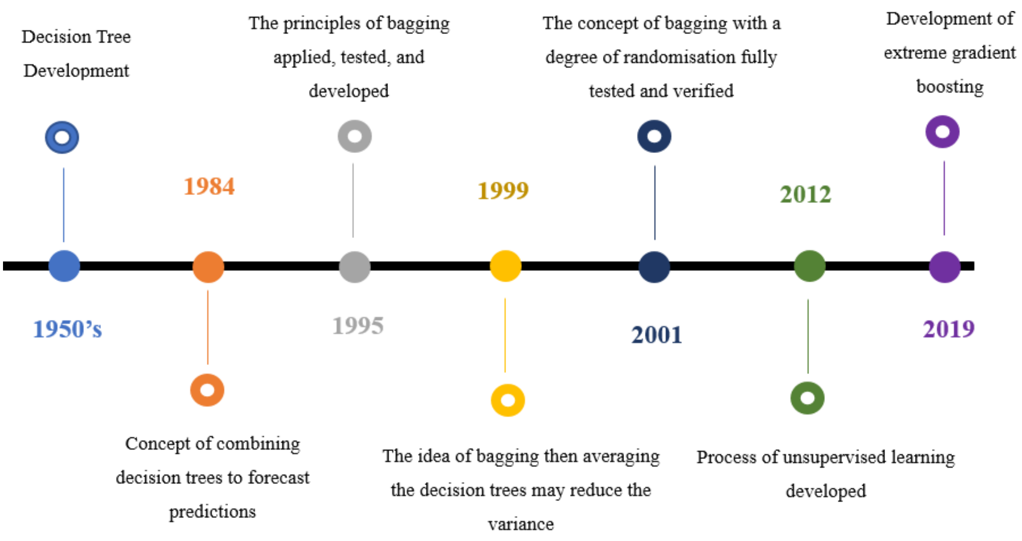

Figure 1.13. *Shows the chronological development of machine and deep learning algorithms. The timeline indicates that algorithms initially made early predictions using single decision-tree learners. The development of bootstrap aggregation enabled multiple decision trees to formulate predictions. This chronology shows that as time progressed, decision tree learners evolved from averaging decisions to learning the mistakes from previous decision trees (XGBoost) (Tyralis et al 2019).*

1.11.3 Machine Learning Extreme Gradient Boosting

XGBoost is an alternative to random forests, potentially achieving improved predictive performance by using a different approach to combining decision trees (Tyralis et al 2019). Rather than deploying the random forest approach of simultaneously averaging multiple decision trees to formulate predictions, XGBoost applies an iterative approach to decision tree learning (Shaheen and Iqbal 2018). For example, a random forest model may use fifty decision trees to formulate a prediction simultaneously. In contrast, XGBoost also uses fifty decision trees, but rather than simultaneously averaging the prediction, one decision tree formulates a prediction, and then the next decision tree updates and improves the previous prediction iteratively fifty times (Cutler et al 2007).

XGBoost can address the inherent challenges of dealing with high variance in random forest modelling (Section 1.11.2) (Hong et al 2019). XGBoost combines “weak” decision tree learners to form “strong” learners (Cutler et al 2007). By learning iteratively from the previous decision tree, the final prediction is less likely to have a high variance because each iteration aims to decrease the mean square error from the previous decision tree (Figure 1.14; Schubach et al 2017).

When a decision tree misclassifies (e.g., a decision tree says the prediction value is “x” when the actual estimate is “y”), an assigned penalty weight is applied (Hong et al 2019). For specific details about this penalty weight, see Chapter 4. The next decision tree iteratively “recognises” this penalty function and corrects the prediction (Hong et al 2019). The decision tree recognises this error by comparing the predicted outcomes with the actual outcomes and then measuring the difference (Hong et al 2019). Assigning penalty weights, recognising, and correcting the prediction iteratively can improve the XGBoost predictive performance by narrowing the differences between the predicted and the actual outcomes (Hong et al 2019).

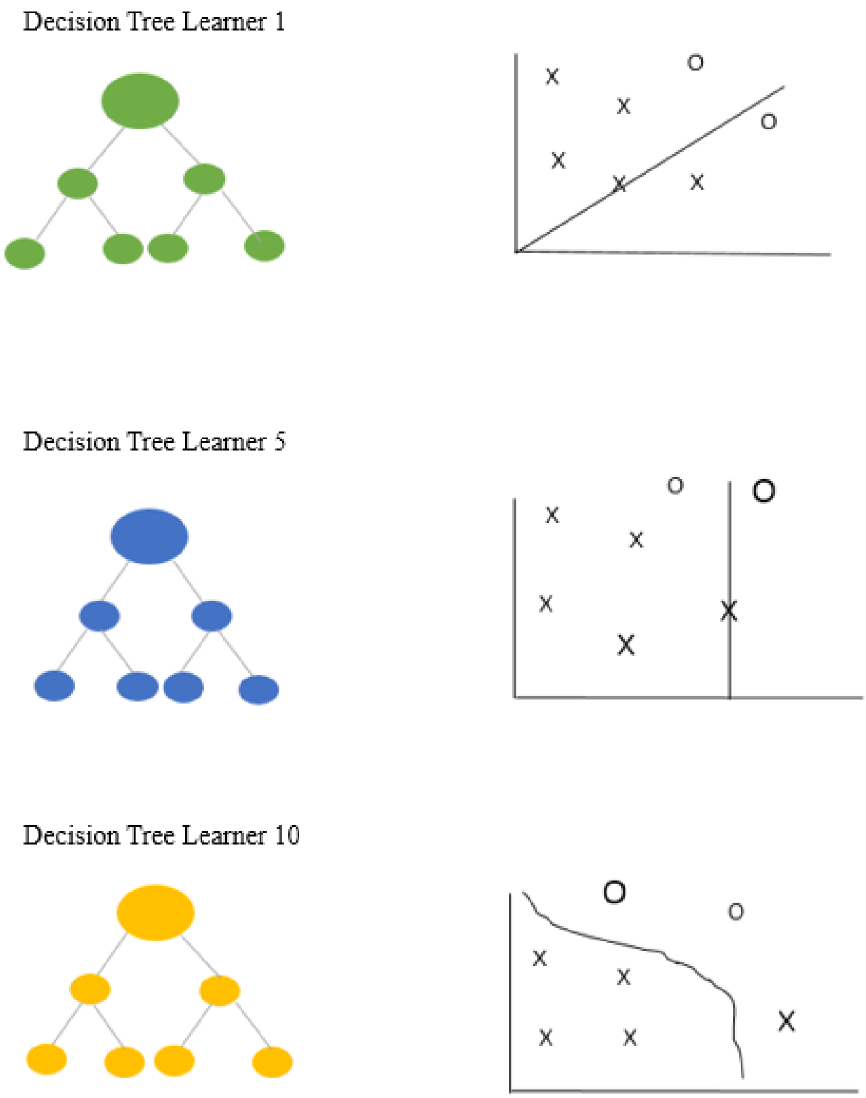

Figure 1.14. *Outlines the mechanisms of how XGBoost algorithms formulate predictions. The figure illustrates that when decision trees split, a mistake is assigned a penalty function (*Schubach et al *2017). The figure shows that decision tree one (green) splits the data; however, it misclassifies since there is an "x" and an "o" in a single split. The values "x" and "o" are assigned a penalty, making "x" and "o" larger for illustrative purposes (i.e., "X" and "O"). In the decision tree learner, the misclassified values "X" and "O," now larger, are seen by the next decision tree learner (yellow); however, again, the decision tree learner misclassifies "O." In decision tree 10 (yellow), with splits forming curvatures or becoming polynomial, attempting to classify the dataset better. The general essence of this figure is to show that when a decision tree misclassifies, this misclassification is emphasised to the next learner, with the attempt to iterate so that the final learner is aware of all the previous mistakes.*

1.11.4 Deep Learning Neural Networks

Deep learning neural networks are a sub-branch of artificial intelligence (Schubach et al 2017). These networks have three processing layers: input, hidden, and output (Figure 1.15; Schubach et al 2017). The input layer contains the dataset with all the feature variables; essentially, the input layer represents the dataset used to train the neural network (Galiano et al 2014). The hidden layer performs the decision-making processes, containing multiple neurons that interpret and analyse the data (Genuer et al 2010). The third layer is the output that produces the final prediction (Schubach et al 2017).

Once the initial prediction is made, the neural network enters a continuous learning phase (Galiano et al 2014). This learning phase is enhanced through the processes of backpropagation and stochastic gradient descent, which iteratively adjust and update the neural networks weights and bias values with the aim of increasing predictive performance (Galiano et al 2014). The process of backpropagation and stochastic gradient descent typically involves multiple steps (Schubach et al 2017).

The neural network is initialised with randomly assigned weights between the input, hidden, and output layers. In neural networks, "weights" determine the strength and direction of neural connections feeding into the hidden layer for decision-making processing (Galiano et al 2014). The input data are processed through the neural network, which produces an initial output prediction with an associated error. This error is calculated by comparing the output prediction with the observed testing data.

The backpropagation process then begins, which involves calculating the gradient of this error as it propagates through the neural network. The neural network evaluates all the randomly assigned weights and bias values through backpropagation. The neural network determines how much each weight contributed to the initial error, known as the loss function, within the hidden and output layers. These weights are updated and optimised to reduce the output error most significantly. Stochastic gradient descent involves updating these weights using a small batch of the training data (batch size) across the input, hidden and output layers, with updates occurring iteratively until the error is minimised. The updated output prediction is tested on unseen data, evaluating the predictive performance.

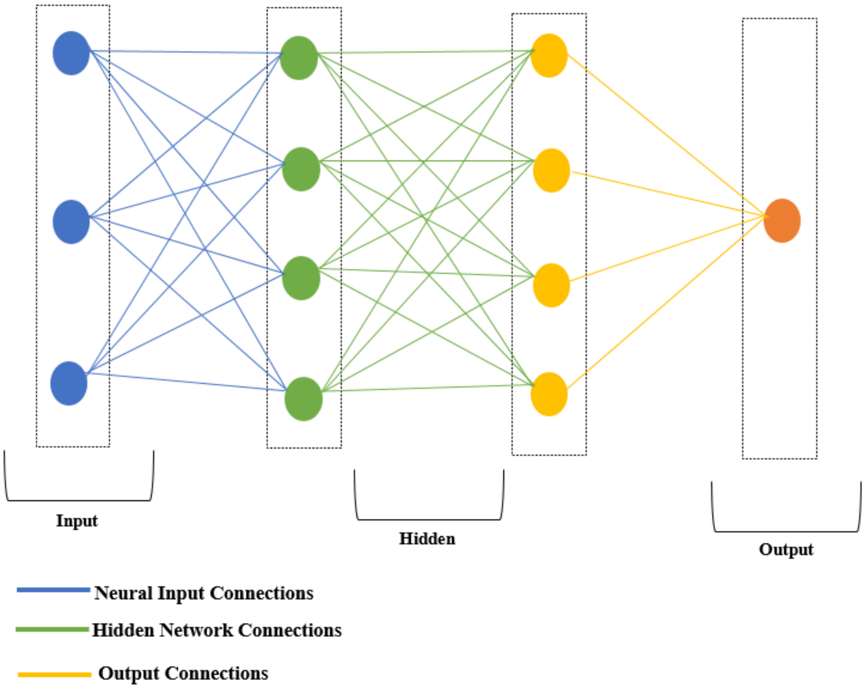

Figure 1.15. *Artificial neural network computational process outlining the input, hidden and output layers. The blue circles and lines denote the input layer of the neural network. This "input" layer equates to the training data implemented into this model. The green and yellow circles denote the "hidden layer." This layer is simply the decision-making center of this model, whereby the model iteratively adjusts its weights and bias based on attempting to reduce the output layer prediction mean square error (Schubach et al 2017).*

1.11.5 Comparing Predictive Model Variants to Estimate PHE Porewater Solubility, Bioaccessibility, and solid phase distribution

A rigorous critical evaluation is essential for utilising artificial intelligence or statistical models to predict and better understand PHE transport, fate, and behaviour (Genuer et al 2010). Statistical models aim to quantify relationships between variables, with the underlying assumption often being that such variables are normally distributed. Such models have provided an insightful analysis of which variables influence PHE dynamics (Gil et al 2015, Seidl et al 2022). AI models learn from the dataset by subdividing the data into testing and training subsets. Such models do not require data to be normally distributed and formulate predictions by learning patterns within the data.

The significant increase in the quantity and availability of data and much cheaper costs of parallel processing both mean there is an abundance of available data, code, and computer processors to perform data-intensive machine and deep learning AI. As discussed in Section 1.11, machine and deep learning models are within the umbrella term “AI.” The fundamental difference between such models are based on the model architecture, with machine learners using decision trees, and deep learners predicting using network designs, inspired by the biological system. Such opportunities for using AI approaches may significantly enhance understanding of how flooding remobilises PHE and how to monitor such transport. The reason why this understanding is enhanced is because such models fundamentally analyse, process and interpret data differently from statistical approaches, by splitting the dataset into training, validation, and testing data. To date, there is limited understanding around analysing and comparing how AI approaches could play a role in predicting PHE porewater solubility, bioaccessibility and solid phase distribution to statistical models.

This thesis literature review qualitatively analyses and then compares, for the first time, the current literature that uses AI and statistical approaches, investigating the suitability of AI and conventional models for estimating PHE porewater solubility, bioaccessibility and solid phase distribution. Such analysis involves comparing statistical and AI models to analyse PHE dynamics regarding the user-friendliness of the model, its robustness, and its predictive performance.

1.11.5.1 User Friendliness and Interpretability

Examining any dataset using AI is straightforward, by automatically capturing non-linear dependencies between the predictor and dependent variables (Galiano et al 2014). Unlike traditional linear models, which only capturing linear relationships, AI can also uncover non-linear trends (Noye et al 2022, Tao et al 2021).

For instance, Cutler et al (2007) showed the success of RF models for chemical species distributions, by capturing non-linear relationships between environmental variables such as temperature and precipitation. This makes RF modelling a powerful tool in environmental research. Such reliability of RFs derive from the non-parametric nature of AI, meaning the model does not rely on assumptions about the underlying data distribution, making the model flexible and versatile (Hong et al 2019).

This flexibility allows AI to handle highly correlated variables (Tyralis et al 2019). On the other hand, statistical models require assumptions around the data distributions, and are incapable of handling non-linear relationships (Tyralis et al 2019). In other words, the main reason why AI approaches can handle highly correlated variables, unlike conventional methods, is because AI methods learn feature relationships at different levels or processing layers. For example, imagine PHE interacting with different physicochemical parameters; these interactions could include with calcium, organic carbon, and iron. In this example, AI approaches can create multiple layers of such interactions with high intricacy; one layer could be PHE interacting with calcium and another layer could be with ionic bonding with iron hydroxide. This layering approach processes relationships much better than conventional statistical models which do not layer such data and, rather, use predefined equations, such as normality, to address non-linearity. A major limitation of AI modelling is that it can be considered a “black box” model, lacking transparency to users around the mechanistic understanding that underpins the predictions (Cutler et al 2007).

The term “black box” refers to the model’s inner workings not often being understood or explained to users (Zednik 2021). Lack of transparency may lead to misinterpretations of the results or assumptions, hindering the identification of potential model biases (Shaheen and Iqbal 2018). Galiano et al (2014) showed the "black box" nature caused many users to interpret the model using simplified and stylised versions (Galiano et al 2014). Statistical models contain inbuilt and highly developed checking mechanisms, ensuring the model is understood and interpreted correctly, including residual analysis, cross-validation, and assumption checks (Tyralis et al 2019). AI models do not require such assumption checks, thus these models have advantages of being able to handle highly correlated variables and noisy datasets from its inbuilt mechanisms and by tuning hyperparameters (Hong et al 2019). The concept "hyperparameters" is outlined in detail in Section 4.1.3 (Chapter 4); however, hyperparameters refers to the black box mechanisms used to generate the predictions, such as the learning rate of the model, how many decision trees process the data, or how many data splits.

In contrast, statistical models have been used extensively to date, offer transparent and interpretable frameworks, and better visualisation and user friendliness around the direction of relationships and quantifying uncertainty, which is not apparent within the AI model's "black box" (Tyralis et al 2019).

1.11.5.2 Model Robustness and Stability

The AI system configurations increase the model robustness because the inbuilt default parameters typically require minimal modification (Genuer et al 2010). Such default parameters (e.g., number of neurons, learning rate, and number of hidden layers) are initially set by developers, who use empirical evidence to allow such default parameters to cover as many data predictions at varying complexities (Feng et al 2015). For example, in MATLAB (MathWorks Inc), the 'fitnet' function, used to program a neural network, has a default parameter of having only a single hidden layer (Shaheen and Iqbal 2018).

Many predictive applications may only require a single layer, given the low to mid-level of complexity, preventing inexperienced users from accidently computing two hidden layers, leading to machine learning issues relating to overfitting, discussed in Chapter 4. By "low to mid-level complexity," this is subjective, but in this context, this means where there is roughly 2-8 feature variables influencing the predictor (Genuer et al 2010). Such default parameters can be adjusted and hyperparameter tuned if necessary (Shaheen and Iqbal 2018).

The central argument is because these models have default parameters, aimed at addressing the most likely data complexity problems - it minimises the likelihood of inexperienced users incorrectly programming such models (Feng et al 2015).

AI model robustness can be limited as it may struggle to extrapolate predictions outside its training range due to reliance on learned patterns within the training data (Sinha et al 2019, Feng et al 2015). Such implications are important to recognise because environmental variables, particularly those associated with physicochemistry, can vary significantly, meaning a model may struggle to generalise the complex relationships in dynamic systems (Sinha et al 2019). Breiman et al (2001) suggested if a RF model is trained on temperature data ranging from 0-30°C for example, it may struggle to formulate accurate predictions outside this temperature range.

The capturing of such non-linear relationships and the ability to handle spatial dependencies within the data may still result in many researchers preferring such models over statistical approaches (Genuer et al 2010). Uriarte and Andres (2006), showed AI modelling performed well (regarding high accuracy, precision, and recall) when addressing noisy datasets within fields of medicine and biology, notably for gene selection predictions. While statistical models, such as regularised regression (e.g., LASSO or ridged), offer variable selection mechanisms to mitigate irrelevant or noisy data (i.e., variables not relevant for predicting the target variable) (Hong et al 2019); statistical models still have a limited ability to handle highly multidimensional data unlike AI models (Hong et al 2019). Multidimensional data can create challenges in model estimation, interpretation and in some cases increase computation demands, decreasing the model robustness, irrespective of such models offering variable selection mechanisms (Hong et al 2019).

In regards to this research attempting to predict PHE porewater solubility, bioaccessibility and solid phase distribution, using physicochemistry data, there are multiple non-linear relationships (see Section 1.10). Such relationships are also potentially very noisy given such high spatial variation of soil contamination and chemical properties, for example, Pb in UK soils (Figure 1.2). This non-linearity and noisy data mean that such data used within this research may become highly multidimensional, emphasising the importance of exploring the role of the machine and deep learning approaches.

1.11.5.3 Predictive Performance

AI models have several tuning parameters (e.g., number of decision trees and tree depth) that help reduce the predictive bias and variance (Ghosal and Hooker 2020). For example, deeper trees may reduce the prediction bias, as more decision tree splits capture more information (Salles et al 2021). Increasing the decision tree numbers can reduce the model variance; each decision tree is trained on different data subsets; when such trees are combined, the prediction errors likely cancel out, known as "averaging out the error" (Ghosal and Hooker 2020).

The ability of RF modelling to use the "out-of-bag data" to assess the "Variable Importance Metric" (VIM), increases predictive performance and addresses data multidimensionality by selectively removing noisy features (Genuer et al 2010). Briefly, the "out-of-bag" data refers to the data points not included in the bootstrap resampling for training such decision trees (Salles et al 2021). Briefly, "bootstrap resampling involves creating several subsets of the original dataset, by sampling with replacement, and creating multiple decision trees based on each subset so that each decision tree is fundamentally unique. This data increases the predictive performance by determining important feature predictive variables (VIM) (Ghosal and Hooker 2020). Such data compares the feature variables with the predictive estimate; if a removal of a particular feature results in a significant decrease in the predictive error, then such feature is removed (Ghosal and Hooker 2020). In contrast, statistical models require no tuning, variable importance metrics or randomisation, however this increases variance and bias, and reduces predictive performance (Ponting et al 2021). Such models are inherently less prone to overfitting as they typically have fewer parameters to estimate in the first place (Roelofs et al 2019).

AI modelling can be more susceptible to the negative impacts of imbalanced data than statistical models, which can negatively impact predictive performance (Jabbar and Khan 2015). Imbalanced data refers to a situation where the dataset classes are unevenly distributed, for example, where one class is significantly more prevalent than another (Krawczyk 2016). Such imbalanced data has "more serious” consequences on RF modelling than statistical approaches because RF make decisions through voting or averaging, resulting in a decision boundary bias towards the majority class (Schubach et al 2017). The term “voting” or “averaging” refer to when multiple decision tree outputs are averaged, if a regression (number) problem occurs, or using a “voting” term, if the problem is binary or classification, whereby the modal value is calculated, essentially having the most “votes” from the decision tree. Despite these differences in the types of models, exploring the effectiveness of both statistical and AI approaches can lead to improvements in the understanding around how these different model types can discover new insights, correlations, patterns and potentially predictions around PHE dynamic changes during flooding (Jabbar and Khan 2015, Krawczyk 2016).

This mini-critical review highlights that while AI models have inherent properties that enhance robustness and predictive performance, statistical models are simpler and more user-friendly. However, AI models are generally more robust because of hyperparameter tuning, randomisation and selection of variable importance. The application of AI can offer unique insights into better understanding of the role solid phase distribution and porewater solubility has on PHE bioaccessibility. Although, there should always be caution around the AI models “black box” nature to avoid making premature assumptions and interpretations. Statistical models may underperform over AI; however, offer opportunities to complement AI approaches through data interpretation, validation, and visualisation.

1.12 Project Aims

This thesis has five central aims addressed individually within the following five chapters. The first aim is to,

- Quantify the effect of flooding on soil PHE porewater solubility and, using a meta-analysis, establish how rising ambient temperatures influence microbial respiration, community structures and thus porewater solubility.

The second aim is to

- Investigate the role of soil physicochemistry in correlating and estimating PHE porewater solubility, bioaccessibility, and solid phase distribution.

Thirdly, this thesis,

- Examines the role of AI machine and deep learning approaches when using physicochemical data to predict PHE solubility, bioaccessibility and solid phase distribution.

Fourthly, to

- Test AI approaches predictive performance when estimating PHE porewater solubility, bioaccessibility and solid phase distribution by comparing outputs to the results from microcosm and mesocosm experiments.

Finally, to

- Verify AI model predictions.
- explore how thermodynamic, biological, and physical data influence PHE dynamics and to see if the inclusion of these data can improve the predictive performance of AI models.

Chapter 2: Thesis Structure

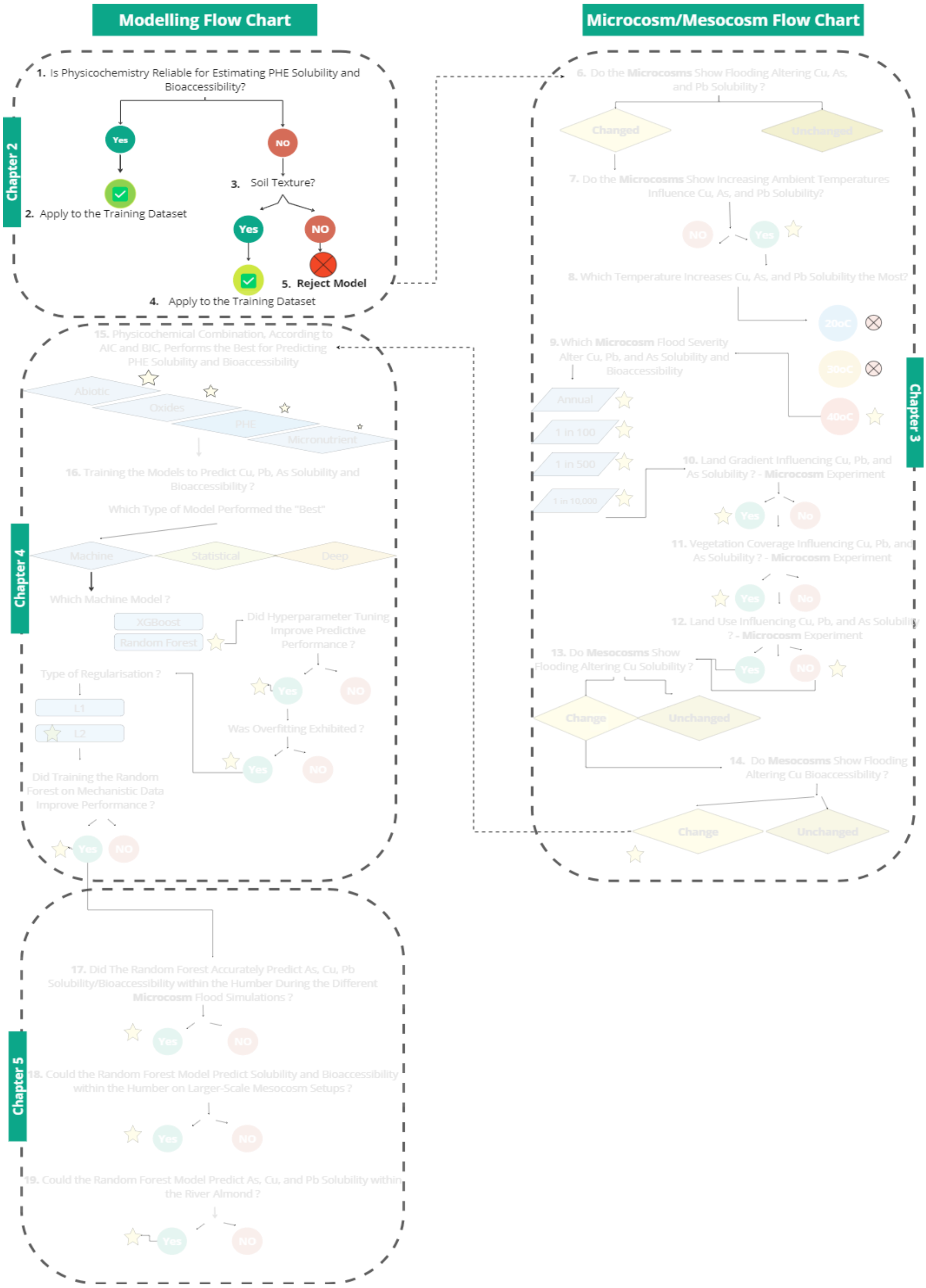

Chapter 2: Flooding, Climate Change, and Physicochemistry: A Potentially Harmful Element Mobility and Bioaccessibility - A Meta Analysis

2.1 Introduction

Anthropogenic climate change and rapid urbanisation have exacerbated the effect of flooding both in terms of frequency and magnitude (Dube et al 2021). Estimates indicate that 52% of the worldwide population will be at risk of flooding by 2100 (Kirezci et al 2020). The phenomena of fluvial flooding may chemically remobilise contaminated riverine sediments. This contamination frequently derives from industrial activities, such as the exploitation of natural resources (e.g., chromite), urban expansion, and intensive agricultural practices, all releasing significant PHE concentrations, such as arsenic, zinc, and lead, into fluvial systems (Nel et al 2018) (Figure 2.1 (1), Shaun Leishman 2023).

Such PHE initially are bound to mineral fractions within geological materials; however, through human exploitation of soil and minerals, these elements eventually become mobilised and distributed within the environment. These PHE overtime sequester and may become immobile within riverine sediments (Devi and Khatua 2017). Turbulent flow velocities can erode, resuspend, and chemically remobilise these sediments downstream still (Figure 2.1, (2)), potentially depositing them onto floodplains (Figure 2.1, (3)). Currently, 68 million people worldwide reside on floodplains susceptible to flooding, and who are therefore potentially exposed to remobilised PHE (Figure 2.1, (4)).

Flooding influences the physicochemistry of soil and water (e.g., redox potential (E_H) and pH) by creating anaerobic conditions (Kilunga et al 2017). These physicochemical changes affect PHE solubility (i.e., the partitioning with sediment mineral phases, such as oxides and carbonates) (Seo et al 2017). For example, higher pH conditions created during a flood, through the consumption of available hydrogen ions, influence PHE solubility with acid-sensitive carbonate phases (Kelly et al 2020). Similarly, lower redox potentials lead to reductive dissolution of iron, solubilising PHE (Liu et al 2021). This inherent correlation between physicochemistry and PHE mobility may provide insights into using physicochemistry data to predict PHE changes during flooding.

This study conducts a meta-analysis, investigating what controls PHE mobilisation during flooding, aiming to quantitatively analyse how flooding affects PHE solubility within different soil types. The study also aims to establish how increasing temperatures from climate change influences mobility.

Figure 2.1. *Flooding remobilises PHE downstream, eventually depositing such contaminated sediments onto floodplains, exposing humans and wildlife to remobilised PHE (Shaun Leishman, 2023).*

2.2 Methods

2.2.1 Search Strategy

Systematic searches were conducted within multiple databases (e.g., Google Scholar, Web of Science, Oxford Journals) (Table A2.1, Appendix A). Literature searches with search strings "*potentially harmful element* " AND "*remobilisation*" identified relevant journal articles using forward and backward searches (Table A2.2, Appendix A). For an example of some search engines, number of results and the search string, see Table 2.1 below.

Table 2.1. *Outlines an example of search engines used within this meta-analysis, indicating the specific words typed into such databases and outlines the number of search results from the input word string.*

Database	Number of Search Hits Per Database	Example Search String
Google Scholar	821	"Contaminant" AND "Remobilisation"
Web of Science	24	"Flooding" AND "Contaminant"
Oxford Journals	197	"Flooding" OR "Contaminant" AND "Remobilisation"

2.2.2 Eligibility Criteria and Selection Process

An inclusion set of criteria, a selection of multiple eligibility statements enabling consistency and objectivity, was used to identify relevant literature (Koricheva et al 2018). These criteria dictated that all identified papers needed to provide statistics for calculating effect sizes, and be peer-reviewed (Table A2.3, Appendix A). Journal articles were selected following the PRISMA (Preferred Reporting Items for Systematic Reviews and Meta-Analyses) guidelines by Fleming et al (2014). This is a multi-stage screening process assessing potential studies for a meta-analysis. The PRISMA guidelines help to identify, using key search strings, relevant journal articles. Abstracts were screened for suitability and the entire text was read and compared against these eligibility statements. The meta-analysis identified 327 journal articles (Figure 2.2, amended from Cohen and Fleiss 1973) and (Tables A2.4, A2.6, and A2.9, Appendix A).

A Cohen's Kappa coefficient analysis determined the inter-rater reliability between two qualified individual reviewers selecting the journal articles. The analysis requires and compares the decisions of two reviewers, based on the meta-analysis eligibility criteria and the PRISMA guidelines, to help determine whether a journal article is included or excluded. This analysis subsampled 15 journal articles for comparison. Conducting a Kappa analysis determined the consistency of judgement and analytical decision-making when selecting journals against the eligibility guidelines. The analysis generated a 62% agreement, exceeding the minimum requirement of 60% for passing a Kappa analysis (Cohen and Fleiss 1973) (Table A2.5, Appendix A)

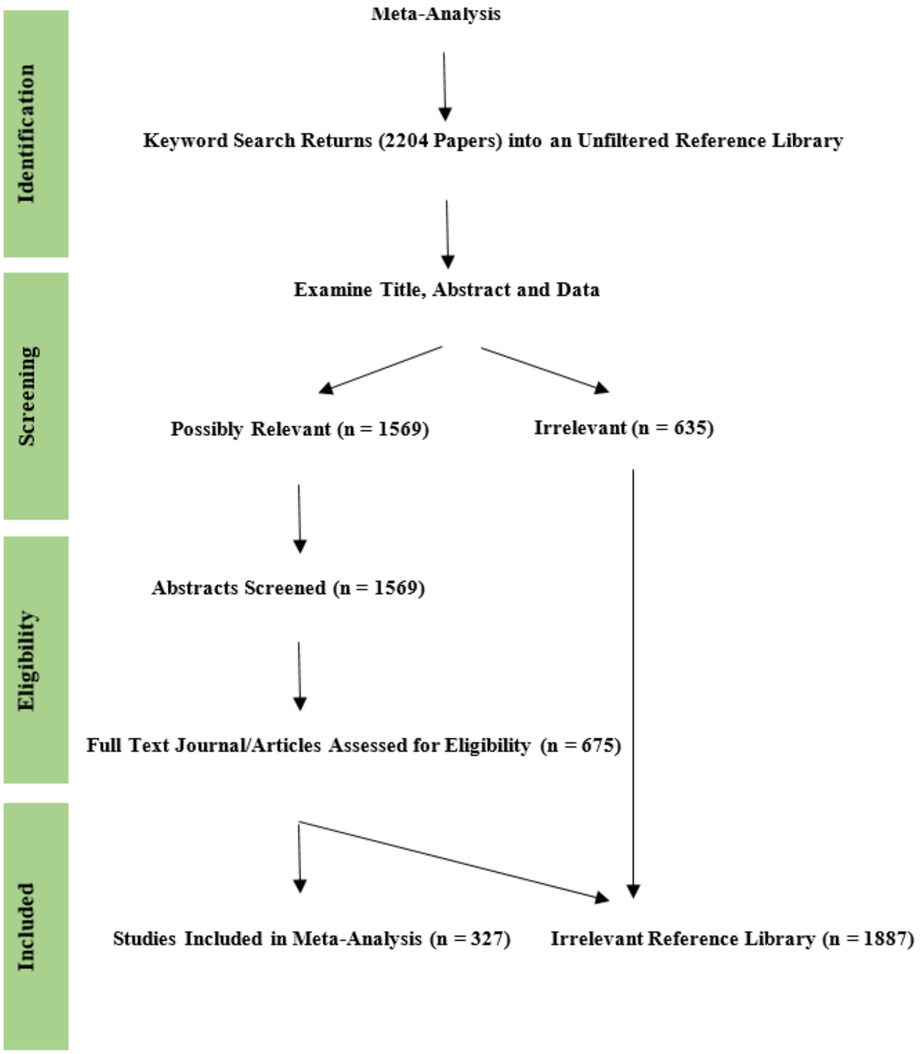

Figure 2.2. *Flowchart showing the search strategy for selecting studies. Such studies meeting the inclusion criteria were included, totalling 327 (Cohen and Fleiss 1973). The number "1887" is generated by two steps. The first step involves placing the 635 irrelevant journals into the irrelevant reference library.*

2.2.3 Effect-Size Calculation

All the total chemically remobilised PHE concentrations within flooded soil porewater were converted to the same unit (µg/L) pre and post flooding. For the specific PHE types analysed, see Table A2.8, Appendix A. Converting all the concentrations to µg/L ensured uniformity and comparability between the studies used within this meta-analysis. Standardising the concentration matrix also allow more straightforward interpretation and analysis of the chemically remobilised PHE concentrations.

The effect sizes were calculated using the control and treatment groups' sample sizes, averages and standard deviations. The control group represents the PHE concentrations before and the treatment group after flooding. Effect sizes were calculated using Hedges'd standardised mean difference (Hedges et al 1999), Equation 2,

$d = [(X_O - X_Y/s]\ J$ **Eq. 2.**

where "X_O" represents the mean PHE concentration before flooding and "X_Y" indicates it post-flooding. The letter "*s*" is the pooled standard deviation, and "*J* " is the correction factor (Hedges et al 1999). Large effect sizes indicate $d = > 0.8$, medium is $d = 0.2 - 0.8$, and small is $d = < 0.2$. Positive effect sizes indicate locations that have higher soil porewater PHE concentrations, and negative effect sizes represent lower soil porewater PHE concentrations after a flooding event. A meta-analysis was computed using a single mixed-effects model with a restricted maximum likelihood estimator using the *dmetar* package within RStudio (Version 3.3.0; Pisanu et al 2019). Mixed-effect models can account for residual heterogeneity and pseudo-replication in the data analysis of soil porewater PHE concentrations across different flooding events and geographical locations. Regression diagnostics evaluated the model assumptions using the *PResiduals* package (Ritter et al 2019). The high residual heterogeneity observed was analysed by splitting and comparing all the subgroup participant data (e.g., inorganic) according to the individual PHE (e.g., lead, copper, arsenic) using a random-effects model. The random-effects model was chosen to make "broad-level" inferences across all the PHE analysed (Higgins et al 2009).

2.2.4 Publication Bias

This meta-analysis examined publication biases (the tendency for studies to only present statistically significant results) using sunset (power-enhanced) and contoured funnel plots using the *metaviz* package (Kossmeier et al 2020). These plots assessed the credibility of effect sizes in the meta-analysis studies. The power analysis depicts the study-level statistical power computed for a two-sided Wald test. Fail-safe N calculations quantified the minimum number of insignificant, unpublishable, or absent studies required to nullify the effect size, creating statistically insignificant results (Rosenberg 2005). Such publication analysis is important for quantifying the quality of the studies that generate such effect sizes (Simmonds 2015). The term “quality” in the last sentence, refers to the likelihood of the study reporting only statistically significant results and deliberately omitting statistically insignificant results, this is referred to a bias.

2.3 Results

2.3.1 Flooding Influencing PHE Porewater Solubility

The post-flooding porewater solubility of radionuclide, microplastic, organic, and inorganic PHE showed statistically significant positive effect sizes (Figure 2.3 and Table 2.2). In Figure 2.3, the plot shows the mean effect sizes (black dots) shifting to the right-side of the dashed line, indicating positive effect sizes. Such findings also show that flooding increases PHE porewater solubility, irrespective of any differences in PHE chemistry as all the PHE types investigated have positive effect sizes to the right hand side of the dashed vertical line (Figure 2.3). Radionuclide PHE (e.g., caesium-137) had the largest, and organic compounds (polycyclic aromatic hydrocarbons) had the lowest positive effect sizes (d = 0.604, d = 0.189, respectively). Fail-safe N calculations showed that between 15 and 1873 additional negative studies were required for these findings to lose their statistical significance (p = < 0.001).

Despite radionuclide, microplastic, organic, and inorganic PHE porewater solubility increasing, there were remobilisation response differences between (Q_m = 9.463; p = 0.024) and within (Q_m = 4.371, p = <0.001) the PHE groups. In simpler terms, all the four PHE types (i.e., radionuclide, microplastics, organic, and inorganic) increased; however, the individual PHE within each group (e.g., lead, cadmium, copper within the inorganic group) did not all uniformly increase.

A subgroup analysis investigated the effect of PHE type on porewater solubility, revealing a statistically significant subgroup effect (Figure 2.4). For example, these findings mean that different PHE types within the inorganic PHE classification (e.g., lead, zinc, nickel) remobilise differently with statistical significance, irrespective of whether these PHE are all inorganic types. Flooding was shown to influence PHE porewater solubility within the four PHE moderator groups differently, meaning the subgroup effect is qualitative with high levels of heterogeneity (Table 2.3). The term "moderator" refers to the PHE grouping (i.e., organic, inorganic, radionuclide, microplastic) which all influence the effect size. By "heterogeneity," this means the effect-size between the different PHE within each subgroup (organic, inorganic, radionuclide and microplastic) exhibit high variance. For example, the porewater solubility of arsenic decreased ($d = -1.671$, $p = 0.064$), whereas the porewater solubility of lead, zinc, and copper increased, suggesting that metals and metalloids mobility differ. Some confounding factors, such as the soil texture and variable physicochemical conditions, may influence this qualitative effect, leading to incorrect conclusions however so care must be taken with the interpretation. These findings reveal that when attempting to predict a PHE mobility during flooding it is significantly important to understand that the mobility of PHE is not all the same within the inorganic, organic, radionuclide and microplastic PHE types. In other words, assuming that if lead PHE remobilises then other inorganic PHE types, such as arsenic, will also mobilise could be misleading and incorrect because of variations in mobility responses between metals and metalloids.

Table 2.2. *Mixed-effects model outputs outlining the effect size statistics for radionuclide, microplastic, organic, and inorganic PHE. All confidence intervals represent the acronym "CI" at the 95% level. The standard error indicates the variance of such meta-analysis estimates.*

Moderator	Estimate	Standard Error	Z-Value	p-Value	I^2	Lower CI	Upper CI
Radionuclides	0.604	0.107	5.684	<0.001**	78%	0.329	1.320
Microplastics	0.276	0.112	2.460	0.014*	99%	0.218	0.638
Organics	0.189	0.067	2.361	0.018*	97%	0.027	0.289
Inorganic	0.267	0.081	4.379	<0.001**	99%	0.222	0.644

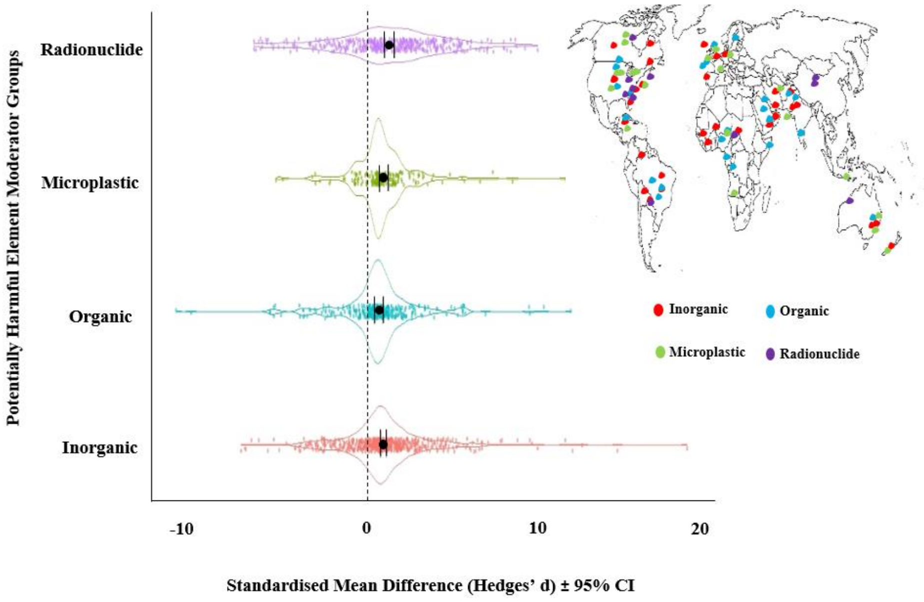

Figure 2.3. *The effects of flooding on radionuclide, microplastic, organic, and inorganic porewater solubility. The black circles denote the mean pooled effect sizes (d) ± one standard deviation. The smaller coloured circles represent the individual effect sizes for each study used to generate the mean effect size, indicates at the black dots. The vertical dashed line differentiates between positive and negative effect sizes. The smaller coloured dots refer to the individual effect sizes used to generate the average effect size (black dot) and is presented to illustrate the variation of data, also aided using violin plots.*

Table 2.2. *Mixed-effects model outputs outlining the effect size statistics for radionuclide, microplastic, organic, and inorganic PHE. All confidence intervals represent the acronym "CI" at the 95% level. The standard error indicates the variance of such meta-analysis estimates. The "I^2" assesses the degree of heterogeneity among the effect sizes. High I^2 percentages indicate high heterogeneity.*

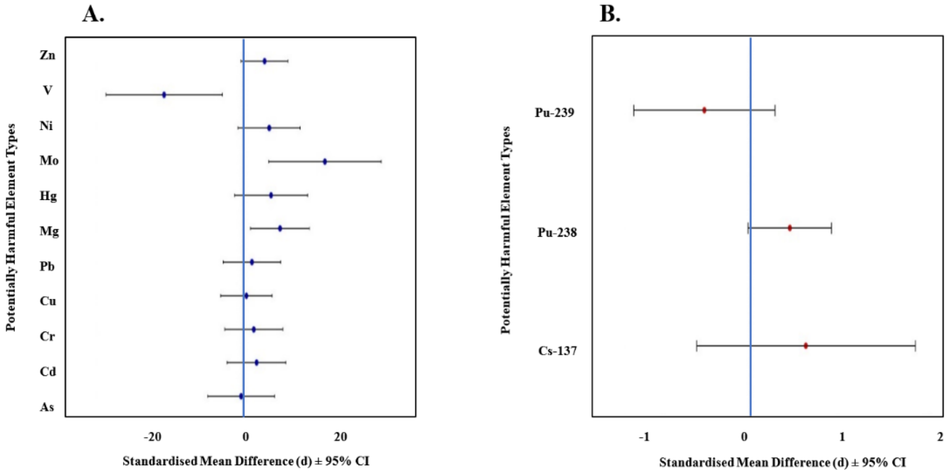

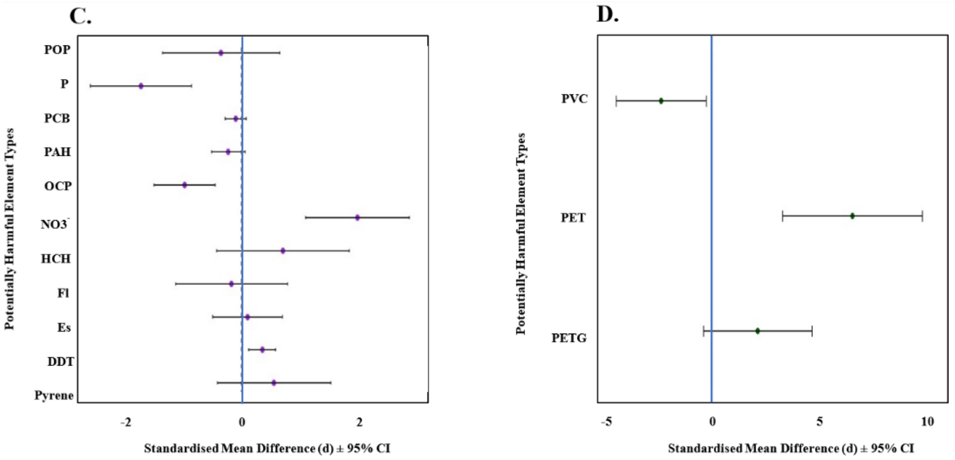

Figure 2.4. *Subgroup analysis showing the mean effect sizes in subgroups A (inorganic), B (radionuclide), C (organic) and D (microplastic) categories in response to flooding (*p = <0.05, **p = <0.01,***p = <0.001). The effect sizes showed the effect of flooding increasing or decreasing the different PHE porewater solubility. The vertical line indicates the division between positive (right hand) and negative (left hand) side of the vertical line. The solid dark dots indicate the mean effect size with the associated upper and lower confidence interval error bars from the mean effect size.*

Table 2.3. *The subgroup affects the impact of flooding on different PHE porewater solubility. The subgroup effects were statistically significant with high levels of variation (I^2).*

Moderator	**Subgroup Effect**	**Level of Heterogeneity (I^2)**
Inorganic	*P* = 0.04*	52%
Radionuclide	*P* = 0.002**	87%
Organic	*P* = 0.002**	98%
Microplastic	*P* = 0.004**	96%

2.3.2 The Effects of Soil Texture on PHE Porewater Solubility

The soil physicochemical properties were shown to influence PHE porewater solubility. Sandy soil type textures statistically significantly increased PHE porewater solubility, especially when compared with silt and clay particle sizes which decreased, remobilisation (Figure 2.5, Table 2.4). Soil properties exhibiting a high organic carbon content (i.e., peat) and an alkaline pH (i.e., calcareous) decreased radionuclide, organic, and inorganic PHE porewater solubility. Fail-safe N calculations show that between 19 and 1624, additional negative studies would be required for these findings to lose statistical significance ($p = 0.041$).

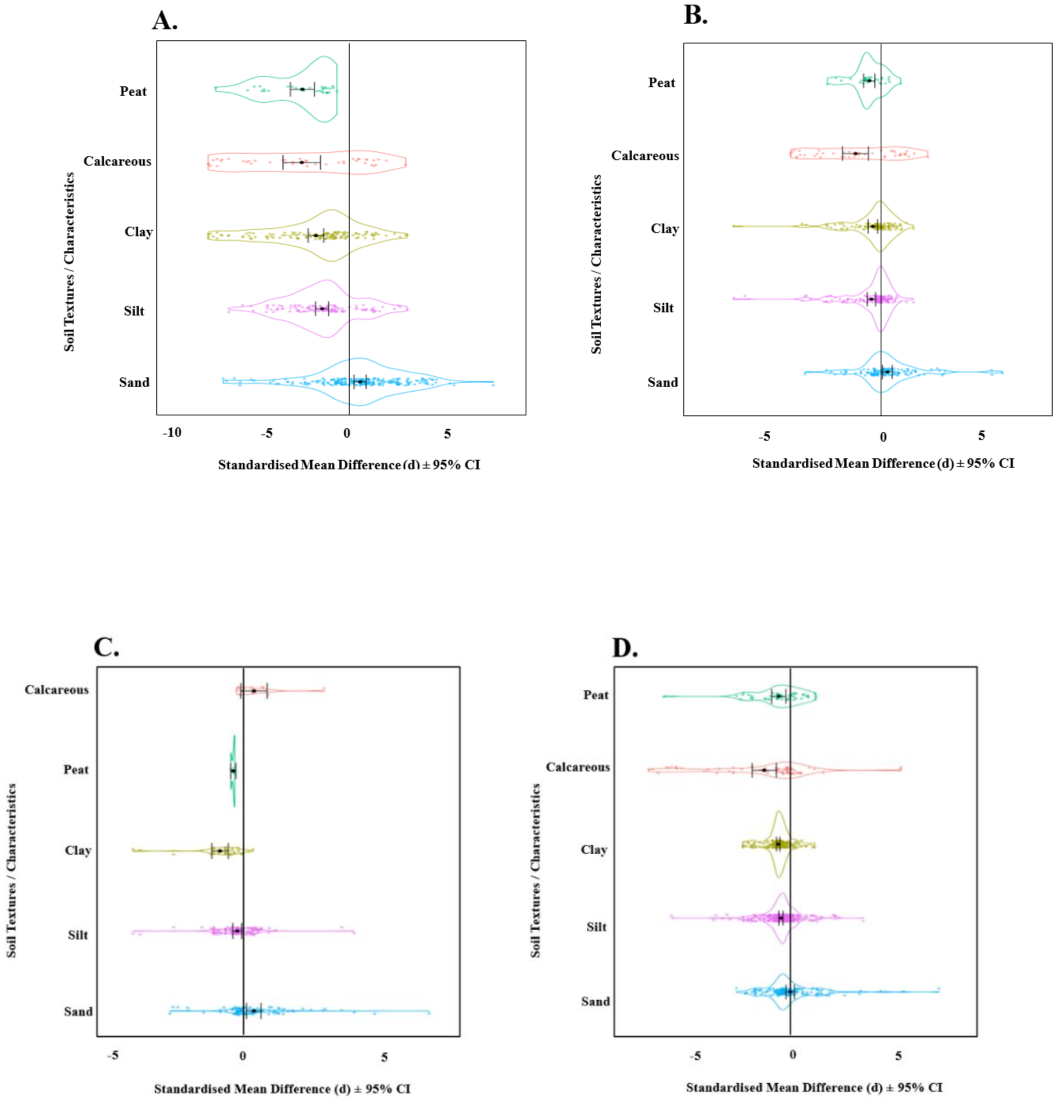

Figure 2.5. *Meta-analysis outputs analysis investigating different soil textures and chemical properties on (A) radionuclide, (B) inorganic, (C) microplastic, (D) organic PHE porewater solubility. The vertical black line denotes the division between positive and negative effect sizes. The circle dots denote the mean effect size for each toil texture and characteristic. The mean effect size contains upper and lower standard deviation confidence error bars (95% confidence level)*

indicating the variation of data used to generate the mean effect size. The smaller circular dots around the mean effect size represent the individual effect size points used to generate the average.

Table 2.4. *Effect-size statistics showing PHE solubility within different soil textures. Such data indicate the effect-size value with the upper and lower confidence intervals with the associated significance level.*

Moderator	Estimate	Standard Error	Z - Value	P - Value	Lower	Upper
Radionuclide (Peat)	-3.012	0.521	-3.393	<0.001	-4.621	-1.923
Radionuclide (Calcareous)	-3.528	0.371	-0.271	0.004	-4.769	-1.321
Radionuclide (Clay)	-2.811	0.411	-0.951	0.008	-4.001	-1.821
Radionuclide (Silt)	-2.132	-0.617	0.414	0.002	-1.625	-2.811
Radionuclide (Sandy)	2.315	0.397	3.925	0.002	1.871	2.985
Organic (Peat)	-2.113	0.379	-2.706	0.007	-0.8713	-2.895
Organic (Calcareous)	-3.214	0.292	0.310	0.0082	-5.382	-1.872
Organic (Clay)	-1.321	0.319	-0.894	0.004	-2.013	-0.5431
Organic (Silt)	-2.114	0.309	-0.739	0.021	-3.016	-1.521
Organic (Sandy)	1.621	0.315	1.251	0.005	0.2131	2.358
Microplastic (Peat)	-0.954	0.312	0.432	0.0032	-1.211	-0.543
Microplastic (Calcareous)	0.323	0.032	0.121	0.232	0.432	0.543
Microplastic (Clay)	-1.983	0.127	-2.972	0.003	-2.531	-1.031
Microplastic (Silt)	0.064	0.127	0.503	0.615	-0.5131	0.4938
Microplastic (Sandy)	2.315	0.199	3.770	<0.001	1.732	3.103
Inorganic (Peat)	-0.9831	0.263	1.295	0.004	-1.321	-0.0021
Inorganic (Calcareous)	-2.031	0.263	1.295	0.032	-2.531	-1.538
Inorganic (Clay)	-1.528	0.285	-2.446	0.014	-1.811	-1.283
Inorganic (Silt)	-1.281	0.278	-1.334	0.008	-1.493	-1.083
Inorganic (Sandy)	0.7214	0.296	-0.044	0.965	0.5541	1.039

2.3.3 Study Publication Bias

The PHE porewater solubility was statistically significantly different between the different soil textures investigated ($Q_m = 5.925$, $p = 0.015$), with high residual heterogeneity ($p < 0.001$). A publication bias assessment investigated this high residual heterogeneity. The purpose of undertaking a publication bias assessment is to ensure the data quality and robustness of the results, investigating whether the data used to generate the effect sizes was valid and not derived from studies only selecting statistical significant findings

The funnel plots (Figure 2.6) exhibit no asymmetrical distribution ($X^2 = 19.52$, degrees of freedom = 2045, $p = 0.212$). Egger's test did not confirm publication bias ($z = 1.928$, $p = 0.054$). The study's median power used within this meta-analysis was moderate at 31.4%. The findings confirmed that there was no publication bias present. The absence of publication bias underpins the validity of the observed differences in PHE porewater solubility across the different soil textures. These findings are important for subsequent modelling chapters in this thesis, emphasising that to predict the PHE porewater solubility, appreciating the mobility differences in different soil textures is significantly important.

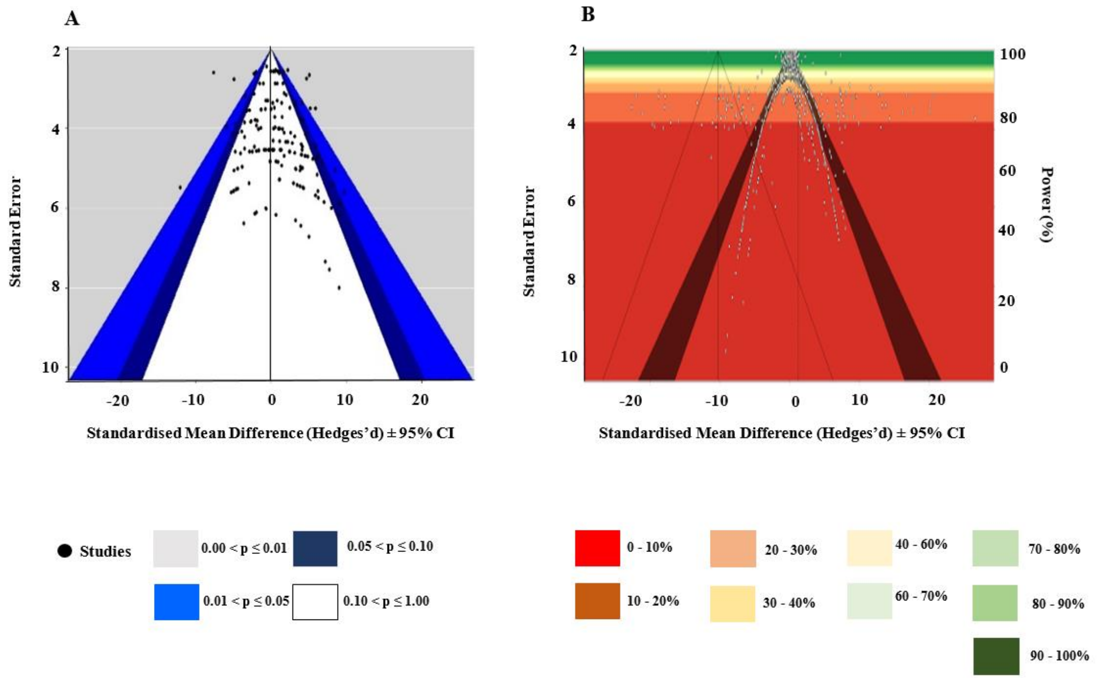

Figure 2.6. *Outlines the mechanism for determining publication bias. Plot (A) shows all the studies represented as small black residuals. Assessing asymmetry in such plots illustrates publication bias. The position of the residuals, either within the white triangle, the dark or light blue outer edges, or within the grey location, indicates the statistical evidence of that study reporting publication bias. For example, many points fall within the white triangle "0.10 < p ≤ 1.00," this suggests a potential but not statistically significant indication of publication bias. This plot shows very few studies showing statistically significant indications of publication bias in this meta-analysis. Plot (B) shows the statistical power of the studies used within this meta-analysis. The different colour shades indicate the alternative power levels.*

2.3.4 Physicochemical Changes Influencing PHE Porewater Solubility

Oxidising redox potentials statistically significantly increased inorganic, organic, microplastic, and radionuclide porewater solubility (Figure 2.7). Fail-safe N calculations showed that between 11 and 345 additional negative studies would be required for these findings to lose statistical significance ($p = < 0.001$). Increasing the pH (alkalinity) statistically significantly decreased inorganic, organic, microplastic, and radionuclide porewater solubility (Figure 2.7). Fail-safe N calculations showed that between 14 and 66 additional negative studies would be required for these findings to lose statistical significance ($p = 0.002$).

The porewater solubility of many PHE decreased with increasing pH alkalinity; however, the results were statistically insignificant ($d = - 0.203$, $p = 0.539$). Fail-safe N calculations showed that 120 additional negative studies would be required for these findings to lose statistical significance ($p = <0.001$). The porewater solubility of many PHE also decreased under increasing DOC concentrations with statistical significance. Overall, these findings show that oxidising redox potentials increase PHE porewater solubility, whereas increasing pH soil porewater levels and DOC concentrations decrease PHE porewater solubility.

Table 2.5 shows the soil texture and chemical properties (i.e., pH and organic carbon) influencing PHE porewater solubility. In Table 2.5, it indicates the different soil textures and chemical properties investigated (i.e., sand, silt, clay, peat, calcareous). Table 2.5 is arranged in a way whereby the order of the table from left to right begins with the soil texture and chemical properties with the lowest soil pH acidity and the highest organic matter content. For example, the left hand side of the table indicates peat soils which have the lowest pH acidity and also the highest fraction of organic materials. The far right hand side of the table indicates calcareous soil classification, which has a much higher pH alkalinity and lower organic matter fraction. Such values were obtained from the global soil indexing classification base from the United States Geological Survey, which provide the same data to the British Geological Survey (USGS 2024). The different colours in the table boxes indicate the statistical significance of these chemical properties and soil texture classification on PHE mobility.

In Table 2.5, soil exhibiting high clay fractions, organic matter content, and a pH range of 5 - 7.9 reduced PHE porewater solubility. The PHE solubility increased irrespective of reasonably high clay content, demonstrating that using soil texture exclusively, without considering the soil's chemical properties (e.g., pH) to predict porewater solubility is unreliable. For instance, Table 2.5 shows that PCB porewater solubility increased within silty type soils; however, as the pH alkalinity increases, such remobilisation decreased, irrespective of the silt texture. Such findings illustrate the importance of appreciating a soil's chemical properties influencing PHE porewater solubility. Sandy soil textures exhibiting an organic matter < 0.05%, and an acidifying pH < 5, increased PHE porewater solubility.

However, PHE porewater solubility, particularly for PAH, lead, plutonium-238, and caesium-137, is mainly influenced by the pH levels of sand textured soils, with higher pH alkalinity decreasing PHE porewater solubility. The porewater solubility is observed irrespective of the sand's soil texture, indicating the importance of some instances appreciating a soil's chemistry more than the texture when influencing PHE porewater solubility. These findings were significant, showing that using a soil's chemical properties combined with texture may reliably forecast areas susceptible to soluble PHE. See Figure A2.1, Appendix A for physicochemical changes influencing contaminant's mobility.

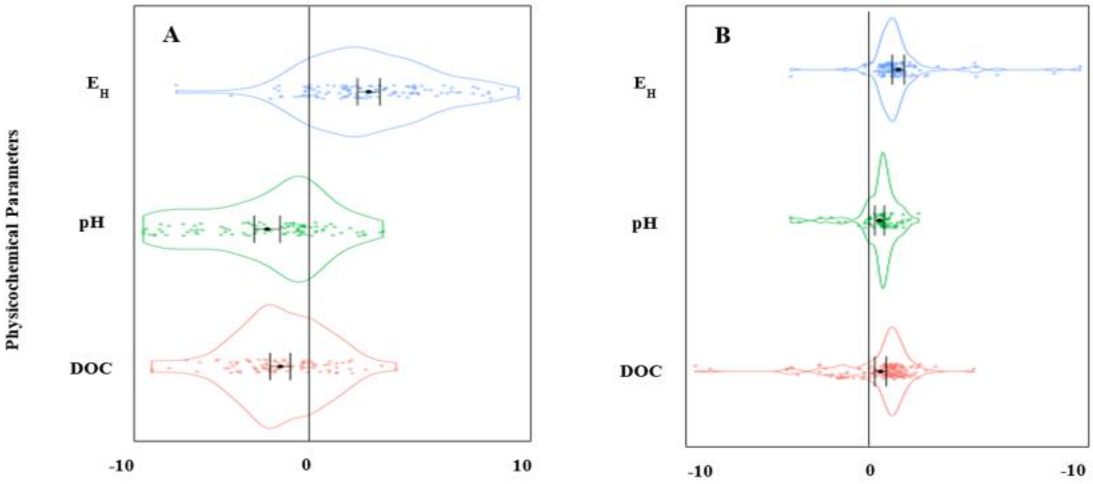

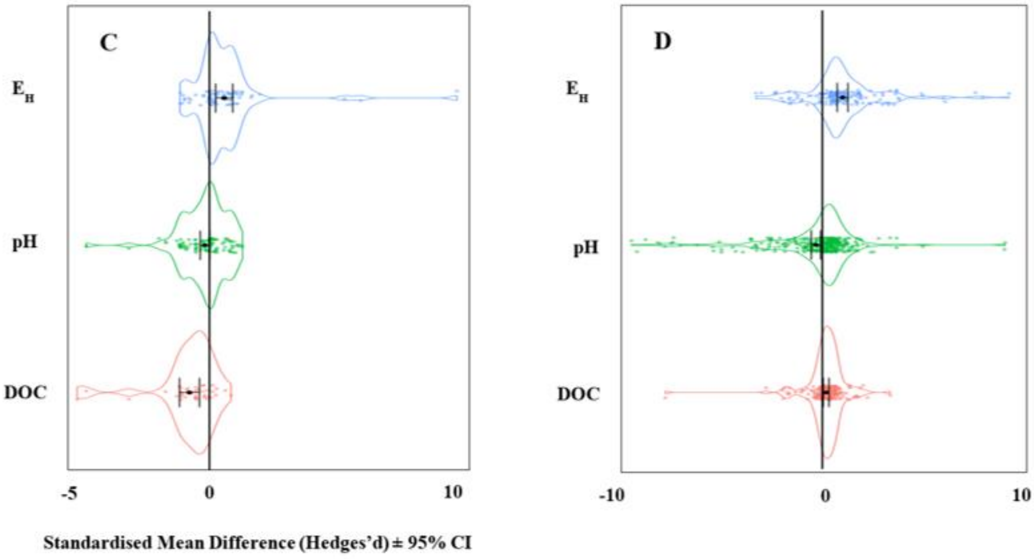

Figure 2.7. *Effects of physicochemical changes on A (organic), B (inorganic), C (radionuclide), and D (microplastic) PHE porewater solubility. The black circular point represents the mean effect size (95% CI). The small coloured circular points indicate the individual effect sizes generating the mean. Violin plots show the spread of data (variance).*

Table 2.5. *Outlines the different soil textures (sand, silt, clay) and chemical properties (pH and Organic carbon from calcareous and peat soils, respectively) on PHE porewater solubility. The table investigates only a select few PHE types from different subgroups.*

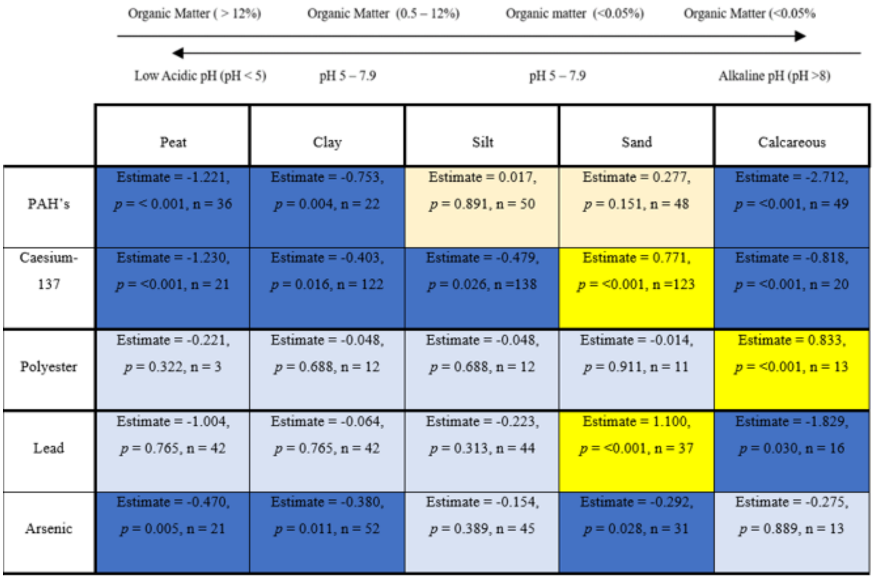

Organic Matter (> 12%) Organic Matter (0.5 – 12%) Organic matter (<0.05%) Organic Matter (<0.05%

Low Acidic pH (pH < 5) pH 5 – 7.9 pH 5 – 7.9 Alkaline pH (pH >8)

	Peat	Clay	Silt	Sand	Calcareous
PAH's	Estimate = -1.221, *p* = < 0.001, n = 36	Estimate = -0.753, *p* = 0.004, n = 22	Estimate = 0.017, *p* = 0.891, n = 50	Estimate = 0.277, *p* = 0.151, n = 48	Estimate = -2.712, *p* = <0.001, n = 49
Caesium-137	Estimate = -1.230, *p* = <0.001, n = 21	Estimate = -0.403, *p* = 0.016, n = 122	Estimate = -0.479, *p* = 0.026, n =138	Estimate = 0.771, *p* = <0.001, n =123	Estimate = -0.818, *p* = <0.001, n = 20
Polyester	Estimate = -0.221, *p* = 0.322, n = 3	Estimate = -0.048, *p* = 0.688, n = 12	Estimate = -0.048, *p* = 0.688, n = 12	Estimate = -0.014, *p* = 0.911, n = 11	Estimate = 0.833, *p* = <0.001, n = 13
Lead	Estimate = -1.004, *p* = 0.765, n = 42	Estimate = -0.064, *p* = 0.765, n = 42	Estimate = -0.223, *p* = 0.313, n = 44	Estimate = 1.100, *p* = <0.001, n = 37	Estimate = -1.829, *p* = 0.030, n = 16
Arsenic	Estimate = -0.470, *p* = 0.005, n = 21	Estimate = -0.380, *p* = 0.011, n = 52	Estimate = -0.154, *p* = 0.389, n = 45	Estimate = -0.292, *p* = 0.028, n = 31	Estimate = -0.275, *p* = 0.889, n = 13

Key

⬜ PHE Chemical Remobilisation Decreasing; Statistically Insignificant

🟦 PHE Chemical Remobilisation Decreasing; Statistically Significant

🟧 PHE Chemical Remobilisation Increasing; Statistically Insignificant

🟨 PHE Chemical Remobilisation Increasing; Statistically Significant

2.3.5 Climate Change Altering Physicochemistry and PHE Mobilisation

Increasing ambient temperatures increased inorganic and organic PHE mobilisation (*d* = 1.38, p = 0.017; *d* = 2.21, p = 0.007, respectively). A statistically significant correlation exists between temperature increase and decreasing dissolved oxygen concentrations (R^2= 0.82, p = <0.001, Figure 2.8A). These oxygen decreases have a profound effect by lowering the redox status. Lowering oxygen and redox conditions increased soil microbial respiration rates (Figure 2.8B; d = 12.43, p = <0.001). The findings show increasing temperatures from climate change influenced PHE remobilisation dynamics by altering microbial biogeochemical cycling processes.

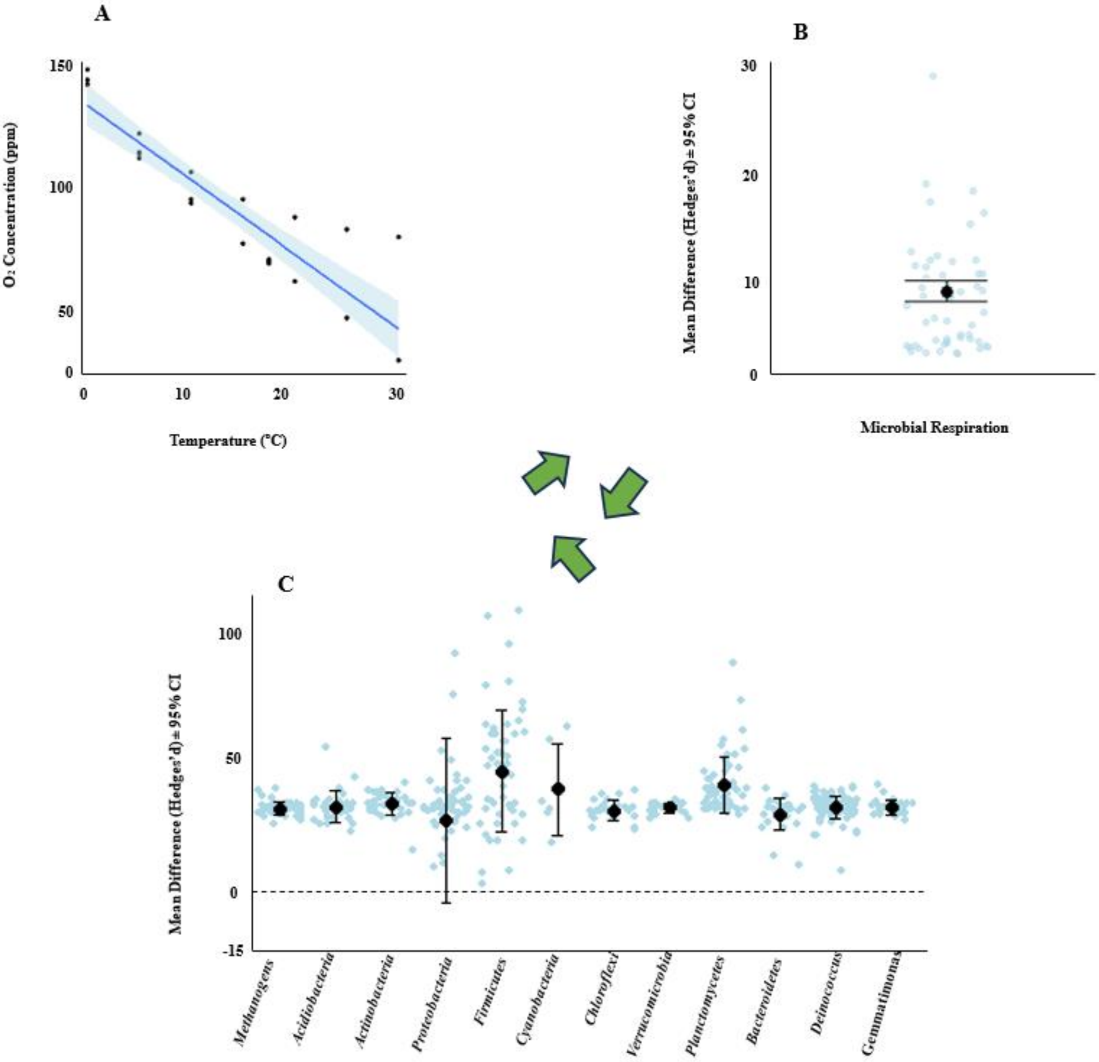

Figure 2.8. (A) *The effects of increasing temperature on soil and water dissolved oxygen concentrations and (B) the impact of higher temperatures on microbial respiration and (C) microbial abundance.*

2.3.6 Flooding, Physicochemical Changes, PHE Bioaccessibility

Increasing temperatures increased organic and inorganic PHE bioaccessibility with statistical significance (Figure 2.9). An increased dissolved organic carbon (DOC) content, salinity, ferrihydrite content, and an oxidising redox potential (E_H) showed a statistically significant decrease in organic and inorganic PHE bioaccessibility. Increasing nitrogen and phosphorus resulted in statistically significant increases in inorganic PHE bioaccessibility but decreased organic PHE bioaccessibility. As calcium and dissolved oxygen concentration increased, a statistically significant decrease in inorganic PHE bioaccessibility was observed, whereas an increasing pH only resulted in a statistically significant decrease in organic PHE bioaccessibility. Fail-safe N calculations showed that 12,760 additional studies would be required for these findings to lose statistical significance ($p = <0.001$).

Statistically significant responses were seen for inorganic and organic PHE bioaccessibility in relation to changes in temperature, dissolved oxygen, and ferrihydrite increases (Q = 21.99, degrees of freedom = 577, $p = <0.001$). There is high residual heterogeneity observed between all the physicochemical parameters influencing organic and inorganic PHE bioaccessibility (Q = 3404, $p = <0.001$).

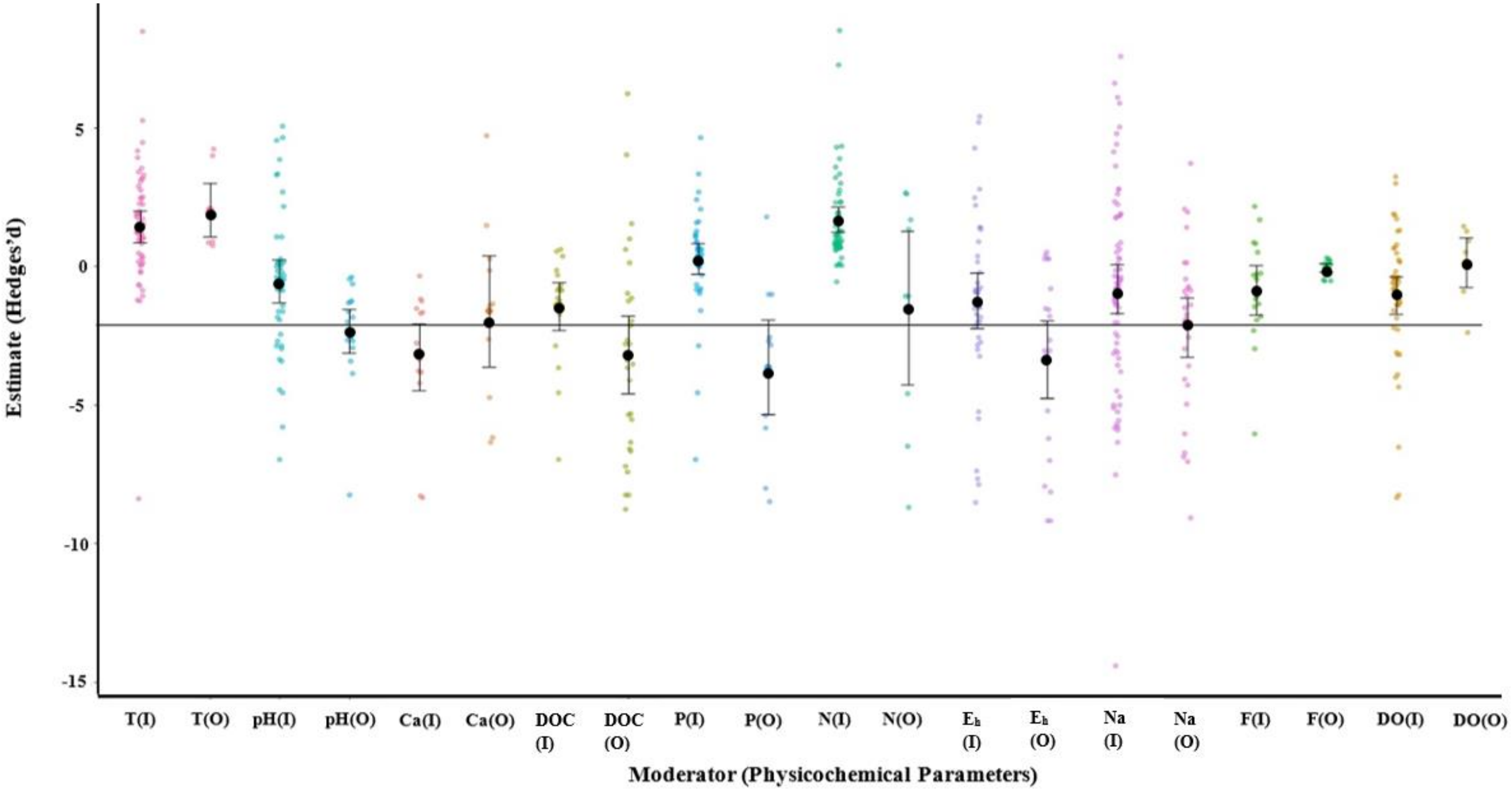

Figure 2.9. *Mean analytical effect sizes showing the influence of different physicochemical parameters influencing PHE bioaccessibility. The letters "I" and "O" indicate inorganic and organic PHE types, respectively. The symbol "T" represents temperature, "Ca" calcium, "DOC" dissolved organic carbon, "P" phosphorus, "N" nitrogen, "E_h" redox potential, "Na" sodium, "F" ferrihydrite and "DO" dissolved oxygen. The large black circles denote the mean effect size, with the upper and lower vertical black lines showing the lower and upper confidence intervals. The smaller coloured circles indicate the individual study effect sizes used to generate the mean.*

2.4 Discussion

2.4.1 How Flooding Influences PHE Porewater Solubility

The meta-analysis results show flooding increases PHE solubility. Increased water velocity can physically erode the sediment beds that are sequestering PHE, causing sediment particles to be resuspended, and physically moved downstream taking the PHE with them. This explains why many PHE exhibit positive effect sizes and is in line with other studies (e.g., Ponting et al 2021).

The rate of solubility can differ for PHE types, primarily attributed to polarity differences (Menger et al 2020). Many PHE investigated, such as arsenic, form polar compounds (e.g., arsenic trioxide and methylarsonic acid) (Menger et al 2020). The term "polarity," refers to the uneven distribution of electric charge around the molecule, which exhibit an electronegativity difference between the bonded atoms (Yoonah et al 2018).

Therefore, compounds containing arsenic may exhibit polarity, meaning such compounds have partial positive and negative charges (Menger et al 2020). Polar compounds like arsenic can attract polar water molecules through dipole-dipole interactions, facilitating PHE porewater solubility (Menger et al 2020). Polyethylene and polycyclic aromatic hydrocarbons are non-polar and less soluble in water, thus reducing PHE porewater solubility (Yoonah et al 2018). Thompson and Goyne (2012) showed that these polarity differences create hydrophobic effects, for example causing segregation of non-polar benzo(a)pyrene from polar water molecules. Other studies observed similar findings, emphasising that the PHE polarity statistically significantly influences solubility (Kile et al 1995; Oepen et al 1991; Site 2000; Wang et al 2020).

For radionuclides, such as strontium-85 and americium-241, solubility was found to decrease. Such findings are unlikely to be attributed to the radionuclide's polarity, but rather their activity concentrations (Oepen et al 1991). These radionuclides have low environmental activity concentrations making it challenging to detect and measure the effects of flooding influencing PHE porewater solubility (Copplestone et al 2020).

2.4.2 Soil Texture and Chemical Properties Influencing PHE Porewater Solubility

Soil texture significantly influences PHE solubility, controls water filtration through the soil, and can provide large surface areas for ligand-exchanges, all of which can be further influenced by microbial community structures (Abdu et al 2008, Zhang and Lin 2020).

The soil texture influences PHE solubility with the particle surface areas complexing with PHE through ligand exchanges (Stewart et al 2009). Sand particles have small surface areas (0.10-2mm), and low surface to volume ratios, containing low organic carbon fractions (0.4-66.9 g C kg^{-1}) (Duplay et al 2014). Clays and silts in contrast have large surface areas containing phyllosilicate mineral fractions, including micas, chlorites, serpentinites, and pyrophyllite (Ndlovu et al 2013). These minerals provide large surface areas for adsorbing PHE (Barre et al 2016; Feng et al 2015; Hassink 1996; Stewart et al 2009).

Soil chemical properties influence PHE solubility. Peats, for example, are rich in soil organic matter, containing significant organic carbon contents, typically ranging from 30-200 kg C m^{-2} (Wang et al 2017). These organic carbon molecules contain humic and fulvic substances, with high affinities of coprecipitating with organometallic compounds through hydrogen bonding, hydrophobic effects, and stacking interactions (Yang et al 2020). Chianese et al (2020) show humic substances having a particular coprecipitating affinity with organometallic compounds, such as PAH's. These interactions are not exclusive to organometallic compounds as Steely et al (2007) showed organometallic compound antimony (III) acetate coprecipitating with humic acid molar mass fractions, reducing remobilisation.

Calcareous soils are characterised by their calcium carbonate content, typically between 0.5% and 10% of the soil mineral composition (Weeks and Hettiarachchi 2020). The divalent 2+ cations present in these soils coprecipitate with and immobilise PHE via calcium bridging, reducing PHE solubility (Ciszewski and Grygar 2016; Gall et al 2018; Huang et al 2021).

2.4.3 Climate Change Altering Soil Physicochemistry and PHE Mobility

Increasing temperatures increase the oxygen demand for microbial communities and the eventual decrease in oxygen concentrations directly lowers the redox conditions (Huang et al 2021). Lowering the redox conditions further and decreasing the transition time between oxidising and reducing conditions, both enhances the reductive dissolution of the oxide mineral phase (e.g., for iron and manganese) (Ponting et al 2021). Such oxides immobilise PHE through ligand-binding exchanges (Heyden and

Roychoudhury 2015). The dissolution of oxides, because of such temperature increases, enhances PHE solubilisation and remobilisation (Mao et al 2021). These findings underpin the central conclusion from the meta-analysis, that temperature, oxygen, redox conditions and oxide concentrations need to be considered when attempting to predict PHE solubility.

This meta-analysis reveals the importance of pH, Eh, and dissolved organic carbon in influencing a contaminant porewater solubility from extensive synthesised searches of laboratory and field-based studies. These variables are significant for predictive modelling purposes, particularly for improving the input feature parameterisation. Appreciating such important variables can reduce the probability of selecting redundant and uninformative variables in such modelling frameworks. The findings from this meta-analysis, recognising the importance of pH, Eh, and dissolved organic carbon influencing contaminant porewater solubility, will be used for subsequent modelling chapters (e.g. chapter 4) to estimate a contaminant porewater solubility using such variables.

2.5 Conclusion

This meta-analysis shows that climate change impacts on flooding frequency and duration and higher temperatures is highly likely to influence soil PHE solubility.

The meta-analysis results demonstrate the importance of including physicochemical parameters when predicting soil PHE solubility because of the inherent relationship the physicochemistry has influencing PHE transport, fate, and behaviour. The findings from this meta-analysis reveal the importance of pH, Eh, and dissolved organic carbon in influencing a contaminant's porewater solubility. Identifying such variables can significantly improve the parameterisation for predictive modelling purposes, which will be analysed in subsequent chapters. Tailoring such input features reduces the likelihood of including redundancy and unnecessary variables in such modelling.

Chapter 3: Thesis Structure

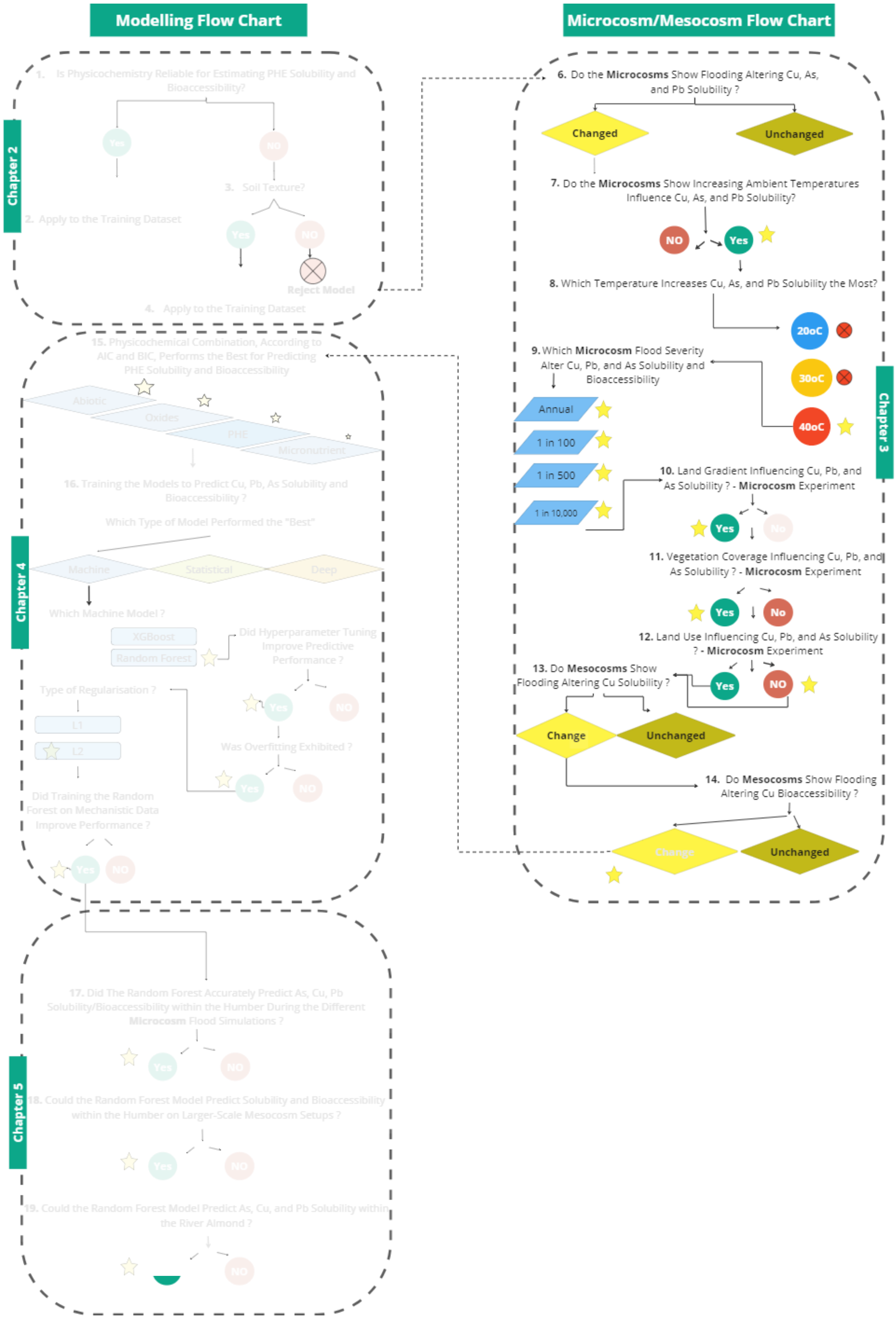

Chapter 3: Investigating the Impact of Flooding on Soil PHE Solubility, Bioaccessibility, and Solid Phase Distribution - A Microcosm and Mesocosm Experiment

3.1 Introduction

The UK and many other countries face increasingly severe flooding events because of anthropogenic climate change, leading to rising economic costs for flood protection and mitigation (Met Office 2020). Flooding alters many soil and water physicochemical parameters, changing PHE porewater solubility and mobility, which may influence the exposure risk levels to contamination for humans and wildlife (Chapter 2) (Koh et al 2021). Chronic and acute exposure to these PHE, either through inhalation, dermal contact, or ingestion of contaminated particles, can be neurotoxic, hepatotoxic, and endotoxinogenic to humans and wildlife (Table 1.1, Chapter 1) (Petruzzelli et al 2019). Flooding can physically erode contaminated soil and sediment particles sequestering PHE, transporting such particles downstream, and if the flooding is severe, onto floodplains where many households reside (Thakur et al 2020). Essentially, flooding can generate an environmental pathway for transporting these contaminated particles (Thakur et al 2020).

Increasing ambient temperatures from climate change alter soil biogeochemical processes, which influence PHE porewater solubility and mobility (Chapter 2, Section 2.3.5) (Szuskiewicz et al 2021). Many policymakers, such as the Scottish Environment Protection Agency, the Environment Agency, and local authorities, urgently require more solutions to address and monitor the impact of increasing temperatures on soil biogeochemistry and PHE dynamics (Devi and Khatua 2017; Foroutan et al 2021; Kilunga et al 2017).

The effects of more frequent flooding and rising temperatures altering soil biogeochemistry and physicochemistry also influence PHE bioaccessibility (Chapter 2) (Petruzzelli et al 2019). The term “bioaccessibility” defines the fraction of PHE soluble within the gastrointestinal tract, readily available for absorption through the intestinal epithelium (Thakur et al 2020). Bioaccessibility is often confused with “bioavailability,” which refers to the bioaccessible PHE fraction crossing the epithelium and being absorbed into the systemic circulation, reaching organs and tissues (Figure 3.1, amended from McLaren 2019). Flooding influences PHE bioaccessibility by creating anaerobic conditions and typically increasing soil and water pH levels, which both influence PHE coprecipitation with different soil mineral phases (Chapter 1, Section 1.8.1 and 1.8.2) (Szuskiewicz et al 2021). For example, changing water and soil pH conditions influence how PHE coprecipitate with the pH-sensitive carbonate mineral phase (Ponting et al 2021). Lowering soil and water redox conditions influence the oxidative reduction of aluminium, manganese, and iron oxides that coprecipitate with PHE (Koh et al 2021). The reducing conditions created during flooding influence the formation of PHE metal sulfide complexes and clusters (Chapter 1, Section 1.8) (Ponting et al 2021). These soil and water physicochemical changes may increase or decrease PHE solubility and bioaccessibility; influencing PHE exposure.

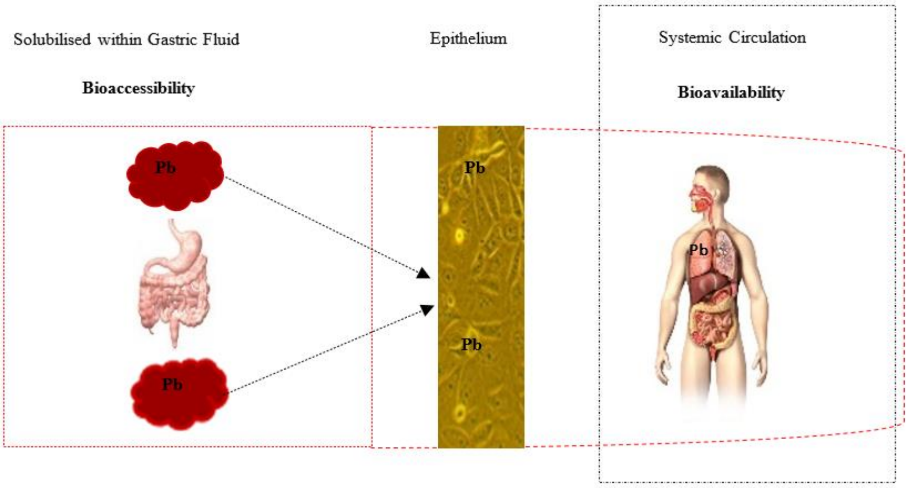

Figure 3.1. *The concepts of "bioaccessibility" and "bioavailability." The square red box on the left illustrates PHE solubilised within the gastric fluid, defined as "bioaccessible." The right-hand box represents a PHE being adsorbed through the intestinal epithelium, "bioavailability" (McLaren 2019).*

The physicochemical changes are only one driver influencing PHE porewater solubility, bioaccessibility, and solid phase distribution during flooding (Wyke et al 2014). Other drivers include physical, thermodynamic, and biological variables (Gu and Wong 2004). Physical parameters include the land gradient, vegetation coverage, and land use type, and may also refer to the flood length and how frequently and quickly the flood recedes. For instance, 1 in 100 year floods last a few days compared to 1 in 500 year floods, because "severity" can be a measure of flood duration (Foroutan et al 2021). Thermodynamic changes refer to the water pressure and temperature; and biological variables relate to the soil microbial community (Wyke et al 2014).

These parameters are not independent; they are highly co-dependent; however, there is very little understanding around how they interact and, more importantly, how they influence PHE porewater solubility, bioaccessibility and solid phase distribution (Karmakar and Srivastava 2017). An understanding of the interaction between these parameters is key for accurately predicting PHE changes during flooding (Figure 3.2, information obtained from Gu and Wong 2004). By "accurately" predicting, this means estimating PHE porewater solubility and bioaccessible concentrations with no statistically significant differences from the observed laboratory results.

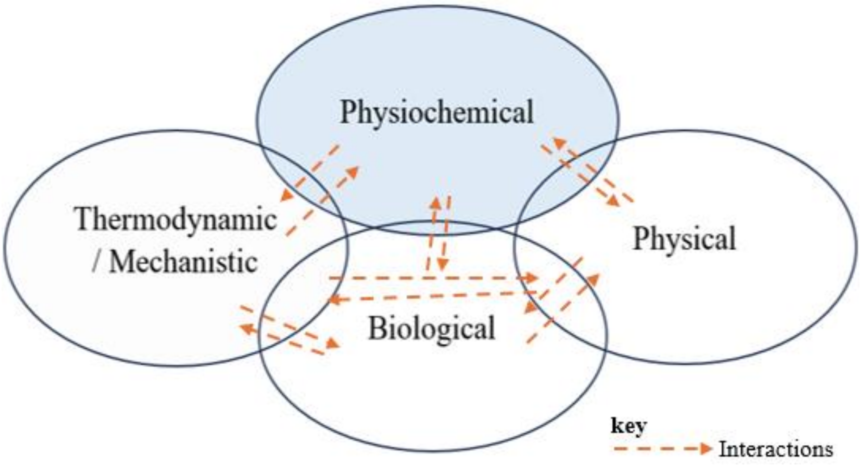

Figure 3.2. *Outlines the complexity between different variables (physicochemistry, thermodynamic, physical and biological) interacting and all influencing PHE porewater solubility and bioaccessibility (Gu and Wong 2004). Such illustration focuses on emphasising how the physicochemistry, highlighted in blue, alone influences PHE porewater solubility, bioaccessibility and solid phase distribution.*

Figure 3.2 shows that PHE porewater solubility, bioaccessibility, and solid phase distribution can be influenced not only by physicochemical changes during flooding, but also thermodynamic changes (such as water pressure), biological (referring to soil microbial and fungal community changes), and physical (relating to the land gradient and vegetation coverage). The purpose of this illustration is to emphasise the importance of appreciating not only how physicochemical changes influence PHE porewater solubility, bioaccessibility and solid phase distribution, but also how thermodynamic, biological, and physical variables interact and also impact PHE dynamics.

These interactions are highly complex and intercorrelated, making understanding how these variables influence PHE porewater solubility, bioaccessibility, and solid phase distribution significantly challenging. To elaborate further on why these interactions are challenging to understand as they relate to PHE dynamics, two hypothetical scenarios are outlined below, both indicating the complexities of these interactions between physicochemical, biological, physical, and thermodynamic changes during a flood (Figure 3.3).

In “Scenario A”, a flood occurs on agricultural land with highly compacted soil from farming machinery (Figure 3.3). The compacted soil reduces the flood water absorption by decreasing the soil pore space, reducing permeability. This soil compaction restricts the diffusion, circulation, and exchange of oxygen molecules due to the minimised pore space, which would previously allow the transfer of oxygen throughout the soil (Zhao and Xu 2024). The weight of the water that cannot absorb and infiltrate through the soil may also eventually increase the soil ambient hydrostatic pressure due to the build-up of this water exerting a force on the soil (Zhao and Xu 2024).

Increasing the pressure conditions and limited oxygen transfer considerably reduces soil oxygen availability, eventually lowering the redox conditions. Such lower redox conditions increase soil microbial respiration rates and community structures, increasing anaerobic microbial compositions. The decreasing soil oxygen concentrations may also increase the anaerobic reductive dissolution of manganese, aluminium, and iron oxides, releasing coprecipitated PHE into solution and increasing PHE porewater solubility and bioaccessibility. Scenario A illustrates the interactions between soil compaction (physical variable), influencing soil oxygen diffusion (physicochemical variable) and pressure (thermodynamic) impacting PHE solubility and bioaccessibility. Such interactions, however, are non-linear; for example, an increase in “X” does not result in a proportional increase or decrease in “Y.”

To illustrate this “non-linearity, ”consider “Scenario B,” which simulates the same scenario of flooding on agricultural soil to “Scenario A” (Figure 3.3). The compacted soil may lower the redox potential by limiting oxygen transfer. Reducing redox conditions; however, may promote metal sulfide complexes, reducing PHE porewater solubility and bioaccessibility. Sulfide cluster formation can occur due to the increase in facultative anaerobic bacteria, which are heavily involved in organic carbon degradation. These bacteria thrive in anaerobic conditions, helping create these sulfide ions. The bacteria are instrumental in organic carbon degradation, which can lead to the byproduct of these sulfide, by utilising sulfate present in the soil as an electron acceptor instead of oxygen (as oxygen is limiting under anaerobic conditions) during organic carbon degradation.

This rapid organic carbon degradation may promote soil aggregation. During the breakdown of organic carbon, the byproducts (humic substances) can act as binding agents for soil particles, eventually forming aggregates. The process of aggregation naturally enhances soil structure by increasing the number of available pore spaces. The increase in aggregation increasing the number of pore spaces may also increase oxygen and water diffusion within the soil profile, reducing the volume of standing infiltrated water, eventually decreasing the exerted soil pressure. In Scenario B, PHE porewater solubility and bioaccessibility may decrease (Figure 3.3, information obtained from Ponting et al 2021). The reason why PHE solubility and bioaccessibility may decrease is that the enhanced exchange of oxygen molecules throughout the soil may increase overall soil redox status, decreasing the likelihood of reducing redox conditions causing iron, aluminium, and manganese oxide dissolution, solubilising and increasing PHE bioaccessibility.

Both hypothetical scenarios A and B are plausible; however, the changing soil and water physicochemistry, thermodynamics, and soil biological community responses result in significantly different outcomes for PHE porewater solubility and bioaccessibility. Scenario B shows a decrease in PHE solubility and bioaccessibility whereas Scenario A increases PHE solubility and bioaccessibility.

Such complexities highlight the potential role of artificial intelligence modelling to predict PHE dynamics during flooding by appreciating the stochastic relationships between physicochemistry, physical parameters, thermodynamics, and biological responses. In this case, an artificial intelligence model based on physicochemistry data alone may predict entirely incorrectly, either completely underestimating or overestimating PHE solubility and bioaccessibility. For a detailed outline of how each physical, thermodynamic, and biological variable influences a PHE dynamic during flooding, see Table 3.1.

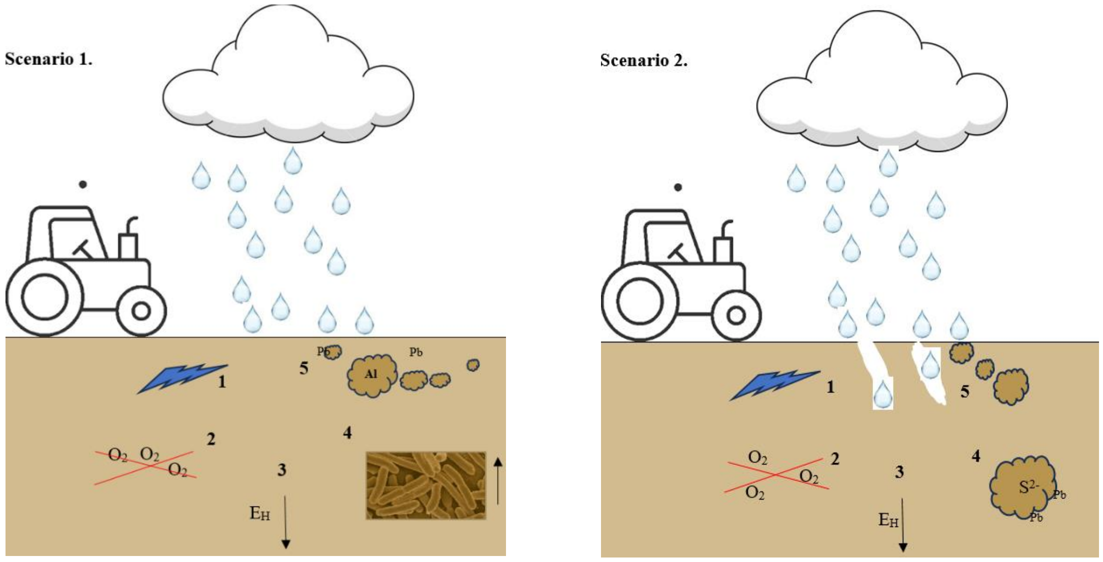

Figure 3.3. *Scenario A. Outlines how compacted soil influences PHE mobility and bioaccessibility during a hypothetic flood. Scenario 1 indicates (1) a pressure increase is created by reducing (2) oxygen flow, which (3) lowers the redox conditions and (4) increases microbial respiration, eventually (5) promoting oxide dissolution, eventually* ***increasing PHE solubility and bioaccessibility*** *(Ponting et al 2021). Scenario B, indicates how (1) soil compaction creates a pressure increase, which (2) reduces oxygen diffusion, (3) lowers the redox conditions; however, (4) promotes sulfide producing anaerobic bacteria, which (5) promote the degradation of soil aggregates (6) increasing soil oxygen diffusion, eventually* ***decreasing PHE solubility and bioaccessibility*** *by increasing the overall soil redox status (Ponting et al 2021).*

Table 3.1. *Outline how different physical (land gradient, vegetation coverage, and land use type), thermodynamic (pressure and temperature) and biological variables influence PHE porewater solubility, bioaccessible and solid phase distribution changes during flooding.*

Modelling Input	Influence on PHE Porewater Solubility, Bioaccessibility and Solid Phase Distribution
Land Gradient	• Alters the flood water velocity, eroding the soil and sediment particles, which sequester PHE (Calderon et al 2023).
Vegetation Coverage	• Locations containing high vegetation coverage may adsorb soluble PHE during flooding (Walton et al 2020).
Thermodynamic Pressure	• Influences the diffusiveness of oxygen molecules which is directly involved in affecting the redox conditions and oxide dissolution kinetics (Ponting et al 2021).
Microbes	• Involved influencing PHE coprecipitation with the organic mineral phase (Romkens et al 2002). • Influences the oxygen concentrations and redox status (McLaren 2019).

3.2 Aims and Objectives

This chapter aims to (1) investigate the influence of physicochemical changes during flooding influencing PHE mobility, bioaccessibility, and solid phase distribution. The chapter assesses (2) the influence of ambient temperature changes influencing soil microbes, potentially impacting PHE dynamics (biological parameter). This chapter explores (3) the influence of different flood severities (e.g., 1 in 100 year and 1 in 500 year) with differing flood lengths, influencing PHE behaviour during flooding (physical parameter). The chapter finally (4) investigates such physicochemical, physical and biological effects on PHE mobility, bioaccessibility and solid phase distribution using larger-scale mesocosm experiments. The purpose of this chapter is to collect and analyse data around how physicochemistry, soil microbes, and different flood severities influence PHE dynamics. This data will train artificial intelligence modelling to predict PHE mobility and bioaccessibility during flooding in subsequent Chapter 4.

3.3 Methods

3.3.1 Sampling Location Selection Process

Each soil sample location was selected using a predefined process in QGIS (Version 3.30.2) (Figure 3.4). This process identified locations susceptible to flooding with large populations (e.g., *flood risk* AND *population number*). The goal was to identify physicochemically unique locations and establish the flood risk probability.

This research focused on arsenic, copper, and lead. These PHE were chosen due to their significance in minimising human and ecological health. Analysing arsenic, copper, and lead allows a comparison between metals (lead and copper) and metalloids (arsenic) regarding porewater solubility, bioaccessibility, and solid phase distribution changes. The meta-analysis in Chapter 2 (Section 2.3.1) concluded that the porewater solubility of metals and metalloids differs, highlighting the importance of comparing lead and copper with arsenic. These metals and metalloids showed high concentrations, exceeding the minimum soil threshold guidelines for CLEA for the land use type at all sampling points across the three catchments (CLEA 2023). Different PHE types, such as zinc and nickel, were also investigated and can be found in Appendices B and C.

These screening values were chosen because they are effective for assessing the health risks of PHE exposure, providing a suite of minimum thresholds based on reliable toxicity data (Middleton et al 2017). Many studies recommend these screening values due to this toxicity data (Cocerva et al 2024; Crispo et al 2021; Meng et al 2020; Middleton et al 2017; Moles et al 2016). The threshold values for freshwater and estuarine environments were chosen because the riverine catchments investigated in this chapter cover both freshwater and estuarine systems (see Section 3.3.2). Selecting locations susceptible to flooding and with high PHE concentrations ensured that the artificial intelligence models (discussed in Chapter 4) were trained with data for previously flooded locations with contamination levels above minimal soil threshold levels for human health risk assessments.

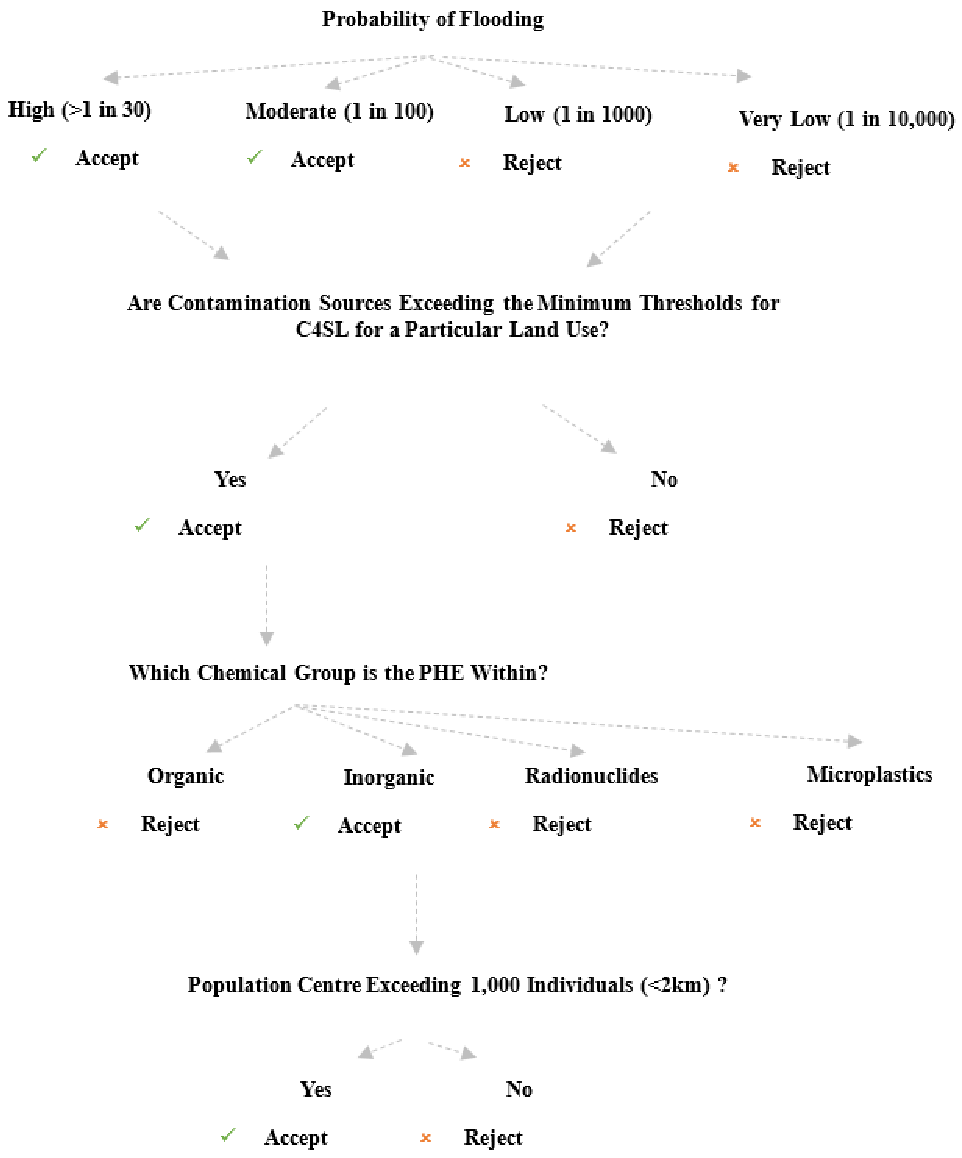

Figure 3.4. *Predefined selection process identifying sampling locations. The process filters potential sampling locations uniquely different in the geology and physicochemistry. The method identifies areas vulnerable to flooding which are highly contaminated.*

3.3.2 Study Areas

Soil samples were collected from three physicochemically and geochemically distinct locations: the Humber and Clyde catchments and the River Almond (Figure 3.5; BGS, 2024). This chapter analysed copper, lead, and arsenic because extensive industries, such as mineral mining, dominate within these locations, polluting the environment with high concentrations of these specific elements (Shokunbi et al 2024). All the physicochemical soil data collected from the Clyde were used to train various artificial intelligence models (random forests, extreme gradient boosting and neural networks) discussed in Chapter 4. The Humber catchment and the River Almond were used to assess the performance of these artificial intelligence models under different physicochemical conditions.

The Humber consists of sedimentary bedrock containing sandy soil textures with a high alkalinity, whereas the Clyde has an underlying igneous bedrock geology with acidic clay textured soils. The River Almond sampling locations have loam textures with neutral soil pH conditions. Each sampling location was divided into 250 x 250-meter blocks. In summary, this Chapter analyses PHE dynamics during flooding within the Clyde, Humber, and River Almond (Chapter 3). The relationship between physicochemistry changes and PHE dynamics within the Clyde catchment were used to train various artificial intelligence models (Chapter 4). These trained models were tested to predict PHE dynamic changes within the Humber catchment and the River Almond (Chapter 5).

Three quadrats were placed 125 meters apart, totalling nine quadrats. Five composite samples were taken from within each quadrat, four from the corners and one from the centre as recommended by United States Environmental Protection Agency for soil sampling (USEPA 2024). A sterilised auger extracted soil samples within the top 0-5cm layer. This depth was selected, as according to Mitran et al (2024), who analysed the vertical depth-wise distribution of soil heavy metals, copper, lead and arsenic, showed these elements having the highest total concentrations within the upper 0-15cm of the soil profile, particularly the upper 0-5cm. This depth was also chosen as the high PHE concentrations present within this depth pose significant risks for human health exposure and the potential for PHE physical movement under flooding (Keller et al 2007). The soil samples were stored airtight, bulked, and dried at 105°C for 72 hours, which is the standard temperature and time for removing soil moisture without compromising and changing the integrity of the soil structure (Dexter and Richard 2009).

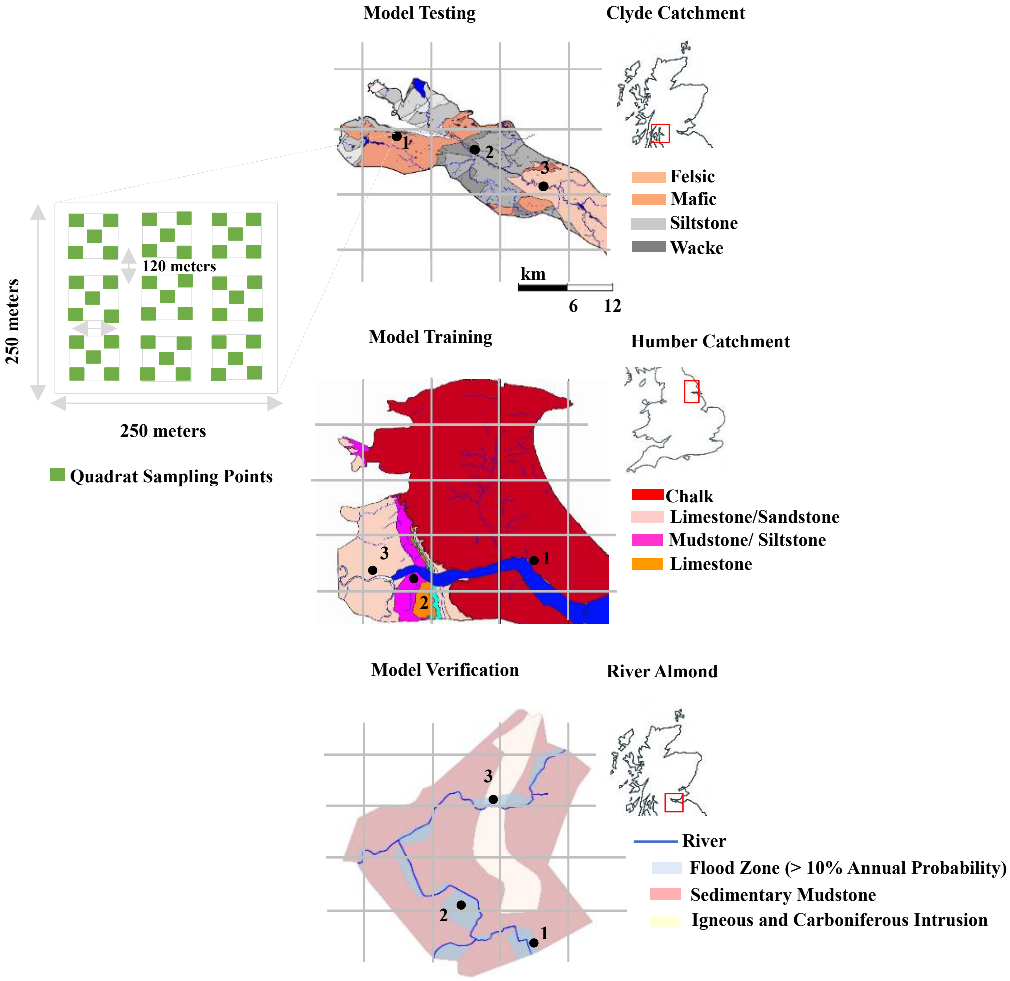

Figure 3.5. *Outlines the three study catchments with the associated sampling locations. The figure illustrates the soil sampling design, totalling nine quadrats per sampling location (BGS, 2023).*

3.3.3 Microcosm Setup

This chapter explores the influence of flooding on copper, lead and arsenic porewater solubility, bioaccessibility and solid phase distribution using microcosm experiments, by simulating a flood event. For information why copper, lead, and arsenic were selected, see Section 3.3.1. Four microcosm experimental designs were used to address the four chapter aims (Section 3.2.2). Microcosm experiment one investigated how soil and water physicochemistry influenced PHE porewater solubility, bioaccessibility and solid phase distribution within the Clyde and Humber catchments. The second microcosm experiment analysed how temperature influenced PHE solubility within the Clyde. Microcosm experiment three explored how differing flood severities influenced

PHE solubility and bioaccessibility within the Humber. The fourth microcosm experiment investigated how physical variations (e.g., land gradient) and land use types (e.g., agriculture) within the River Almond sampling points influenced copper, lead, and arsenic solubility within soil (Table 3.2).

The first microcosm experiment was conducted within the Humber and Clyde because these catchments were physicochemically different, allowing for comparison. These physicochemical differences enabled a detailed investigation of how significant physicochemistry changes impact PHE dynamics. The second microcosm experiment examined the effects of temperature on PHE dynamics only within the Clyde catchment because of its proximity to the laboratory; collecting soil with biological samples from the Humber, with extended travel time, may negatively impact the quality of results. The third microcosm experiment on different flood severities was conducted within the Humber because this catchment is susceptible to coastal flooding, increasing the likelihood of more severe flooding than riverine flooding. The impact of physical variations on PHE dynamics was only investigated across the River Almond because this location contained significant variation in land gradients, vegetation coverage and land use types, unlike the other catchments investigated.

The total soil organic matter content of all the soils within the different sampling locations was determined using the Loss on Ignition method (Zhang and Wang 2014). Soil pH was determined using 0.01M of calcium chloride extractant reagent, following the Houba et al (2000) procedure. The soil moisture content was determined using a field capacity procedure, following Assi et al (2019) guidelines. Total concentrations of soil heavy metals (e.g., lead, copper, and arsenic) were determined using microwave digestion (Sandroni et al 2003). For a detailed outline regarding the experimental methodologies estimating the total soil organic matter content, pH, soil moisture content, and microwave digestion, see Appendix B, Section 2.

Table 3.2 *The four microcosm setups, outlining the catchment, research aim, microcosm number and where in thesis, derived from the flow chart part, this section is attempting to address.*

Microcosm Setup	Location	Research Aim	No. of Microcosms	Flow Chart Number
1	Clyde and Humber	1	54	6
2	Clyde	2	27	7, 8
3	Humber	3	108	9
4	River Almond	1	27	10, 11, 12

3.3.4 Microcosm Design One

Microcosm Experiment One aims to analyse PHE solubility and bioaccessibility across three sampling locations, each within the Humber and the Clyde catchments. For each sampling location, nine subsampling points for soil were analysed. Selecting nine replicate samples captures the balance of accounting for the wide spatial variations in soil chemistry within each sampling location, whilst appreciating resource and time limitations, as recommended by Messing et al (2024). The nine replicates were mixed using an end-over-end shaker for nine hours at 15 rotations per minute (rpm).

Approximately 250g ±2 of dried < 6.3mm soil fractions was placed into one-litre microcosms for an initial one-week pre-incubation (at 21°C). This pre-incubation equilibrated soil microbial respiration following the sieving/homogenisation processes, applying the recommendations proposed by Comeau et al (2018). The particle fraction of < 6.3mm was used within all the microcosm setup experiments. A < 6.3mm soil fraction was selected to ensure soil fraction uniformity, allowing variables, such as water retention and aeration to be controlled, whilst striking the balance of removing larger organic debris (leaves, wood, and roots) and maintaining the soil particle structure (Messing et al 2024).

The microcosms were initially flooded for 14 days and then air dried for five days (Table 3.3). Each microcosm was flooded with 600 mL of artificial rainwater (11.6 mg/L of NH_4NO_3, 7.85 mg/L of K_2SO_4, 1.11 mg/L of Na_2SO_4, 1.31 mg/L of $MgSO_4 \cdot 7H2O$, and 4.32 mg/L of $CaCl_2$) according to the UK average rain composition (Tyler et al 2016). The 600 ml volume was selected to ensure the entire MicroRhizon^{TM} sampler, pH, and Eh probes were fully submerged when making recordings, and also, several studies recommend using this volume to provide the sufficient submersion of soil for conducting microcosms (Arth and Frenzel 2000; Gao et al 2018; Mehrotra and Sedlak 2005; Schwartz et al 2016). Selecting 14 days for flooding ensured ample time for the redox potential to transition from oxidising to reducing redox conditions, and to observe such redox transitions on copper, lead, and arsenic solubility and bioaccessibility (Wisawapipat et al 2024).

Many floods worldwide are less than 14 days of inundation, allowing the findings from this microcosm setup, regarding how copper, lead, and arsenic solubility and bioaccessibility change, applicable to wider flooding contexts (Basso et al 2023).

Selecting five days for drying ensured considerable time to remove soil moisture, allowing the transition from reducing to oxidising redox conditions, influencing copper, lead, and arsenic solubility and bioaccessibility, to be observed (Wisawapipat et al 2024).

The microcosms were stored in sealed incubators at a constant temperature of 21°C throughout the flooding and drying periods. Selecting 21°C is close to room temperature, which is conducive for microbial activity and growth. The soil porewater was sampled throughout using MicroRhizon^{TM} samplers, placed into the microcosm and embedded 7cm into the soil at a 45° angle. The porewater collected for analysis during the experiment was immediately acidified to 2% nitric acid to preserve the samples by inhibiting microbial growth (Argumedo et al 2023). The porewater samples were analysed for major cations (e.g., sodium, potassium, and magnesium), trace elements (e.g., iron, aluminium, and manganese), and the PHE of interest (copper, lead, and arsenic) using inductively coupled plasma optical emission spectrometry (ICP-OES). Major porewater anions (e.g., chloride, bromide, fluoride, and sulfate) were also analysed using ion chromatography. The porewater samples were collected daily (Table 3.3). The porewater pH and Eh were recorded immediately when the porewater was collected by using a HANNA HI-98107 probe inserted at the soil surface for 20 seconds. The probe was calibrated using pH 4 and pH 10 buffer solutions for every ten samples.

Table 3.3. *Microcosm experimental design indicating the sampling periods and the flood and drying periods.*

Days Flooding														Days Drying				
1	2	3	4	5	6	7	8	9	10	11	12	13	14	1	2	3	4	5
★	★	★	★	★	★	★	★	★	★	★	★	★	★	★	★	★	★	★

Key

★ Porewater Sampling

The microcosm experiments for the Humber and the Clyde were conducted simultaneously. The three sampling locations for the Humber and the Clyde were subdivided into groups. For both locations, blocks one, two, and three (B1, B2, B3) represented sampling location One for both catchments. Blocks four, five, and six (B4, B5, B6) indicated sampling location Two for the Humber and Clyde catchments. Blocks seven, eight, and nine (B7, B8, B9) represented sampling location Three for both catchments (Figure 3.6).The purpose of dividing the microcosms in these block systems was to ensure that during the initial porewater sampling, there was enough time for the microcosms to recover and stabilise. By "recover" and "stabilise," when the pH probes were inserted into the microcosms and the porewater was extracted, this may have created a slight alteration to the biogeochemistry (e.g., turbidity of the flood water, oxygen flow, and movement of the floodwater). The study by Hu et al (2019) shows this soil disturbance interfering with microbial and fungal community respiration processes, and recommended minimising such disturbance during porewater sampling, by creating a larger time gap between porewater sampling. The block microcosms design (Figure 3.6) shows at 9 am B1, B4, and B7, representing sampling locations One, Two and Three being sampled. The subsequent time at 10 am shows B2, B5, and B8, representing sampling locations One, Two and Three; however, as these microcosms were not previously sampled at 10 am, allowing the previous microcosm setups to "recover," following the recommendations by Hu et al (2019).

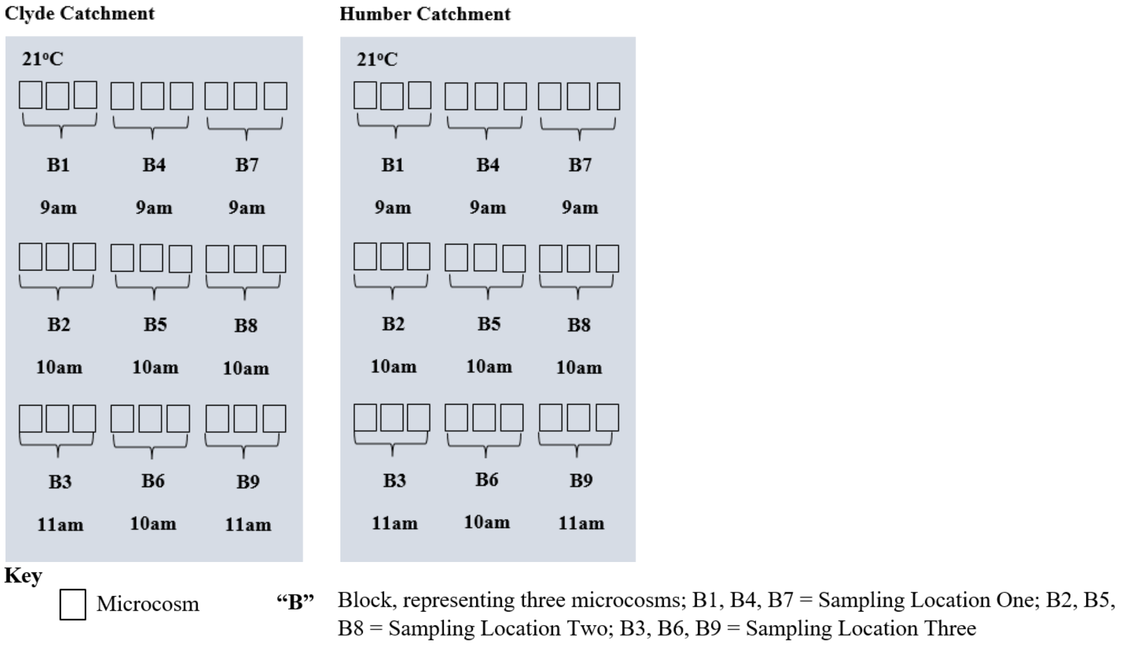

Figure 3.6. *Shows the Microcosm One sampling design. The figure illustrates two rectangular blue boxes representing the microcosm incubator chambers for Clyde (left) and Humber (right). The incubators were both consistently set at 21°C ambient temperature. The smaller square boxes represent the individual microcosm setups. The codes "B1, B2, and B3" represent sampling location one for both catchments, "B4, B5, B6" denote sampling location two and "B7","B8", and "B9" indicate sampling location three. The figure demonstrates that at 9 am, 10 am, and 11 am, each sampling location is analysed; however, the design of the experiment ensures that in a single sampling day from 9 am to 11 am, no microcosm setups are sampled twice.*

3.3.5 Microcosm Design Two

This microcosm design investigated the influence of changing ambient temperatures on soil microbial communities and PHE porewater solubility. This experimental setup involved microcosm experiments with soil samples collected from the Clyde Catchment (Figure 3.5, Section 3.3.1).

The microcosm experiment ambient air temperatures were incubated at 20ºC, 30ºC and 40ºC. These temperature gradients were selected by covering a significant range of ambient temperatures within many terrestrial environments (Li et al 2024). At 20ºC, it covers many European and North American regions, 30ºC in tropical and temperate locations, and 40ºC in semi-arid regions (Prigent et al 2024). This span of temperatures means that the relationships observed between temperature and soil microbial activity in this experiment may apply to a variety of environments (Li et al 2024). Mesophilic bacteria, which are the most common soil bacteria, have optimal enzymatic activity within these temperature ranges (20 - 40ºC) (Wang et al 2023). The 40ºC threshold approaches the upper tolerance limit of many soil microbial enzymes, particularly mesophilic bacteria, allowing an analysis of how the beginning of enzymatic denaturing at this temperature influences PHE dynamics (Lepock et al 1990).

Approximately 250g ± 2g of air dried soil was placed into 27 microcosms (9 microcosms for each sampling location). Three replicate microcosms were placed at each temperature point. These microcosms were flooded with 600ml of artificial rainwater for fourteen days before being allowed to dry out for five days. Soil porewater was regularly sampled at the same frequency as microcosm design one (see Table 3.3) and analysed for physicochemical parameters and PHE porewater solubility using ICP-OES analysis. The microcosms were subdivided into block systems (B1, B2 and B3 = sampling location One, B4, B5, and B6 = sampling location Two, B7, B8, and B9 = sampling location Three). Each block (e.g., B1) contained three replicates. For the entire experimental setup, outlining the temperature treatments and sampling design, see Figure 3.7 below.

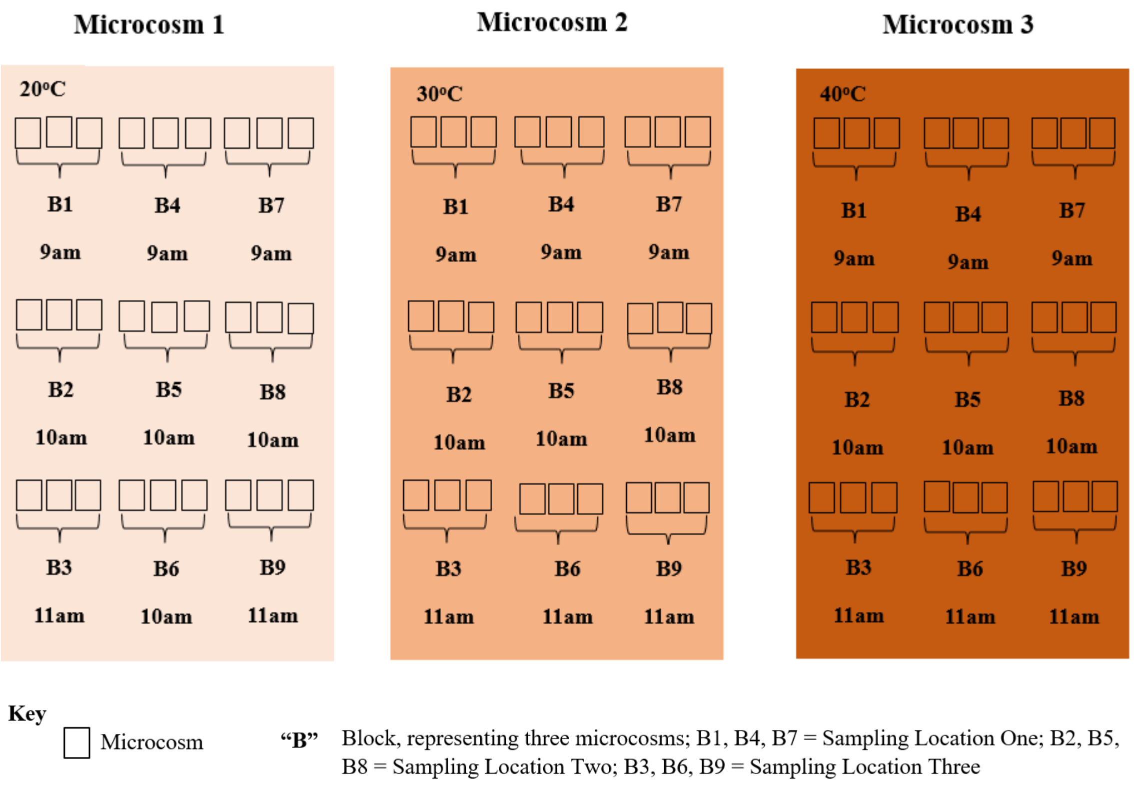

Figure 3.7. *The experimental design shows that each of the three setups (20°C, 30°C and 40°C) contains 27 microcosms. The square boxes indicate the microcosms and show the microcosm groupings and the associated porewater sampling times. The experimental setup replicates the design undertaken in the morning between 9-11 am.*

3.3.6 Microcosm Design Three

The third microcosm investigated the impact of different flood severities, ranging from a (1) typical annual flood, (2) 1 in 100-year flood, (3) 1 in 500-year flood, and (4) 1 in 10,000-year flood (Figure 3.7, Section 3.3.3). This microcosm examined PHE porewater solubility and bioaccessibility within the Humber catchment under these different flood treatments. These flood experiments mimicked real flooding events by extracting data from flood monitoring stations, which recorded the flood length. The data from these flood monitoring stations were derived from the National Oceanic and Atmospheric Administration (NOAA, 2022), UK Centre for Ecology and Hydrology (UKCEH, 2022), United States Geological Survey (USGS, 2022), and the United States Environmental Protection Agency (USEPA, 2022).

In terms of mimicking such floods, these microcosms simulated the flood length and how frequently the floodwater receded and then returned. The microcosms were drained and reflooded according to the time intervals from real flood data (Figure 3.8).

The number of microcosm experiments used within this setup replicated the previous microcosm design one (Section 3.3.3.1) and design two (Section 3.3.3.2).

Each of the four flood severity setups mimicked, using the real flood data, 27 microcosm floods (9 per sampling location). For a detailed methodology around how the microcosms were prepared, see Section 3.3.3.1. The microcosms were incubated at 21°C throughout the flooding and drying periods. The porewater was extracted using MicroRhizons^{TM}, and then acidified (2% HNO_3) before analysing copper, lead, and arsenic porewater solubility and other physicochemical parameters.

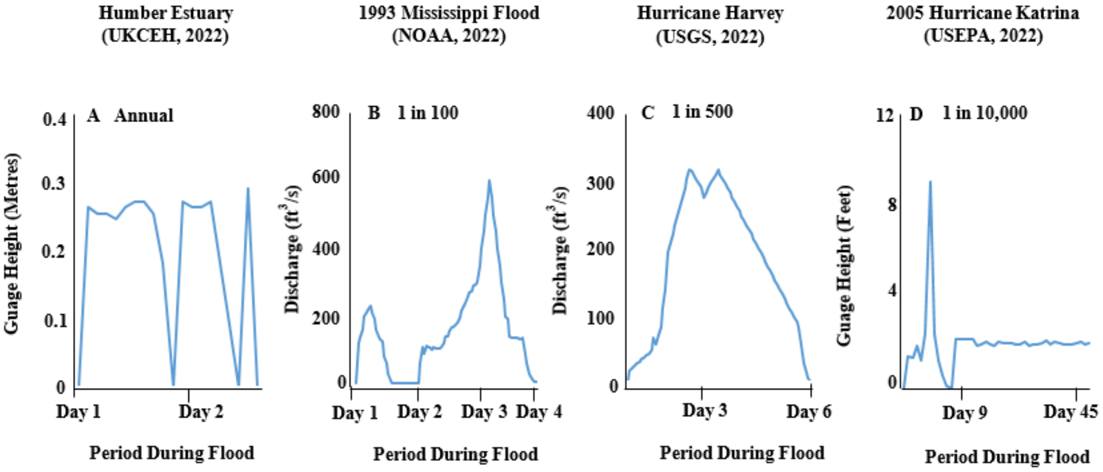

Figure 3.8. *Flood hydrological regimes mimicking real flood data. The titles of the different flood names are denoted above. The flood ranges differ in duration by flood length and the frequency of drying cycles (NOAA 2022; UKCEH 2022; USEPA 2022; USGS 2022). The flood severity (e.g., 1 in 100, 1 in 500) denotes the flood length and the repeated flooding and drying cycles. For instance, a flood length considerably long (e.g., over 20 days) would be considered a severe flood (i.e., > 1 in 500).*

3.3.7 Microcosm Design Four

This microcosm experiment investigated the influence of land use type and land slope gradient on soil copper, lead, and arsenic porewater solubility within the three sampling locations along the River Almond embankment. Land gradient and slope data were obtained from the inbuilt QGIS databases on land use information extracted from Google Maps (Google Maps, 2024).

The microcosm simulated the flood length of a recorded flood across three sampling locations along the River Almond embankment in December 2020, occurring for five days (Figure 3.9), where flood data was obtained from the River Almond flood gauging station (River Levels, 2023). This microcosm experiment analysed soil copper, lead, and arsenic PHE porewater solubility within the three sampling locations. Nine microcosms were flooded per sampling location, totalling 27 (Section 3.3.3.1). The land gradient and vegetation coverage, expressed as percentage coverage per square meter, were different across the three sampling locations investigated.

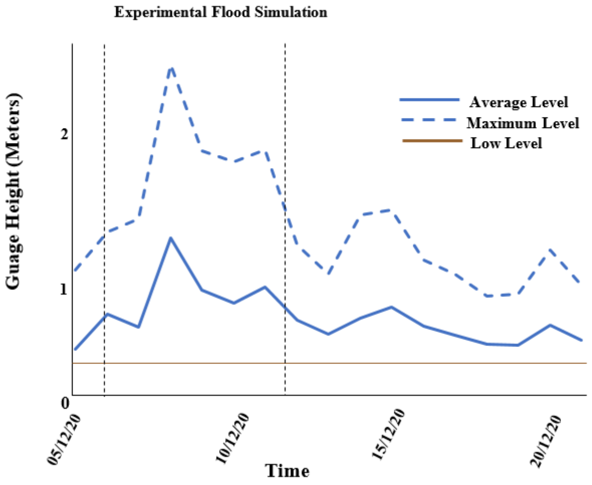

Figure 3.9. *Outlines the recorded flood depth within the River Almond between the dates 05/12/2010 and 10/12/2020. The flood in the three sampling locations along the River Almond embankment occurred for five days. This microcosm experiment's purpose was to use flood monitoring data for this specific flood (derived from River Levels, 2023) to artificially mimic this flood within the laboratory (i.e., exact flood duration and flood and drying cycles), assessing how different land gradients, vegetation coverage, and land use types influence copper, lead, and arsenic solubility.*

3.3.8 Mesocosm Setups

The mesocosm experiments were designed to mimic a real flood scenario within the Clyde catchment (Table 3.4). The flood data were obtained from the ClydeINFO weather monitoring station (ClydeINFO 2023). This flood was recorded between June 12th and June 25th, 2021. Six mesocosms were flooded for eight days, dried for six hours (receding flood time), and was then reflooded again for another two days, mimicking the flood data from ClydeINFO.

These mesocosms flooded 2.5kg of air-dried soil using 6 litres of artificial rainwater (Section 3.3.3.1). This water volume ensured the full submersion of the soil and the MicroRhizon™ porewater sampler. The quantities of soil mass and flood water volume in these experiments were scaled up to be ten times larger than those in the microcosm flooding experiments. This scaling aimed to maintain the same soil-to-water ratio as the microcosm, with the only difference being the scaling-up of water and soil in these mesocosm setups. This scaling-up also aims to simulate flooding conditions more representative within real-world scenarios, thereby enhancing the experimental relevance and findings to natural settings (Byun et al 2017).

These mesocosm also represent more realistic and natural soil systems because flooding larger quantities of soil creates more stratified soil structures and biological diversity, leading to different nutrient cycling and biological activity changes compared to microcosms (Graupner et al 2017). These mesocosms were stored in large sealed incubation chambers. Each chamber was programmed to mimic the hourly change in humidity, light irradiance, and temperature throughout the flood.

Table 3.4. *Mesocosm setup outlining the catchment, research aim, mesocosm number and where in thesis, derived from the flow chart part, this section is attempting to address.*

Mesocosm Setup	Sampling Location	Addressing Research Aim	No. of Mesocosms	Flow Chart Part
1	Clyde	4	27	13, 14

The six incubator setups, labelled “T1-T6”, were used to replicate different temperature and humidity levels (Figure 3.10). The first group of three incubators mimicked the actual temperatures observed during the real flood and at three different humidities (35%, 65% and 95%). The base temperature, therefore, was the actual hourly temperature recordings during the flood. For example, if the recorded ambient temperature at 14:30 was 14.5^{o}C, then the mesocosm chamber’s base temperature at this time was also 14.5^{o}C. This first group investigated how humidity alone influences PHE dynamics. The second group of three incubators mimicked a climate change scenario by increasing all the temperature changes by 1.5^{o}C from the base temperature at 35%, 65%, and 95% humidity. This second group investigated whether a climate change scenario could influence PHE dynamics (Figure 3.10).

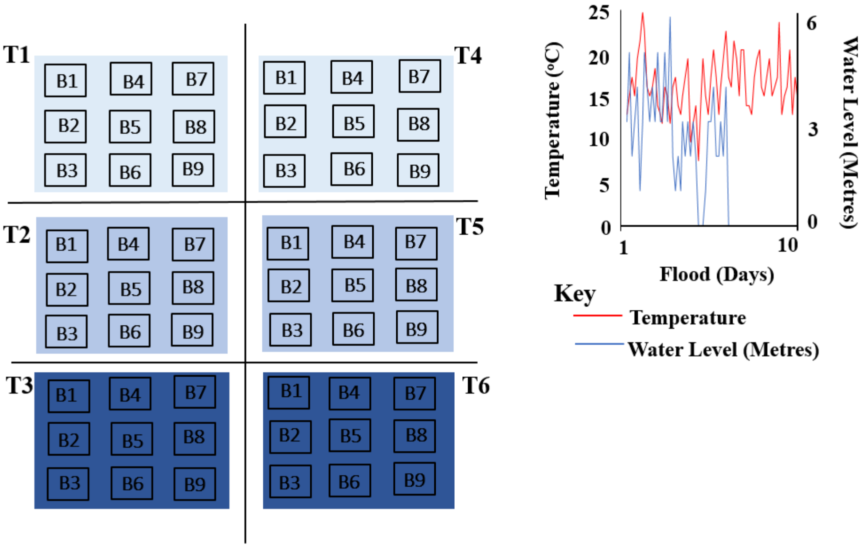

Figure 3.10. *The groupings "B1, B2, and B3" represent sampling location one, "B4, B5, and B6" denote sampling location two, and "B7, B8, and B9" is sampling location three. The different shades of blue represent the humidity levels, with light blue indicating a low humidity of 35%, medium shade of blue at 65%, and darkest blue at 95%. Treatments 1-3 indicate the current ambient temperature scenario, whereas treatments 4-6 indicate a climate change scenario of a 1.5°C increase. The graph indicates the flood hydrological and temperature data.*

3.3.9 Bioaccessibility

The PHE bioaccessibility was determined using the method developed by the BioAccessibility Research Group of Europe (BARGE) and known as the Unified BARGE Method (Wragg et al 2011). Since development this method has become ISO standard (ISO 17924:2018) (Zingaretti et al 2021). Briefly, 2g ± 0.2 of < 250µm of each soil sample was subjected to extraction by simulated saliva and gastric fluids (gastric phase) rotated at 15rpm for 1 hour at 37°C, centrifuged at 4500rpm, and the supernatant removed for analysis by ICP-OES. A second extraction was undertaken where a separate aliquot of soil was subjected to saliva/gastric fluids for 1 hour (as above), followed by the addition of bile/duodenal solutions, rotated at 15rpm for 4 hour at 37°C, centrifuged at 4500rpm and the supernatant removed for analysis (Figure 3.11, based on information obtained from Wragg et al (2011). The < 250µm size fraction was used in the bioaccessibility experiments as this is the upper bound of the size fraction that adheres to children's hands (Wragg et al 2011).

Each sample was extracted in triplicate (Figure 3.11) and each BARGE experiment contained one black sample, which only contained the gastric and intestinal solutions but with no soil. To determine the accuracy of the BARGE method, a British

Geological Survey (BGS) reference material was used (BGS 102). This reference material is a homogenised ferritic brown earth soil containing slightly elevated concentrations of lead and arsenic of geogenic origin and is described as “naturally contaminated” (Wragg 2009).

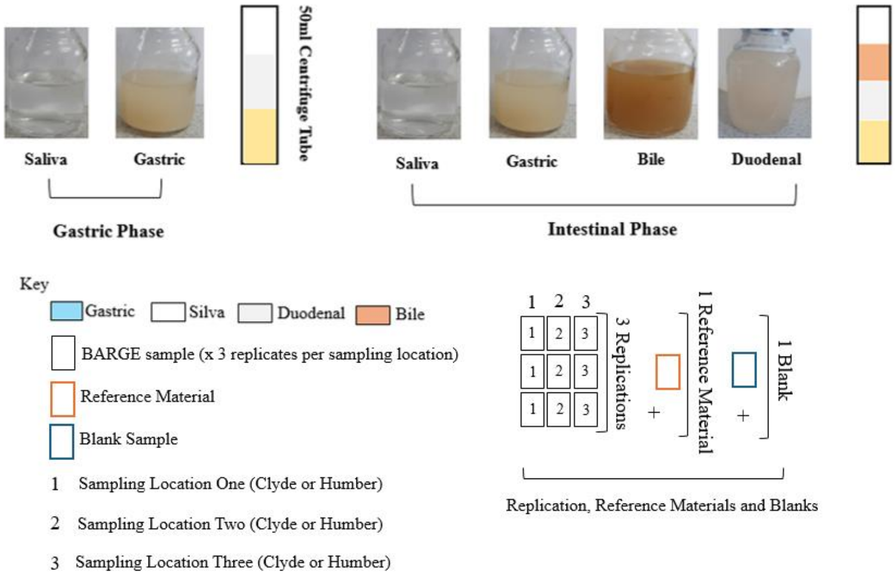

Figure 3.11. *BARGE experimental procedure. The 50ml test tubes represent the different samples (i.e., silva, gastric, bile and duodenal) being added to the tubes before being rotated and centrifuged (i.e., the tubes are rotated and centrifuged with the added samples). The left 50ml test tube represents the added silva and gastric solutions. The right 50ml test tube indicates the added silva, gastric, bile and duodenal solutions. The numbers “1”, “2” and “3” represent sampling locations 1,2 and 3 within either the Clyde or Humber catchment. The purpose of these number is to illustrate that per BARGE experiment there were three replicates per sampling location, 1 reference material, and 1 blank sample.*

3.3.10 Physicochemical Speciation

The non-specific sequential extraction procedure chemometric identification of substrates and element distribution (CISED) was used to identify the PHE fractionation between the physicochemical components of the test material (Cave 2004). This CISED method was chosen over other types of sequential extraction (e.g., Tessier extraction) by being significantly effective at processing large and complex datasets (Giacomino et al 2011; Tessier et al 1979). Multivariate chemometric techniques, which allow multiple parameters to be taken into account simultaneously, aid the visualisation and analysis of the sequential extraction results (Giacomino et al 2011).

Briefly, 2g (<250μm) of soil was sequentially extracted using increasing concentrations of aqua regia (0.01M-5M). The extracts from each step were analysed for major and trace elements by ICP-OES including calcium, potassium, magnesium, iron, manganese, sodium, phosphorous, aluminium, zinc, copper, lead, arsenic, chromium, titanium, nickel, and vanadium (Figure 3.11; Table B3.1, Appendix B). The elemental data from each extractant was subjected to a chemometric mixture resolution algorithm described by Cave (2004) to determine the number and proportion of physicochemical components and the distribution of PHE therein (Figure 4B, Appendix B) (McLaren 2019).

The number of sample replicates, blanks and reference materials was the same as outlined in the BARGE setup (Section 3.3.39, Figure 3.11). Each of the three sampling locations within each of the catchments (Clyde and Humber) were sequentially extracted simultaneously. The CISED extraction used one blank sample and one reference material (BGS 102). For an overview of the CISED extraction procedure, see Figure 3.12 (Cave 2004).

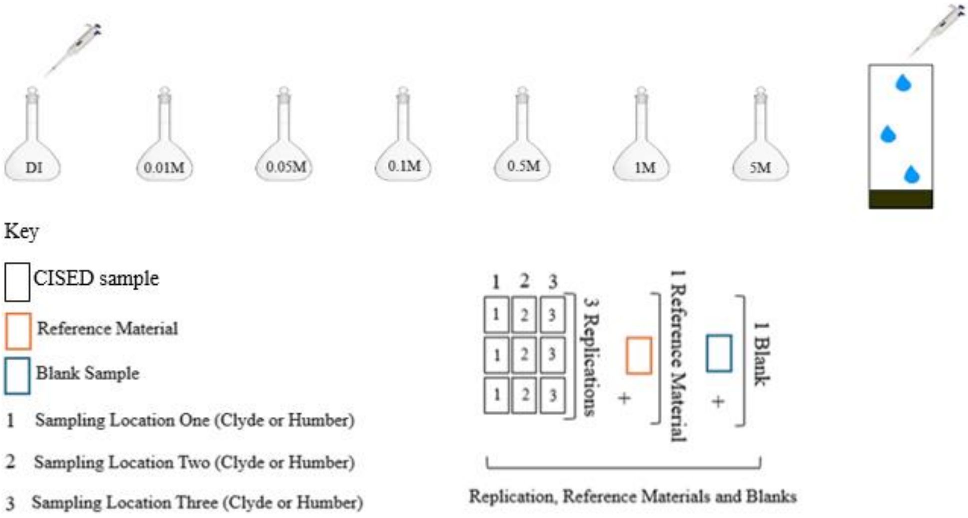

Figure 3.12. *CISED extraction protocol. The soil samples are sequentially exposed to gradually increasing aqua regia concentrations . ICP-OES analysed the total metals leached within each phase. Elemental data leached within each sample are then subjected to a chemometric algorithm, determining the PHE concentration, proportion and composition (Cave 2004). The numbers "1", "2" and "3" represent sampling locations 1,2 and 3 within either the Clyde or Humber catchment. The purpose of these number is to illustrate that per BAGRE experiment there were three replicates per sampling location, 1 reference material, and 1 blank sample per CISED extraction.*

3.3.11 Statistical Analysis

All data, including the results from BARGE and CISED, were subjected to normality testing, and outliers were removed from the upper and lower median interquartile ranges (IQR) at the 95% confidence level. This approach of removing the outliers from the lower and upper IQR follows the methodologies outlined in Mishra et al (2019), suggesting such an approach minimises skewing the analysis.

Residual diagnostic plots (i.e., q-q plot and residuals Vs fitted) visualised the data normality using the *ggplot2* package in RStudio (Version 2023.03) (Bengtsson et al 2017). Data quality control was regulated using a pre-defined eligibility criteria (Figure 3.13). Multicollinearity was assessed using the variance inflation factor.

Principal component analysis (PCA) was programmed using the *FactoMineR* package in RStudio, and such information was analysed for clustering and data relationships around physicochemistry influencing PHE dynamics (Husson et al 2016). PCA was not applied to the CISED data as the chemometric algorithm already applies PCA clustering. Any feature variables exhibiting clustering were implemented into a linear regression model examining statistically significant correlations using the *lme4* package (Feng et al 2015).

Hierarchical heatmaps clustered PHE mineral phases derived from the chemometric algorithm using the *pheatmap* package in RStudio (Couch and Kuhn 2022). The purpose of producing such heatmaps is to identify patterns and relationships in the soil PHE chemical component data across each sampling location. This data was scaled and transformed into z scores by dividing the standard deviation and maximising the sample difference. Scaling data into z-scores serves the purpose of detecting data anomalies. A distance matrix between the components was generated, and using the Euclidean distance by complete linkage, clustering was performed by agglomerative nesting aids in grouping the data and identifying correlations.

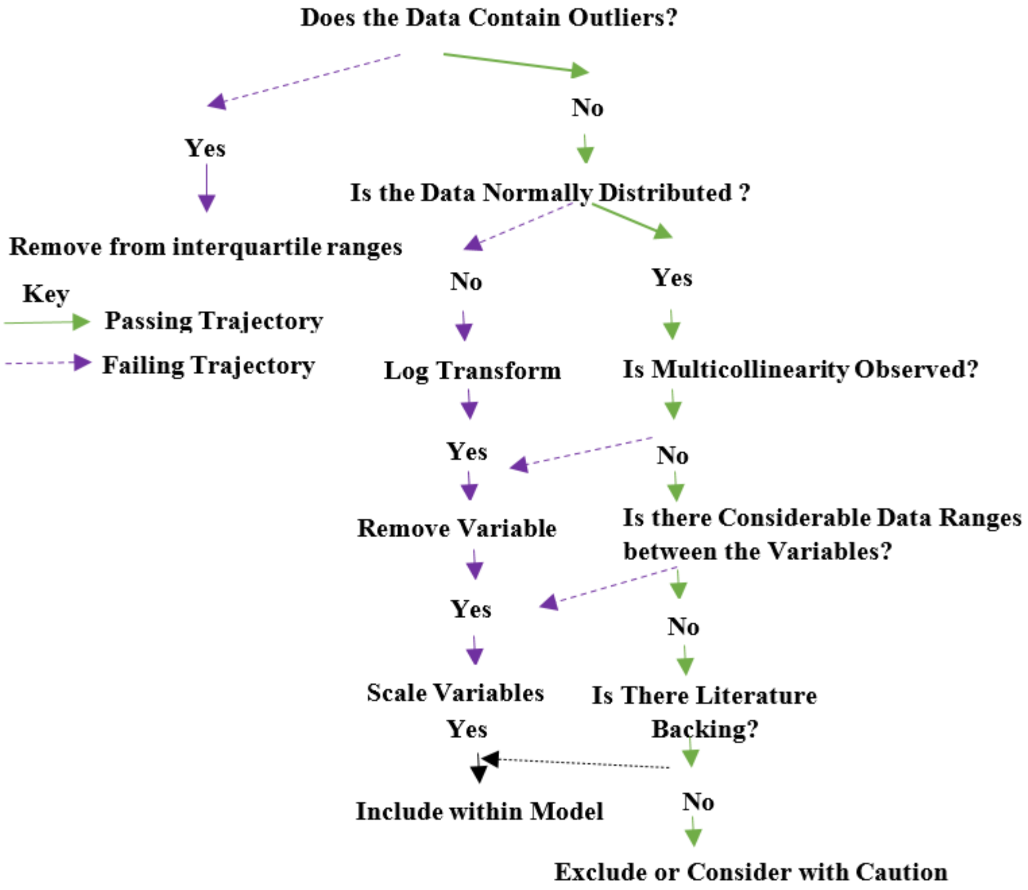

Figure 3.13. *Outlines the schematic process of ensuring data quality before implementing such data into the predictive model. The solid green arrows indicate the direction which the data would be accepted into the model. Any dashed purple arrows denote procedural steps that violate the model criteria.*

3.3.12 Quality Assurance

All reagents used were of analytical grade, purchased from Fisher Scientific and Sigma Aldrich. Purified Milli-Q deionised water was used throughout all the experimental procedures and cleaning processes. All the experimental methods used reference materials and procedural blanks (British Geological Survey, 102 Arsenic bioaccessibility guidance soil) (Wragg 2011). For information around the reference material used, see Section 3.3.9. Depending on the experimental procedure, these blanks consisted of either deionised water or acid matrix solutions. The BARGE and CISED experimental analysis contained three replicates per sampling location.

3.4 Results

3.4.1 Soil/Sediment Characteristics

Soils from the Clyde catchment were more acidic than those collected from the Humber and River Almond (Table 3.5), with average soil pH of 5.86, 7.13, and 7.04, respectively. The total soil organic carbon content was the highest within the Clyde, with an average content of 77.9 mg/L C. The Humber had the lowest total soil organic carbon content, averaging 6.55 mg/L C. The average soil moisture content within the Humber, Clyde and the River Almond was 7.5%, 23% and 16.3%, respectively, due to the Humber and the River Almond having a more sand-based soil texture (Figure B3.2, Appendix B). For information around how the soil pH, total organic carbon and moisture content were determined, see Section 3.3.3 and Appendix B, Section 2.

Many PHE concentrations, notably lead, based on estuarine concentrations exceeded CLEA's (Contaminated Land Exposure Assessment) minimum threshold levels for all the sampling locations investigated (Table 3.5; CLEA 2023). The Clyde catchment has the highest average total soil lead concentration (183 mg/kg), followed by the River Almond (92 mg/kg), and the Humber (57 mg/kg). The average total soil copper was the highest in the Clyde (65.3 mg/kg), followed by the River Almond (61 mg/kg) and the Humber (22.9 mg/kg). The Humber has the highest total soil arsenic concentration at 20 mg/kg, the Riv er Almond at 9 mg/kg and the Clyde at 8 mg/kg. For information around how these concentrations were established, see Section 3.3.3 or Appendix B, Section 2.

Table 3.5. *Outlines the soil/sediment characteristics of the three sampling locations investigated and across the associated sampling points.*

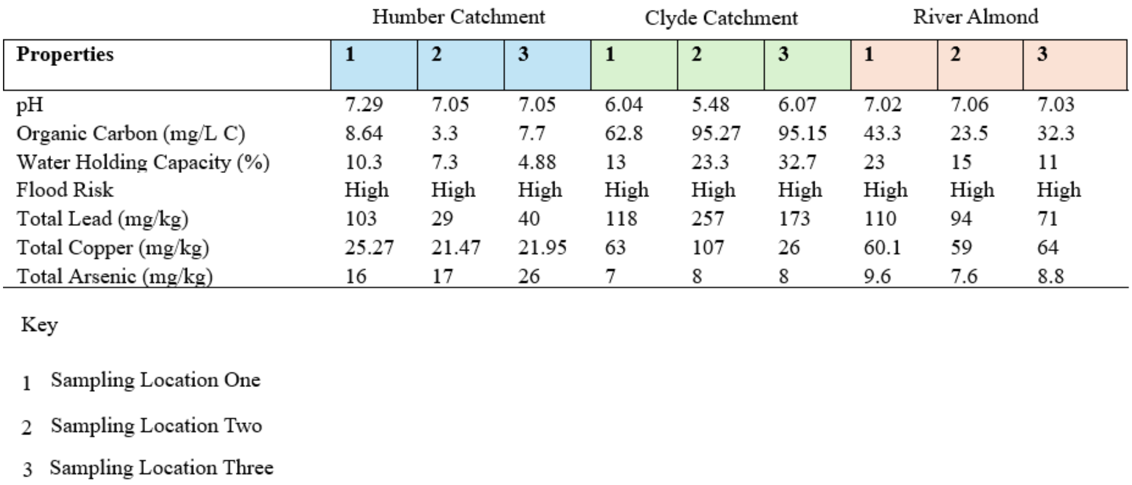

	Humber Catchment			Clyde Catchment			River Almond		
Properties	**1**	**2**	**3**	**1**	**2**	**3**	**1**	**2**	**3**
pH	7.29	7.05	7.05	6.04	5.48	6.07	7.02	7.06	7.03
Organic Carbon (mg/L C)	8.64	3.3	7.7	62.8	95.27	95.15	43.3	23.5	32.3
Water Holding Capacity (%)	10.3	7.3	4.88	13	23.3	32.7	23	15	11
Flood Risk	High	High	High	High	High	High	High	High	High
Total Lead (mg/kg)	103	29	40	118	257	173	110	94	71
Total Copper (mg/kg)	25.27	21.47	21.95	63	107	26	60.1	59	64
Total Arsenic (mg/kg)	16	17	26	7	8	8	9.6	7.6	8.8

Key

1	Sampling Location One
2	Sampling Location Two
3	Sampling Location Three

3.4.2 Analysing the Influence of Flooding on PHE Porewater Solubility - Microcosm Design One

This analysis focuses on the influence of flooding on the porewater solubility of copper, lead, and arsenic within both the Humber and Clyde catchments. For a complete overview of how flooding influences other PHE solubility within the Humber and Clyde, see Appendix B.

The solubility of arsenic in porewater increased with inundation time (Figure 3.14, Figures B3.3, B3.4 and B3.5, Appendix B). From days one to fourteen, the average arsenic porewater concentration increased from 3.09µg/L to 3.6µg/L and 20.3µg/L to 23.7µg/L within the Humber and Clyde with statistical significance, respectively. Copper solubility significantly decreased as flood duration increased from days one to fourteen, with average porewater concentrations decreasing from 576µg/L to 48µg/L and 399µg/L to 126µg/L with the Humber and Clyde. Lead solubility increased slightly from 13.7µg/L to 13.9µg/L between days one and fourteen within the Humber; however, decreased from 139µg/L to 93µg/L within the Clyde.

The decreased copper and lead mobility at the end of the flood compared to the beginning may be attributed to dilution effects within larger water volumes; however, complexation reactions with, for example, organic carbon and sulfide, may also explain the significant mobility decrease (Laing et al 2008). The variation between the average porewater solubility concentrations of arsenic, lead, and copper in porewater is significantly higher within the Clyde. One-Way ANOVA statistics showed the soluble porewater concentrations of arsenic, lead, and coper statistically significantly differs between the three sampling locations across the Clyde and Humber ($F = 10.7$, $p = < 0.001$; $F = 5.17$, $p = 0.01$; $F = 6.26$, $p = 0.01$, respectively). The redox potential transitions from oxidising to reducing conditions, and the pH gradually increased at all the sampling locations within the Humber and Clyde. Average pH conditions between the three sampling locations increased from pH 6 to pH 9.2 and from pH 5.3 to pH 6.2 within the Humber and Clyde, respectively. The average redox potential decreased from E_h 139 to E_h (-) 171 and E_h 290 to E_h (-) 30.6 within the Humber and Clyde, respectively. For information regarding the average, minimum, and maximum values of the different physicochemical variables in the Clyde and Humber, see Tables X and Y.

Many PHE demonstrate strong interaction effects, particularly for Pb and Zn ($R^2 = 0.88$) indicating they frequently co-occur in contaminated environments (Figure X). Cr and Ni show the highest correlation ($R^2 = 0.95$), likely due to their common sources and oxidation state similarities (Ponting et al 2021). Arsenic has a weak correlation with lead ($R^2 = 0.26$). Va and Ni and Va and Cr also indicate a strong correlation ($R^2 = 0.81$, $R^2 = 0.81$, respectively).

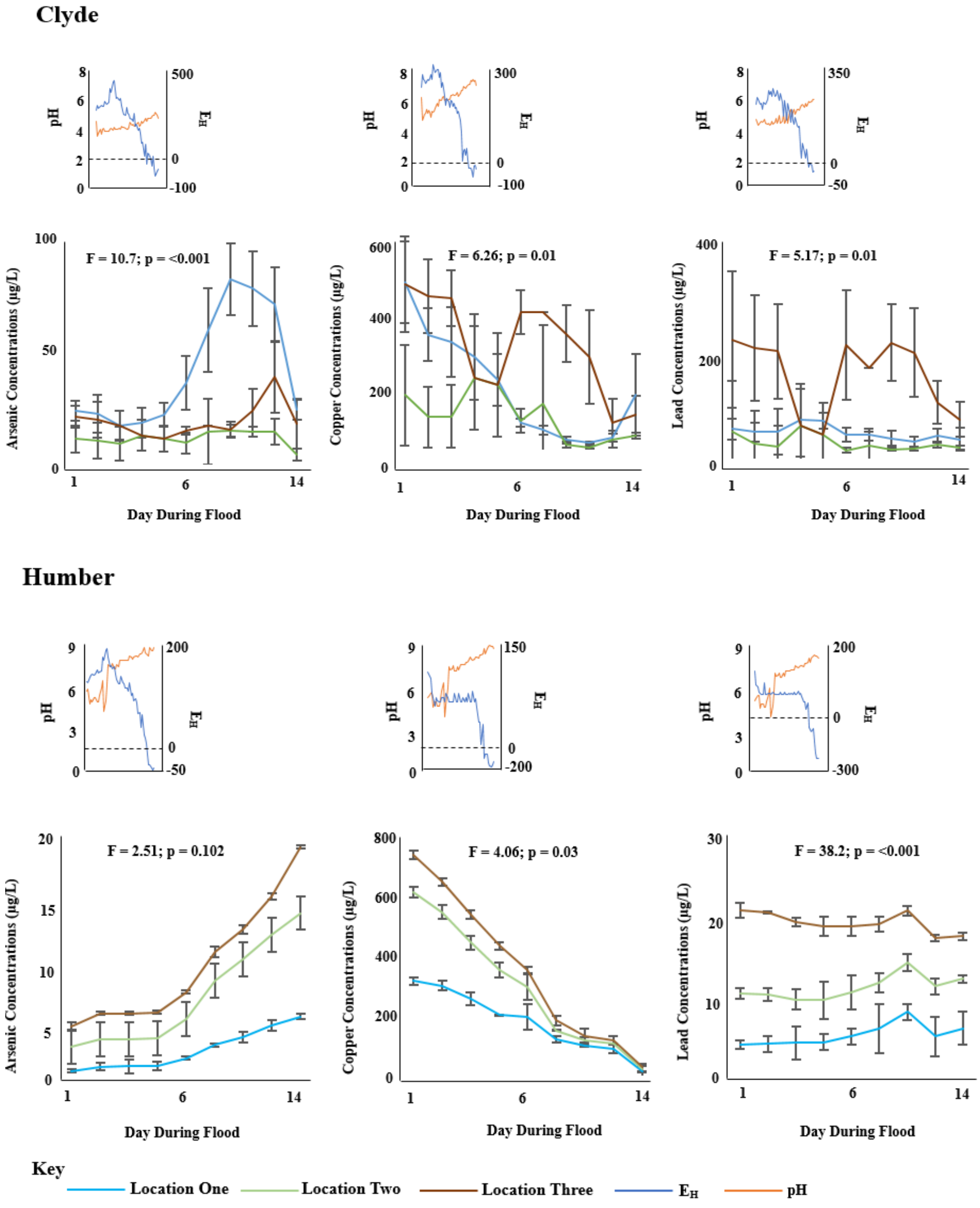

Figure 3.14. *Indicates arsenic, copper and leads porewater solubility within Clyde and Humber catchments with the associated pH and Eh changes. Error bars represent average concentrations (n=3) at the 95% CI. The top three graphs denote the Clyde and the bottom the Humber.*

Table 3.6. *Descriptive statistics (average, standard deviation, minimum, and maximum values for the different physicochemical properties in the Clyde and Humber catchment.*

	Clyde				Humber			
Physicochemical Variable	Average	Standard Deviation	Min	Max	Average	Standard Deviation	Min	Max
pH	5.83	0.78	4.12	6.45	7.13	0.98	6.12	8.32
OC(mg/L)	6.55	1.12	3.11	10	84.4	12.22	123	65
Pb (mg/kg)	183	12.4	152	189	57.3	5.66	106	43
Cu (mg/kg)	65.3	6.4	43	79	22.89	4.45	56	2
As (mg/kg)	8	0.87	3.4	13.1	20	2.2	34	3.4
K (µg/L)	38612	28224	12123	126810	34211	4533	23111	89078
Mg (µg/L)	39668	15852	13758	82274	87382	14565	67988	101900
Ca (µg/L)	193638	83416	55266	489675	124521	3233	80989	179089
Fe (µg/L)	33055	53952	1131	331584	12322	8092	4099	23498
Na (µg/L)	32085	11451	8619	109253	12865	4532	5625	23009
Al (µg/L)	19155	13319	1109	56947	11421	1011	8667	19029
Mn (µg/L)	35058	11424	105960	105960	9053	1211	4321	17922

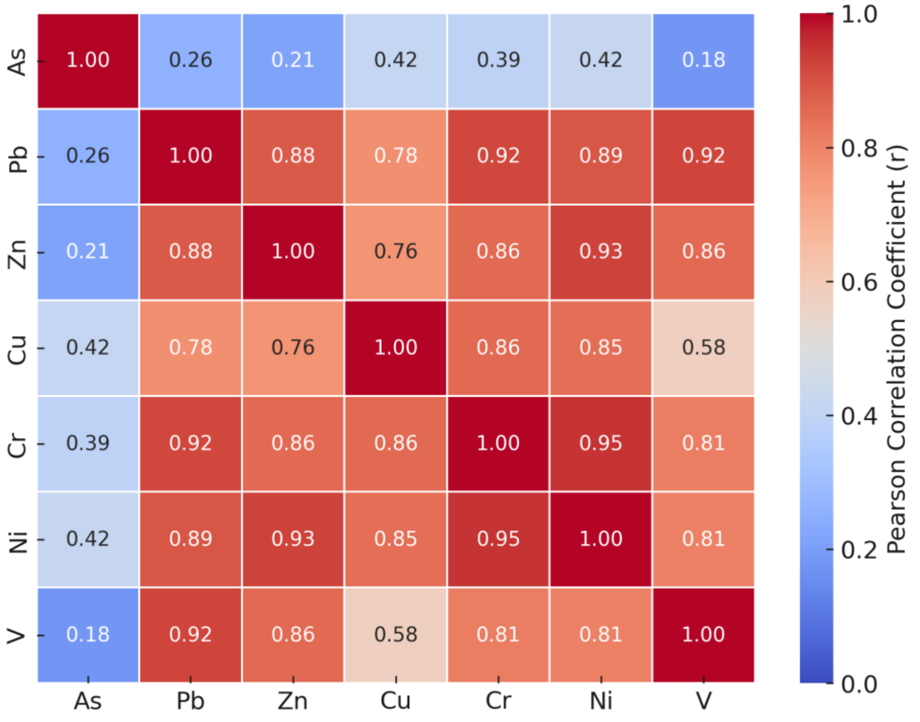

	As	Pb	Zn	Cu	Cr	Ni	V
As	1.00	0.26	0.21	0.42	0.39	0.42	0.18
Pb	0.26	1.00	0.88	0.78	0.92	0.89	0.92
Zn	0.21	0.88	1.00	0.76	0.86	0.93	0.86
Cu	0.42	0.78	0.76	1.00	0.86	0.85	0.58
Cr	0.39	0.92	0.86	0.86	1.00	0.95	0.81
Ni	0.42	0.89	0.93	0.85	0.95	1.00	0.81
V	0.18	0.92	0.86	0.58	0.81	0.81	1.00

Figure 3.15. *Correlation heat map indicating the interaction effects between the different PHE investigated.*

The PCA results, which analyse the influence of various physicochemical parameters on the mobility of copper, lead, and arsenic, indicate several discernible clusters (Figure 3.15, Figure B3.6, Appendix B). The first two axes for arsenic within the Clyde and Humber catchments explain 66.1% and 60.2% of the total variation in arsenic mobility during flooding, respectively. Such percent values are derived from PCA1 and PCA2 axes and they are percentages of variance explained by each principal component. These principal components were retained as they capture the majority of the dataset variance, reducing dimensionality, while preserving key patterns in contaminant mobility. High order PCA components contribute less variance and are therefore excluded to minimise overfitting, as these high order components explain variance which is more likely noise rather than signal. These two PCA components, explaining the majority of variation, is verified from the scree plots, illustrating two main principal components influencing PHE mobility concentrations (Figure 6). The scree plots illustrate a distinct "elbow" at PCA2, indicating that additional PCA components exceeding PCA1 and PCA2 do not contribute significantly to explaining the variance in PHE mobility. The eigenvalues for PCA1 and PCA2 exceed 1, which is commonly used as a threshold for retaining such components, further confirming PCA1 and PCA2 significance.

PCA1 predominately captures redox-sensitive processes, indicated by the influence of arsenic and manganese, suggesting that transitions in reducing to oxidising redox states likely influence arsenic mobility. Under reducing redox states, arsenic exists as arsenite; however, under oxidising conditions is arsenate, with both chemical forms of arsenic having different mobility factors. PCA2 is driven by cation exchange and pH variations, which are key variables influencing lead and copper concentrations. pH alters cation exchange capacity, ligand exchanges and the dissolution of acid sensitive mineral phases, which all influence PHE mobility.

The axes for copper within the Clyde and Humber explain 64.1% and 63.5% of the total variation in copper porewater solubility, respectively. The axes for lead within the Clyde and Humber explain 63.5% and 62.1% of the total variation in lead's mobility explained, respectively.

The PCA analysis indicates manganese negatively correlated with soluble arsenic within the Clyde catchment (based on the angle between their vectors from the PCA plot). This negative cosine means that the presence of soil manganese may associate with lower arsenic concentrations. Suda and Makino (2016) show similar findings, indicating that manganese can oxidise arsenite [As(III)] to less soluble arsenate [As(V)]. Physicochemical change during flooding is determinant of the flood length;

for example, how much a particular physicochemical variable alters with time throughout inundation (Figure 3.16). For instance, does the soil porewater solubility of potassium alter with increasing flood length? The initial results from the Humber and Clyde microcosm experiments reveal that increasing flood lengths alter soluble porewater potassium concentrations but also changes many other physicochemical parameters, such as calcium, pH, and magnesium.

These PCA results are highly significant for future work by clustering the most important physicochemical parameters influencing PHE mobility. This clustering can improve the parameterisation of machine learning features, by avoiding training such models on poorly explanatory variables, likely reducing the probability of overfitting. Identifying the most relevant feature inputs can significantly improve PHE modelling, potentially identifying locations of interest based on these clustering parameters. Integrating such PCA-driven features into predictive models, such as machine learners, can enhance the ability to estimate PHE mobility under varying flood environments and improving the risk assessment approach for contaminated sites.

These findings also reveal that the level or rate of these physicochemical changes shows a distinct pattern with increasing flood length. This pattern shows three major physicochemical changes, or what this investigation calls “phases,” that occur with flood length. In other words, these physicochemical changes with increasing flood length can be captured within three segments of change, which this experiment calls “phases.” The first phase indicates that some physicochemical variables, within the first three days of the flood, change the most significantly; this phase, for the purpose of this investigation, is called the “critical phase.” After three days of flooding to around five or six days, the physicochemical change remains statistically significant; however, gradually, the rate of change declines compared to the critical phase; this phase is called the “sub-critical phase.” The final phase is that the physicochemical changes typically do not change significantly after six days and begin to remain relatively constant, referred to as the “lag phase.” Given the clustering between physicochemistry and arsenic, lead, and copper solubility, these findings may suggest that PHE mobility changes the most significantly during the beginning of a flood.

This initial increase in the solubility of copper, lead, and arsenic in porewater may be attributed to the enhanced de-sorption of exchangeable metals from the soil during this rapid alteration of physicochemical conditions at the beginning of the flood (Daramola et al 2024). Further research is required to assess whether this pattern of physicochemical changes during flooding is observed within different locations. For an example illustrating these "physicochemical phases" with some data from this investigation, see Figure 3.16. The purpose of Figure 3.16 presents sulfate, nitrate, nitrogen oxide, and sodium to illustrate the impact of physicochemistry changes influencing PHE mobility.

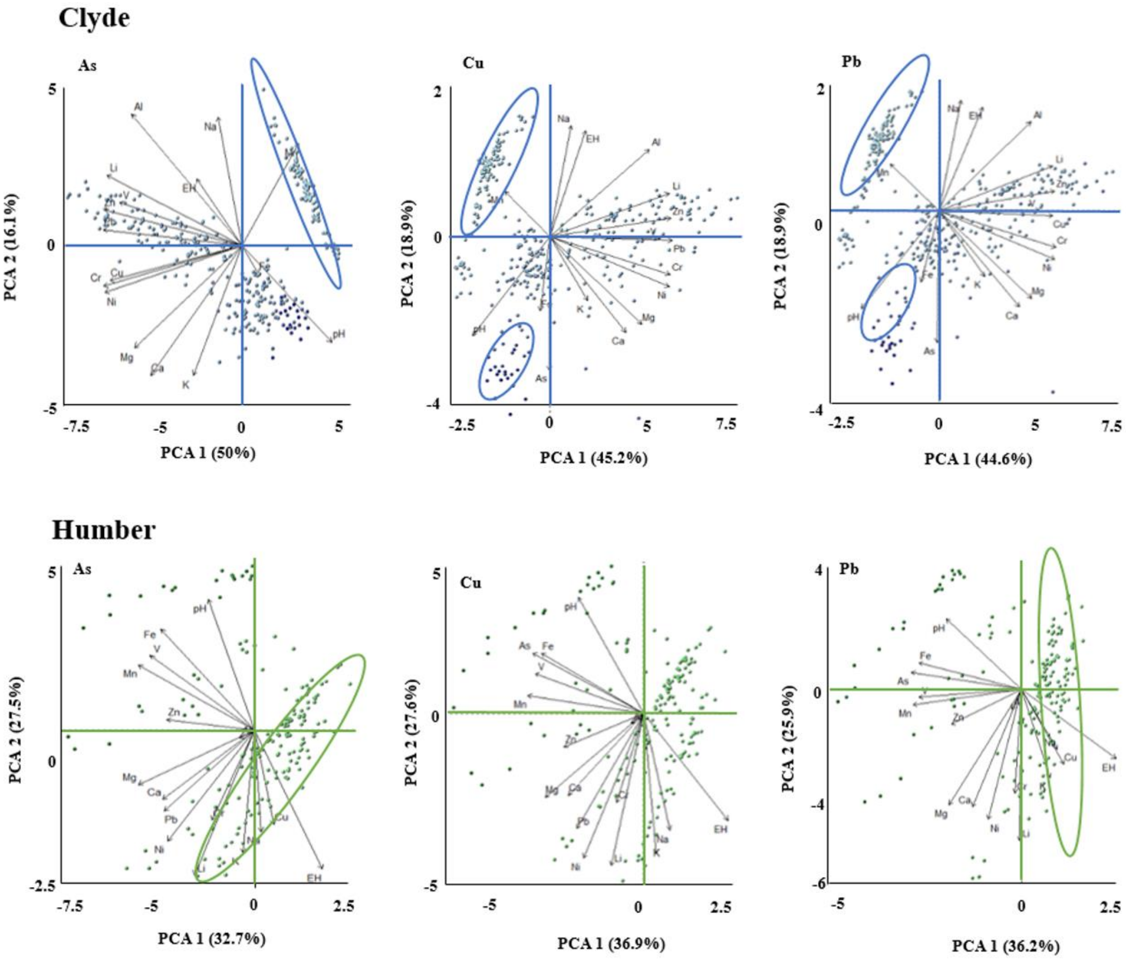

Figure 3.15. *Outlines PCA graphs illustrating how different physicochemical parameters influence arsenic, copper, and lead soil porewater solubility. The top three graphs indicate the Clyde, and the bottom three are the Humber. The PCA axes indicate a percentage value (x and y), indicating how much variance is captured from the different PCA components. The small green and blue dots represent the individual observations of copper, arsenic or lead porewater solubility concentrations. The black arrows represent the PCA vectors, illustrating the magnitude and direction of a particular feature variable (e.g., E_h, pH, K, Ca, Mg) contribution to the principal component.*

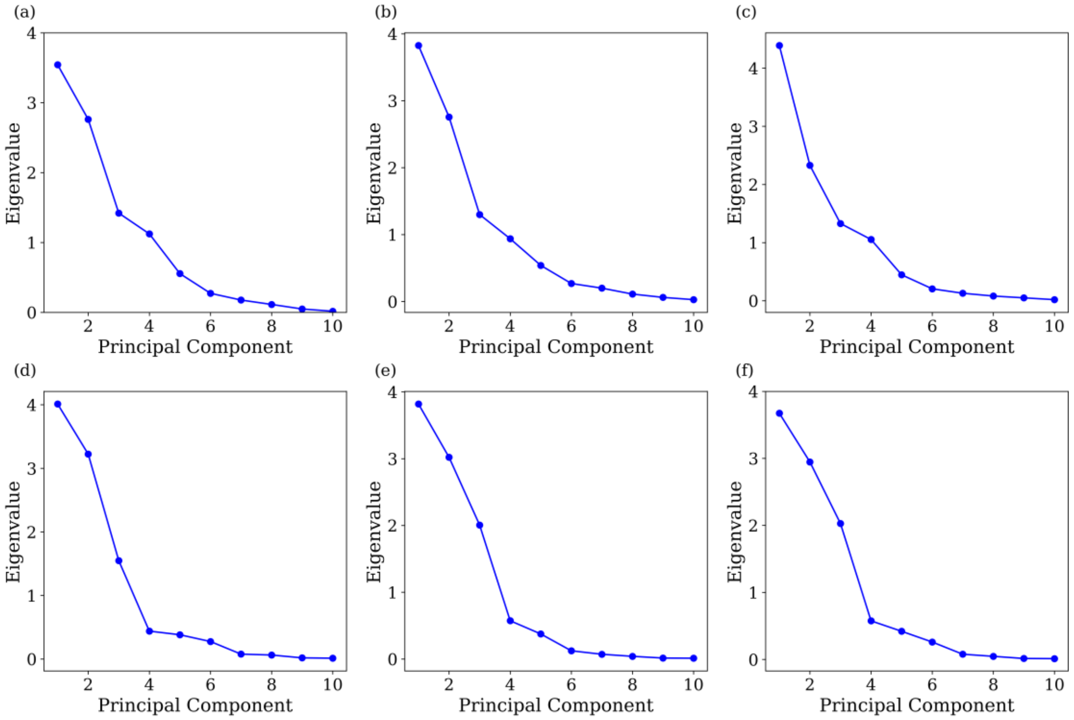

Figure 7. *Scree plot analysis outlining the number of principal components influencing PHE mobility concentrations.*

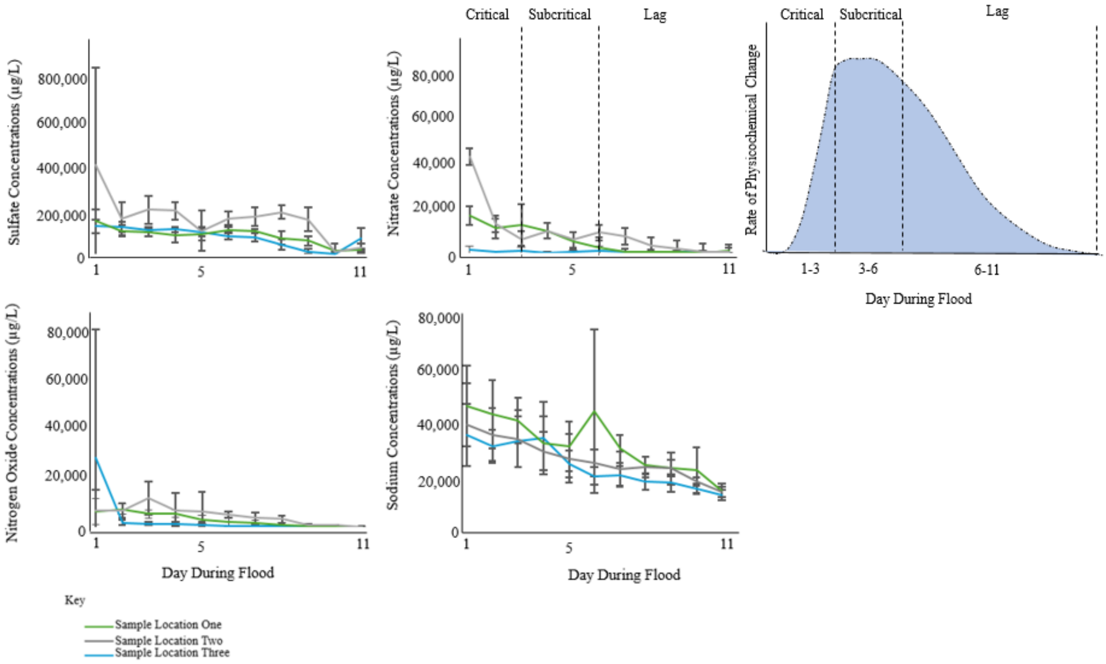

Figure 3.16. *Changing physicochemical variables during flooding within the Clyde. The figure outlines the three major phases of physicochemical change during flooding: "critical", "subcritical," and "lag." The figure shows the rate of physicochemical changes during flooding, which is illustrated using a "bell-shaped" curve, as indicated in the figure.*

3.4.3 Ambient Temperature on PHE Porewater Solubility - Microcosm Design Two

This section analyses the influence of increasing ambient temperatures (20ºC, 30ºC, and 40ºC) on copper, lead and arsenic porewater solubility within the Clyde..

At sampling locations One, Two and Three, copper solubility on the first day of flooding was the highest at 40ºC, initially at 362µg/L, 591µg/L, and 539µg/L, respectively, and at 41µg/L, 37µg/L, and 92µg/L, respectively on the last day of flooding (Figures 3.16 A, 3.16B, 3.16C). Copper's solubility within sampling locations One, Two, and Three was the lowest at 20ºC, initially at 161µg/L, 198µg/L, and 195µg/L, respectively, during the first day of flooding, and at 37µg/L, 29µg/L, and 87µg/L, respectively, on the last day of flooding.

These findings show that increasing ambient temperatures increase copper solubility during flooding; however, the results also indicate that despite copper solubility increasing, the results are not statistically significant (p = 0.85, F-crit = 3.40). These statistically insignificant findings may be attributed to the small sample size, which only covered one catchment, meaning this experiment may not be able to detect a true effect (Kontopantelis et al 2010). By "true effect," this means a real non-zero relationship between variables in a sample size or, in other words, the actual impact that is happening due to the experimental intervention (i.e., ambient temperature) (Nakagawa and Cuthill 2007). The variability of soluble copper at the beginning of the flood was also relatively high (greater than one standard deviation from the mean), again making it harder to detect a true effect (Kontopantelis et al 2010).

The solubility of lead within sampling locations One, Two and Three showed similar results to copper, exhibiting the highest soluble lead concentrations throughout the flood at 40ºC and the lowest concentrations at 20ºC (Figures 3.17D, 3.17E, 3.17F). Lead's solubility, however, increases initially between days one to five during flooding at 20ºC (71-125µg/L), 30ºC (105-289µg/L), and 40ºC (100-228µg/L). The reason why soluble lead is initially increasing during the flood are attributed to the oxide dissolution (e.g., iron and manganese) that is causing lead to become solubilised (Ponting et al 2021). Despite the higher temperatures increasing lead solubility throughout the flood, the results are statistically insignificant (p = 0.53, F-crit = 3.47).

Throughout the flood, higher ambient temperatures (40ºC) increased the soil arsenic porewater concentrations compared to lower temperatures (20ºC) (Figure 3.17G, 3.16H, 3.16I). The highest solubilised arsenic concentrations throughout the flood were around day eight of flooding at 40°C within sampling locations One, Two and Three at 24µg/L, 26.6µg/L, and 21.3µg/L, respectively. These high soluble arsenic concentrations at the end of the flood attribute to the reducing conditions transforming arsenic [(V)] into more soluble arsenic ([AsIII]) (Connolly et al 2021).

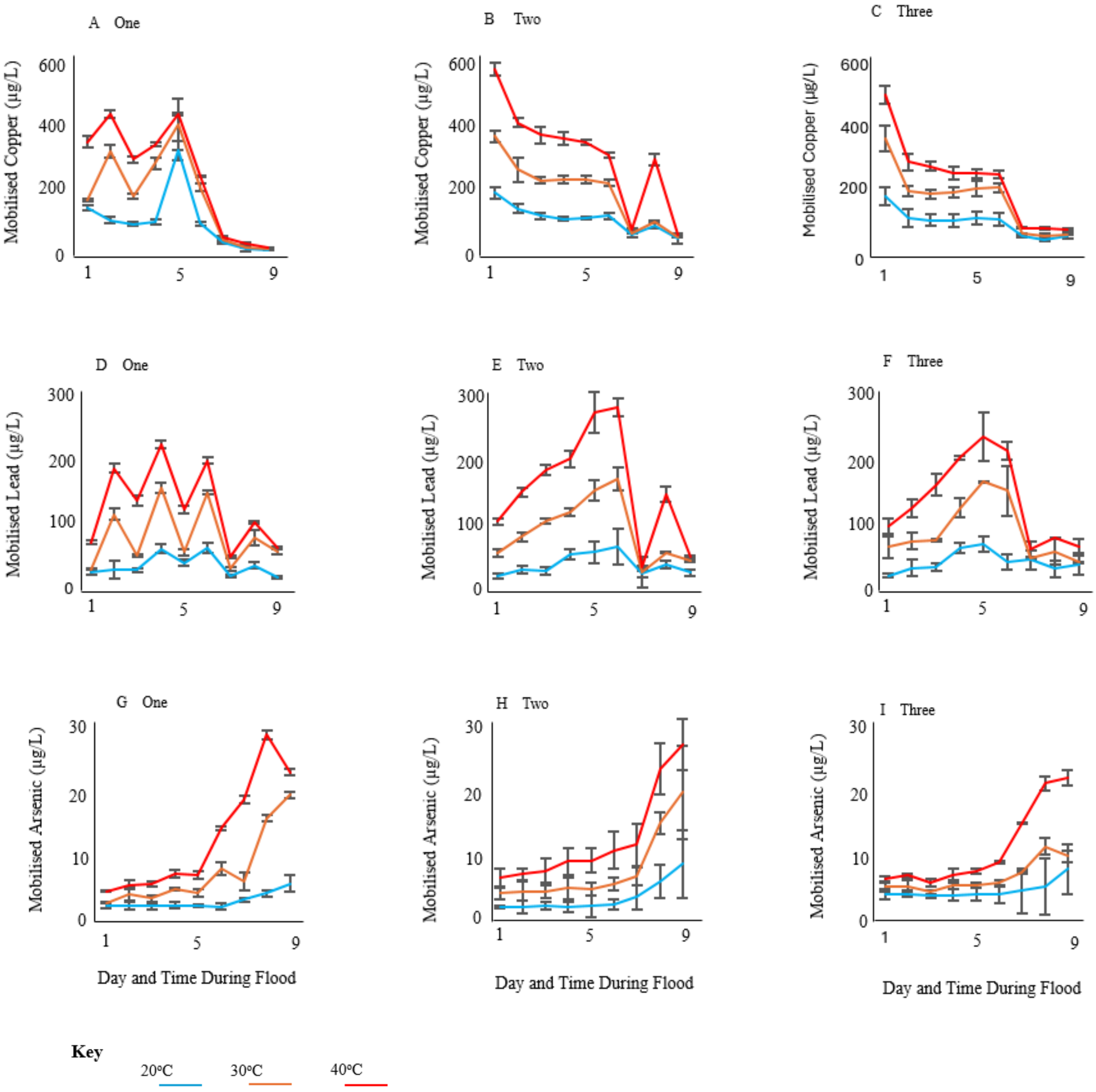

Figure 3.17. *Different temperature incubation experiments influencing soil enzymatic activity altering PHE porewater solubility. The error bars denote the standard deviation (n=3) at the 95% confidence interval.*

3.4.4 Evaluating the Influence of Different Flood Severities on PHE Porewater Solubility - Microcosm Design Three

This microcosm experiment investigated the influence of different flood severities (i.e., annual, 1 in 100, 1 in 500, 1 in 10,000) with altering flood lengths and flood receding frequencies on copper porewater solubility within the Humber. For the purposes of space (given that four separate flood severity experiments were conducted) copper was used as an example; however, for information on the different flood severities on lead and arsenic porewater solubility, see Appendix B. The purpose of investigating copper porewater solubility within different flood severities within the Humber is highlighted in Section 3.3.3.

The porewater solubility of copper decreased as flood duration increased during all the flood severities and within all the sampling locations (Figure 3.18). During the beginning of the flood, the lowest copper porewater solubility was observed at the most severe flood scenario, the 1 in 10,000-year flood, with a concentration of 10µg/L. This concentration was significantly lower compared to the beginning of the 1 in 500-year (137µg/L), 1 in 100-year (211µg/L), and annual (211µg/L) flood. Copper's solubility during the beginning of the 1 in 10,000-year flood was also much lower than sampling locations Two (321µg/L) and Three (139µg/L).

The low copper solubility within sampling location One, compared to the other flood severities, and the different sampling locations, may attribute to the soil organic carbon contents. For instance, the total soil organic carbon content was the highest within sampling location One compared to locations Two and Three (8.64mg/L C, 3.3mg/L C, and 7.7mg/L C, respectively) (Table 3.5). This organic carbon, through humic and fulvic substances, may form stable complexes with copper, facilitating ligand exchanges, reducing copper solubility (Ponting et al 2021).

As the flood inundation time increases, particularly for the severe 1 in 10,000-year scenario, the standard deviation, measuring copper's solubility variation, decreases. This variation decrease is indicated by the small error bars across the different sampling locations, highlighting the repeatability of the results. The results show that the variability of copper's solubility decreases as the flood length increases. As the flood duration increases beyond three days (i.e., the annual flood), observant across the 1 in 100, 1 in 500 and 1 in 10,000-year flood simulations, copper's porewater solubility significantly decreases. These findings indicate that longer flood lengths, exceeding three days, may significantly reduce copper's solubility more than shorter flood durations, less than three days.

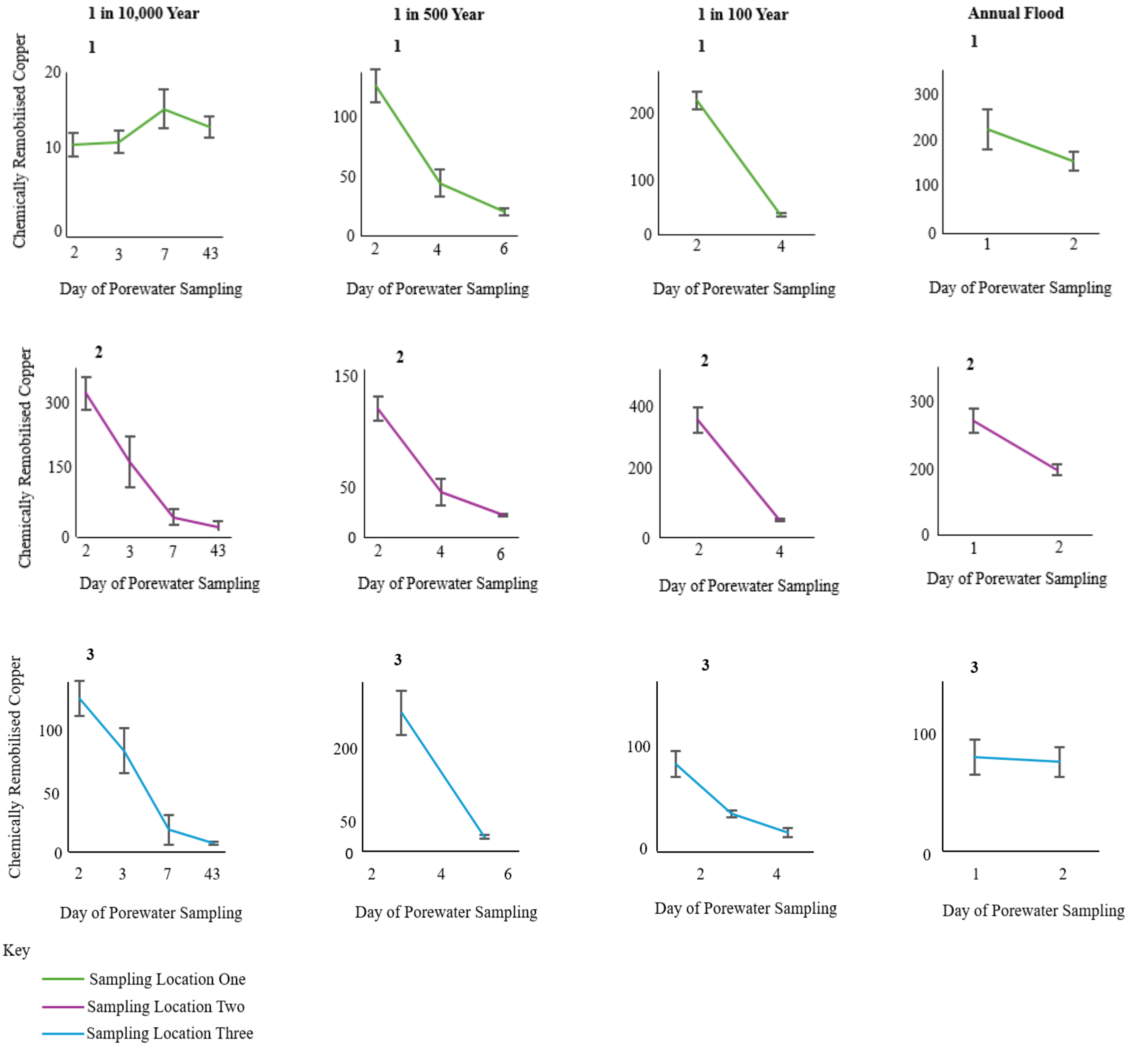

Figure 3.18. *Outlines the porewater solubility of copper across the different flood severity treatments within sampling locations one, two, and three across the Humber catchment. The results represent the average chemically remobilised copper concentration (n=3) with the associated standard deviation bars (95% confidence interval).*

3.4.5 Investigating the Influence of Physical Elements on PHE Porewater Solubility - Microcosm Design Four

This section focuses on investigating how changing land gradients (4.35°, 7.22°, and 16°) and vegetation coverages (35%, 55%, 90%) influence copper, lead, and arsenic porewater solubility across the three sampling locations along the River Almond embankment, respectively. The "physical elements" in this section refer to the land gradient and vegetation coverage. For information on how the land gradient and vegetation coverage were calculated, including why copper, lead, and arsenic were selected, see Section 3.3.7 and Section 3.3.1.

For all the sampling locations, increasing the flood duration (1-4 days) decreased copper and lead porewater solubility; however, it increased the solubility of arsenic present in the soil (Figure 3.19). Arsenic solubility was the highest during day four of flooding (5.6µg/L, 6µg/L, and 6.7µg/L, respectively). The solubility of arsenic at the end of the flood was the lowest under the flattest land gradient (4.35° at 5.6µg/L) and the highest under the steepest gradient (16° at 6.7µg/L). At the end of the flood, copper and lead solubility decreased considerably within all the sampling locations. Copper and lead solubility under the steepest land gradient did not decrease significantly from the beginning to the end of the flood, only by a 6.6% and 13.5% decrease, respectively. The steady decrease in copper and lead solubility suggests that steeper land gradients do not significantly alter copper and lead porewater solubility. Copper and lead porewater solubility was the highest at the end of the flood within the sampling location containing the highest vegetation coverage (51µg/L and 2.1µg/, respectively).

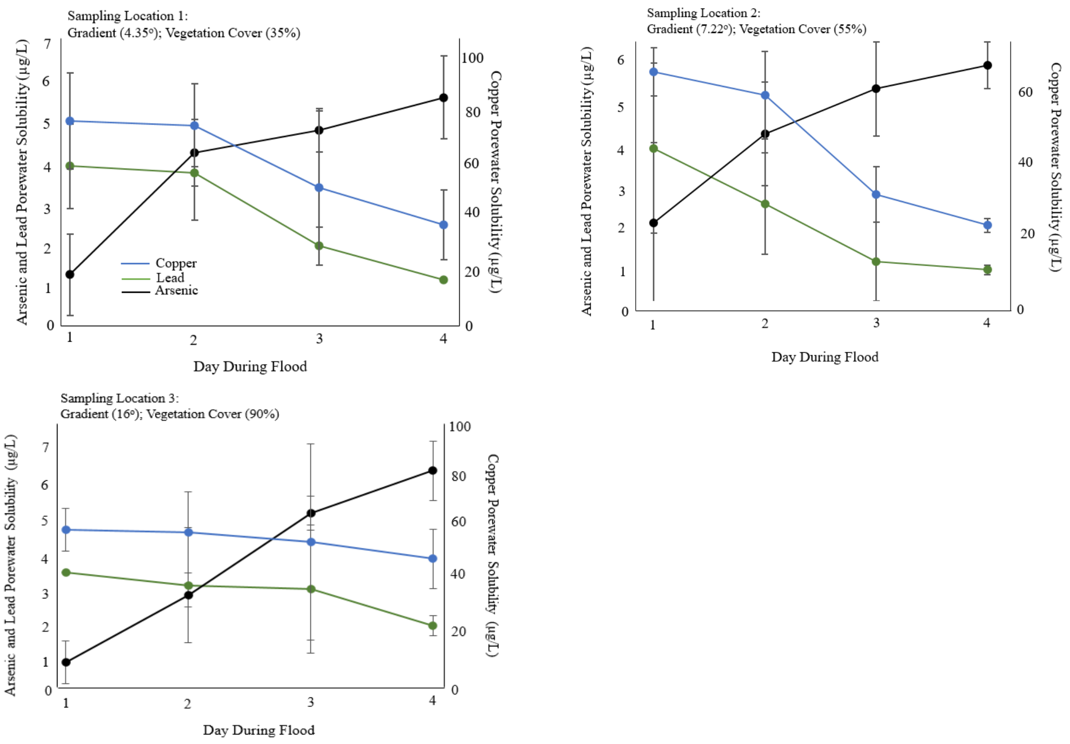

Figure 3.19. *Outlines the changing soluble arsenic, lead, and copper concentrations within the soil porewater across the three different sampling points along the River Almond embankment. Such concentration changes refer during the four day flood. The large points represent the average porewater concentration (n=9) with the associated standard deviation bars (95% confidence interval). The black line represents arsenic, green is lead and blue is copper.*

3.4.6 Investigating the Influence of Flooding on PHE Porewater Solubility Within Large-Scale Designs - A Mesocosm Experiment

This mesocosm experiment examined the influence of flooding on PHE mobility within larger-scale mesocosm experiments. The purpose of conducting such setups are outlined in Section 3.3.8. This discussion only focuses on copper; however, for more information around the influence of flooding within these mesocosms for different PHE, see Appendix D.

Copper is a priority in environmental monitoring because of its dual role as an important micronutrient for plants and wildlife; however, copper is also a non-degradable and persistent PHE which is highly toxic when total soil copper concentrations exceed 20-30mg/kg (see Section 1.4.2) (Hayat et al 2021). Compared to other PHE (e.g., lead and arsenic), copper interacts with a wider range of organic and inorganic soil components, including organic matter, iron, manganese, and aluminium, making it significantly challenging to analyse the effects of flooding influencing the porewater solubility of copper (Poggere et al 2023) (see Section 1.4.2). The non-degradable persistence of copper and the complexity of understanding how copper interacts with different inorganic and organic soil components emphasise the importance of focusing on copper (Hayat et al 2021; Kah et al 2022; Kumar et al 2021; Lair et al 2007; Poggere et al 2023).

During inundation and drying, the different ambient humidity levels (35%, 65%, 95%) statistically significantly influenced copper porewater solubility (F-Crit = 3.21; p = 0.004; F-Crit = 3.17; p = 0.03) (Figure 3.20). The climate warming scenario of + 1.5°C also statistically significantly increased copper porewater solubility (t = 3.49, p = 0.00074). The results show similar findings with the microcosm design one (Figure 3.14), confirming that as flood duration increases, copper porewater solubility decreases. Such findings show copper's remobilisation alters the most significantly within the first five days during inundation, showing similar results with Figure 3.16, indicating the physicochemical changes most significantly during such periods, potentially influencing copper's mobility.

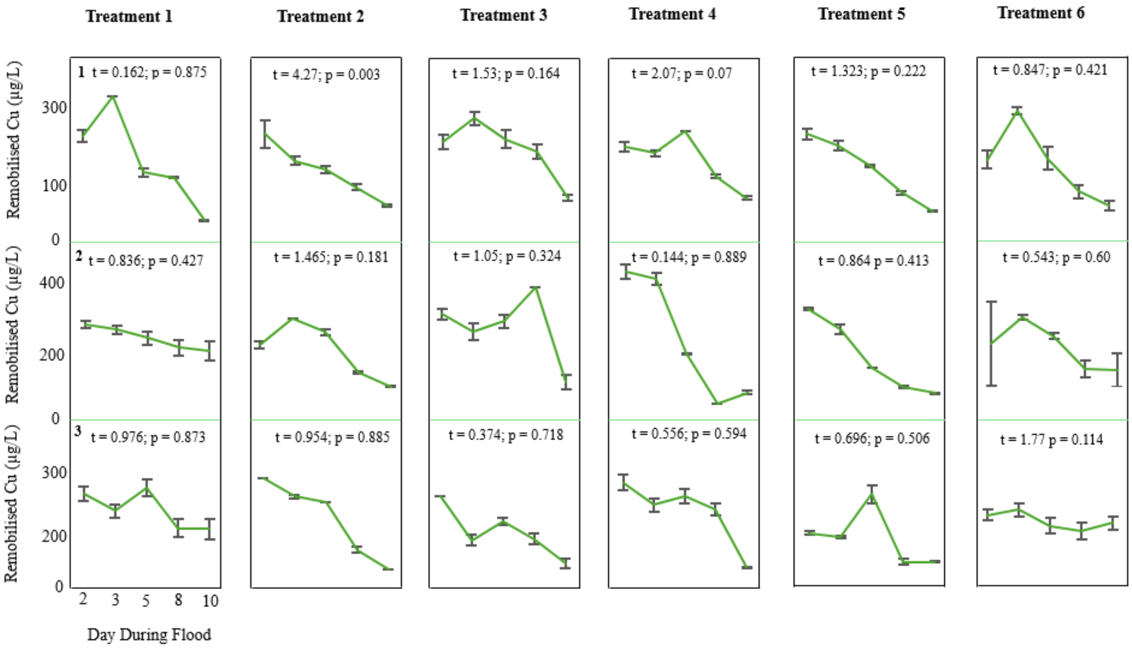

Figure 3.20. *Outlines the mesocosm results investigating copper's porewater solubility across sampling locations 1-3 for the different treatment groups (1-6). The microcosm results denote averages (n=3) at the 95% confidence interval. These figures outline the observed laboratory copper concentrations remobilising throughout the flood (indicated in green). The random forest models (blue line) compared these observations with the predicted chemically remobilised copper concentrations. The "t" value denotes the results from the independent sampled t-test results, comparing the observations with the predictions at the 95% confidence interval. The significance of providing the t-test statistic and significance level is to investigate the effect of the random forest predictions having the reliability to estimate remobilised PHE fractions.*

3.4.7 Analysing the Influence of Flooding on PHE Bioaccessibility

Microcosm Design One

This section investigates the influence of flooding on copper, lead, and arsenic bioaccessibility within the Humber and Clyde catchments. Copper, lead, and arsenic bioaccessibility concentrations were significantly higher in the gastric phase than the gastrointestinal phase (Figure 3.21). This decrease in bioaccessible concentrations within the gastrointestinal phase occurs within all the sampling locations in the Clyde and Humber catchments. The most notable bioaccessibility decrease is post-flooding, most likely because all the bioaccessible copper was loosely bound and no longer available (Xu et al 2023). The gastric bioaccessibility of lead, copper, and arsenic was significantly higher within the Humber compared to the Clyde catchment. This difference in bioaccessibility within the Humber compared to the Clyde is particularly apparent for copper and lead bioaccessibility. The gastrointestinal bioaccessibility of lead, copper, and arsenic was observed to be higher in the Humber than in the Clyde. These findings suggest that the significant differences in PHE gastrointestinal bioaccessibility between the Humber and Clyde could be attributed to their distinct physicochemical and geochemical properties (Ponting et al 2021). The disparity in gastrointestinal bioaccessibility could result from the differences in total soil PHE concentrations (Table 3.5). These differences of total soil PHE concentrations are linked to the differences in the bedrock geology between these two catchments, as well as the industrial sources and types. However, the error bars are significantly large for the gastric and intestinal PHE bioaccessibility concentrations, indicating high bioaccessibility variations between the replicates. These variations in bioaccessibility may be attributed to the large spatial differences in soil PHE concentrations.

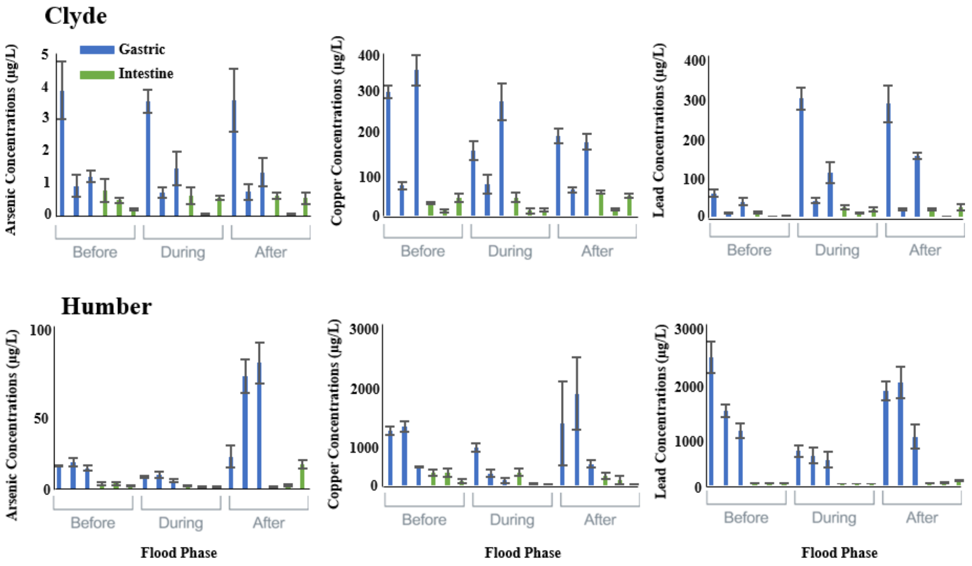

Figure 3.21. *BARGE gastric and intestinal bioaccessibility results before, during and after flooding within the Clyde and Humber catchment. The error bars indicate the data variation at the 95% confidence interval (n=3).*

3.4.8 Evaluating the Influence of Different Flood Severities on a PHE Bioaccessibility - Microcosm Design Three

This section investigates flooding on PHE bioaccessibility within the Humber. For the purpose of space, copper will be investigated; however, for information relating to different PHE types, see Appendix C. The small standard deviation bars across the various flood severities indicate that despite the physicochemical changes associated with the different flooding treatments, the gastric and gastrointestinal bioaccessibility of copper remains unchanged within each treatment (Figure 3.22). For example, within the annual flood, consisting of oxidising redox potentials, copper bioaccessibility variations remain low; however, within the 1 in 10,000-year flood, with low reductive redox conditions, copper bioaccessibility variation is also low. These findings suggest that the differences in physicochemical conditions between the different flood treatments do not significantly impact the variability of copper bioaccessibility. If a particular flooding severity (e.g., 1 in 100 year) did have high variations in copper bioaccessibility, potentially attributing to the physicochemical conditions during that flood, this may be challenging to predict; however, as mentioned, these variations were not observed within any of the flooding experiments.

The total gastric bioaccessibility is highest at the beginning of the flood within the annual flood severity group at 1364µg/L. This 1364µg/L value exceeds the maximum daily dose for copper in drinking water, which is 1300µg/L (Environment Agency 2008). As the flood duration increases gastric concentrations decrease. Again, like with the rapid physicochemical changes observed during the beginning of the flood (Figure 3.22), copper bioaccessibility rapidly decreases between days one and three within the 1 in 500 years and 1 in 10,000 treatment and slowly declines after such days.

Increasing the flood duration (i.e., annual flood at three days compared to 1 in 10,000 year flood at 43 days) does not reduce copper's gastric concentration compared to the shorter durational annual floods. For example, at the end of day for the annual flooding experiment, the average copper bioaccessibility was 53µg/L, whereas at the end of day 43, copper bioaccessibility was higher 501µg/L, suggesting longer duration floods significantly increase copper gastric bioaccessibility. Sharma et al (2022) agrees, showing that prolonged flooding increases copper bioaccessibility within wetland soils through the reducing redox potentials causing the reductive dissolution of metal-bearing oxides.

At the end of the flood, the gastrointestinal bioaccessible concentrations of copper are the highest within the 1 in 10,000-year flood (1183µg/L) and the lowest within the 1 in 500-year flooding treatment (51µg/L). These findings are significant, indicating that increasing the flood duration does not increase gastrointestinal copper bioaccessibility. The findings reveal a key difference between the influence of flood duration and copper bioaccessibility, indicating that longer floods increase copper gastric bioaccessibility; however, flooding does not influence increasing copper gastrointestinal bioaccessibility.

These findings emphasise the need to understand more about how copper's gastric bioaccessibility changes during flooding and how this influences human and wildlife health through conducting more flooding experiments to confirm these findings and analyse relationships within different locations to verify and validate the results (Kulsum et al 2023).

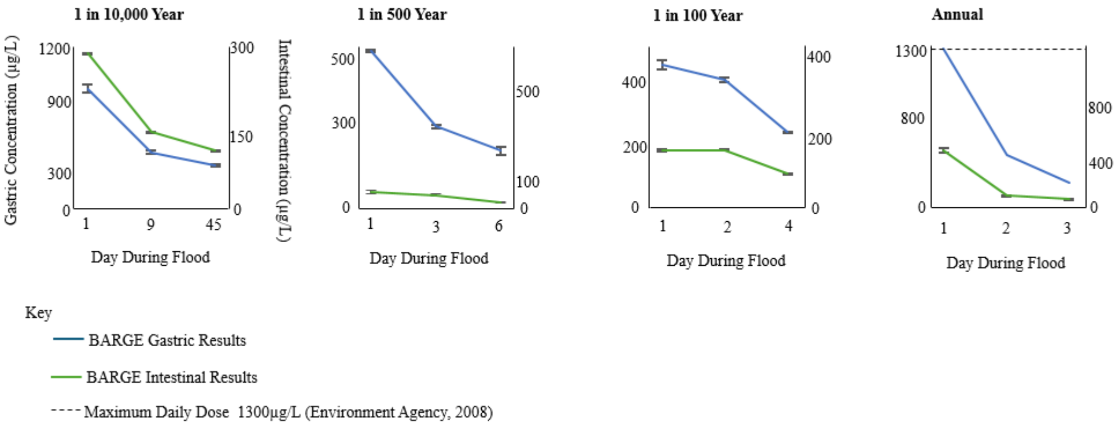

Figure 3.22. *Outlines the changing bioaccessible gastric (blue) and intestinal (green) concentrations throughout the flooding treatment microcosms within the Humber (annual, 1 in 100-year, 1 in 500-year, and 1 in 10000-year). Such data represents the average bioaccessible concentrations for copper (n = 3) with the associated standard deviation bars (95% confidence interval).*

3.4.9 Investigating the Influence of Flooding on PHE Bioaccessibility within Large-Scale Designs - A Mesocosm Experiment

This section focuses on analysing the influence of flooding on lead bioaccessibility during flooding within large-scale mesocosms experiments using soil extracted from the Clyde catchment. This section selects lead because of the significant health consequences of exposure to bioaccessible lead (Table 1.1, Chapter 1). For information about the changes in bioaccessibility of different PHE during this experiment, see Appendix B.

There are statistically significant differences in bioaccessible lead concentrations at different humidity levels during flooding (F = 18.5; p = 0.02) (Table 3.6). The results indicate that lead bioaccessibility increases under higher humidity levels (95%). These findings suggest that floods during the summer within the UK, which experience average ambient humidity levels between 50-60%, are associated with lower lead bioaccessibility compared to winter floods, where the ambient humidity levels range between 80-90%, potentially increasing lead bioaccessibility (Brugnara et al 2023).

This chapter does not investigate extensively the implications of such findings on predictive models; however, it emphasises the importance of any predictive model when estimating lead bioaccessibility changes during flooding to account for ambient humidity, particularly during the winter periods with higher humidity levels. Increasing the ambient temperatures by 1.5°C under a climate change scenario did not statistically influence lead bioaccessibility during flooding and drying ($F = 4.54$; $p = 0.905$). These results do not necessarily imply that temperature is not a significant variable influencing bioaccessibility; instead, an ambient temperature increase of 1.5°C is not enough to statistically influence lead's bioaccessibility. The results are significant from a predictive model estimation, indicating that slight ambient temperature increases, irrespective of the importance of the temperature influencing soil microbial communities, are not statistically necessary for predicting lead bioaccessibility.

Table 3.6. *Outlines the changing gastric bioaccessibility concentrations of lead during the flooding and drying process within the six different mesocosms flooding groups. The table outlines average bioaccessibility concentrations (n = 3) recorded at the end of the flooding experiment. For information relating to the different treatment designs, see Section 3.3.8.*

Mesocosm Treatment	Humidity Level (%)	Ambient Temperature (°C)	Gastric Bioaccessibility (µg/L) Flooding	Gastric Bioaccessibility (µg/L) Drying
1	35	Ambient	418	355
2	65	Ambient	169	183
3	95	Ambient	151	182
4	35	+ 1.5°C	153	321
5	65	+ 1.5°C	421	643
6	96	+ 1.5°C	503	532

3.4.10 The impact of Flooding Influencing a PHE Solid Phase Distribution - A Microcosm Experiment

This section investigates the influence of flooding on lead's solid phase distribution within the Clyde catchment. For an overview explaining the purposes for selecting the Clyde catchment, see Section 3.3.3. Lead was selected to compare with the results showing lead's bioaccessibility changes during flooding within the Clyde (Section 3.4.9). Lead is also highly neurotoxic, with lead toxicity changing depending on the solid phase distribution of lead (Kushwaha et al 2018; Peana et al 2021) (Table 1.1, Chapter 1). Briefly, the “solid phase distribution” refers to the fractionation of lead between soil mineral phases (e.g., carbonates, exchangeable, residual) (Cave et al 2015). The process of adsorption and dissolution of lead ions in different soil mineral phases can directly influences lead solubility and bioaccessibility (Goodland 2013). For example, lead ions coprecipitating with organic matter are much less soluble than lead soluble within soil porewater not coprecipitating with any soil organic matter (Nigg 2016).

The chemometric mixture resolution algorithm identified the soil components and how lead is distributed among these different components. These findings from the algorithm reveal six different soil components (Tardif et al 2019). The six components were determined using hierarchical cluster analysis, which was chosen to visually cluster these components and distinguish the difference between the components. Before flooding, lead was not associated with oxides; instead, such complexation was with aluminium, specifically aluminium-phosphorus and copper and arsenic associating with oxides (indicated by light blue coefficient on the plot, see dashed circle) (i.e., Al-Fe-Ca, Fe-Al-P and Fe) (Figure 3.23, Figure B3.7, Appendix B).

During flooding, many PHE coprecipitated with oxides instead of carbonates. (Figure B3.8, Appendix B). Lead strongly dissociated with iron and aluminium during flooding (indicated by the darker blue coefficient values within the plot). Arsenic dissociated with many mineral phases, particularly the oxide phases, such as aluminium. Such findings reveal that physicochemistry influences PHE solid phase distribution, confirmed by the identified PCA clustering (Figure B3.9, Appendix B).

In figure 3.13, it shows how different mineral phases (i.e., carbonates, porewater, exchangeable) influence different physicochemical variables. The individual component within each mineral phase is also computed. The colour from each gird cell denotes the correlation coefficient between the mineral component and the physic alchemical parameter. The tables below (Table 3.23, 3.24) indicate the total variation (R^2) of each mineral phase with the different physicochemical components. The results reveal before and after flooding, many of the PHE have relationships (binding sorption and dissolution properties) with iron and aluminium oxides.

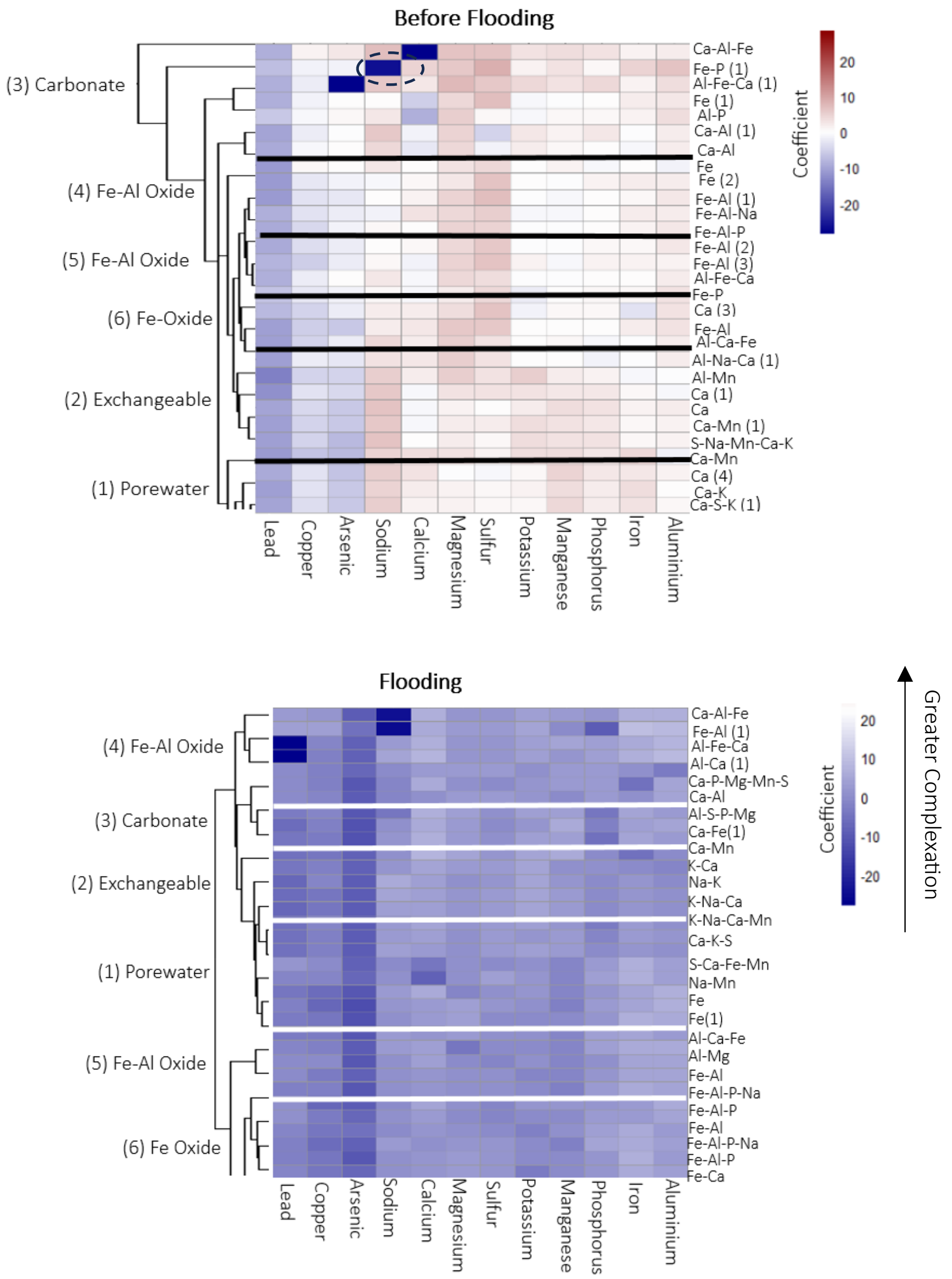

Figure 3.23. *Hierarchical clustering heat map. The figures display the data as a grid with columns indicating the different physicochemistry parameters, and the rows show the different speciation clusters. Each cell represents a coefficient strength. High coefficients mean stronger and higher values, whereas low coefficients show weaker and lower values. The coefficient represents the R^2. For example the cell in the very top right box for before flooding (Ca-Al-Fe) indicates an R2 of 0.06, meaning Ca-Al-Fe explains 0.06 of the variation in aluminium concentrations. The different rows (speciation) cluster groups based on this coefficient. Rows with similar colours are related and are therefore clustered. For example, take the physicochemical parameter aluminium in plot A. This parameter shows a darker red colour with the carbonate cluster, indicating high correlations aluminium may have with influencing PHE within the carbonate mineral phase. Plot B shows the same relationships, the only difference being how physicochemical changes during flooding influence PHE within different clusters. For example, in*

contrast with plot A, aluminium has a darker blue coefficient (meaning a strong relationship) with the exchangeable cluster more than the carbonate phase.

Table 3.23. Compares the statistical correlation (R^2) between the different mineral phases and soil physicochemical components before flooding.

Mineral Phase Cluster	Pb R^2	Cu R^2	As R^2	Na R^2	Ca R^2	Mg R^2	S R^2	K R^2	Mn R^2	P R^2	Fe R^2	Al R^2
Porewater	-0.15	-0.08	-0.05	0.05	0.04	0.02	0.02	0.02	0.06	0.06	0.04	0.02
Exchangeable	-0.17	-0.04	-0.02	0.04	0.02	0.03	0.03	0.02	0.04	0.03	0.02	0.02
Carbonate	-0.12	-0.01	-0.05	-0.02	-0.03	0.09	0.05	0.02	0.03	0.03	0.02	0.05
Fe-Al (1)	-0.11	-0.04	-0.03	0.01	0.04	0.09	0.13	0.04	0.04	0.03	0.04	0.05
Fe-Al (2)	-0.11	-0.04	-0.03	0.05	0.04	0.12	0.15	0.05	0.02	0.02	0.02	0.02
Fe-Oxide	-0.15	-0.10	-0.04	0.05	0.05	0.07	0.08	0.02	0.02	0.02	0.01	0.03

Table 3.24. Compares the statistical correlation (R^2) between the different mineral phases and soil physicochemical components after flooding.

Mineral Phase Cluster	Pb R^2	Cu R^2	As R^2	Na R^2	Ca R^2	Mg R^2	S R^2	K R^2	Mn R^2	P R^2	Fe R^2	Al R^2
Porewater	-0.04	-0.06	-0.11	0.03	0.03	0.04	0.03	0.01	0.01	0.03	0.06	0.05
Exchangeable	-0.06	-0.04	-0.15	0.05	0.06	0.03	0.03	0.07	0.05	0.04	0.02	0.01
Carbonate	-0.08	-0.03	-0.12	-0.04	0.04	0.04	0.04	0.05	0.03	-0.02	0.03	0.05
Fe-Al (1)	-0.16	-0.12	-0.14	-0.19	0.07	0.04	0.04	0.04	0.04	0.02	0.02	0.04
Fe-Al (2)	-0.02	-0.05	-0.09	-0.01	0.03	0.05	0.05	0.05	0.06	0.05	0.06	0.04
Fe-Oxide	-0.05	-0.06	-0.09	0.03	0.05	0.05	0.04	0.06	0.04	0.03	0.04	0.04

3.5 Discussion

3.5.1 The Influence of Physicochemical Changes During Flooding Impacting PHE Porewater Solubility

Flooding generally decreased the soil porewater solubility of metals; however, flooding increased the arsenic's solubility. Such findings can be attributed to increased interactions with oxides, PHE surface charge, and PHE competition (Whitby and Berg 2015).

The anoxic reductive redox potentials created during flooding promoted sulfate reduction into sulfide (Bindal and Singh 2019). These sulfides complexed with PHE through clustering, forming insoluble complexes or precipitates through sulfide ions acting as ligands and binding with PHE (Izaditame et al 2022). Lytle et al (2020) showed that the negatively charged sulfide species attract positively charged lead and copper ions. The association between sulfide formation, created from reducing conditions, indicates the mechanism for decreasing PHE mobility, emphasising the correlation between physicochemical changes influencing PHE mobility (Simmler et al 2017).

Arsenic's porewater solubility increased during flooding, irrespective of such sulfide minerals potentially forming stable complexes with arsenic (e.g., As_2S_2); potentially immobilising arsenic's porewater solubility (Izaditame et al 2022). These findings can be attributed to arsenic's surface charge changing during flooding through the reducing redox conditions because lowering redox conditions transforming arsenate to less negatively charged arsenite, which has a lower affinity of adsorbing to positively charged mineral phases (Izaditame et al 2022). Many PHE compete for ligand receptors on mineral phase surfaces (e.g., clays, organic carbon, and aluminium) (Simmler et al 2017). Such competition may mean lead and copper are outcompeting arsenic for ligand exchanges (Jaruga et al 2017). This competition heightens when many lead and copper ions are reductively dissolved from iron, aluminium, and manganese oxides (Heyden and Roychoudhury 2015). The findings here support such evidence, showing that solubilised arsenic significantly increased after day six during flooding, most likely attributed to the oxides dissolving and the metals outcompeting arsenic for sulfide binding (McCauley et al 2009).

3.5.2 The Influence of Physicochemistry Changes During Flooding Influencing PHE Bioaccessibility

The results showed flooding decreased bioaccessible PHE concentrations. This decrease in bioaccessible PHE concentrations may be attributed to the reductive redox conditions that form metal-sulfide clusters (Mendez et al 2017). These clusters, as mentioned previously, form ligand exchanges with PHE, reducing PHE solubility and bioaccessibility (Huang et al 2021). However, the Unified BARGE method uses a pH 1.2 gastric solution, effectively acidifying soil mineral phases, such as carbonates, iron, and aluminium oxides, potentially affecting these metal-sulfide complexes (Wragg et al 2011). The pH of the human stomach ranges between 1.5 - 3.5, making the BARGE procedure using a pH of 1.2 considerably lower than the typical stomach pH conditions (Takegawa et al 2022).

This lower BARGE pH level represents the stomach pH at the more extreme conditions, with no food intake, whereby food typically raises the stomach pH conditions (McLaren 2017). The issue with such low pH conditions simulated during

BARGE is it typically does not consider a realistic scenario of the actual stomach pH levels, and because the pH 1.2 is significantly low, this likely acidifies these sulfide complexes more compared to the normal pH levels between 1.5 - 3.5 (Takegawa et al 2022). This low pH level raises concerns regarding the validity of these BARGE results because the low pH levels most likely dissolve these sulfide complexes more compared to a scenario typical of the stomach pH. By dissolving these sulfide complexes more, the BARGE procedure likely will increase PHE bioaccessibility (by dissolving these sulfide complexes) and potentially overestimate the actual PHE bioaccessibility because of the extreme pH conditions (Takegawa et al 2022).

Irrespective of the highly acidic pH conditions dissolving many soil mineral phases, the metal-sulfide clusters potentially exhibit some resistance to these acidifying conditions (Huang et al 2021). These metal-sulfide clusters have shown significant resistance to acidifying conditions by forming passivation layers (Ghita et al 2013). The passivation layers can shield the metal-sulfide complex clusters, reducing the contact and exposure of these clusters with the acidic gastric solution (Ghita et al 2013). These metal-sulfides, which form exclusively during reductive redox conditions, and typically form under anaerobic conditions, potentially significantly influence PHE bioaccessibility, irrespective of the acidifying gastric pH conditions (Huang et al 2021).

3.5.3 The Influence of Physicochemical Changes During Flooding Influencing PHE Solid Phase Distribution

The results indicated that physicochemical changes during flooding alter a PHE solid phase distribution; however, the findings highlight the intricacy of solid phase distribution changes (Bindal and Singh 2019). Such solid phase distribution changes are distinguishable by clustering, showing specific PHE (e.g., arsenic) speciate less with some mineral phases than others (e.g., copper and lead, which speciate more with oxides and carbonates) (McLaren 2019). The most significant finding is that soil heterogeneity itself influences PHE solid phase distribution within such clusters, emphasising the challenges of predicting PHE solid phase distribution using physicochemistry alone (Huang et al 2021).

These challenges are further exacerbated because soils are highly heterogeneous on the micro and macro scales (Nunan et al 2020). These microcosm and mesocosms experiments showed the explicit links between how flooding alters physicochemistry and how this change influences PHE mobility, bioaccessibility and solid phase distribution. The results highlight the need for research on how physicochemistry can benefit understanding PHE dynamics and surveillance. Such complexities around how flooding changes PHE solid phase distribution may mean predicting such mechanisms using physicochemistry is challenging.

3.6 Conclusion

This chapter highlights the importance of developing of improving mechanisms for estimating PHE porewater solubility, bioaccessibility and solid phase distribution changes during flooding. The implications of future climate change increasing the frequency and magnitude of riverine and coastal flooding underscores the need for monitoring such PHE changes in real time. This chapter highlights the opportunities of using physicochemical information to estimate such PHE changes during flooding.

The chapter recommends further research around developing computer models to predict, using this physicochemical data, PHE porewater solubility, bioaccessibility and solid phase distribution. Such models should identify the relevant physicochemical variables to predict these PHE changes. These models should also explore different modelling types, such as statistical, machine and deep learning approaches to investigate and compare such predictions.

These findings have significant implications for modelling purposes, emphasising the unique opportunities of using the correlations between soil physicochemistry changes during flooding to predict PHE dynamics. The key messages for modelling purposes would be:

- Training different modelling approaches to estimate which soil physicochemical changes during flooding influence PHE porewater solubility, bioaccessibility, and speciation.
- Analyse the opportunities of novel artificial intelligence approaches and compare this to existing statistical models to estimate PHE dynamics.
- Analyse the predictive performance of different modelling approaches trained on these data to predict PHE dynamics.

Chapter 4: Thesis Structure

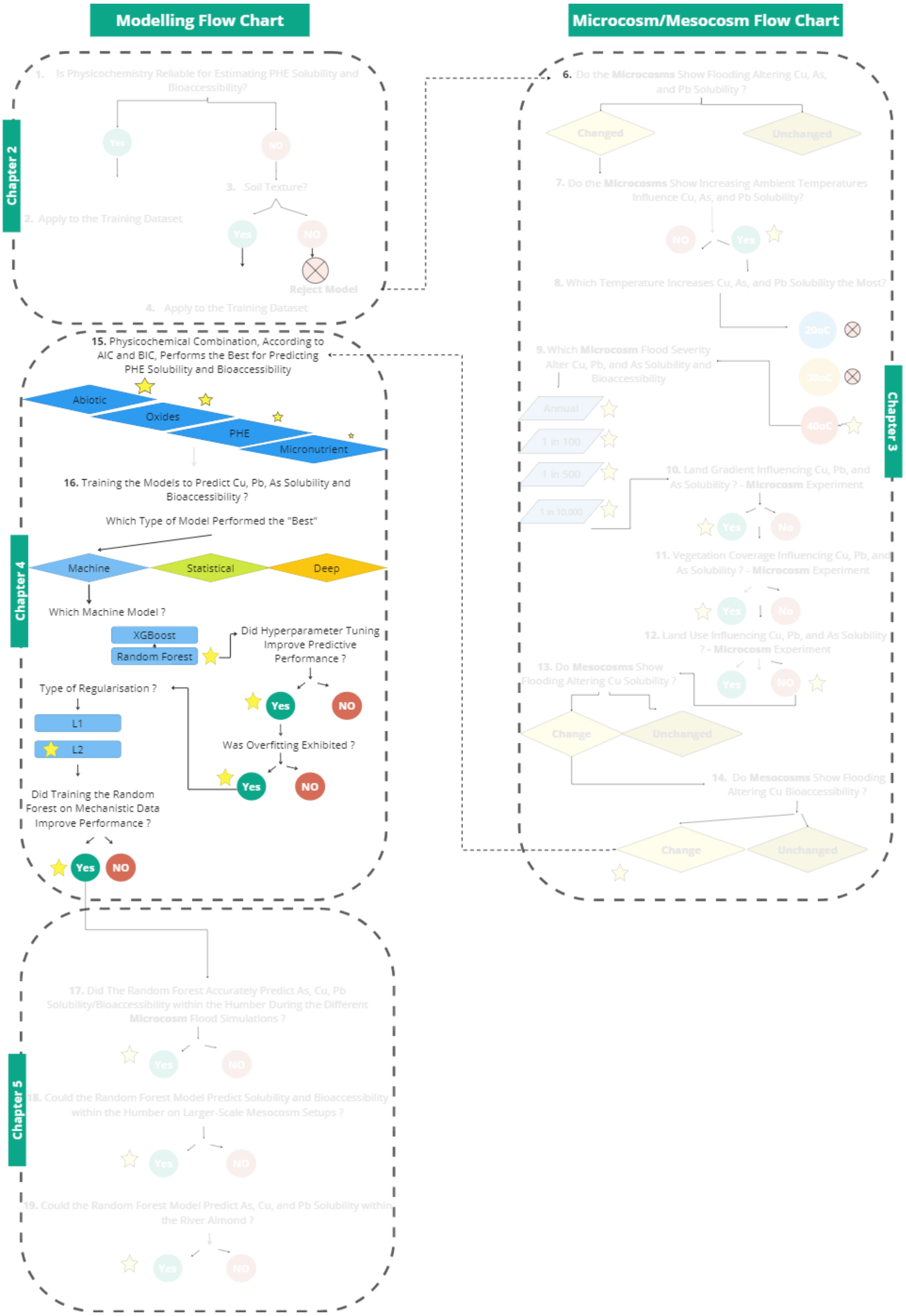

Chapter 4: Developing Statistical, Machine, and Deep Learning Models for Estimating PHE Porewater Solubility, Bioaccessibility, and Solid Phase Distribution

4.1 Introduction

Recent developments of computer algorithms, parallel processing and quantum computing have created opportunities for exploring intricate and unknown relationships between soil physicochemistry and PHE dynamics. The previous chapter indicated that physicochemical changes during flooding can have statistically significant influence on PHE porewater solubility, bioaccessibility, and solid phase distribution. There are opportunities for incorporating such data into AI models for estimating a PHE transport, fate, and behaviour during flooding (Feng et al 2015). Such models may overcome the resource intensive field and laboratory procedures for scientists and instead, for the first time, provide reliable, fast, and cost-effective predictions.

This chapter will review the mechanistic “black box” nature of random forest models, extreme gradient boosting algorithms, and neural networks. These AI models were selected, examined, and compared in their predictive performance between decision-tree learners and neural network architectural designs. The review focuses on decision-tree splitting, bias and variance trade-off’s within AI modelling, hyperparameter tuning and regularisation, bootstrap aggregation, gradient boosting and neural network designs, respectively. This investigation statistically compares, for the first time, different statistical and AI designs (decision-tree and neural networks), using physicochemical data, to predict PHE changes during flooding.

4.1.1 Decision Trees and Data Splitting

A decision tree approach formulates a prediction, which can quantify the soluble porewater PHE concentration and bioaccessibility during flooding (Genuer et al 2010). To do this, a decision tree comprises of many attributes, such as roots, nodes (parents and children), and leaves (Galiano et al 2014). A root node is the top of the tree, containing the entire dataset (Galiano et al 2014). The branches represent a potential outcome after splitting a particular feature (Cutler et al 2007). A parent node is the topmost node in a decision tree, which splits into smaller child nodes (Galiano et al 2014). As the tree splits, the data within each node gets smaller, decreasing the information transfer from the parent to the child nodes (Cutler et al 2007). The final decision is represented in the leaf node. The collective combination of the root, branches, nodes and leaves form the decision tree (Figure 4.1, information obtained from Galiano et al 2014).

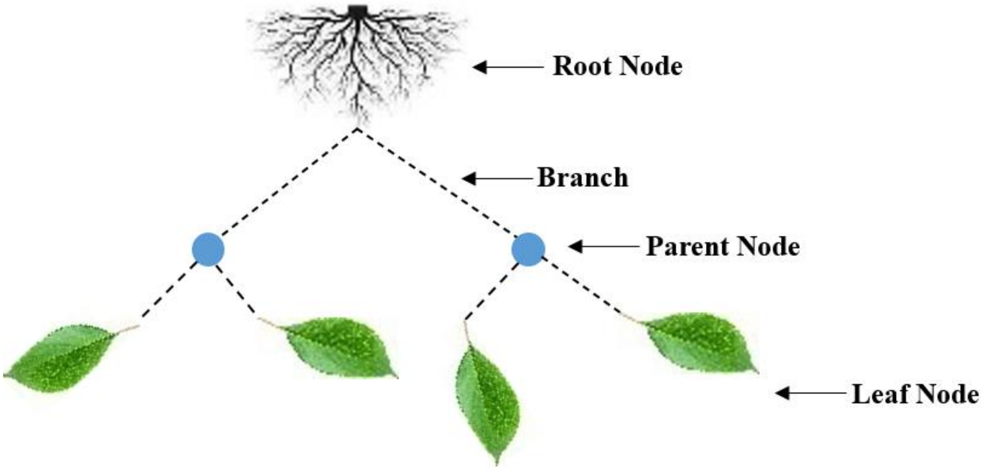

Figure 4.1. *Outlines the computational process of tree learning AI. The figure outlines the root note containing the dataset, which is split into subsequent parent nodes, the final decision split represents the leaf node (Galiano et al 2014).*

Decision trees split data, identifying nonlinear patterns and relationships (Cutler et al 2007). The criterion function for splitting the root to the parent node follows the principles of entropy and information gain (Hong et al 2019). Entropy refers to the datasets disorder (chaos) (Galiano et al 2014). Calculating the datasets entropy can determine the degree of randomness or variation in the data (Hong et al 2019). For example, a fruit basket containing only apples will have a very low entropy because there are just apples. In contrast, a fruit basket containing apples, oranges, pears, and mixed tropical fruits contains higher entropy and randomness. The decision tree calculates the dataset entropy using the equation proposed by Springel and Hernquist (2002),

$$\text{Entropy(s)} = \sum_{i=0}^{c} - p \ log2 \ pi \qquad \text{Eq. 2}$$

where “S” is the dataset, “c” is the number of target variable classes, “p” is the proportion of data points that belong to the class “i,” and the summation “Σ” denotes this is calculated across all the classes. The information gain defines the amount of entropy reduction after feature splitting (Galiano et al 2014). Calculating the information gain using entropy allows the model to determine which feature is best to split based on the principles of which features reduce the entropy most significantly

(Shaheen and Iqbal 2018). The decision tree calculates the information gain using the following equation by Nelson (2017),

$$\text{Gain (S,A)} = \text{Entropy(s)} - \sum_{vValues(A)} * \frac{Sv}{|S|} * \text{Entropy}(Sv) \qquad \text{Eq. 3}$$

where “S_V” is the number of elements in a set, “S” is the number of total elements, and “*veValues(A)*” is the value of all attributes.” The “Gain(S, A)” is the expected reduction in entropy upon setting on “A.” Very simply, the first split from the root node is decided based on which split from the feature variable decreases the dataset entropy the most significantly, contributing to the highest information gain (Shaheen and Iqbal 2018). The root node contains highly unordered “chaotic” data with high entropy (Cutler et al 2007). The purpose of the decision tree is to transform this “chaos” data into orderly low entropy data (Cutler et al 2007). If splitting a feature has a greater information gain and a lower entropy, that feature is split first from the root node (Shaheen and Iqbal 2018). When a particular feature is identified to split, splitting is performed through recursively partitioning the feature data (Hong et al 2019). The recursive aspect is placing the data into a two-axis hyperplane (X, Y) (Hong et al 2019).

The hyperplane data are partitioned into groups (or splits) in which the algorithm is clustering (Shaheen and Iqbal 2018). For example, assume the algorithm calculated, based on entropy and information gain, that splitting pH data to predict copper’s porewater solubility creates the lowest entropy and highest information gain (Hong et al 2019). The algorithm places all the pH values on the X-axis and copper concentrations on the Y-axis (recursive) (Hong et al 2019). The algorithm decides to split on the right-hand side with “pH > 9” with copper concentrations “>100µg/L” and the left-hand side with “pH < 9” with copper concentrations “< 100µg/L” (Cutler et al 2007).

When a hyperplane is partitioned based on such a command and it is then split (Shaheen and Iqbal 2018). Adding to the degree of randomness and addressing highly multi-dimensional data, a random forest model uses feature sampling when splitting the data (Cutler et al 2007). Simply, feature sampling is when the random forest choose features to split; when the randomly selected features are identified, the split function will begin based on information theory (Shaheen and Iqbal 2018). Not all decision tree splits will have the same features to split; however, the number of features is randomly allocated to the decision tree; typically, the value is the square root of all the features. (Figure 4.2, information obtained from Shaheen and Iqbal 2018).

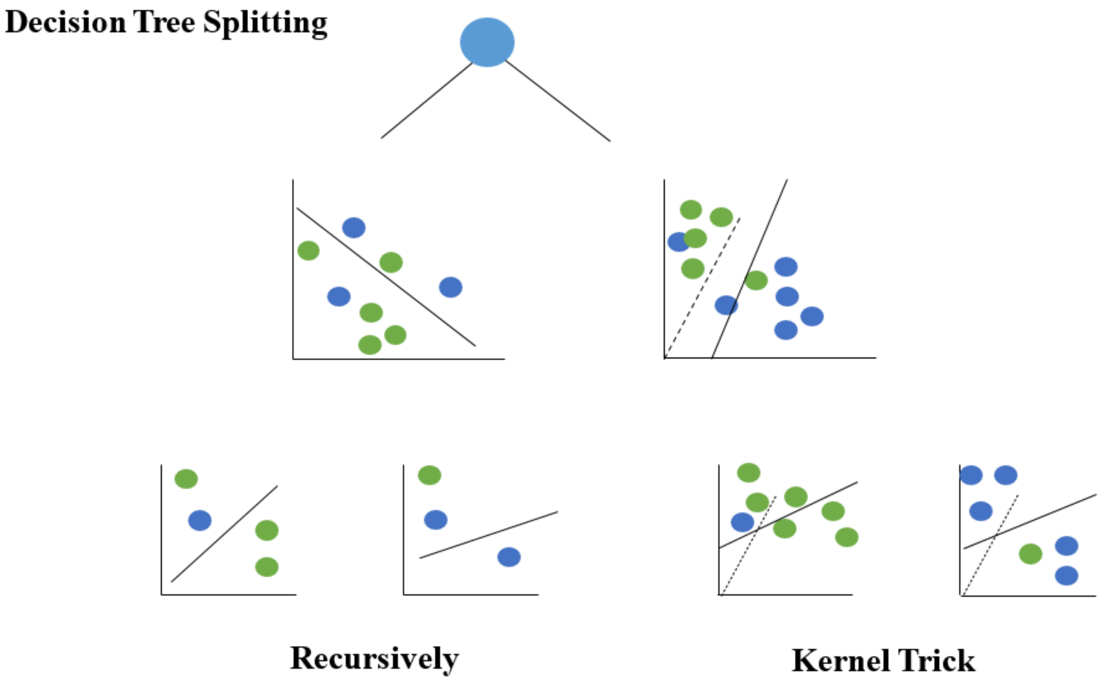

Figure 4.2. *Outlines the mechanistic "black box" process of splitting the dataset from a high entropy towards a lower entropy using the recursive or kerel trick process (Shaheen and Iqbal 2018). This figure outlines how information splits using the techniques.*

Randomly selecting features also helps reduce the model bias and multidimensionality (Tyralis et al 2019). Feature sampling addresses multidimensionality by forcing the model to focus on a subset of features, reducing the influence of noisy features (Hong et al 2019). The bias is addressed because each decision trees works with different data, increasing the model's diversity and lowering the bias (Hong et al 2019). If such splitting cannot be performed; for example, where there is a lot of noise in the dataset, then the random forest model can perform the Kernel trick (Tyralis et al 2019). Such a 'trick' projects the data into a higher dimensional space, improving the ability to identify clusters or patterns, similar to PCA, allowing decision trees to capture more intricate relationships (Tyralis et al 2019).

The Gini impurity assesses the degree of entropy in the final leaf node (Cutler et al 2007) and quantifies the probability of misclassifying elements within the data (Shaheen and Iqbal 2018). When the decision tree continuously splits using recursive partitioning, it is anticipated in the leaf node that the data contains the results the user needs (i.e., the predictions) (Feng et al 2015). The Gini impurity measures how frequently a randomly chosen element from a set would be incorrectly labelled if it were randomly labelled according to the label distribution in the subset (Shaheen and Iqbal 2018). For example, if the subset of data in the leaf node contained nine oranges and one apple, then the Gini impurity is 0.9; however, if there were five oranges and five apples, then the impurity is 0.5, meaning the leaf node has a higher entropy and generalisation error (Feng et al 2015). See Figure 4.3 outlining how the Gini impurity is defined (information taken from Feng et al 2015).

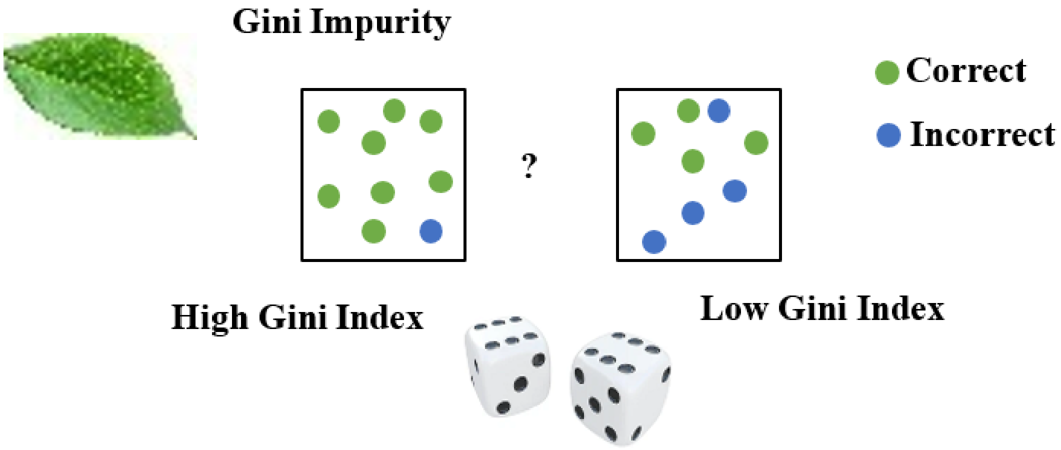

Figure 4.3. *Indicates how the definition of the "Gini impurity" is calculated. The figure indicates within the leaf node the number of correctly and incorrectly data contained (Feng et al 2015).*

The Gini impurity is used for classification trees; however, for regression problems, the mean squared error of the leaf is used for assessing the impurity level, where the mean is purer if all the points are closer to the mean (Shaheen and Iqbal 2018). This impurity reflects the entropy of the decision tree, assessing the quality of decision tree splitting (Feng et al 2015).

4.1.2 Bias and Variance in Random Forest Modelling

Any machine learning algorithm has inherent issues and trade-offs concerning bias and variance (Sinha et al 2019). High bias refers to the tendency of the model to consistently make unreliable predictions because the model is generalising the results, leading to underfitting and a generalisation error (Sinha et al 2019). Typically, such a model is too simplistic, consisting of a poor linear relationship, creating a high bias, requiring extreme gradient boosting (discussed in Sections 4.1.3, 4.1.4, 4.1.6).

Bias can occurs in simplistic models which do not capture data patterns, where the model has very strong preconceptions (Belkin et al 2019). Oppositely, high variance means the model is overly complex and has learned to fit the training dataset almost perfectly; however, when confronted with unfamiliar test data, the model fails to generalise well, causing overfitting (Belkin et al 2019). High variance can occur when the decision trees are split too frequently, and the trees are too deep, typically creating a polynomial data fit (Biau and Scornet 2016). Complex models generally contain high variance because they capture intricate relationships, potentially capturing noise data, and thus can result in poor generalisation (Belkin et al 2019).

The goal for any decision tree model is to strike a delicate balance between bias and variance, finding the appropriate level of model complexity, where the training error is minimised, without potentially causing a testing error increase (Belkin et al 2019). Diagnosing overfitting and underfitting is challenging; however, when the training error is reduced considerably at the expense of the testing error increase, this is the first sign that overfitting is occurring (Biau and Scornet 2016). For an illustration of bias and variance concepts within decision tree splitting, see Figure 4.4 (information taken from Biau and Scornet, 2016).

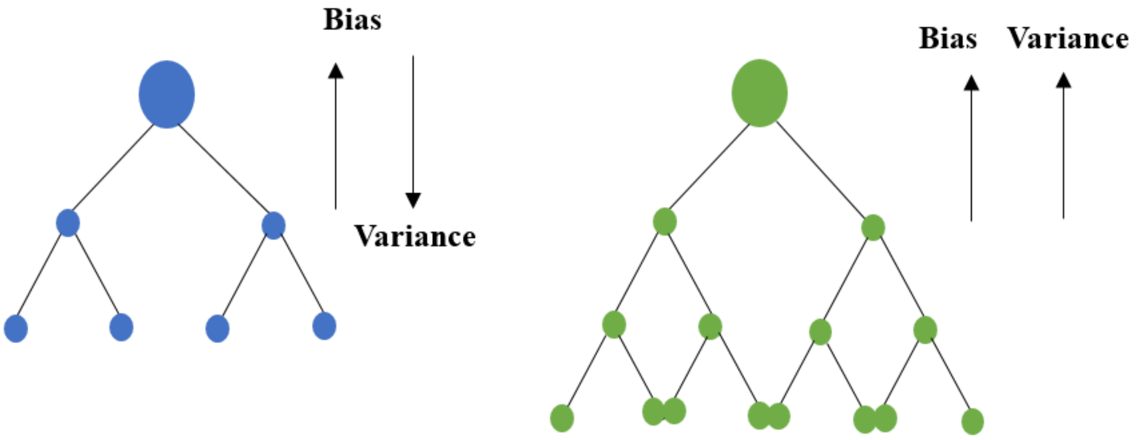

Figure 4.4. *Outlines how the decision tree size, number of branch connections and nodes influence the bias and variance of the model predictions. The figure illustrates that increasing the decision tree size with the attempt to lower the Gini impurity has negative consequences for increasing the variance (Biau and Scornet 2016).*

4.1.3 Hyperparameter Tuning

The purpose of hyperparameter tuning is to maximise the model's generalisation performance on unseen testing data. Such tuning helps locate the bias-variance sweet spot discussed in the previous section (Belkin et al 2019). However, different hyperparameter values impact on model predictive performance; thus finding the right combination is crucial for achieving the optimal bias-variance trade-off (established using cross-validation) (Cutler et al 2007). Some common tuning hyperparameters include the number of decision trees, the tree depth, and feature randomisation (Sinha et al 2019).

For the number of decision tree hyperparameters, the typical default setting is 500 decision trees for an ensemble classifier; however, tuning such a parameter by altering the number of trees can address this bias-variance problem (Springel and Hernquist 2002). Increasing the number of trees can minimise bias, by capturing more complex relationships, and increase the variance, leading to overfitting (Feng et al 2015). Conversely, decreasing the decision tree number can reduce the variance but increase bias by reducing the likelihood of capturing such intricate relationships. Tuning this hyperparameter can help establish the correct balance (Hong et al 2019).

Adjusting the tree depth hyperparameter alters the number of decision tree splits (Belkin et al 2019). Such tuning may reduce overfitting, minimising the complete training purity and bringing in some generalisation or “guessing” work for the decision tree (Biau and Scornet 2016). A deeper tree can capture more detailed complex relationships but may cause overfitting. The hyperparameter applies the cost complexity penalty to each split (Biau and Scornet 2016). The level of entropy usually represents the penalty; the branches with the highest cost (i.e., greatest entropy) are removed (Feng et al 2015). The feature randomisation hyperparameter may also address overfitting and underfitting (Hong et al 2019). Such a hyperparameter determines the number and type of features considered at each decision tree split (Sinha et al 2019). For instance, such a hyperparameter can be tuned to ensure each decision tree split has only a third of the subsampled features (Schubach et al 2017). This tuning ensures randomisation and diversity within the decision trees, helping address the multidimensionality issues, by not accounting for all the feature variables, ensuring the decision tree ensemble is different (Figure 4.5; amended from Schubach et al 2017).

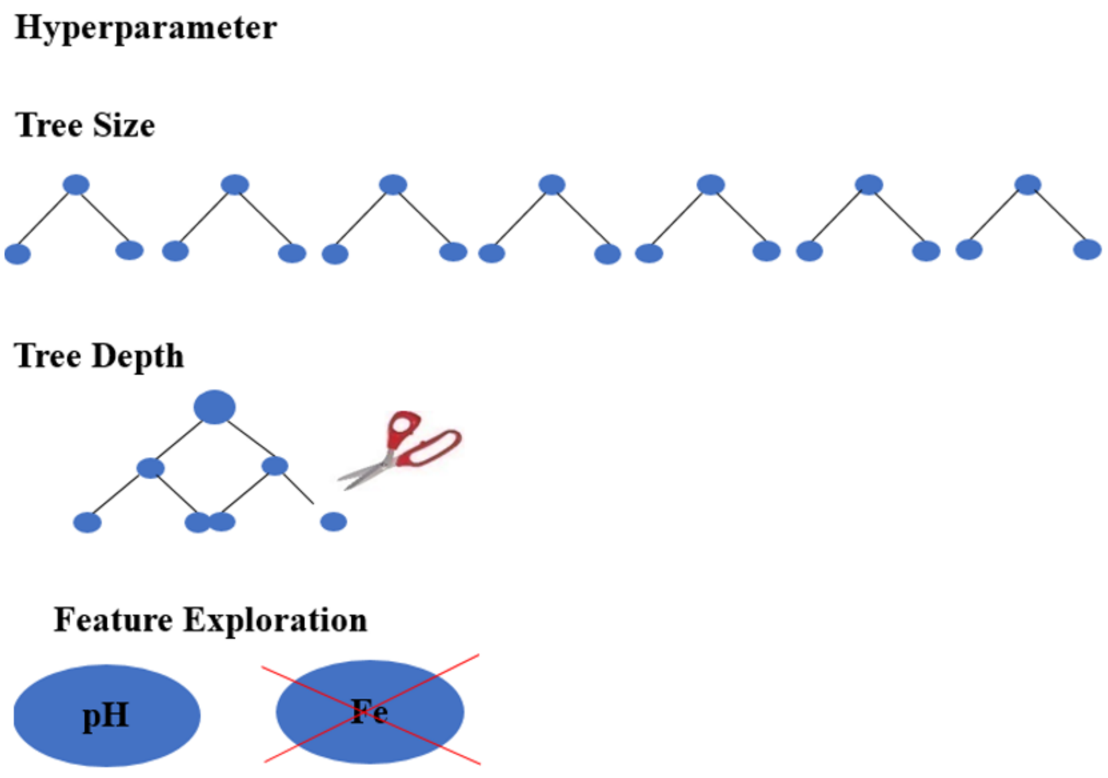

Figure 4.5. *Outlines the various different hyperparameter tuning mechanisms. The figure indicates the number of decision trees, the tree depth and the number of feature splits all influencing the model tuning (Schubach et al 2017).*

There are several tuning hyperparameters to assign (e.g., number of trees, tree depth, number of features) (Feng et al 2015). Frequent mistakes are either tuning using all the hyperparameters, randomly guessing which parameters to tune, or applying the default hyperparameter values (Biau and Scornet 2016). Systematic grid searches can avoid such mistakes (Biau and Scornet 2016). Grid searching systematically explores the different combinations of hyperparameters to identify, establishing the type and value of hyperparameters to use by applying cross-validation (Hong et al 2019). The statistical technique "cross-validation" involves splitting data into parts, which train the model, and is then tested on different parts (Tougui et al 2021). The term "K-fold" in cross-validation refers to how many parts the machine learners train on (Tougui et al 2021).

4.1.4 Model Regularisation

Regularisation helps prevent overfitting by adding a penalty term to the model, discouraging the model from overly relying on a single feature or overfitting the dataset (Lopez et al 2021). Regularisation is widely used to address overfitting, by adding a penalty term to the model for the misclassification of variables (Sorenson et al 2019). The purpose of such a penalty is to discourage the model from misclassifying subsequent predictions by deliberately placing a weight (penalty) on the misclassified values (Sun et al 2019). For example, if a student performed poorly in a particular section within an exam, that student attempts to work harder at addressing the mistakes they made for the next exam (Feng et al 2015, Lopez et al 2021, Sorenson et al 2019, Sun et al 2019). There are two main regularisation types: one being L1 and the other being L2 regularisation (Breiman 2001). These regularisation penalties are similar; however, the difference is the nature of the regularisation penalty (Couronne et al 2018). In L1 lasso regularisation, the penalty function is proportional to the sum of the absolute values of the model coefficients. See equation the proposed by Kavuk et al (2011),

$$R(W) = ʎ * ||w|| \qquad \text{Eq. 3}$$

where “ʎ” is the regularisation parameter, and “W” is the weight added to each feature. In L2 ridge regularisation, the equation is very similar; only the penalty function is proportional to the sum of squares of the model coefficients (Breiman 2001). See below by Kavuk et al (2011).

$$R(W) = ʎ * ||w||_2 \qquad \text{Eq. 4}$$

The aim of regularisation is to fit the training data using a quadratic fit, which is the sweet spot between a linear fit and a polynomial fit (Breiman 2001). In other words, a polynomial fit attempts to fit the data perfectly, leading to overfitting, and a linear fit, in many instances, does not understand the intricates of the data patterns, leading to underfitting (Kavuk et al 2011). The idea of regularisation is to bridge the gap between overfitting and underfitting using quadratic fits (Breiman 2001) (see Figure 4.6, information obtained from Feng et al 2015).

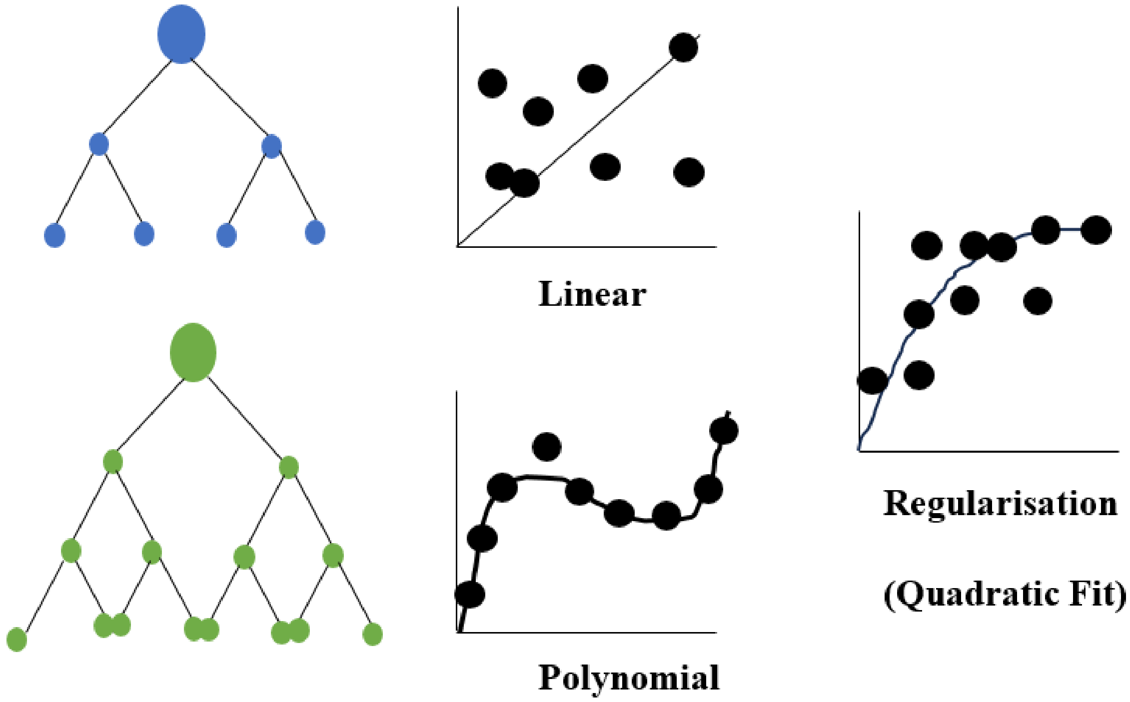

Figure 4.6. *Outlines the mechanistic understanding of regularisation in machine learning. The illustration shows two limitation of training data (1) linear generalisation error, showing the predictions not encapsulating small data variations and (2) a polynomial fit leading to making poor predictive performances outside its testing range. The process of regularisation "smooths" the model fit closer to quadratic fits*

4.1.5 Random Forest Bagging

Bagging, also known as bootstrap aggregation, is an ensemble learning method designed to improve decision tree models by reducing the variance and enhancing the stability and accuracy (James et al 2013). Multiple decision trees are trained on a training dataset (McLaren 2019).

There is no standard method for deciding the number of decision trees; however, grid searches are a systematic approach to searching for the best hyperparameters, including the number of decision trees as well as other model-specific parameters that need to be set before training the model (e.g., max_depth and max_features) (James et al 2013). The number of decision trees depends on the model complexity, the number of features, and the complex interactions among such features (Breiman 2001). The term "feature" refers to the input variables the machine learning models use to predict (Breiman 2001).

Each sample can be selected multiple times with replacement, ensuring randomisation (Sorenson et al 2019). For example, if the dataset contains singular values representing calcium, potassium and iron concentrations, sampling with replacement could result in selecting the same value multiple times, such as two calcium values and one potassium value chosen randomly (Sinha et al 2019). For example, the same value can be chosen more than once (Cutler et al 2007).

A decision tree is different from the training dataset because it is trained on bootstrap samples from the training dataset, meaning that each sample can be selected multiple times, ensuring randomisation (Schubach et al 2017). These decision trees also ensure feature randomisation, meaning the decision tree will only take calcium and potassium values, for example, whereas another tree will extract iron and manganese, for example. (Shaheen and Iqbal 2018).

Typically, two-thirds of the total number of data points from the training dataset will be extracted for such decision trees. The remaining one-third of data is used for testing, known as out-of-bag samples, which are used to estimate the model's generalisation performance and assess feature importance (Shaheen and Iqbal 2018). Such features (e.g., calcium, potassium, and iron) are compared to predict this out-of-bag testing data.

The predictions are only made for out-of-bag samples (Kavuk et al 2011). If removing a particular feature increases the out-of-bag prediction error, such a feature is considered important (Sinha et al 2019). By "important" means it has a strong statistically significant influence on the predictor variable (McLaren 2019). If removing a feature variable significantly reduces the out-of-bag testing error this variable is considered "important." The out-of-bag data offers a unique advantage of assessing the variable importance without requiring the actual test data bank (James et al 2013).

The feature importance is measured by assessing how much each feature contributes to reducing the impurity (Gini for classification and mean square error for regression); the more significant the reduction in the impurity, the more important the feature (James et al 2013). The "Gini" metric determines the "purity" of the leaf node and refers to the number of misclassified variables within the final prediction (Kavuk et al 2011). Gini values closer to 1 equal low purity and closer to zero equal perfect classification or purity (Kavuk et al 2011).

Alongside calculating the feature importance using the out-of-bag data, there are various other ways of calculating the feature importance, such as using SHapley Additive exPlanations (SHAP), Gini importance, entropy and information gain (Cutler et al 2007). SHAP derives from Shapley values from the cooperative game theory

(James et al 2013). Initially, these Shapley values are fairly distributed "payout" among the different players "features" (Tougui et al 2021). For each feature variable, or "player" in the game, it calculates that features contribution by considering all the different feature combinations (Tougui et al 2021). The combination of all the features equate to the model's predicted value minus the baseline (e.g. mean prediction) (Cutler et al 2007). Gini importance, as described before, measures the purity of the leaf node, with higher gini values denoting feature variables which are more important for increasing the purity or categorisation of splits (Cutler et al 2007). If removing a particular feature causes a decrease in the gini impurity this means that exclusion of that feature could negatively impact the predictive performance. Entropy measures the uncertainty or randomness in a dataset (see Section 4.2.5 for future information) (Sorenson et al 2019). Information gain measures the reduction in entropy after splitting a dataset based on a feature, essentially measuring how much a feature contributes to classifying the dataset (Sorenson et al 2019).

The number of predictions depends on the number of decision trees trained and the number of testing samples, resulting in a total number of predictions equal to the product of these values. For example, if you have 100 decision trees and 100 testing samples, you create 10,000 predictions, meaning that the prediction number is equal to the product of the number of decision trees and the number of testing samples (Sinha et al 2019). The overall prediction is obtained by averaging all the decision trees using a majority classifier (Schubach et al 2017). If the problem is a classification task then the mode of the predictions is collected.

The purpose of averaging or selecting the mode of the predictions, is that this significantly reduces the model variance, helping to improve the model's generalisation performance, decreasing the probability of overfitting the training data (Feng et al 2015). Averaging the predictions provide a single estimate for each testing sample (Feng et al 2015).

4.1.6 Algorithmic Boosting

Extreme gradient boosting is an alternative to the random forest method that may achieve improved predictive performance by using a different approach to combining decision trees (Genuer et al 2010). Rather than ensemble approaching, extreme gradient boosting applies an iterative means to decision tree learning (McLaren 2019).

Extreme gradient boosting can address the inherent bias errors within random forest modelling and be used for regression and classification problems (Cutler et al 2007). A regression problem refers to a prediction using numbers and a classification problem indicates a prediction using image processing. Such a technique combines “weak” decision tree learners with “strong” learners (Feng et al 2015). Extreme gradient boosting begins with a weak decision tree learner attempting to predict an outcome using feature data (Kavuk et al 2011).

When such a tree misclassifies specific data, then the algorithm places more weight on that misclassified data (Sinha et al 2019). Another weak decision tree then places more emphasis on correcting the misclassified data from the previous tree, and this continues with the aim to minimise the overall error (training and validation) (see Figure 4.7, information obtained from Lopez et al 2021).

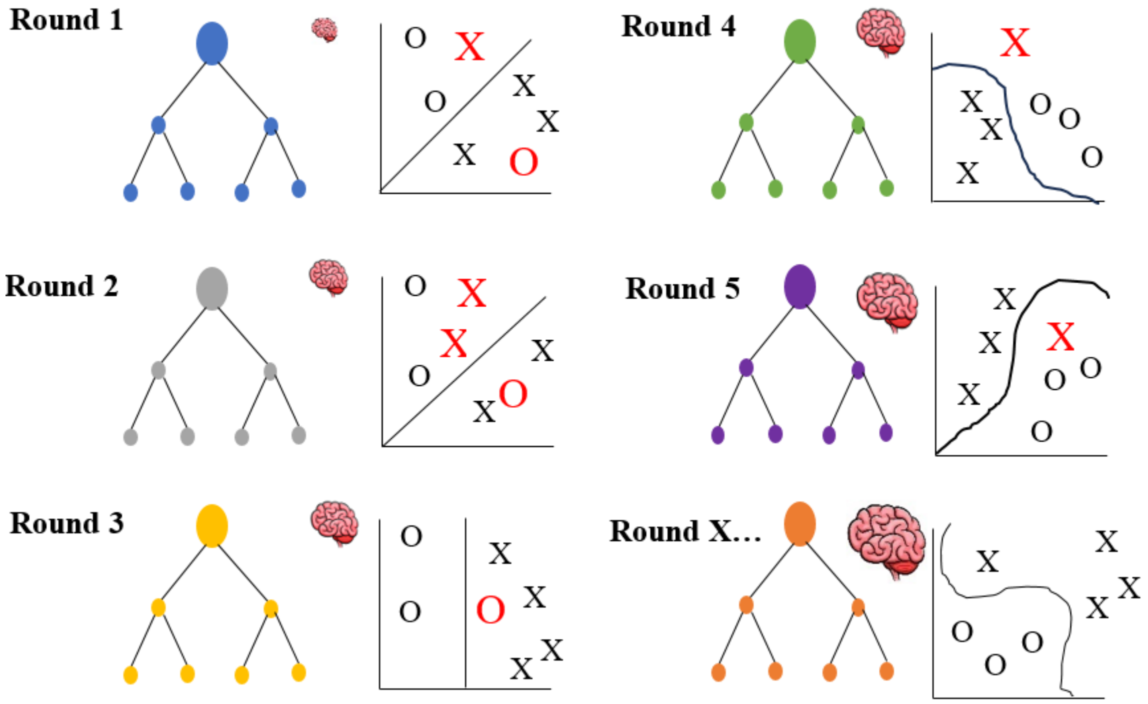

Figure 4.7. *Indicating the computational process of extreme gradient boosting. The figure shows every misclassified prediction assigning a weighted value. This weighted value is noticed and learned by the next decision tree learner (information obtained from Lopez et al 2021).*

Assigning weight to the misclassified data adjusts the loss function for the subsequent iteration of training (Hong et al 2019). The loss function describes how well the model fits the data; assigning weights tells the next learners to focus on such misclassified data will lower the loss function for the next iteration (Springel and Hernquist 2002).

By learning from the previous mistakes of the last decision tree, a strong learner can be created from all the misclassified mistakes from the previous learners (Springel and Hernquist 2002). Extreme gradient boosting is iterative, and there is no means of absolutely deciding how many decision tree learners are required (Breiman 2001).

Key hyperparameters such as learning rate, number of trees, and maximum tree depth can be tuned to help identify the number of learners, aided by systematic grid searching (Breiman 2001). Extreme gradient boosting is not restricted to decision tree algorithms but can also use other models, such as linear models; however, decision trees are the most used base learners (Feng et al 2015). For an overview of all the black box components within this chapter, see Figure C4.1 Appendix C.

4.1.7 Neural Networks

Deep learning artificial neural nets is a sub-branch of AI (Schubach et al 2017). These networks have three layers (input, hidden, and output). The input layer is the dataset containing all feature variables; essentially, the input layer represents the dataset implemented into the model (Galiano et al 2014). The hidden layer formulates decision-making, and the output presents the final prediction (Schubach et al 2017).

When data are added to the input layer, a neuron within the hidden layer receives the data (Lopez et al 2021). The function of a neuron calculates the strength of the input signal or, in other words, the significance of that specific feature relating to the prediction (Galiano et al 2014). Such signal strength derives from several metrics (Schubach et al 2017). The input is initially assigned an arbitrary weight (“weight” means the strength of the relationship) and bias value (Schubach et al 2017).

This weight and bias value are added, and then the neuron within the hidden layer passes such values through an activation function (e.g., sigmoid curve) (Biau and Scornet 2016). This function takes the combined value and "squashes" it into a range between 0 and 1 using a logistic function to introduce non-linearity (Lopez et al 2021). The output value combines all the sigmoid values from the hidden layer (Galiano et al

2014). The actual value is subtracted from the prediction output, and such differences denote the loss functions (e.g., mean square error) (Biau and Scornet 2016).

The neural network then reconfigures and updates its weights by applying back propagation using stochastic gradient descent (SGD) (Lopez et al 2021). Briefly, the gradient of each neural loss function concerning the weights is calculated by dividing the loss function by the individual weights iteratively (Schubach et al 2017). The data are continuously run through the model, and the derivatives concerning the weight changes update the initial weights, gradually reducing this loss function closer to zero and improving the prediction (Lopez et al 2021).

4.1.8 Aims and Objectives

This chapter aims to investigate (1) which physicochemical parameters are the most and least reliable for estimating PHE changes during flooding. The chapter seeks to incorporate such physicochemical data into statistical, machine, and deep learning AI *modelling to predict a (2) PHE porewater solubility, (3) bioaccessibility, and (4)* solid phase distribution during flooding. The physicochemical data to train such models were obtained from the Clyde catchment during the experimental analysis in Chapter 3. This chapter also aims (5) enhancing the statistical and machine learning models, training on mechanistic data for improving the predictive performance. For an overview of the objectives of this chapter in relation to the thesis structure, see Table 4.1 below. For the purposes of space, this chapter will focus on predicting lead mobility, bioaccessibility and solid phase distribution. For information regarding the training and testing of such models to predict different PHE, see Appendix C and D.

Table 4.1. *Outlines the different research aims and how such aims relate the overall thesis structure. The table outlines the catchments in which the physicochemical data was obtained to train such models, indicating also the PHE type such models are predicting.*

Research Aim	Flow Chart Part	Catchment	PHE Type
1	15	Clyde	Lead
2	16	Clyde	Lead
3	16	Clyde	Lead
4	16	Clyde	Lead
5	16	Clyde	Lead

4.2 Methods

4.2.1 Programming the Statistical Model

The physicochemical data were collected from the microcosm experiments within the Clyde catchment, and to ensure the independence of the data points and avoid pseudoreplication, a mixed model was programmed on the physicochemical data using the *lm34* package in RStudio (Feng et al 2015). Mixed models can address pseudoreplication by incorporating fixed effects to adjust for non-independence (Arnqvist 2020). The statistical model, therefore, compared with the machine and deep learners, was a mixed model because such models address pseudoreplication. A mixed model was also selected over other statistical models, such as a multiple regression or generalised linear model, because mixed models are highly capable of handling hierarchical data structures (or data with clustering) through random effects.

4.2.2 Programming the Machine Learning Models

A random forest regression model was computed using the *RandomForest* package in RStudio (Doran et al 2007). The physicochemical data were split into training (70%), validation (10%), and testing (20%). The training dataset is the largest portion and is used to train and fit the model, where the algorithm learns patterns, correlations, and relationships within the training dataset (Kanevski et al 2008). The validation set assesses the model performance during the training, estimating the prediction error for model selection (e.g. tuning hyperparameters) (Kanevski et al 2008). The testing dataset is completely separate from the training data, giving an unbiased estimate of the generalisation error of the final chosen model (Kanevski et al 2011). Data partitioning to training, validation, and testing was performed by random splitting, using the *train_test_split* function.

The out-of-bag data were used to determine the variable importance of the physicochemical data for estimating lead porewater solubility during flooding (Section 4.1.5). This study did not include a validation dataset; instead, it conserved such data and used the out-of-bag error to estimate the training error (Breiman 2001). Systematic grid searches optimised hyperparameter tuning (see Section 4.1.3). This study compared such grid searches using performance autoplots (Figure 3C, Appendix C). A classification random forest model was computed to predict the PHE solid phase distribution. The model sensitivity, specificity, and receiver operating characteristic (ROC) metrics were examined to determine the ability of the random forest model to predict lead solid phase distribution. These metrics are important for the random forest model to train and correctly identify and classify different predictor variables.

An extreme gradient boosting algorithm was computed using the *xgboost* package, with the data splits, hyperparameter tuning, and regularisation addressed similarly to the random forest model (Lee et al 2017). The number of rounds of learning (30 rounds) was defined using systematic grid searching.

4.2.3 Programming the Deep Learning Model

A neural network was constructed using the *TensorFlow* Python interface*, caret,* and *keras* packages in RStudio (Pang et al 2016, Kuhn 2012, Arnold 2017, respectively). The data were partitioned into training (70%), validation (10%) and testing (20%) datasets. This study computed a neural network containing two hidden layers using a rectified linear activation function to address non-linearity. This activation function aims to address regression problems and allow the network to address non-linearity by setting all negative inputs to zero.

The neural network was trained, applying stochastic gradient descent, using the Adam optimiser, running through a specified epoch number, and attempting to lower the model output training and testing mean square error. The Adam optimiser helps the neural network learn from the data (Su et al 2023). The optimiser adjusts the model's learning rate to aid in minimising the training and testing loss function (Su et al 2023). The term "epoch" in machine learning refers to the entire network processing all the data, allowing the network to learn and adjust its weights and bias values (Siddique et al 2018). This epoch value controls the number of complete passes of data to update such weights through the network (Siddique et al 2018). For example, an epoch of "50" means the entire training data passes through the network 50 times, continuously updating the network's weights and bias values.

This study used a learning rate of 0.001% to enhance the model's generalisation performance and reduce overfitting. In other words, having a minimal learning rate of 0.001% means the model slowly analyses the data, minimising the likelihood of misclassifying intricate relationships. The epoch number was selected by visually inspecting when increasing the epoch number increases the validation error and secondly with systematic grid searches (Figure 4.8).

The batch was 32, randomly shuffled each epoch, specified by systematic grid searches, which is relatively large for ensuring stable gradient estimates. As mentioned, each epoch passes through the entire dataset to update the network weights; however, this can be computationally expensive. To minimise this computational demand, the purpose of the batch size refers to how much data from the training dataset passes through one epoch; after each epoch, the batch number remains the same; however, it randomly selects another 32 data points to circulate through the network.

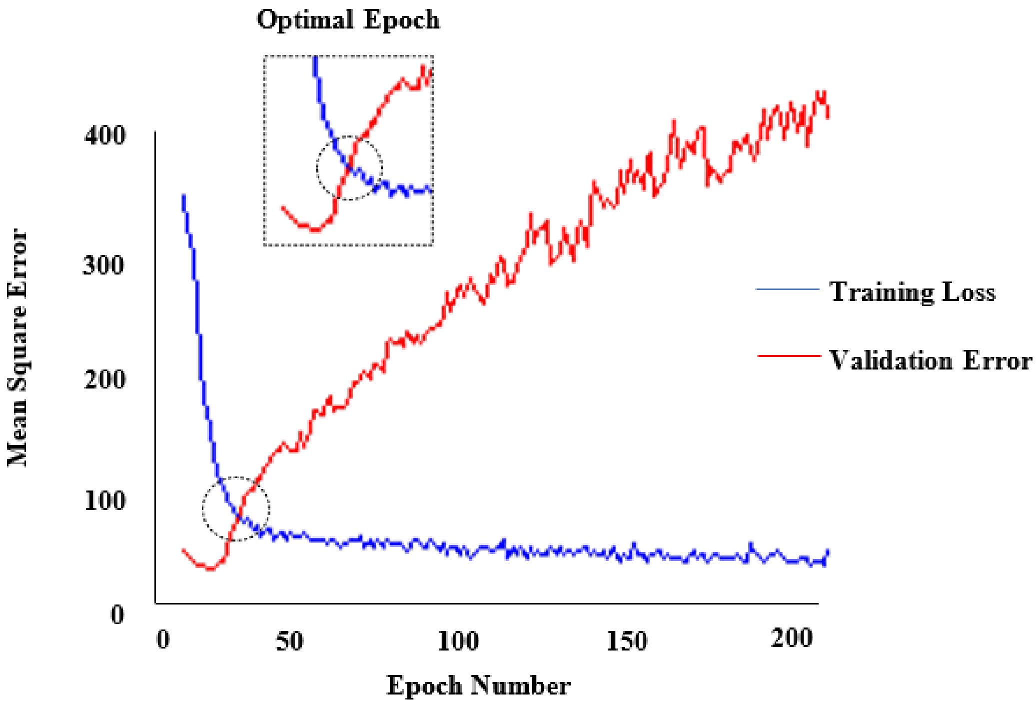

Figure 4.8. *Outlines the effects of increasing the epoch number on the training and validation loss. The Figure outlines the optimal epoch number (26), which significantly reduces the training and validation loss.*

4.2.4 Mechanistic Modelling

The best performing model (either mixed, random forest, extreme gradient booster or neural network), which will be established in Sections 4.3.2, 4.3.3 and 4.3.4, were enhanced by "learning" mechanistic information derived from inputting physicochemical data into PHREEQC (version 3.37.3) and Visual MINTEQ software (version 4) and then using their outputs to help train the best performing model established in Sections 4.3.2, 4.3.3, and 4.3.4.

PHREEQC (PH REdox EQuilibrium) analyses a PHE solid phase distribution (e.g., $CuSO_4$, $PbSO_4$, $AsCl_3$) by inputting hydrodynamic and physicochemical data (e.g., water temperature, volume, iron concentration) into its geochemical speciation model (Lu et al 2022). This study implemented the composition of the solution and specified the thermodynamic and kinetic reactions (i.e., sorption, ion exchanges, aqueous complexation, dissolution, and precipitation). PHREEQC ensures the element's total mass and the ionic charge remain conserved under such simulations by applying the Law of Mass Action Equation. This determines the species (e.g., copper) composition and distribution (Lu et al 2022).

Visual MINTEQ (MINeral and TEQuilibrium) analyses the concentration of sorbed and reductively dissolved PHE from oxide and carbonate mineral phases during flooding (Gustafsson 2011). This chapter conducted microwave digestion to gain an understanding around the soil's total heavy mental concentration. For information around the specific microwave digestion procedure, see Appendix B, Section 2. Abiotic inputs (i.e., Eh and pH) changes throughout the flood were implemented. Using mass-balance equations, this software calculated the concentration of lead sorbed and dissolved from key mineral phases (i.e., iron, manganese, and calcium) throughout the flood. The investigation incorporated this mechanistic understanding from both these software programs into the models examining the predictive performance change.

The types of PHE analysed were copper, lead, and arsenic. These PHE, particularly lead and arsenic, are toxic to humans and wildlife and is important to understand how flooding influences these PHE for human and wildlife health purposes (Ponting et al 2021). These PHE represent the chemical form and characteristics of different PHE; for example, lead interaction with different soil mineral phases during flooding is similar to cadmium and chromium, and copper interactions are similar to zinc and nickel.

4.2.5. Performance Evaluation

The performance of the machine learning and statistical models were evaluated using widely recognised metrics, such as the R^2, root mean square error (RMSE), mean absolute error (MAE), and mean square error (MSE). While additional metrics, such as L1 and L2 norms, are also commonly used to evaluate predictive performance, they are not employed in this chapter. The L1 norm (Manhattan Distance) calculates the average of the absolute differences between predicted and observed values, while the L2 norm

(Euclidean Distance) computes the square root of the average squared differences (Pang et al., 2016). These metrics emphasise absolute error magnitudes, with L2 placing greater weight on larger deviations.

This chapter focuses on evaluating performance through R², MAE, MSE, and RMSE for two key reasons. Firstly, the study's objective is to assess relative explanatory power (variance captured) rather than solely minimising absolute error magnitudes, which makes R² particularly relevant. Secondly, while L1 and L2 metrics are effective for penalising errors, they do not provide intuitive insights into the proportionality of variability explained by the model, which is central to understanding trends in contaminant mobility and bioaccessibility.

The entropy and information gain from the model predictions within the testing dataset were quantified and compared to measure the uncertainty in the observed outcomes and the reduction in uncertainty achieved by the model predictions. Entropy is a measure of the uncertainty in a dataset by quantifying how unpredictable the outcomes are (Feng et al 2015). High entropy indicates greater uncertainty, higher data diversity, or less predictable categorisation, which could mean the predictions lack alignment with the observed outcomes. Low entropy indicates greater order, reduced variability, and potentially better alignment with the observations(Feng et al 2015). Entropy is calculated below,

$$H(X) = -\sum_{i=1}^{n} P(x\mathrm{i})\log 2\, P(X\mathrm{i}) \qquad \text{Eq. 5}$$

where "H" is the entropy "(X)" and "P(xi)" is the probability of the datapoints within each interquartile range (e.g., 5th to 95th) and "n" is the total number of interquartile ranges (). Information gain measures the reduction in entropy, see Equation 3,

$$\text{Information Gain} = \mathrm{H}(Y) - \mathrm{H}(Y) - \mathrm{H}(Y \mid X) \qquad \text{Eq. 6}$$

where "H(Y)" is the entropy of the observed dataset. The calculated entropy and information gain form each of the random forest, XGBoost, neural network and the mixed model was compared. A lower entropy and higher information gain suggests the model reduces uncertainty and aligns well with the observed outcomes.

4.3 Results

4.3.1 Identifying Optimal Physicochemical Feature Variables for Predictive Modelling of PHE Porewater Solubility and Bioaccessibility

Many types of physicochemical parameters exist, such as oxides, micronutrients, and abiotic variables. The physicochemical data from the microcosm and mesocosm experiments conducted within the Humber and Clyde catchments, discussed in Chapter Three, was computed into a linear regression model, identifying correlations between the physicochemical and copper, lead, and arsenic porewater solubility. The physicochemical variables were grouped into different classes (e.g., abiotic, micronutrients) and treated as separate linear models to predict PHE porewater solubility.

Many physicochemical features correlate with PHE porewater solubility (Table 4.2). Such physicochemical groupings show the importance of appreciating oxides, PHE, micronutrients and abiotic features when predicting mobility. This analysis indicates that for reliably estimating PHE porewater solubility, incorporating physicochemical information across different groups (e.g., oxides, micronutrients, abiotic) provides the highest performing model, accounting for AIC and BIC estimates. For a more detailed breakdown indicating the physicochemical combination of different PHE, see Table B3.2 and Figure B3.7, Appendix B.

The literature view (Chapter 1) and quantitative meta-analysis (Chapter 2) show the importance of different physicochemical parameters influencing PHE dynamics during flooding. This Chapter builds upon such analysis, indicating the importance of physicochemistry; however, adding the importance of using a single physicochemical parameter that strongly correlates with PHE porewater solubility (e.g., iron) yields low predictive reliability. This analysis emphasises the importance of training machine, deep and statistical models to predict PHE porewater solubility, bioaccessibility and solid phase distribution using physicochemical data all across the different groupings (e.g., oxides, abiotic, and micronutrients).

In this section, predictions for bioaccessibility were made using the “best” combination of feature physicochemical variables to predict PHE porewater solubility and its influence on bioaccessibility. The results showed a good correlation with arsenic, copper and lead with very low mean square errors (Figure 4.9, Tables B3.2, Appendix

B). The correlation fit decreased though as PHE concentration increased. Such correlation was weakest for arsenic but exhibits the lowest mean error (Table 4.3). These findings reveal the opportunities of programming different statistical, machine and deep learning models using this physicochemical combination to estimate PHE porewater solubility and bioaccessibility.

Table 4.2. *Outlines the linear model outputs investigating the correlation between physicochemical predictive features estimating PHE porewater solubility. The table outlines the model selection, error and correlation statistics.*

Feature Combination	AIC	BIC	R^2 (adjusted)	Mean Square Error	Mean Absolute Error	Root Mean Square Error
Micronutrients (K, Ca, Mg, Na)	Cu - 1893 Pb - 806 As - 521	Cu - 1912 Pb - 824 As - 541	Cu - 0.75 Pb - 0.57 As - 0.67	Cu - 3520 Pb - 6.1 As - 1.15	Cu - 43 Pb - 1.73 As - 0.83	Cu - 59.3 Pb - 2.5 As - 1.1
PHE (Li, Cr, Cu, As, Ni, V, Zn, Pb)	Cu - 1968 Pb - 806 As - 488	Cu -1997 Pb - 834 As - 516	Cu - 0.62 Pb - 0.58 As - 0.74	Cu - 5274 Pb - 5.86 As - 0.92	Cu - 57.2 Pb - 1.65 As - 0.69	Cu - 27.3 Pb - 2.32 As - 0.96
Oxides (Fe, Al, Mn)	Cu - 2079 Pb - 902 As - 399	Cu - 2094 Pb - 918 As - 415	Cu - 0.25 Pb - 0.25 As - 0.84	Cu - 10527 Pb - 10.8 As - 0.57	Cu - 85.6 Pb - 2.41 As - 0.53	Cu - 103 Pb - 3.29 As - 0.76
Abiotic (pH, E_H)	Cu - 2022 Pb - 945 As - 500	Cu - 2035 Pb - 957 As - 513	Cu - 0.45 Pb - 0.02 As - 0.71	Cu - 7660 Pb - 14 As - 1.04	Cu - 66.1 Pb - 2.84 As - 6.35	Cu - 87.5 Pb - 3.7 As - 1.02
Optimal Combination (Al, Cu, Fe, Mn, pH, As, Ca, Na, K)	Cu - 1704 Pb - 797 As - 328	Cu - 1741 Pb - 834 As - 365	Cu - 0.92 Pb - 0.61 As - 0.90	Cu - 39142 Pb - 5.39 As - 0.35	Cu - 162 Pb - 1.68 As - 0.59	Cu -197 Pb - 2.32 As - 0.42

Key 🟨 **Poor** ⬜ **Low** 🟦 **Average** 🟩 **Strong** 🟩 **Excellent**

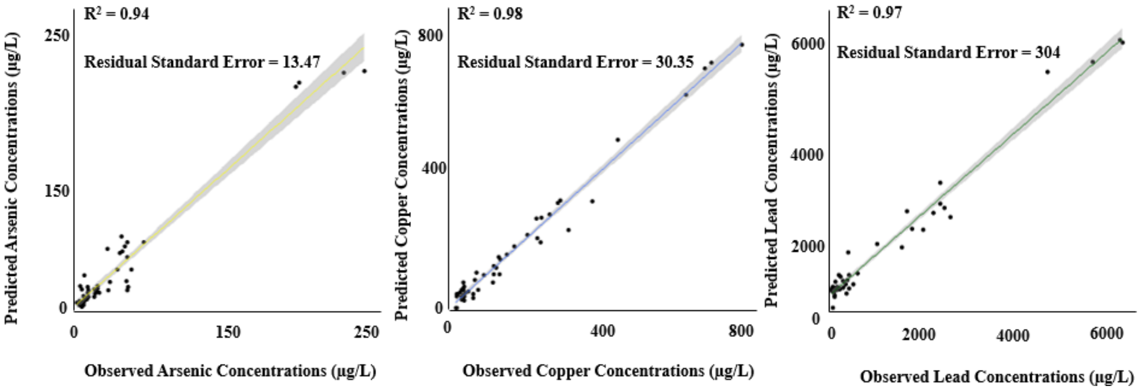

Figure 4.9. *Regression correlation output comparing the effects of incorporating physicochemical features to predict arsenic (yellow), copper (blue) and lead (green) bioaccessibility. The figures provide the regression error, indicated by the grey outline over the regression line, referring to the uncertainty in the residual data points around the regression line. Residual points not within this error area represent outliers.*

Table 4.3. *Regression output analysis investigating the effects of the major cationic physicochemical parameters, identified from PCA, influencing the bioaccessibility of the different PHE during flooding. Such outputs verify the PCA findings and aid in interpreting which physicochemical parameters to use in the predictive model.*

PHE	Optimal Physicochemical Combination	Standard Error	R^2	Adjusted R^2	P-Value	F-Statistic	df
Arsenic	Al, Cu, Fe, Mn, pH, Ca, Na, K, Pb	0.23	0.99	0.98	<0.001	53.3	69
Copper	Al, Cu, Fe, Mn, pH, Ca, Na, K, Pb	36	0.98	0.88	0.02	10.5	69
Lead	Al, Cu, Fe, Mn, pH, Ca, Na, K, Pb	61.4	0.96	0.79	0.04	5.86	69

4.3.2 Comparing Statistical, Machine, and Deep Learning for Estimating PHE Porewater Solubility During Flooding

This section uses all the physicochemical data derived from Chapter 3 from the Humber and Clyde catchments to train different statistical, machine and deep learning models to estimate PHE porewater solubility. Specifically, based on the analysis in Table 4.2, the input features for all the machine learning models and the statistical mixed model were major ions (i.e. Ca, K, Na, Fe, Al, and Mn) and physicochemical properties (i.e. pH and Eh) with the target variables (output) were predicting the porewater solubility of As, Pb, and Cu. The types of feature variables to train such models derive from the optimal combination from Section 4.3.1. For the purposes of space, this section will focus on predicting the lead porewater solubility. Lead is also highly toxic through exposure and exhibits high concentrations within soil and sediment across the United Kingdom (Tables 1.1 and 1.2).

Predicting lead porewater solubility using the “optimal” physicochemical feature combination estimated lead’s mobility using all the model types investigated (Figure 4.10). Using t-test statistics showed no statistically significant difference between the predictions and the experimentally derived data. Such findings are important and emphasise these AI approaches as a novel means of potentially aiding risk assessment procedures for assessing PHE porewater solubility during flooding. The order of the best model by having the highest correlation coefficient and the lowest testing root mean square error was the extreme gradient boosting, random forest, neural network, and mixed model (16.3, 17.6, 20.7, 26.9, respectively).

However, the importance of physicochemical features to each model varies. For example, all the models agreed that aluminium and other PHE (i.e., copper and arsenic) were significantly important predictive features. Whereas, the machine learning random forests and extreme gradient boosters and also statistical mixed models agreed micronutrients (i.e., potassium, sodium, calcium) were not important predictive features. While deep learning neural networks placed micronutrients much higher in importance, particularly sodium. According to the AI models, the pH is not as significant a feature as expected; however, the statistical model ranked it as the most important. For predicting different PHE, see Figures C4.2 and C4.3, Appendix C.

These findings all emphasise machine and deep learning models, using physicochemistry to train and reliably predict PHE porewater solubility. The results show that, based on the variable importance, each model may “learn” the data differently; however, it still predicts reliably. Such findings suggest two conclusions. Physicochemical influence on PHE porewater solubility is highly multidimensional and complex, and the understanding of how each variable relates to another to formulate an outcome can be interpreted differently. Lastly, understanding the intricate relationships between physicochemistry and estimating PHE porewater solubility is not fundamentally important; it’s more important for the models to understand how the main variables influence the prediction.

The machine learning predictions yielded predictions exhibiting lower entropy and higher information gain compared to the mixed model. Specifically, the random forest, XGBoost, and neural network yielded an entropy of 2.12, 2.45, 2.54, respectively, whereas the mix model yielded an entropy of 4.54. These findings suggest the machine learning models, particularly the random forests, where better at categorising and providing order to the predictions. Similarly, the information gain was the highest for the machine learning model random forests, XGBoost, and neural network at 0.78, 0.67, 0.58, respectively, whereas the mixed model exhibited a lower information gain of 0.16.

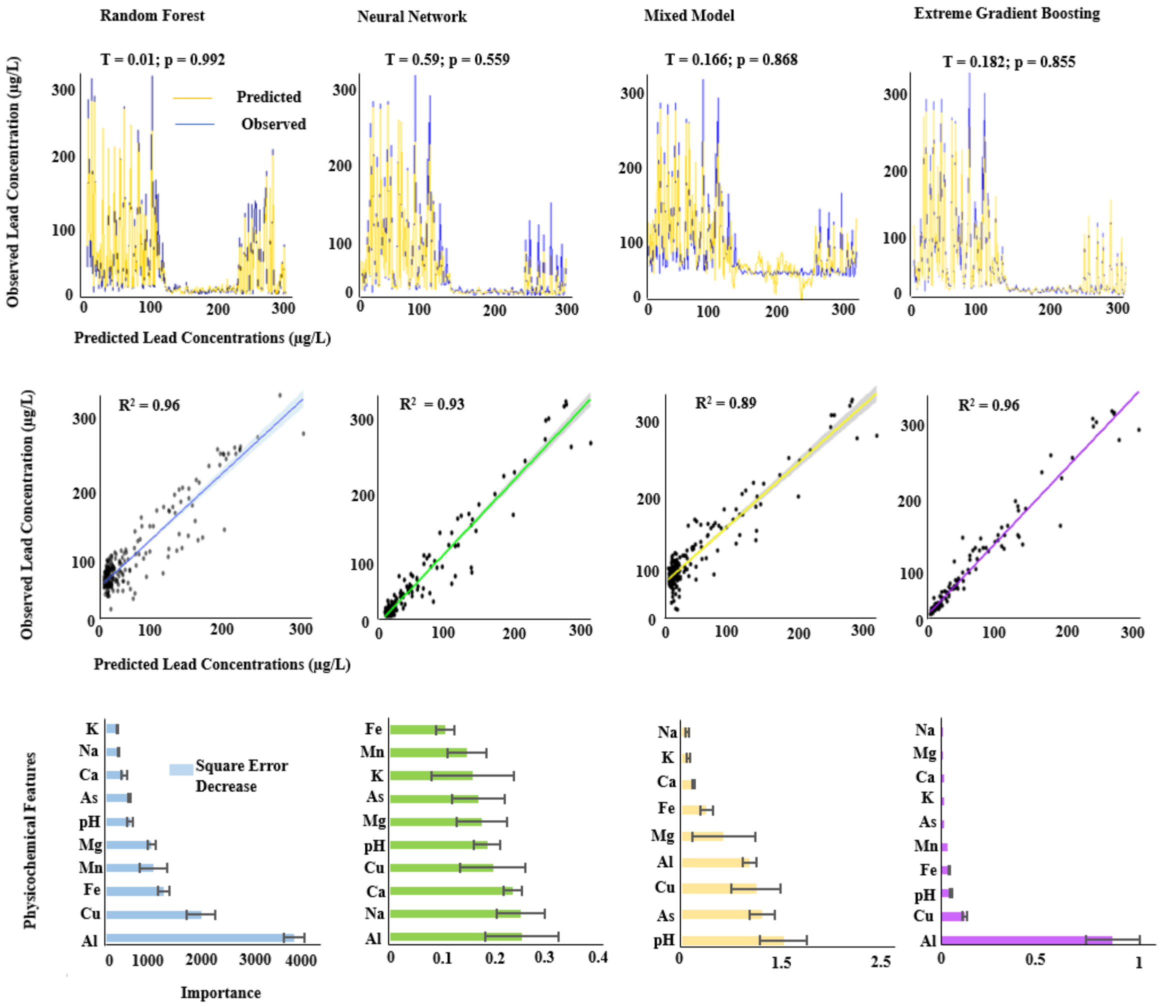

Figure 4.10. *Comparing the different model predictions (yellow) against the observed laboratory results (blue). The strength of such predictions is represented using regression analysis. The "importance" of each physicochemistry feature influencing the prediction is also presented. By "importance", this defines how much the mean square error would change if such a variable was removed from the model. For example, if removing the variable iron caused a significant increase in the mean square error, then this variable would be regarded as statistically important. If the removal of calcium results in little mean square error change, this variable implies having little change in the predictive performance and minor importance.*

4.3.3 Comparing Statistical, Machine, and Deep Learning for Estimating PHE Bioaccessibility During Flooding

Predicting the bioaccessibility using physicochemistry is highly reliable using the models investigated, except for the neural network, as there are no statistically significant differences between the experimental data and the different models predictions (Figure 4.11). The deep learner performed poorly, with a higher RMSE of 666. The best model incorporating physicochemistry was the extreme gradient booster, exhibiting the highest correlation coefficient and the lowest RMSE of 48.62. The next best model was the random forest and then the mixed model with an RMSE of 97.6 and 123, respectively.

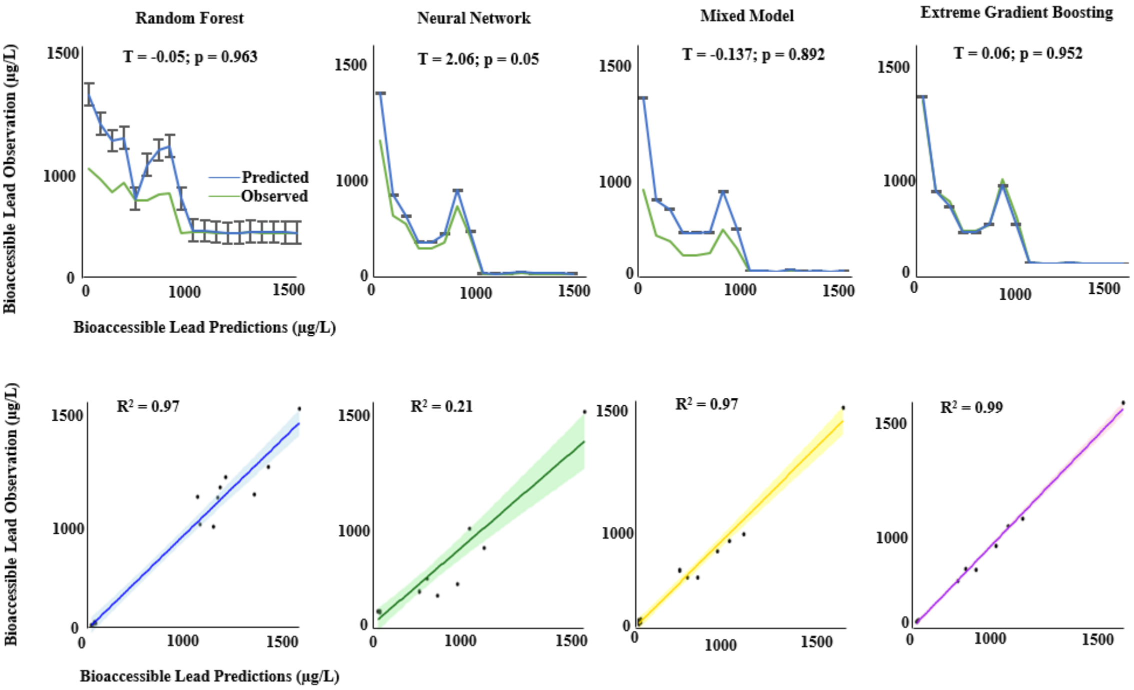

Figure 4.11. *Outlines the effects of predicting lead's bioaccessibility using different modelling approaches. The upper figures compare estimating lead's bioaccessible concentrations with the observed laboratory results. The lower set indicates the relationship's strength. The figure suggests the different model types have a significant predictive variation. The coloured band over the regression line represents the confidence interval for the fitted regression curve. The width of the band indicates the confidence level (95%). Data points falling within the confidence interval are considered within the 95% confidence interval of the model. Such points outside the 95% confidence interval band denote outliers.*

4.3.4 Comparing Statistical, Machine, and Deep Learning for Estimating PHE Solid Phase Distribution During Flooding

The area under the curve, in relation to the ROC analysis (see Section 4.2.2) indicates a very suitable and reliable predictive model analysing a PHE solid phase distribution. Again, the best predictive model was the extreme gradient booster, which showed a very high area under the curve and prediction accuracy against the testing data (Figure 4.12). The metric for assessing the "best predictive model" was by evaluating the area under the ROC curve for classification accuracy and also the testing data mean square prediction error. Statistical and neural networks provided a very low predictive accuracy; however, the area under the curve remains high. These two models suggest that such models do not explain much variance in the target variable, but they perform well distinguishing between classes (by "classes," this means the mineral phases). The random forest performs very well, exhibiting a high classification accuracy and area under the curve.

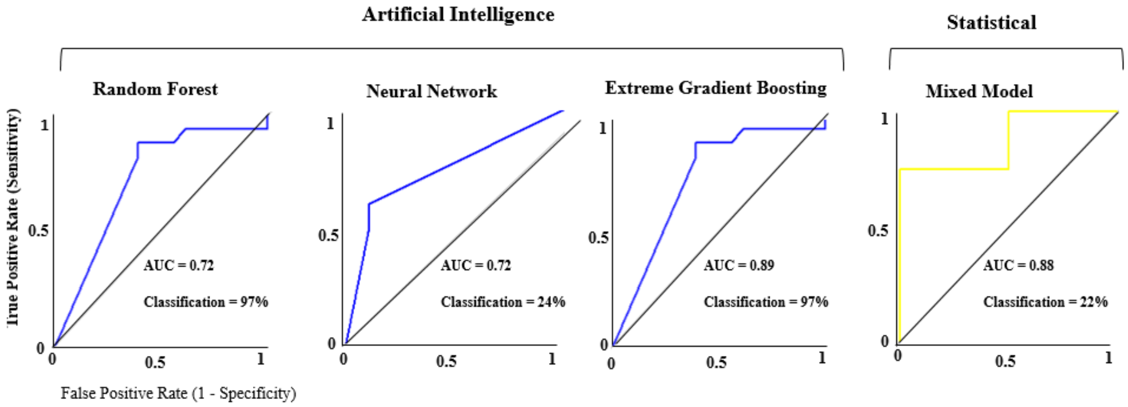

Figure 4.12. *The receiver operating characteristic curve indicates each predictive model's performance, using physicochemistry to predict lead solid phase distribution. This figure illustrates the trade-off between the true positive rate (sensitivity) and the false positive rate (1-specificity) as the model discrimination threshold is adjusted.*

4.3.5 Enhancing Random Forest Machine Learners Predicting PHE Porewater Solubility Using Mechanistic Data

The previous section evaluated different predictive models, using the optimal physicochemical combination (Section 4.3.1) to predict PHE porewater solubility, bioaccessibility, and solid phase distribution, concluding the machine learning random forest models having the highest predictive performance. This section explores the opportunities of training and improving these random forest models, using mechanistic data, derived from VISUAL MINTEQ and PHREEQC to estimate PHE dynamics.

4.3.5.1 Training Random Forests to Address Sorption and Dissolution Kinetics - Visual MINTEQ and PHREEQC

Incorporating mechanistic data into the random forest models significantly improves its correlation and predictive performance of these models for estimating lead porewater solubility. The inclusion of this mechanistic information improved the random forest predictive performance by lowering the testing and training root mean square errors while improving the testing and training correlation coefficient (Figure 4.13). Such mechanistic information shows that the concentration of lead reductively dissolved from iron, manganese, and calcium changes between pH 6 and pH 6.5 (Figure 4.13). Incorporating this mechanistic information increased the model fit (+ R^2 of 0.03). Lead adsorption increased with iron and decreased with manganese concentrations throughout the flood, and there is no change with calcium mineral phases (Figure 4.13).

Specifically, as the flood duration increased, approximately 2.5mol/L of lead was adsorbed onto iron, whereas 2.3mol/L of lead was dissolved from manganese. Such findings also reveal calcium to be a poor predictive variable as the results indicate almost negligible concentrations of lead either dissolving or adsorbing with calcium throughout the flood. For a specific breakdown of how different physicochemistry elements (iron, manganese, and calcium) release and adsorb PHE during different hydrodynamic pressures see such sections below for copper, arsenic, and lead. For an overview comparing the mechanistic predictions with non-mechanistic data for different PHE types, see Figure C6.1, Appendix C.

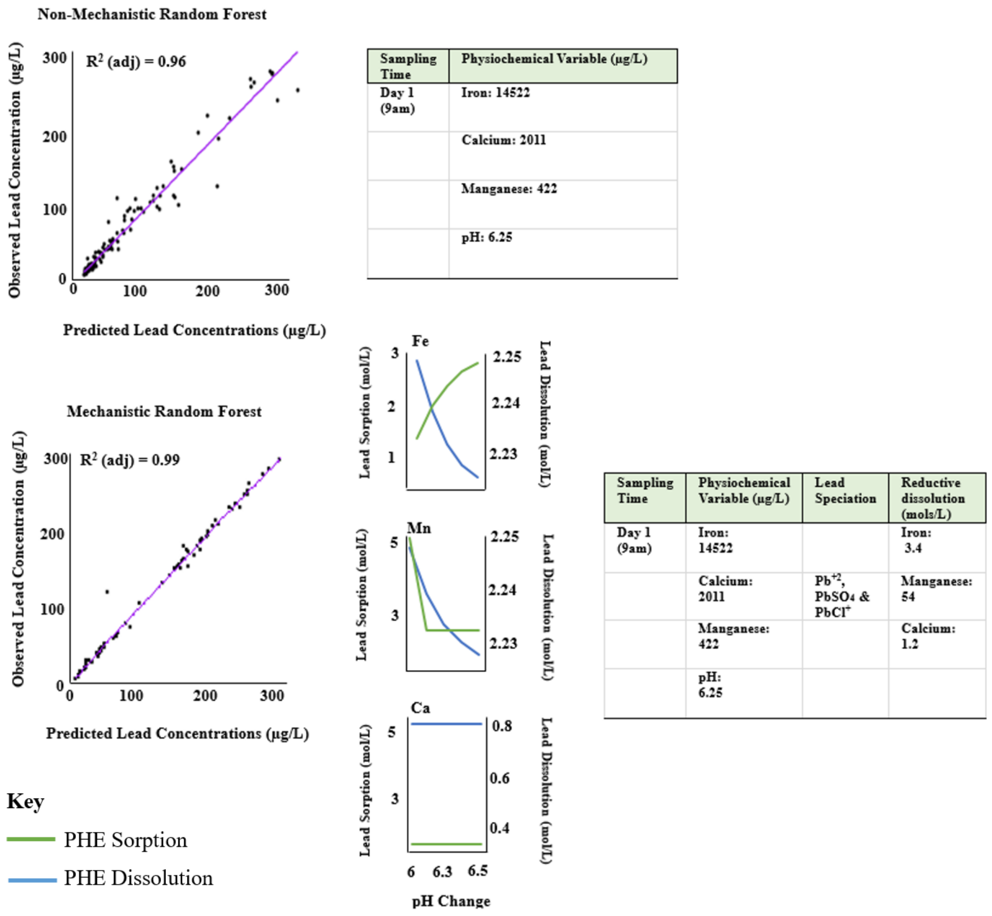

Sampling Time	Physiochemical Variable (µg/L)
Day 1 (9am)	Iron: 14522
	Calcium: 2011
	Manganese: 422
	pH: 6.25

Sampling Time	Physiochemical Variable (µg/L)	Lead Speciation	Reductive dissolution (mols/L)
Day 1 (9am)	Iron: 14522		Iron: 3.4
	Calcium: 2011	Pb^{+2}, $PbSO_4$ & $PbCl^+$	Manganese: 54
	Manganese: 422		Calcium: 1.2
	pH: 6.25		

Figure 4.13. *The effects of incorporating mechanistic speciation and kinetic sorption and dissolution data into the random forest algorithm. Using lead as an example, the figure highlights how lead sorption and dissolution changes with iron, manganese, and calcium during pH changes throughout the flood.*

Iron Ferrihydrite Oxides - VISUAL MINTEQ and PHREEQC Modelling Results

All this data represents Visual MINTEQ model outputs. For example, the physicochemical data, derived from Chapter 3, was inputted into VISUAL MINTEQ. The software then calculated, based from the physicochemistry data, how much, as a concentration, copper, lead, and arsenic during the flood was being adsorbed and dissolved from iron. The output data, indicated below, from VISUAL MINTEQ, could then be incorporated back into the random forest models, allowing the models to train on the physicochemistry data and also this mechanistic data outputs from VISUAL MINTEQ.

Across the three microcosm setups, representing the three sampling locations across the Clyde, the pH was recorded, investigating the magnitude of the pH change from the beginning to the end of the flooding experiments. The pH within sampling location One from the beginning to the end of the flood increased from pH 6 to pH 6.5, sampling location Two from pH 5.6 to pH 6.4, and sampling location Three from pH 4.4 to pH 6.0. These pH changes were not manipulated or altered, rather, these pH changes were a natural outcome of the flooding conditions. These findings are consistent with the wider literature, which shows flooding increasing water and soil ambient pH conditions (Ponting et al 2021, Konsten et al 1994, Xiao et al 2021, Xie et al 2018).

This data (denoting the microcosm pH changes) were implemented into PHREEQC. The PHREEQC outputs show the incremental pH changes, observed within sample locations One, Two, and Three, directly increased the modelled copper sorption onto ferrihydrite by 4.8%, 91%, and 63%, respectively (Figure 4.14). In other words, the microcosm pH increases throughout the flood within all the sampling locations indicate from the PHREEQC model that copper is speciating more with ferrihydrite with increasing flood duration because of this pH increase. The implication of such findings show the importance of random forest models accounting for the increasing pH conditions increasing copper sorption with ferrihydrite.

Moreover, the pH increase from the microcosm setups One, Two, and Three show PHREEQC modelled lead chemical sorption onto ferrihydrite also increasing by 1.8%, 2.1%, and 27%, respectively. Arsenic exhibited the opposite effect, with the modelled Arsenic dissolution concentrations increasing within all the sampling locations during an incremental pH increase. Such findings highlight that any predictive modelling should account for lead and copper's sorption with ferrihydrite and the dissolution of arsenic from ferrihydrite. These results can use such percentages from PHREEQC outputs, representing as concentrations and apply correction factors to the modelled concentration to estimate change.

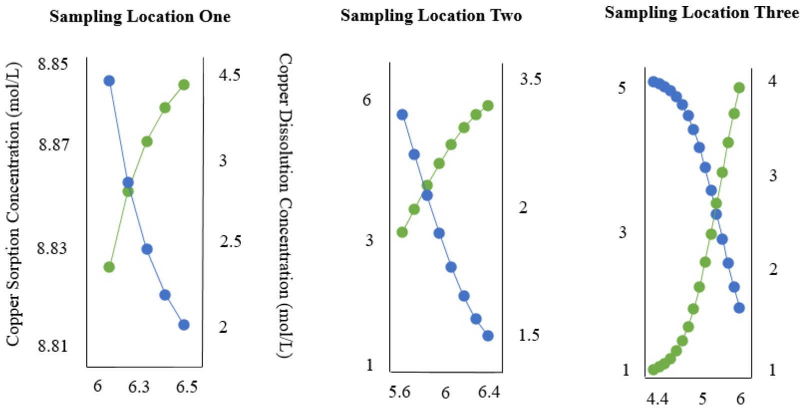

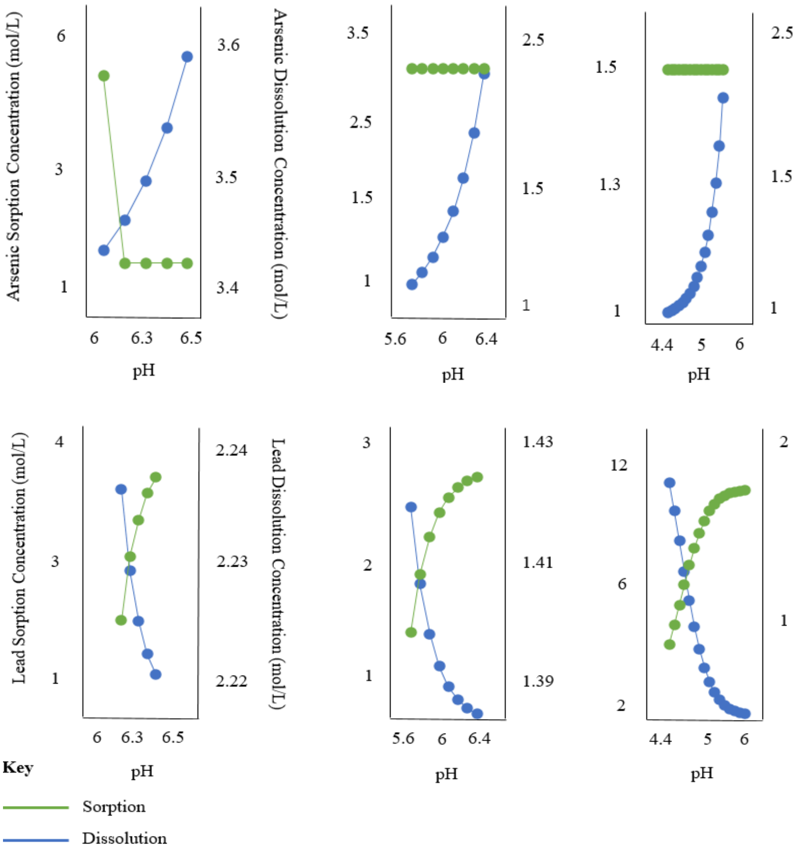

Figure 4.14. *Outlines the Visual MINTEQ outputs indicating the effects of increasing pH conditions and pressure differences during flooding influencing the adsorption (green) and dissolution (blue) of arsenic, copper and lead ions from iron oxides.*

Manganese - VISUAL MINTEQ and PHREEQC Modelling Results

The data from Chapter 3 indicating the physicochemical changes during flooding were inputted into VISUAL MINTEQ to assess copper sorption and dissolution with different soil mineral phases. The differences between sampling locations One, Two and Three represent the study locations for assessing flooding on PHE dynamics across the Clyde catchment. These locations are physicochemically different, analysing the implications of changing physicochemical conditions of PHE dynamics. This section aims to investigate how flooding influences copper sorption and dissolution with manganese across these physicochemically different locations using Visual MINTEQ software.

Copper’s sorption onto manganese oxides increased under more alkaline conditions by 1.3%, 1.5%, and 1.3%, respectively; however, the sorption stabilised at pH 5.5. 5.7, and

5.2, respectively (Figure 4.15). The sorption of metals and metalloids onto manganese oxides differed under incremental pH increases during flooding. Copper sorption onto manganese oxides averaged only 0.01%; lead sorption decreased by 4.4%. Such values are negligible, concluding that these metals have minor associations with manganese oxides regarding sorption kinetics.

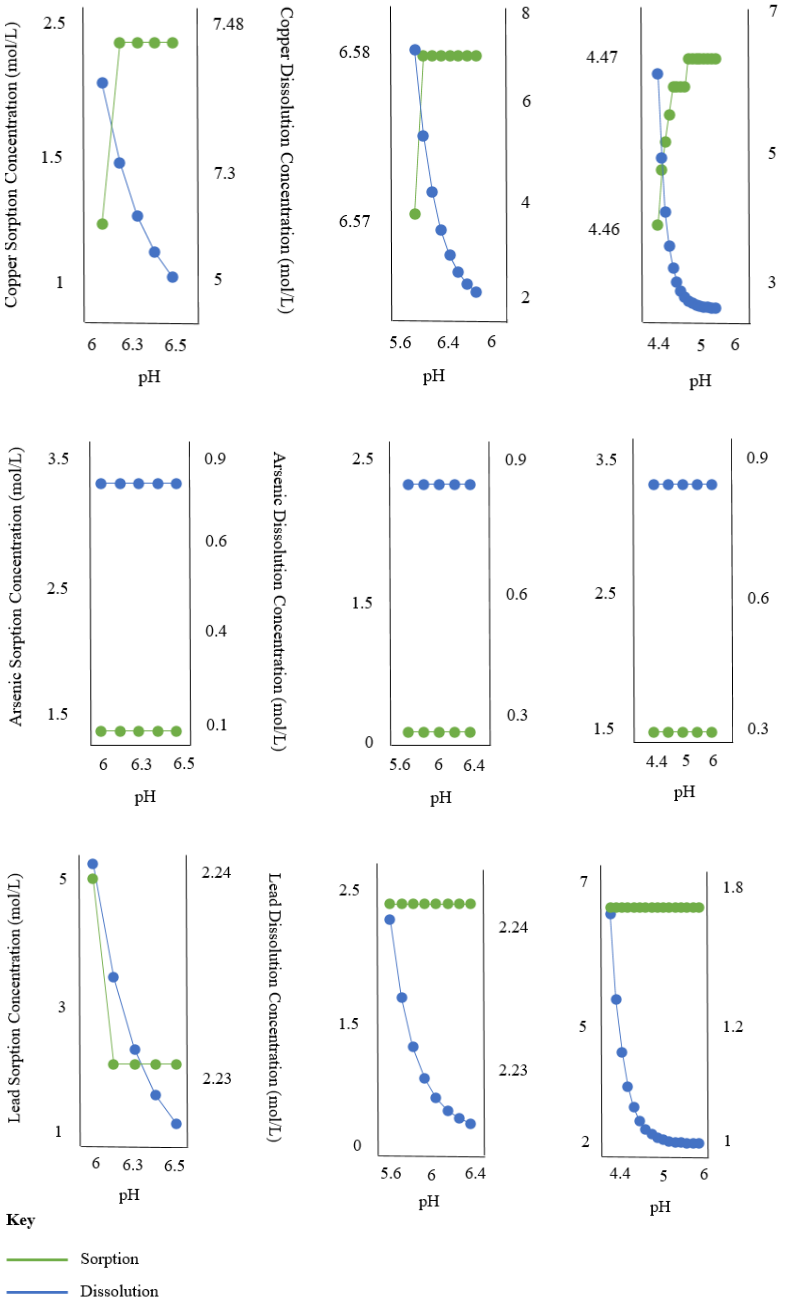

Figure 4.15. *Outlines the Visual MINTEQ outputs indicating the effects of increasing pH conditions and pressure differences during flooding influencing the adsorption (green) and dissolution (blue) of arsenic, copper and lead ions from manganese oxides.*

Carbonates - VISUAL MINTEQ and PHREEQC Modelling Results

The term “carbonates” is a mineral phase defined within this investigation as calcium carbonate. The results showed that increasing the pH does not influence the adsorption and dissolution kinetics of the investigated metals and metalloids with calcium carbonate (Figure 4.16).

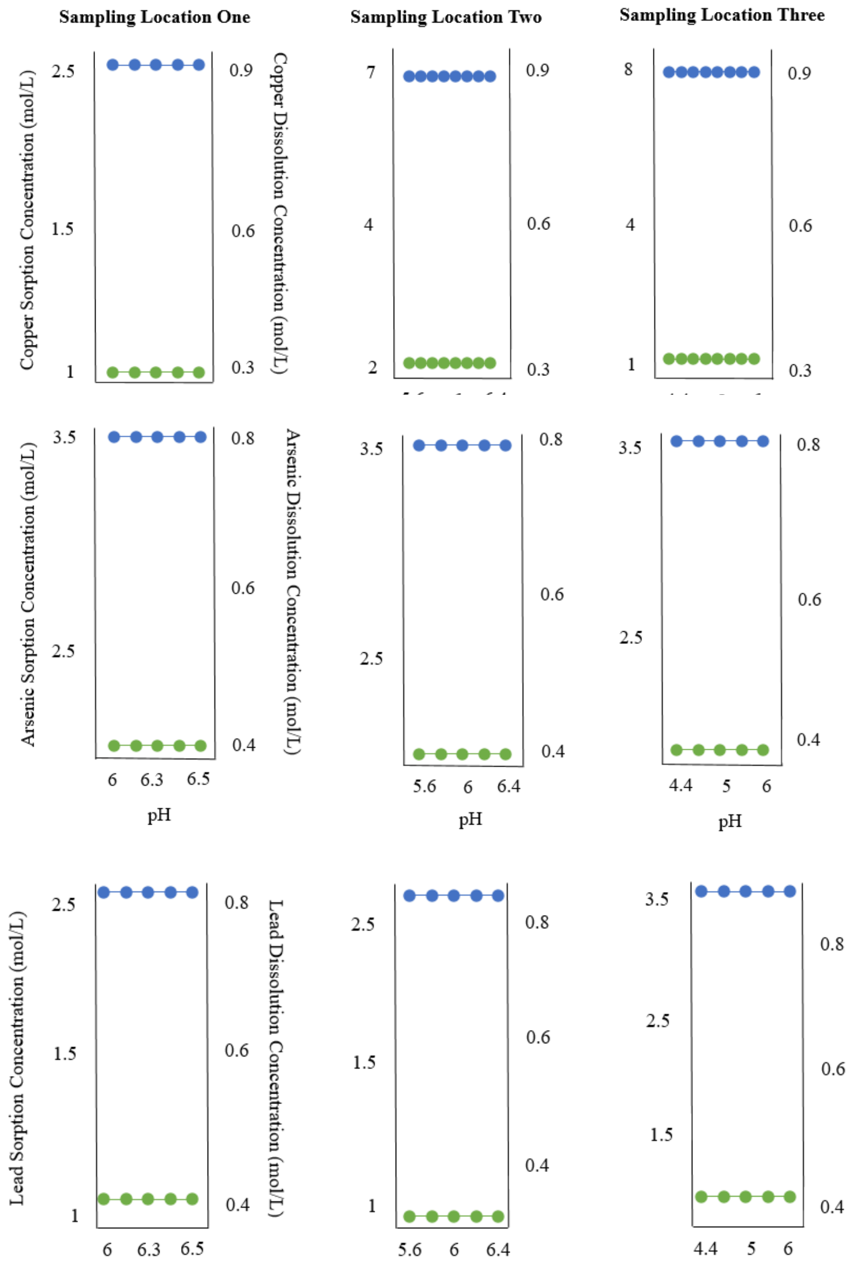

Figure 4.16. *Outlines the Visual MINTEQ outputs indicating the effects of increasing pH conditions and pressure differences during flooding influencing the adsorption (green) and dissolution (blue) of arsenic, copper and lead ions from calcium carbonate.*

4.4 Discussion

4.4.1 Predicting PHE Porewater Solubility

All the predictive models performed well when estimating PHE porewater solubility, emphasising the role using AI and physicochemistry could play as predictive tools. The results indicated that decision-tree models performed better for estimating PHE porewater solubility. The higher performance is attributed to the capabilities of addressing feature interactions, non-linear relationships and high robustness (Genuer et al 2010). Random forests predict using multiple decision trees, training on different subsets of the data (i.e., sampling by replacement), which average out the complex non-linear relationships (Breiman 2001).

The mechanism of feature randomisation in the splitting of data within AI approaches meant specific "important" variables were not prioritised (Probst et al 2019). By avoiding the prioritisation of such features, the model can understand intricate interactions between non-significant relationships, minimising the model bias towards a select few variables and reducing generalisation errors (Ding et al 2020). Feature randomisation improved the predictive performance, by training the random forest model to account for all potentially relevant predictor variables, which statistical models and artificial neural nets may ignore as they assume all the variables are inherently linear (Huang et al 2021). Probst et al (2019) showed that the feature randomisation mechanism of decision tree learners identified complex feature interactions within environmental data because it ignored competing and highly correlated variables.

This study by Probst et al (2019) supports the findings from this study, concluding that because random forests have inbuilt mechanisms to ensure randomness in analysing the data (i.e., feature randomisation), the model has less tendency to predict using unreliable predictor features. In other words, if there are only a few “dominant” feature variables influencing a PHE mobility (e.g., pH), then by randomly selecting other features to train on, the model avoids placing too much emphasis on pH and omitting other important intricate relationships influencing PHE mobility asides from the pH. Such “feature randomisation” outlined in Probst et al (2019), and indicated in Section 4.3.2, demonstrate the high confidence and reliability of training random forest models on extensive databases (e.g., BGS G-BASE) to predict PHE mobility because such models are “learning” differently from other predictive models. In other words, the feature randomisation metric means the model learns more intricately and is less likely to focus on a select few “dominant” variables.

4.4.2 Predicting PHE Bioaccessibility

The results indicate that machine-learning random forests provides the highest and most reliable predictions for estimating a PHE bioaccessibility. Such findings may derive from the linearity of the data, feature importance, and sample size (McLaren 2019).

Physicochemical interactions with PHE operate nonlinearly. By “nonlinear,” there are no direct correlations between the two variables (e.g., increasing calcium concentrations decreasing iron concentrations) (Sun et al 2019). Deep neural networks contain hidden layers that can address data nonlinearly, especially deep nonlinear relationships, where dozens of physicochemical features may interact to produce an outcome (Ponting et al 2021). By “deep nonlinear relationships,” this means the neural network can account for intricate multilayered correlations between multiple variables (Abdolrasol et al 2021). For example, under a hypothetical flooding scenario, the flood lowers the redox conditions, which increases sulfide clustering with lead and copper; however, increases arsenic’s solubility because of the competitive ion exchanges with sulfide. This “competitiveness” then increases arsenic solid phase distribution with calcium, forming calcium arsenate. Under this hypothetical, multiple interactions occur at different levels, indicating the “deep nonlinear relationships.”

Machine learning random forests can also handle nonlinear and linear relationships (Hui et al 2012). The findings here reveal that physicochemistry and bioaccessibility are nonlinear; however, the “depth” of non-linearity is “shallow” (Ponting et al 2021). By “depth” and “shallow,” this means that based on the variable importance plots, only a few variables influence the absolute mean square error. Such predictions are not derived from several minor intricately nonlinear dependencies but are dominated by a few nonlinear correlations.

This “shallowness” regarding linearity is captured by random forest better because the individually constructed decision trees investigate linear dependencies between two feature variables, unlike neural nets, which tend to delve deeper, potentially overcomplicating the problem (Sun et al 2019). These findings do not preclude neural nets from serving a purpose in predicting bioaccessibility; instead, the optimal model most likely should involve using a shallow network containing only a single hidden layer (Malik et al 2018). This investigation uses a two-hidden-layer neural network rather than a one-hidden-layer, meaning the neural network does not represent a shallow network. Selecting two hidden layers may offer enhanced predictions by increasing the model's ability to handle more data and high complexity between interacting variables; however, it may overfit the data, leading to lower predictive performance. A future research approach would be to test a one hidden layer neural network and investigate its performance in estimating PHE dynamic changes during flooding.

Machine learning random forests can assess feature importance from its bagging data (Kah et al 2022). This feature importance can train the model to understand important patterns, correlations, and relationships of feature data (Zhang et al 2004). The results indicate that the non-linearity should be "shallow," meaning that if the decision tree can correctly identify the critical variables to reduce the mean square error, the random forest model can better predict by placing more weight on the relevant predictive features (Malik et al 2018). The data size may also not be sufficient for deep learning neural networks to understand such complex patterns (Liu et al 2019). The laboratory work carried out in Chapter 3 used to train this neural network did not produce thousands of rows of training data. Many neural networks require training using thousands of data rows with multiple feature variables to formulate predictions (Abdolrasol et al 2021). Predicting bioaccessibility is likely to be a moderately to high complexity problem, with multiple feature variables to consider, meaning the training data amount needs to increase for the neural net to compete with decision-tree learners (Malik et al 2018).

4.4.3 Predicting PHE Solid Phase Distribution

Estimating PHE solid phase distribution changes during flooding proved significantly more challenging than analysing the chemical mobility and bioaccessibility, perhaps related to the data available and classification problems (Chapter 1, Section 1.7 and Chapter 3, Section 3.4.10) (Grabowska et al 2014). Many models, particularly random forests, and extreme gradient boosters, reliably predicted solid phase distribution; however, the limited training data available in this study hindered the performance of these models (Kebede et al 2021). The CISED procedure data set for estimating the solid phase distribution was significantly smaller than those investigating the mobility and bioaccessibility. Having fewer training data points potentially causes models to miss intricate relationships around how physicochemistry influences PHE solid phase distribution (Hewins et al 2016). Undertaking further speciation tests to increase the training dataset may improve the predictive performance, and reduce the likelihood of a generalisation error (Ponting et al 2021).

Predicting PHE solid phase distribution is a classification problem, whereby to address the issue, models attempt to reduce the entropy (i.e., the Gini Impurity value for decision tree learners) instead of the mean square error (Breiman 2001). This difference means the discrete nature of classification makes predicting more challenging because there is no inherent continuity between the classes (Breiman 2001). Classification problems face the challenges of class imbalance, meaning the different classes are not evenly distributed, making it challenging to learn and generalise as the model may unknowingly through weighted bias, favour a particular class (Grabowska et al 2014). Many discrete classes overlap more than regression problems as they contain poorly defined boundaries, making it challenging for the model to separate classes for predicting PHE dynamics (Ponting et al 2021).

4.4.4. Upscaling Random Forest Predictions

This random forest was trained and tested to predict PHE porewater solubility, bioaccessibility, and solid-phase distribution within microcosm flooding experiments. These small-scale setups, however, are not representative of flooding, given their small spatial scales. It is significantly important to scale up the simulated flooding experiments to represent real flooding conditions. This scaling up involves using greater soil mass and flood water volumes. Scaling-up can alter the heterogeneity of soil used, potentially changing the soil biological community, soil chemistry etc, which are all important for influencing PHE dynamics. The next chapter aims to explore testing these trained random forests to predict PHE dynamics across larger-scale flooding setups - mesocosm experiments.

This chapter has explored predicting PHE dynamics within a select few locations across the Clyde catchment, anticipating scaling up and testing this random forest to predict across a few locations in the Humber, which has very different soil chemistry characteristics. The concept of training and testing the random forest across varying soil chemistries aims to build a general-purpose predictive model, which can estimate PHE dynamics across multiple catchments. Given the significant heterogeneities in land use characteristics, soil chemistry, flood type etc, training a random forest on data representative of all such varying conditions is significantly challenging, emphasising the importance of selecting locations very different physiochemically.

The mixed model indicated the weakest predictive performer for estimating PHE porewater solubility, bioaccessibility, and solid-phase distribution. These findings indicate that while mixed modelling is highly effective for handling fixed and random effects and managing pseudoreplication, scaling up to predict such PHE dynamics using mixed models would not be appropriate. Mixed models often assume linear relationships between the predictor variables and outcomes; however, many of the relationships between physicochemical changes and PHE dynamics are non-linear, which may not be captured by the mixed model (Sun et al 2019). While mixed models capture fixed and random effects, they are unable to capture highly dynamic interactions between the fixed and random effects, with multiple variables interacting (Sun et al 2019).

A limitation of this research was the metrics used to evaluate the machine learning and statistical model performances. This chapter focuses on using the R^2 statistic, which measures the proportion of variance in the dependent variable that is predictable from the independent variables. The R^2 does not always fit well for non-linear relationships and does not penalise large errors. The L2 loss is another performance metric, which is the average of the squared differences between the predicted and actual values (Grabowska et al 2014). The L2 statistic penalises large errors and the quadratic nature of the L2 creates a smooth and convex loss surface, particularly useful for gradient boosting optimisation (Grabowska et al 2014). Future research should evaluate the machine and statistical models using a variety of performance metrics, such as L2.

4.5 Conclusion

This chapter aimed to identify which physicochemical parameters are reliable for estimating PHE porewater solubility and bioaccessibility. The specific physicochemical parameters include iron, manganese, aluminium, pH, Eh, magnesium, potassium, and calcium. The chapter also explored the effects of testing and comparing different predictive models (i.e., statistical, machine, and deep learning), using physicochemistry information to estimate PHE porewater solubility, bioaccessibility, and solid phase distribution

The optimal combination of physicochemical parameters to predict PHE mobility and bioaccessibility covers different physicochemical groupings (i.e., micronutrients, oxides, and abiotic variables). Specifically, the optimal combination of physicochemical parameters for training all the different modelling approaches used are calcium, iron, aluminium, manganese, pH, and Eh. Predicting a PHE mobility and bioaccessibility using physicochemical variables from one group (e.g., oxides) proves statistically unreliable, exhibiting high testing mean square errors with low correlation coefficients. The machine learners (i.e., random forests and extreme gradient boosters) outperformed statistical and neural networks for estimating PHE porewater solubility, bioaccessibility, and solid phase distribution by exhibiting high predictive performance with low training and testing errors. Training machine learners using mechanistic data slightly improves the predictive performance for estimating PHE porewater solubility.

This chapter shows, for the first time, that incorporating the relevant data into machine-learning random forests, established as the most appropriate predictive model type, can estimate PHE dynamics during flooding. This is measured by evaluating the modelling performance and error metrics within the training and testing datasets. The results offer a novel approach for future research to identify locations susceptible to future flooding from climate change and estimate, using the location's baseline soil physicochemistry, to predict future PHE dynamic changes. Predicting PHE dynamics using physicochemistry requires appreciating the intricate physicochemical correlations instead of focusing on a select few.

The subsequent chapter (Chapter 5) aims to test the random forest model, trained on the physicochemical and mechanistic data from the Clyde catchment, to predict PHE porewater solubility, bioaccessibility and solid phase distribution during flooding within the Humber. Chapter 5 also verifies the predictive performance of this developed random forest within the River Almond. By testing, this means comparing the random forest testing dataset performance and error metrics with the observed laboratory results carried out in Chapter 3.

Chapter 5: Thesis Structure

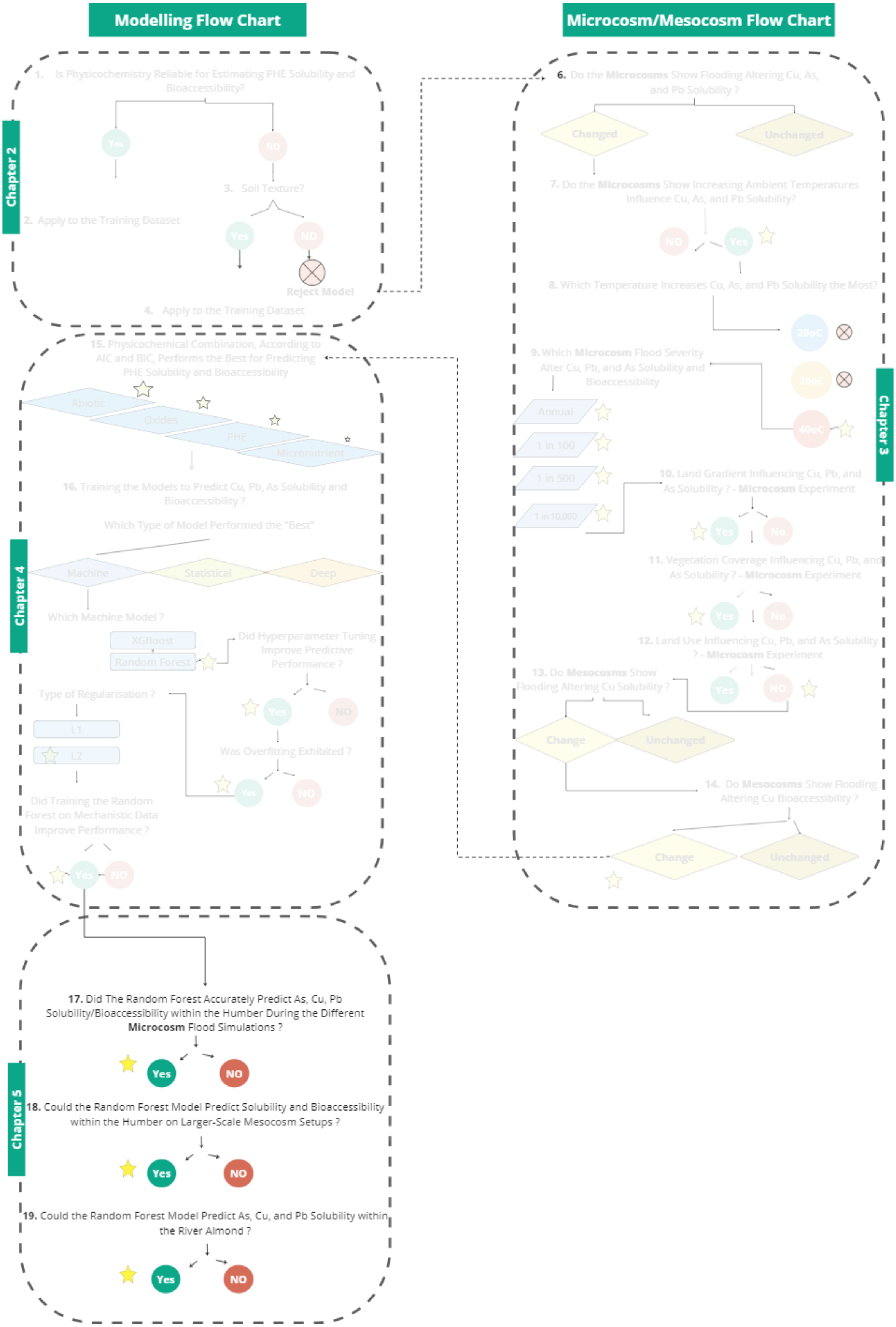

Chapter 5: Testing Random Forest Model Predictions for Estimating PHE Porewater Solubility, Bioaccessibility, and Solid Phase Distribution

5.1 Introduction

Increasing temperatures from climate change can significantly influence microbial activities, such as decomposition and respiration, which can alter soil biogeochemical processes (e.g., nutrient cycling) (Szuskiewicz et al 2021). These altered soil biogeochemical processes may influence PHE solubility in soil porewater, bioaccessibility, and solid phase distribution (Sorenson et al 2019). For example, higher temperatures may enhance soil organic matter decomposition, reducing the ability of organic humic substances and fulvic acids to adsorb PHE (Koh et al 2021).

The UK, along with many other locations worldwide, is also currently facing increasingly severe and more frequent flooding, with increasing economic costs ensuing for flood protection and mitigation (Figure 5.1; Met Office 2020). More flooding also has opportunities, like with higher ambient temperatures, to significantly alter PHE dynamics. For example, flooding alters soil redox potentials, pH levels, organic matter contents, and oxygen concentrations, significantly influencing PHE porewater solubility, bioaccessibility, and solid phase distribution (Koh et al 2021). For a detailed analysis of why flooding influences soil physicochemistry, and how this influences PHE dynamics, see Chapter 1, Sections 1.8.1, 1.8.2, 1.8.3.

Increasing temperatures and more frequent and severe flooding may result in significant changes in soil physicochemistry unseen before (Koh et al 2021). Many studies have highlighted that the coupling of higher temperatures and more frequent flooding may create the "perfect storm" of increasing PHE solubility and bioaccessibility (Coro et al 2021, Kilunga et al 2017, Kumar et al 2021, Ponting et al 2021, Roe et al 2015). This "perfect storm" may also influence oral exposure to soil PHE (Cave et al 2011, Ng et al 2015, Mclaren 2019, Mehta et al 2020, Ponting et al 2021). Exposure to such PHE, for example, lead, can have severe neurotoxic health consequences, with correlations of lead exposure with stunted growth and neurological development (Gamboa et al 2023). For a detailed analysis of why the soil physicochemistry influences PHE bioaccessibility and oral exposure, see Chapter 1, Section 1.9.1.

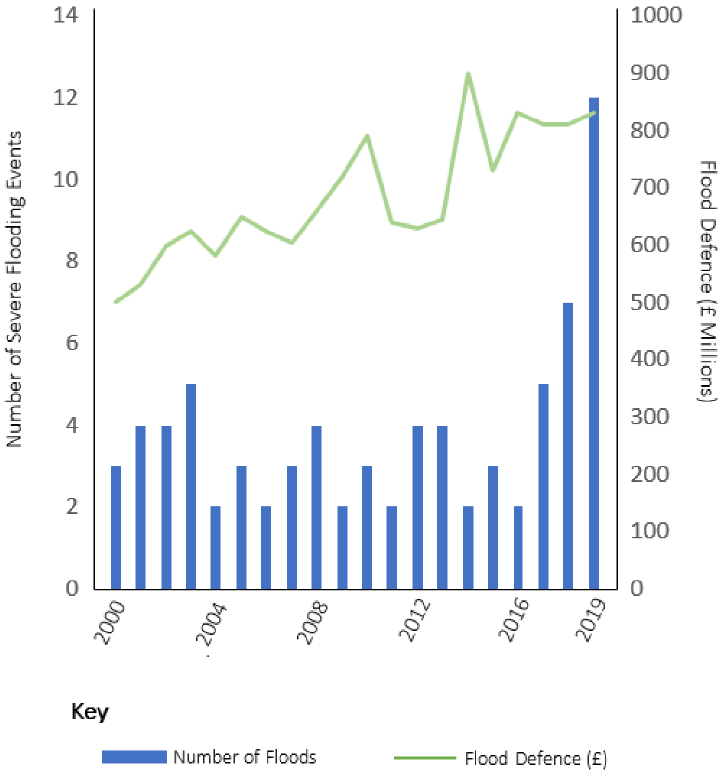

Figure 5.1. *Number of recorded flooding events (blue bars) with the associated economic costs of flood defence (green line) within the UK between 2000 and 2019 (blue bars) (Met Office 2020).*

The previous results from Chapters 3 and 4 show the opportunities of using soil physicochemical information to predict PHE porewater solubility, bioaccessibility, and solid phase distribution. Chapter 4 highlights the significance of machine learning random forest models predicting PHE porewater solubility, bioaccessibility, and solid phase distribution using soil physicochemical data.

The purpose of this chapter is to test the reliability of this random forest model for predicting PHE porewater solubility, bioaccessibility, and solid phase distribution during flooding. The previous chapter trained the random forest model using soil physicochemical data from the Clyde catchment, which contained acidic clay-textured soil. This chapter tests the predictive performance of the random forest model to predict PHE dynamics within the Humber catchment, which contained alkaline and sandy textured soil that was very different physicochemically from the Clyde. After testing the random forest model within the Humber, this chapter finally verifies the random forest model predictions within three sampling locations along the embankment of the River Almond, which all contain silt-textured soils with a slight pH alkalinity.

5.2 Chapter Aims and Objectives

The aim of this chapter is to test the reliability of the trained random forest model to predict PHE porewater solubility, bioaccessibility, and solid phase distribution within (1) small-scale microcosms and (2) larger-scale mesocosms with soils taken from the Humber catchment. This chapter then (3) verifies the random forest model predictions along sampling points across the embankment of the River Almond. Briefly, this chapter begins by testing this random forest model to predict PHE dynamics within the Humber and then verifies the predictions within the River Almond.

The main aim of this chapter is to test the random forest predictions within the Humber and then verify the predictions along the River Almond. For information on how each research aim relates to the thesis flow chart, the experiment design of each research aim, and the PHE types being investigated, see Table 5.1.

Table 5.1. *Outlines the how the chapter's research aims relate to the different thesis structure. The table indicates that all the testing of the model predictions were performed within the Humber, investigating lead and copper soil porewater solubility, solid phase distribution, and bioaccessibility changes.*

Research Aim	Flow Chart Part	Catchment	PHE Investigated	Experimental Type
1	17	Humber	Copper	Microcosm
2	18	Humber	Copper	Mesocosm
3	19	River Almond	Copper, Lead, Arsenic	Microcosm

5.3 Methods

5.3.1 Sampling Locations

All the experimental analyses, including the microcosms, mesocosms, BARGE, and CISED, were conducted within the Humber and the River Almond (see Section 3.2.2, Chapter 3). PHE porewater solubility, bioaccessibility, and solid phase distribution were investigated within three sampling locations across the Humber and River Almond. Each of the three sampling locations within the Humber and River Almond were physicochemically different, which was determined using QGIS (see Section 3.3.1, Chapter 3). The purpose of selecting physicochemically different sampling locations was to test the random forest model's predictive ability within various physicochemical conditions.

5.3.2 Microcosm Experiment

The soil collected were dried at 105°C for 48 hours and mixed for 10 hours using a mechanical end-over-end rotator (15 rpm). The soil was then sieved to a < 6.3 soil particle fraction. For information about why this particle size fraction was selected, see Chapter 3, Section 3.3.4. Approximately 250g ±10 of the mixed soil (< 6.3 soil particle fraction) from each sampling location were placed into one-litre microcosm containers in a sealed incubator at a constant ambient temperature of 21°C. The soil placed in these microcosms underwent a one-week pre-incubation. Essentially, the soil microcosms were untouched and not flooded for one week to equilibrate microbial respiration following the sieving/homogenisation processes, applying the recommendations by Comeau et al 2018.

The soils were all flooded, following exactly the experimental treatment conducted within Microcosm Design Three (Chapter 3, Section 3.3.6). Briefly, four separate microcosm setups occurred, mimicking different flooding severities (i.e., annual flood, 1 in 100-year, 1 in 500-year, 1 in 10,000-year). The purpose of this chapter's microcosm experiment was to test the random forest model predictions for estimating PHE porewater solubility, bioaccessibility, and solid phase distribution within the Humber catchment across these different flood severities. For a detailed outline of how the microcosm experiments were setup, the different flood severities, and the porewater sample analysis, see Section 3.3.6, Chapter 3. For the River Almond microcosm setups, used to verify the random forest predictions, the microcosm experiment was again set up the same as the Microcosm Design Four (conducted previously within the River Almond), see Section 3.3.7, Chapter 4. Essentially, the setup, experimental analysis, and porewater sampling for both the Humber and River Almond Microcosm experiments followed the same procedures outlined in Chapter 3, with the only difference being that the random forest predictions are being compared to the microcosm results.

5.3.3 Mesocosm Experiment

To test the random forest model to predict PHE solubility, bioaccessibility, and solid phase distribution on larger-scale setups, this chapter simulated mesocosm flooding experiments. These mesocosm experiments were only conducted across the three sampling locations within the Humber catchment. The experimental design (e.g., flood length and porewater sampling) was the same as the mesocosm setup within the Humber in Chapter 3, Section 3.3.7.

5.3.4 PHE Bioaccessibility and Solid Phase Distribution Analysis

The procedure of analysing PHE bioaccessibility and solid phase distribution changes within the Humber was analysed by conducting BARGE and CISED experiments, following the same procedure within Chapter 3, Section 3.3.9 and Section 3.3.10, respectively.

5.4 Results

5.4.1 Testing Random Forest Model Predictions for Estimating PHE Porewater Solubility - A Microcosm Experiment

This section uses microcosm experiments to investigate the random forest predictive performance for estimating copper porewater solubility during flooding. As mentioned, these microcosm experiments were conducted using soil samples from the Humber, mimicking different flooding severities, and were carried the same as Microcosm Design Three (Chapter 3, Section 3.3.6). The random forest predictions were evaluated by comparing such predictions with the porewater solubility of copper established from the microcosms. Specifically, the random forest was trained using the following input features: Ca, K, Na, Fe, Al, Mn, pH, and Eh to predict Cu porewater solubility. A two-tailed t-test was used to compare the statistical differences between the predictions and the microcosm results. The t-test was selected because of the ability to handle large sample sizes and deal with data which is not normally distributed (Kim 2015). For a description of why copper was selected, see Chapter 3, Section 3.3.1. For information on the random forest predictions for estimating other PHE porewater solubility, see Appendices B, C, and D.

There were no statistically significant differences between the random forest predictions and the laboratory microcosm results for estimating copper’s porewater solubility during flooding for all the different flooding simulations (Figure 5.2). These findings show the opportunities of random forest models to predict copper porewater solubility within various flood lengths and severities. However, the random forest predictions frequently overpredicted copper solubility. This overprediction may be attributed to the random forest model slightly overfitting the data (see Chapter 4, Section 4.1.4).

As the flood duration increases for all the microcosm setups, copper porewater solubility decreases. The random forest model captures this trend with the predictions also decreasing with increasing flood length. The random forest predictions align closely with the microcosm results more towards the end of the flood rather than at the beginning. An explanation of why the random forest predictions align more towards the end of flooding may be attributed to the findings from Chapter 3, specifically Figure 3.10. The results in Figure 3.10 show that soil physicochemical changes during flooding are the most significant at the beginning of the flood, with such physicochemical changes decreasing with increasing flood length. Minimal physicochemical changes during the end of flood may simplify predicting copper solubility, since these changes can significantly influence copper solubility.

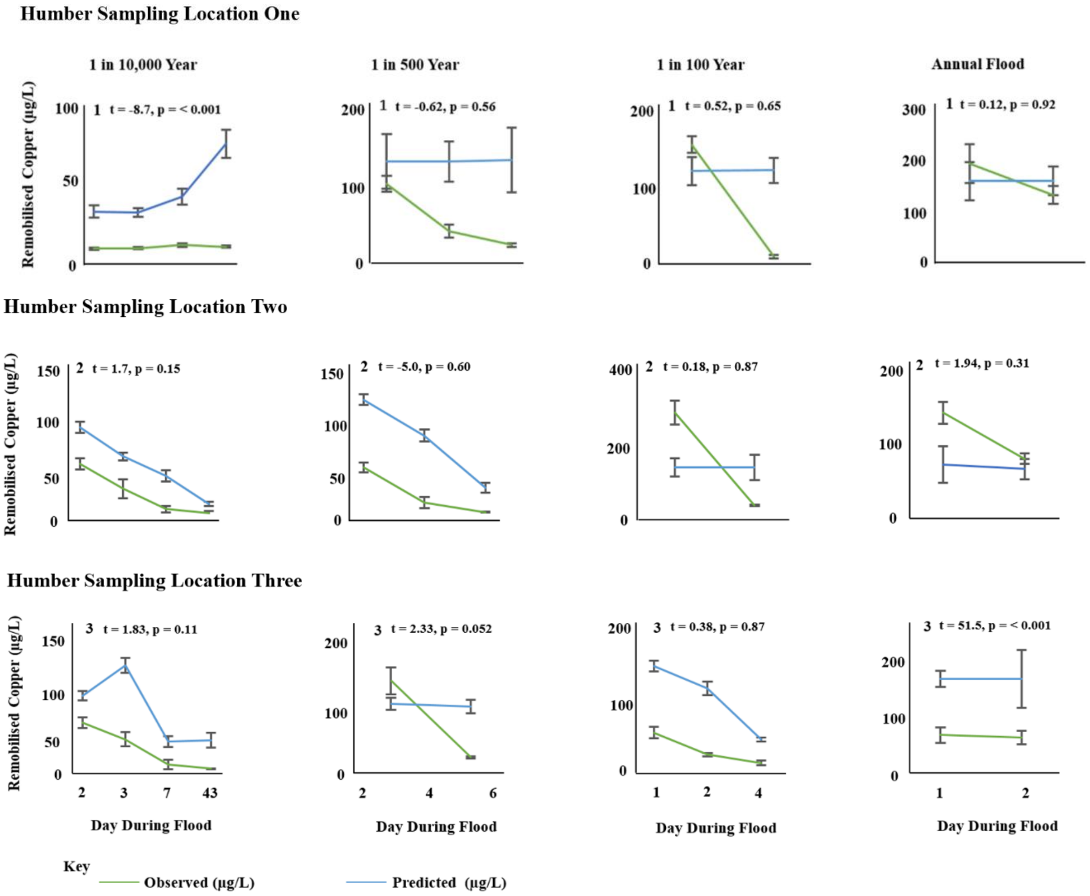

Figure 5.2. *Compares the microcosm results and the random forest predictions for estimating copper porewater solubility within the annual, 1 in 100-year, 1 in 500-year, and 1 in 10,000-year flood simulation experiments. The microcosm results represent the average copper porewater solubility (n=9) with the associated standard deviation bars at the 95% confidence interval. At the top of each figure is*

the two-tailed t-test statistic comparing the statistical differences between the average porewater solubility of copper during the microcosm experiments and the random forest predictions. The number just before the t-test (1-3) indicates the sampling location number.

5.4.2 Testing Random Forest Model Predictions for Estimating PHE Bioaccessibility - A Microcosm Experiment

This section investigated the predictive performance of the random forest model to estimate PHE bioaccessibility across the Humber catchment. The section tests the random forest model using microcosm experiments of varying flood severities, mimicking the Microcosm Design Three setup (see Chapter 3, Section 3.3.6). The random forest model reliability predicted gastric bioaccessible copper concentrations, with no statistically significant differences between the predictions and the microcosm results (Figure 5.3).

The gastric predictions, similar to predicting copper porewater solubility, align closer towards the end of the flood than the beginning. This random forest model also reliably predicted gastrointestinal bioaccessible copper concentrations, with no statistically significant differences between the predictions and the microcosm estimates (see t-test scores above each figure). Predicting gastrointestinal copper concentrations was the most reliable and accurate within the 1 in 10,000-year flood.

This reliability is most likely attributed to this flooding setup having the longest inundation period (43-days), whereby the physicochemical parameters do not change significantly with increasing flood length (see Section 5.4.1 for an extensive discussion). In other words, after a given period (typically five days), during this 43-day flood, physicochemical changes do not vary significantly, which makes predicting PHE bioaccessibility easier after five days. Irrespective of the high variation of gastric and gastrointestinal copper bioaccessibility concentrations, particularly within the 1 in 100-year setup, the random forest model can still reliably predict copper bioaccessibility. These findings conclude the reliability of random forests predicting copper bioaccessibility within different flood lengths and severities. For a complete overview of the results, including for different PHE, see Figure D5.3, Appendix D.

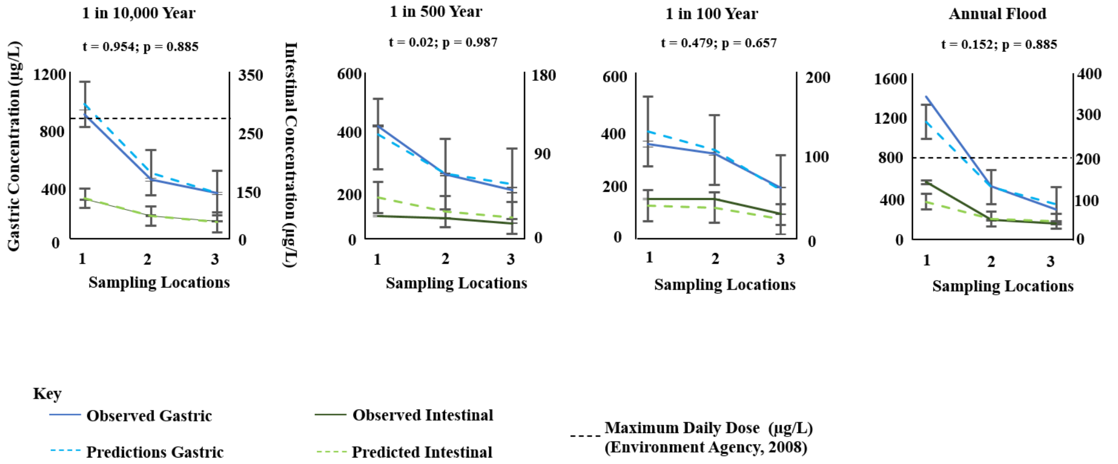

Figure 5.3. *Compares the random forest model predictions with the microcosm results for estimating gastric (blue) and gastrointestinal (green) bioaccessibility concentrations for copper. This comparison is made for the different flood simulation experiments (annual, 1 in 100-year, 1 in 500-year, and 1 in 10,000-year). The BARGE points represent average concentrations (n = 3) with the associated standard deviation bars at the 95% confidence interval. T-test statistics are provided at the 95% confidence interval, comparing the statistical difference between the random forest predictions and the microcosm results. The black horizontal dashed line denotes the maximum daily dose limit of copper (µg/L)*

5.4.3 Testing Random Forest Model for Estimating PHE Solid Phase Distribution - A Microcosm Experiment

The purpose of this section is to investigate the ability of the random forest model to predict copper solid phase distribution during flooding within the Humber catchment across the different flood severities. This analysis only focuses on copper; however, for further information about predicting the solid phase distribution of different PHE types, see Appendices B and D. The aim of this section is to test the random forest model's ability to predict the CISED extraction phase for copper. For example, if the model reliability estimated that the extraction phase was 0.01M, then this gives some insight into copper's solid phase distribution, indicating copper was unlikely to coprecipitate with acid-resistant mineral phases, such as iron oxides (McLaren 2019).

The random forest model reliably predicts copper CISED extraction phase, particularly for lower acid dissolvable phases (i.e., deionised water, 0.01M and 0.05M) within all the flood simulations (Figure 5.4). By reliably, this means the random forest model is predicting the exact same extraction phase compared to the laboratory results. For a detailed explanation of the meaning around the different CISED extraction phases, see

Chapter 3, Section 3.3.10. The random forest model's ability to predict copper coprecipitating with mineral phases, such as residuals, was less reliable. Such findings are unclear as to why the performances for estimating the copper solid phase distribution were unreliable; however, potential data limitations around training the random forest models on solid phase distribution data may explain such results.

This limited training dataset makes it challenging for the random forest model to learn intricate relationships and correlations around copper solid phase distribution changes (Boateng et al 2020). These findings highlight the challenges of the random forest model predicting precisely copper's solid-phase distribution (e.g., Cu-Al-Fe, Mg-Cu-Pb); however, despite these challenges, the random forest model can estimate the soil mineral phase that may coprecipitate with copper, such as oxides, carbonates and sulfide. In other words, the random forest model can predict which soil mineral phase copper coprecipitates with (e.g., sulfide); however, has challenges predicting copper's speciation within that mineral phase in more detail (e.g., Cu-Al-Fe).

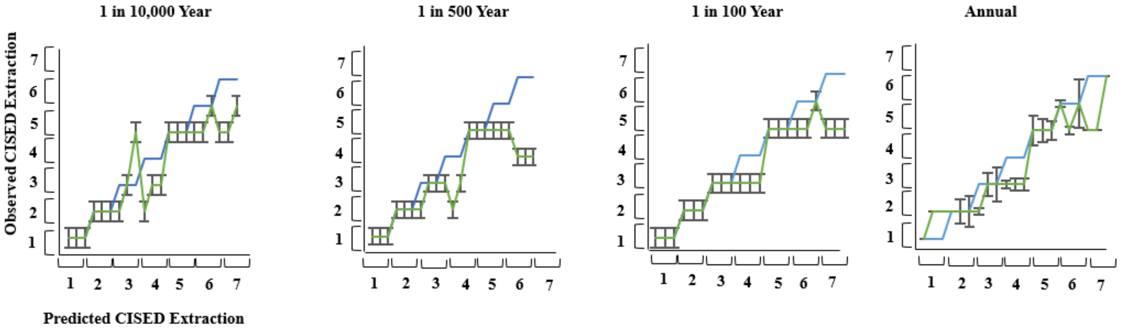

Number	Sequential Extraction (Aqua Regia Molarity)
1	Deionised Water
2	0.01M
3	0.05M
4	0.1M
5	0.5M
6	1M
7	5M

Key

🟩 Observed

🟦 Predicted

Figure 5.4. *Compares the AI predictions for estimating the CISED extraction phase with the laboratory results. The error bars represent the averages at the 95% confidence interval (2 standard deviations). Predicting the extraction phases means the random forest model can estimate which extraction phase will leach a particular PHE. For example, the AI predictions successfully predicted in the 1 in 500 treatment that copper was extracted from the deionised water phase. Such information on the extraction phase of a particular PHE does not determine its solid phase distribution; rather, it indicates the mineral phase the PHE coprecipitates. In the case of extraction from deionised water, these copper species were unlikely to speciate with oxides resistant to high acid strengths.*

5.4.4 Testing Random Forest Model Predictions for Estimating PHE Porewater Solubility - A Mesocosm Experiment

This section analyses the random forest models' predictive performance for estimating copper porewater solubility within large-scale mesocosms. The previous section (5.4.1) showed the reliability of random forests predicting copper porewater solubility within small-scale microcosms. This experiment tests the random forest predictions to estimate copper porewater solubility using larger-scale setups. As mentioned in Section 5.3.3, this mesocosm experiment was conducted within the Humber catchment. For information about the mesocosm design, such as the descriptions for treatments 1-6, see Chapter 3, Section 3.3.6.

The random forest predictions aligned with the mesocosm results, with almost all treatments (1-6) showing no statistically significant differences between the random forest predictions and the mesocosm results (Figure 5.5). Almost all the t-test statistics exceed $p > 0.05$ (see above each figure), indicating no statistical differences between the predictions and the mesocosm results. These findings highlight the reliability of training random forest models to predict PHE porewater solubility during flooding within large-scale setups. Unlike the microcosm setups, the random forest predictions typically underpredicted copper porewater solubility. This random forest model was originally trained to predict copper porewater solubility using data from small-scale microcosm experiments. Training the random forest model on smaller-scale setups may mean the random forest minimises copper solubility concentrations by not appreciating the larger spatial scale.

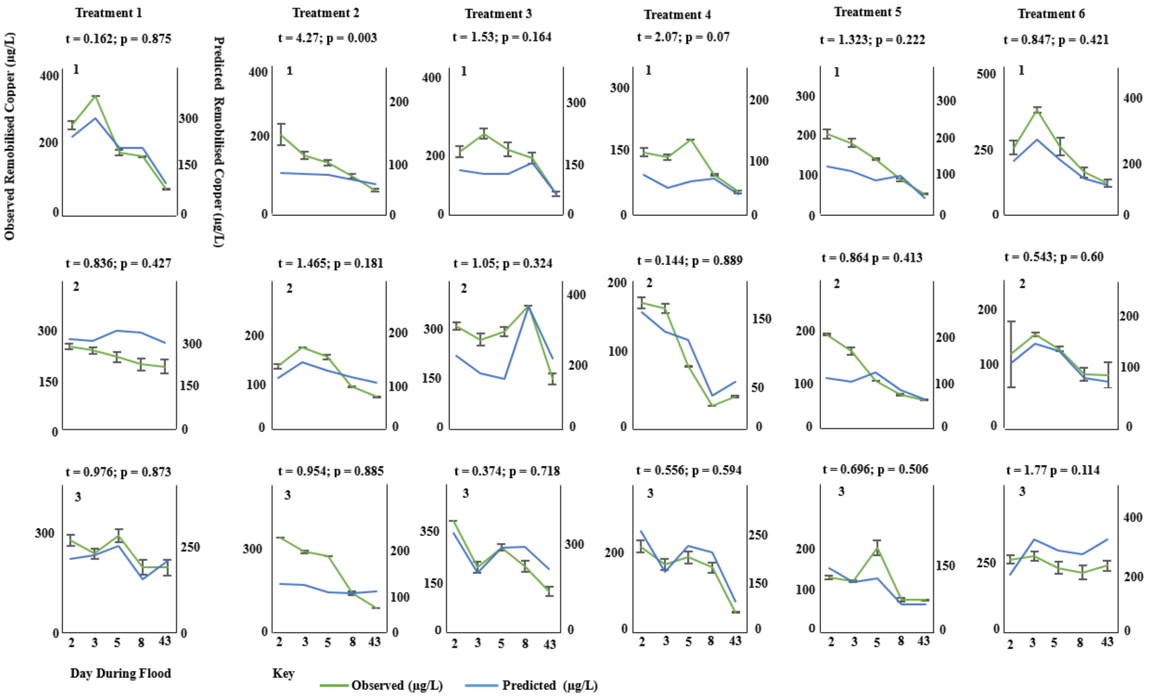

Figure 5.5. *Outlines the mesocosm results investigating copper porewater solubility across sampling locations 1-3 for the different treatment groups (1-6). For information about what each treatment group means, see Section 3.3.6, Chapter 3. The mesocosm results indicate copper porewater solubility averages (n=9) at the 95% confidence interval, with the associated standard deviation bars indicating the spread of data from the average. This figure outlines the mesocosm results for copper porewater solubility, which is indicated in green. The random forest model predictions are indicated in blue. The "t" value denotes the two-tailed t-test results, comparing the observations with the predictions at the 95% confidence interval.*

5.4.5 Testing Random Forest Model Predictions for Estimating PHE Bioaccessibility - A Mesocosm Experiment

In Section 5.4.3, the random forest model estimated copper bioaccessibility within three sampling locations across the Humber under the different flood severities (i.e., annual, 1 in 100-year, 1 in 500-year, 1 in 10,000-year). The previous section showed the reliability of the random forest model in predicting copper bioaccessibility within the different flood severity experiments. This section tests the random forest model predictions for estimating copper bioaccessibility within larger-scale mesocosms (see Section 3.3.8, Chapter 3 for further information). For information about the experimental design of the mesocosm experiments, including what Treatments 1-6 mean, see Chapter 3, Section 3.3.6.

There were no statistically significant differences, according to the t-test estimates, between the random forest model predictions estimating copper bioaccessibility within many of the mesocosm setups (Table 5.2). These findings conclude the reliability of random forest models, trained using physicochemical data, to estimate copper bioaccessibility within larger-scale setups. Predicting copper bioaccessibility post-flooding was more challenging, with some of the random forest predictions being statistically significantly different from the mesocosm results, particularly within Treatments 3 and 6 (t = 2.32, p = 0.001; t = 0.689, p = <0.001, respectively). Treatments 3 and 6 contained the highest ambient humidity levels (95%), potentially altering copper bioaccessibility, which the random forest model does not account for. These findings reveal the random forest model estimates better copper bioaccessibility during flooding rather than post-flooding. The results are unsurprising because much of the physicochemical data the random forest models were trained on were collected during a flood instead of during the drying phase.

Table 5.2. *Outlines the random forest model predictions for estimating copper bioaccessibility within the six treatment groups (T1-T6), comparing such predictions with the BARGE laboratory results. The six treatment groups represented the different flooding conditions. Treatments 1-3 mimicked real flood data for a ten-day flood, indicating the temperature and humidity fluctuations. The difference between such treatments was the humidity levels (35%, 65% and 95%). Treatments 4-6 mimicked the exact flood with fluctuating humidity levels (35%, 65% and 95%); however, the only difference was throughout the day and night, there was a 1.5ºC temperature increase.*

Treatment	Design	Phase	BARGE Mesocosm	BARGE Prediction	T-Test	One-Way ANOVA
1	Ambient Temperature	Flooding	418 µg/l	831 µg/l	t = 1.25; p = 0.279	F = 1.56; p = 0.28
	35% Humidity	Drying	355 µg/l	574 µg/l	t = 0.908; p = 0.415	F = 7.71; p = 0.416
2	Ambient Temperature	Flooding	169 µg/l	578 µg/l	t = 1.09; p = 0.386	F = 18.51; p = 0.39
	65% Humidity	Drying	183 µg/l	506 µg/l	t = 2.03; p = 0.112	F = 7.71; p = 0.11
3	Ambient Temperature	Flooding	151 µg/l	432 µg/l	t = 3.21; p = 0.232	F = 12.2; p = 0.43
	95% Humidity	Drying	182 µg/l	521 µg/l	t = 2.32; P = 0.001	F = 13.6; P = 0.002
4	+ 1.5ºC	Flooding	153 µg/l	452 µg/l	t = 4.32; P = 0.543	F = 2.12; P = 0.622
	35% Humidity	Drying	321 µg/l	389 µg/l	t = 2.11; P = 0.984	F = 1.34; P = 0.872
5	+ 1.5ºC	Flooding	421 µg/l	502 µg/l	t = 3.11; P = 0.482	F = 4.21; P = 0.352
	65% Humidity	Drying	643 µg/l	421 µg/l	t = -4.21; P = 0.422	F = 3.21; P = 0.657
6	+ 1.5ºC	Flooding	503 µg/l	932 µg/l	t = 0.321; P = 0.211	F = 0.454; P = 0.421
	95% Humidity	Drying	532 µg/l	1002 µg/l	t = 0.689; P = <0.001	F = 0.492; P = 0.003

5.4.6. Verifying the Random Forest Model Estimating PHE Porewater Solubility - The River Almond

The random forest model was verified to predict copper, lead, and arsenic porewater solubility within the three sampling locations along the embankment of the River Almond (Figure 3.5, Chapter 3). These three sampling locations have different land gradients (4.35°, 7.22°, and 16°) and vegetation coverages (35%, 55%, 90% per $1m^2$). For information about each location's physicochemistry, total soil PHE concentrations, why the River Almond was selected, and the microcosm experimental design, see Sections 3.3.3, 3.3.7, and 3.4.1.

No statistically significant differences existed between the random forest predictions and the microcosm results within sampling location One (Figure 5.6). The predictions slightly underpredicted copper and overpredicted lead and arsenic's solubility. The microcosm results for copper exhibited large standard deviations; however, despite these variations, the predictions aligned with the microcosm results ($t = 0.198$, $p = 0.857$).

The predictions did not differ statistically from the microcosm results for estimating lead and arsenic solubility within sampling location Two ($t = 0.322$, $p = 0.154$; $t = 0.322$, $p = 0.433$, respectively). These predictions for lead and arsenic solubility again overpredicted slightly. There were also statistically significant differences between the predictions for estimating copper solubility ($t = 0.356$, $p = 0.04$). These statistically significant differences may be attributed to the steeper land gradient (7.22°). This steeper land gradient exerts a greater gravitational downward force on the flooded water (Marr et al 2001). Steeper land gradients can increase the flow and movement of floodwater, which, as demonstrated with copper, can potentially enhance the remobilisation of various PHE.

The random forest models were originally trained on data within the Clyde catchment, within sampling locations much less steep (< 5°) than across sampling location Two along the River Almond embankment, making it harder for the model to predict on steeper gradients. The challenges arise for the random forest to generalise on unseen data, which are strongly influenced by steep gradients that the random forest did not originally train on (see Section 4.1.2, Chapter 4 for the term “generalise”). For example, using an unrelated hypothetical for illustrative purposes, if the random forest model was only trained to predict arsenic solubility during flooding and was asked to predict zinc solubility, there is a high probability the random forest would fail to generalise; just like predicting copper solubility within steeper land gradients the model is unfamiliar to.

Lead and arsenic within sampling location Three were not statistically different from the microcosm results (t = 4.32, p = 0.564; t = 3.42, p = 0.312). The model predictions slightly overpredicted lead and arsenic solubility throughout the flood. These overpredictions may be attributed to the random forest model overfitting (see Section 4.1.5 for information about overfitting). This overfitting may be attributed to the addition of addressing the land gradient and vegetation coverage, causing the model to become overly complex with too many variables. Overfitting is likely mild, given that the predictions and the microcosm results were not statistically insignificant (Brieman et al 2001).

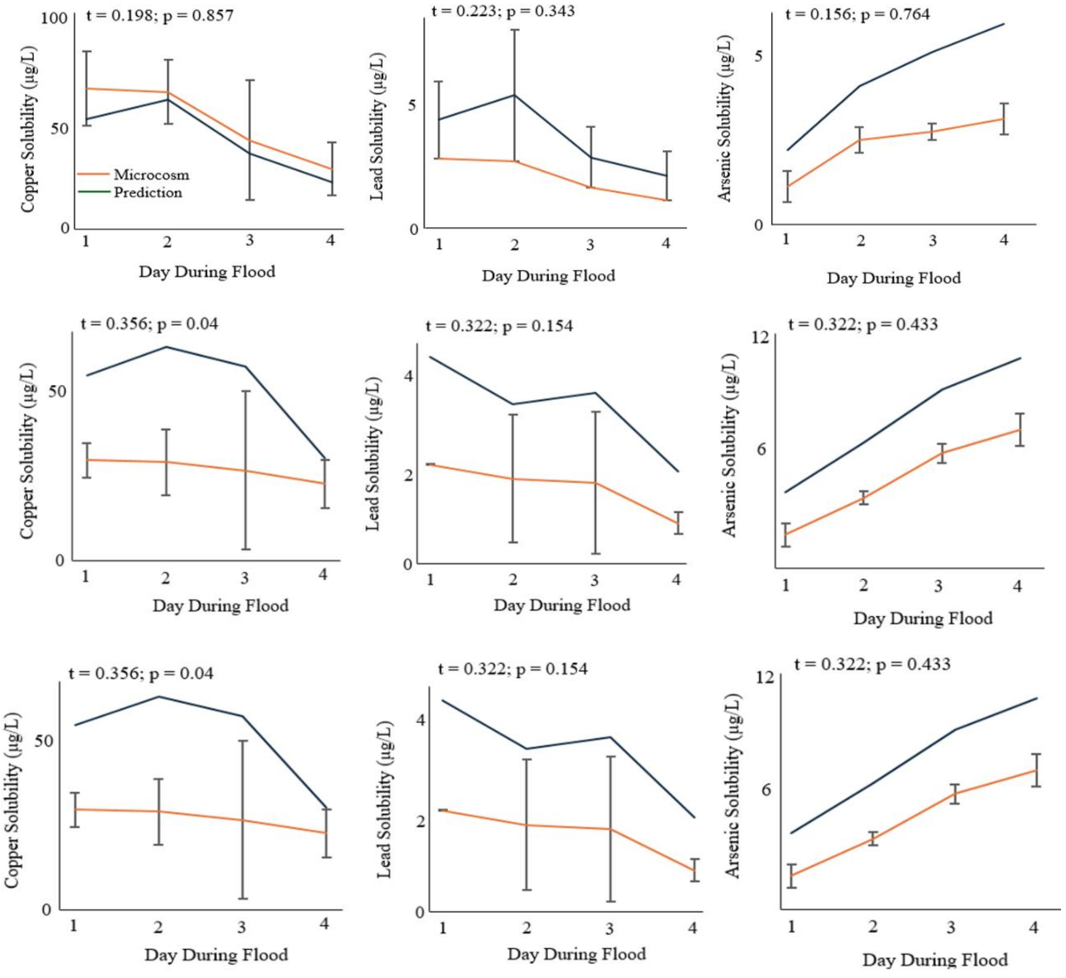

Figure 5.6. *Outlines copper, arsenic and lead porewater solubility within sampling locations One, Two and Three along the embankment of the River Almond. The figure compares the microcosm results, indicating the average copper, arsenic, and lead porewater solubility for each day during the flood (n=9) at the 95% confidence interval). The random forest predictions (blue line) is compared with the microcosm results (orange line) and the statistical difference between the values is indicated using the two-tailed t test statistic.*

5.5 Discussion

5.5.1 Investigating the Predictive Modelling Estimating PHE Dynamics

This chapter tested random forest predictions to estimate PHE porewater solubility, bioaccessibility, and solid phase distribution within microcosm and mesocosm using soil samples from the Humber. Predicting copper porewater solubility, bioaccessibility, and solid phase distribution was highly reliable within the Humber catchment. Such findings reveal the opportunities of training random forests to predict PHE porewater solubility, bioaccessibility, and solid phase distribution during flooding within small and larger scale setups, potentially across multiple river catchments susceptible to regular flooding. However, such predictions, in some cases, overestimated copper porewater solubility and bioaccessibility. From a precautionary approach, for risk assessment purposes, overpredicting the porewater solubility of copper is more reliable than underpredicting. Overpredicting such concentrations avoids misrepresenting or underappreciating the severity of PHE solubility and bioaccessibility, avoiding scenarios of where the random forest model gives the “green light” to locations not at risk which are at risk (Mendes et al 2020).

Overpredicting may introduce additional monitoring costs and resources around issues concerning false positives, or in other words, where the random forest says there is risk where there is no risk (Mendes et al 2020). Such overpredictions may attribute to the random forest model requiring more training data. As discussed previously, the random forest model was trained using the microcosm data obtained from the Clyde, as well as using mechanistic data derived from PHREEQC and Visual MINTEQ (Chapter 3). This data limitation may cause the predictions to generalise, leading to overpredictions (Feng et al 2015). Limited data means the random forest model has challenges learning intricate correlations between soil physicochemistry and PHE porewater and solubility, meaning the model is more likely to predict using limited detail (generalise). Future research must include sampling physicochemical data from other catchments to train further these random forest models, aiming to improve the generalisation of the random forest model. For specific information around “generalisation”, see Chapter 4.

The slight overprediction of the random forest model might attribute to the incorrect decision tree depth and tree size (Brieman 2001). For specific information around the decision tree depth, see Chapter 4; however, briefly, if the models are trained on decision trees which are not “pruned” then the model may overfit the dataset (Lopez et al 2021). By not having the correct decision tree depth, the random forest model will continuously split the training dataset until it minimises the model mean square error close to zero, resulting on overfitting (Sorenson et al 2019).

In other words, the continuous splitting of the training dataset means the random forest model is learning the training dataset significantly well; however, at the cost of failing to generalise well on the testing dataset, leading to overfitting (Sorenson et al 2019). Future research must explore feature engineering to minimise this model from overpredicting (Feng et al 2015, Lopez et al 2021, Sorenson et al 2019, Sun et al 2019). Such feature engineering may include conducting systematic grid searches to identify the optimal combination of hyperparameter tuning variables (e.g., tree depth) (Breiman 2001).

5.5.2 Assessing the Predictive Model Estimating PHE Dynamics on Large-Scale Setups

Three major findings arise from estimating PHE porewater solubility, bioaccessibility, and solid phase distribution from these larger-scale setups. Such findings include that changing humidity levels, and an increasing ambient temperature of 1.5°C, both influence PHE porewater solubility. Irrespective of changing humidity and increasing ambient temperatures, the random forest models can still estimate PHE porewater solubility.

Humidity levels influence PHE porewater solubility, solid phase distribution, and bioaccessibility by influencing soil respiration and the soil redox status (Liu et al 2019). Studies show high humidity levels (>90%) promote soil sulfate formation (De et al 2017, Kukumagi et al 2014, Martin et al 2015, Stewart et al 1995). Liu et al (2019) show that a relative humidity exceeding 90%, enhancing soil sulfate formation. Wang et al (2017) analysed the humidity levels within a Beijing haze, indicating that the humidity can increase atmospheric sulfur, which was transferred into the soil as sulfate, increasing soil sulfate concentrations. Increasing soil sulfate significantly influences PHE dynamics, particularly during flooding as sulfate is transformed into sulfides, eventually forming metal-sulfide complexes (De et al 2017). Soil sulfate increases with humidity by increasing atmospheric nitrogen concentrations, triggering atmospheric sulfur oxidation (Martin et al 2015). The increased atmospheric nitrogen may also inadvertently change the soil pH, influencing PHE dynamics (Ponting et al 2021).

The relative humidity is also known to influence the organic carbon phase, specifically the coprecipitation of PHE with fulvic acids and humic substances (Wang et al 2023). Cabbar (1999) showed an exponential reduction in the adsorption capacity of organic carbon with a humidity increase from 30-90%. Stewart et al (1995) showed PHE coprecipitate less with the organic phase because of the competitive displacement between the water molecule’s hydrogen bonding and the PHE. Such findings emphasise that when flooding recedes, locations with higher humidity levels may alter PHE dynamics differently compared to those with lower humidity levels (Ponting et al 2021).

Higher humidity levels (>90%) showed to increase PHE porewater solubility and bioaccessibility during post-flooding; however, the humidity had no significant influence on PHE dynamics during flooding. Such insignificant effect is because the humidity may decrease such PHE mobility or bioaccessibility by promoting sulfide formation or increase mobility or bioaccessibility by reducing coprecipitation reactions with organic carbon, essentially promoting PHE solubilisation (Ponting et al 2021). The humidity levels also influence soil respiration processes. Kukumagi et al (2014) investigated the elevated humidity levels on soil respiration within a forest ecosystem. Such findings reveal that the relative humidity correlated with gross primary production, influencing soil microbial enzymatic processes. These findings are justified by the humidity limiting oxygen diffusion across soil micropores, increasing microbial oxygen demand (Ponting et al 2021). Nielsen et al (2004) show increasing humidity levels alter the soil bacterial growth and secondary metabolism. Humidity fluctuations inadvertently influence the redox status (Huang et al 2021). Such alterations in oxygen diffusion, microbial oxygen demand, and soil respiration impact soil redox status (McLaren 2019). The redox status significantly influences PHE dynamics, affecting sulfide formation and reductive and oxidative dissolution processes of mineral phases (McLaren 2019).

When using these random forest models for large-scale predictions, potentially integrated with GIS (discussed in the subsequent chapter) it is essential to address spatial heterogeneity within datasets, particularly those derived from models such as G-BASE. G-BASE provides valuable large-scale predictions of soil PHE concentrations (Figure 1.2); however, G-BASE model does not capture sub-grid resolution or variability within the 500 x 500m grid cells provided. Addressing such limitations is important to improve the accuracy and precision of macro-scale predictions, ensuring that the random forest model accurately reflects the inherent spatial heterogeneity of soil PHE dynamics. Future modelling efforts should incorporate methods to account for sub-grid variability to reduce uncertainties when scaling predictions to regional or national levels.

5.6 Conclusion

This chapter aimed to assess and test the reliability of the random forest model to estimate PHE porewater solubility, bioaccessibility, and solid phase distribution within the Humber. This random forest model was not originally trained on any physicochemical data from the Humber, and because the Humber was very different physicochemically from the Clyde, it served as a reliable catchment for testing the random forest predictions. This chapter tested the random forest predictions on microcosm and mesocosm setups. This research aimed to explore the opportunities of combining physicochemical data with random forests to forecast PHE porewater solubility, bioaccessibility, and solid phase distribution changes during flooding reliably.

The data showed the reliability of predicting PHE porewater solubility using these trained random forest models within the microcosm and mesocosm setups. Predicting the bioaccessibility provided reliability; however, it was less reliable during the drying phase of the flood, emphasising the need to train these random forest models on more physicochemical data post-flooding. The random forest model could not predict the exact PHE solid phase distribution during flooding (e.g., copper sulfate, copper chloride). Instead, the random forest measured how copper coprecipitated into broader extraction mineral phases (e.g., oxides), rather than specific mineral phases. This lack of specificity highlights a limitation of the random forest model, likely attributing to the few training data, which impacts the model to generalise to more precise mineral phases.

The data revealed significant findings, particularly around the novelty of using physicochemistry and random forest models to predict future PHE porewater solubility, bioaccessibility, and solid phase distribution changes during future flooding. This chapter calls for further research around cross-validating these random forests on riverine catchments physicochemically different, which are not originally trained on these random forest models. Future research should also examine the role of geospatial analysis to map locations, using these trained random forests, of high vulnerability to PHE mobility and bioaccessibility. Such geospatial analysis may involve extracting a soil's physicochemical data from a known location, using online tools such BGS GBASE, and incorporating such data into these random forests to formulate predictions (BGS 2024).

Chapter 6: Estimating the Effectiveness of Combing Random Forest Models with Geospatial Analysis to Predict PHE Porewater Solubility During Flooding

6.1 Introduction

The influence of anthropogenic climate change increasing flooding's frequency and magnitude poses risks of increasing the mobility and altering the bioaccessibility and solid phase distribution of PHE (Kilunga et al 2017, Nel et al 2018, Peck et al 2004). Exposure to such remobilised PHE, such as lead, arsenic, and cadmium, may cause adverse neurotoxic health effects (Table 1.1, Chapter 1). The influence of flooding altering a PHE solid phase distribution can transform PHE into more toxic forms (e.g., arsenite (III) to more toxic arsenate (V)) (Ponting et al 2021).

Flooding alters a soil and water physicochemistry (e.g., pH, E_H, organic carbon) (Laurent et al 2017). These physicochemical alterations influence a PHE solid phase distribution with soil mineral phases like carbonates, oxides, and residuals (Doherty et al 2022). The purpose of the chapter within this thesis was to determine the correlation between physicochemistry and PHE porewater solubility, bioaccessibility, and solid phase distribution. Such correlations are statistically significant, indicating that the physicochemistry may become a reliable indicator for estimating a PHE mobility and bioaccessibility change during flooding. For example, Chapter 2 established that higher pH conditions reduce copper, lead, and arsenic porewater solubility.

This analysis may infer that locations with highly acidic soil may become susceptible to high fractions of soluble and bioaccessible PHE (Ponting et al 2021). Chapter 2 also revealed that assuming that a pH increase directly decreases PHE mobility and bioaccessibility is incorrect; and rather, physicochemistry is multi-dimensional. By "multi-dimensional," this means such physicochemical parameters all interact differently, and predicting PHE dynamics using a single physicochemical variable (i.e., an increase in pH increases PHE mobility) is unreliable. This unreliability extends to using multiple physicochemical variables to predict PHE dynamics because it is inherently unknown how these variables interact. While it is valuable to model using these physicochemical parameters to estimate PHE dynamics, much work is still needed. Future research must solely investigate deeply the interactions between these variables to understand between when using these variables for predictive artificial intelligence purposes. In essence, there are two black box systems at place: one black box being the artificial intelligence and the second being the interactions between these variables, both of which require a deeper understanding.

The opportunities of machine learning algorithms, particularly random forest models, proved highly reliable at predicting PHE porewater solubility, bioaccessibility, and solid phase distribution during flooding (see Chapter 4 and 6). Such predictions were reliable by training these random forest models on physicochemical data and also mechanistic data.

This Chapter expands upon the previous chapters, investigating the role of combining these random forest predictions with geospatial data analysis (i.e., geographical information systems (GIS)). There are multiple government and non-government agencies providing reliable information about soil’s physicochemical information across the UK. Such agencies include the British Geological Survey, the UK Centre for Ecology and Hydrology, the Environment Agency, and the James Hutton Institute.

This Chapter proposes, for the first time, dividing the United Kingdom into spatial grids, using GIS, and extracting the relevant physicochemical information relating to the soil type from these agencies. These data will be concatenated to each grid, which can then be transferred to the developed random forest model to predict the likelihood of PHE mobility changes during flooding.

6.2 Aims and Objectives

This chapter aims (1) to explore the opportunities of GIS spatial analysis combined with machine learning random forests to predict PHE porewater solubility fraction within the River Thames. The chapter aims to incorporate the physicochemical data into the random forest model to predict the PHE porewater solubility within the Thames catchment. Other relevant information, such as the flood risk probability and the population number for a given location, will also be incorporated into the random forest model as feature variables. Training the random forest model with this physicochemical data, population numbers, and flood risk enhances the understanding of better predicting PHE porewater solubility risk to humans. This chapter, given computational constraints, will only focus on lead, given how abundant lead is within the environment and how neurotoxic lead is from exposure. For example, given the number of variables, predicting lead mobility changes during flooding would require at least 48 hours to concatenate and process the data on QGIS. Lead was selected given its abundance within soil and its severe toxicity from exposure.

This chapter builds upon the previous chapters, identifying the future role of this random forest model in risk assessment procedures. For an overview outlining the random forest model development and where this chapter aims to develop the model, see Figure 6.1 below.

Table 6.1. *Outlines the research aim and how this aim relates to the wider structure of this thesis. The thesis indicates the investigation's catchment, the PHE type, and the experimental analysis technique.*

Research Aim	Flow Chart Part	Catchment	PHE Type	Experimental Type
1	20	Thames	Lead	Geospatial Analysis

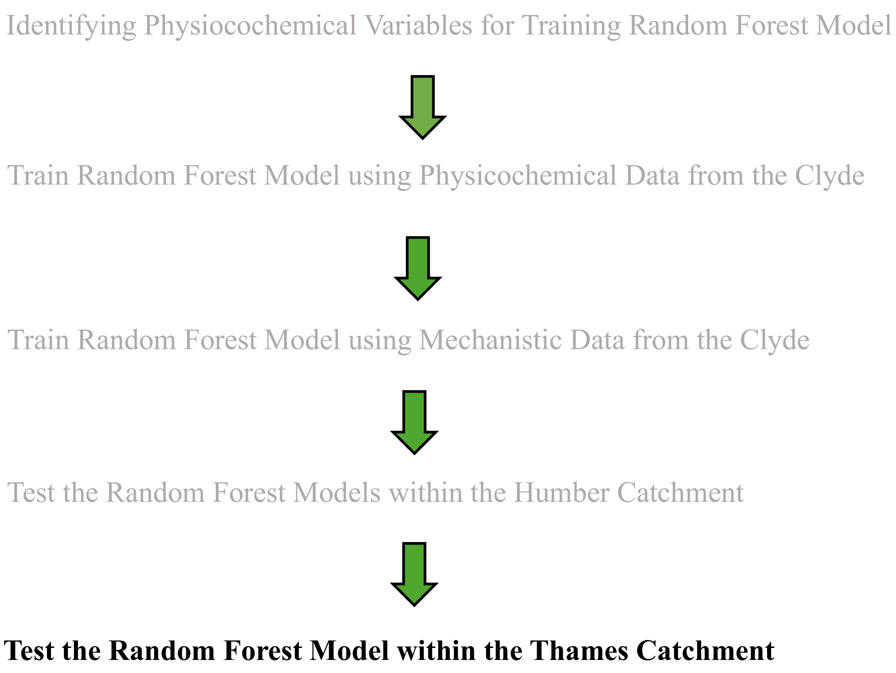

Figure 6.1. *Outlines the random forest model development throughout the thesis. The step denoted in bold represents the purpose of this chapter regarding the random forest development.*

6.3 Methods

6.3.1 Map Projections

The random forest model predictions were forecast across the Thames catchment, with the purpose of identifying locations of high vulnerability to PHE porewater solubility using QGIS (Version 3.30.2).

Establishing the locations of high vulnerability was done by creating a polygon map of the UK, and a one-mile squared grid was overlayed across the polygon map. The baseline physicochemical conditions of the different soils in the Thames catchment were obtained from the BGS G-BASE (BGS 2024). All data were imported into QGIS, vectorised, and joined onto each polygon grid cell. The combined attribute table was downloaded and implemented into the random forest model, allowing PHE porewater solubility predictions for a ten-day flood scenario, the average flood length for the UK (EA and DEFRA, 2016) to be made. The prediction hazard was obtained by comparing these predictions with environmental quality standard pollution indices for freshwater and estuarine environments for lead (EA and DEFRA, 2016). The Environment Agency estimates that freshwater and estuarine soluble lead concentrations of 14µg/L or higher would exceed minimum threshold levels, causing "significant" health consequences through exposure (EA and DEFRA, 2016). The risk level was assessed by determining the likelihood of flooding and the hazard based on the flood probability (high, medium, low, very low) (Table 6.2).

The random forest was trained using the following input features: Ca, K, Na, Fe, Al, Mn, pH, and Eh to predict Pb porewater solubility across the Humber catchment. These input features were selected based on PCA and statistical analysis (AIC and BIC scores) derived from Chapter 4.

Table 6.2. *Outlines the risk rubric for classifying locations within the Thames catchment vulnerable to lead mobility. This rubric shows that estimating the risk level must first appreciate the probability of flooding. If the flood probability is low, there is a low-risk likelihood as the hazard is absent (flooding).*

Very High	**High**	**Medium**	**Low**	**Very Low**
Flood Risk: High Remobilised Lead: > 20µg/L Population: >100 per mile square	Flood Risk: High Remobilised Lead: 14-20µg/L Population: > 100 per mile square	Flood Risk: Medium Remobilised Lead: 10-14µg/L Population: > 100 per mile square	Flood Risk: Low Remobilised Lead: 5-10µg/L Population: > 100 per mile square	Flood Risk: Very Low Remobilised Lead: <5µg/L Population: <100 per mile square

6.4 Results

6.4.1 Predictive Forecasting the Mobility of Lead

The results from the random forest model training dataset shows predicting lead mobility is non-clustering, meaning that lead mobility can be high within one location and very low within the immediate next area (Figure 6.2). Lead's mobility is the highest in the central to southwest of the Thames catchment, with low mobility within the north of the catchment. These findings are in agreement with Premier et al (2019), which used multivariant statistical analysis, showing high metal concentrations occurring within the central part of the Thames estuary.

Many locations show high risk-levels of remobilised lead. Such findings indicate that addressing lead's mobility can be tailored to specific locations of high remobilisation concern (i.e., southwestern locations).

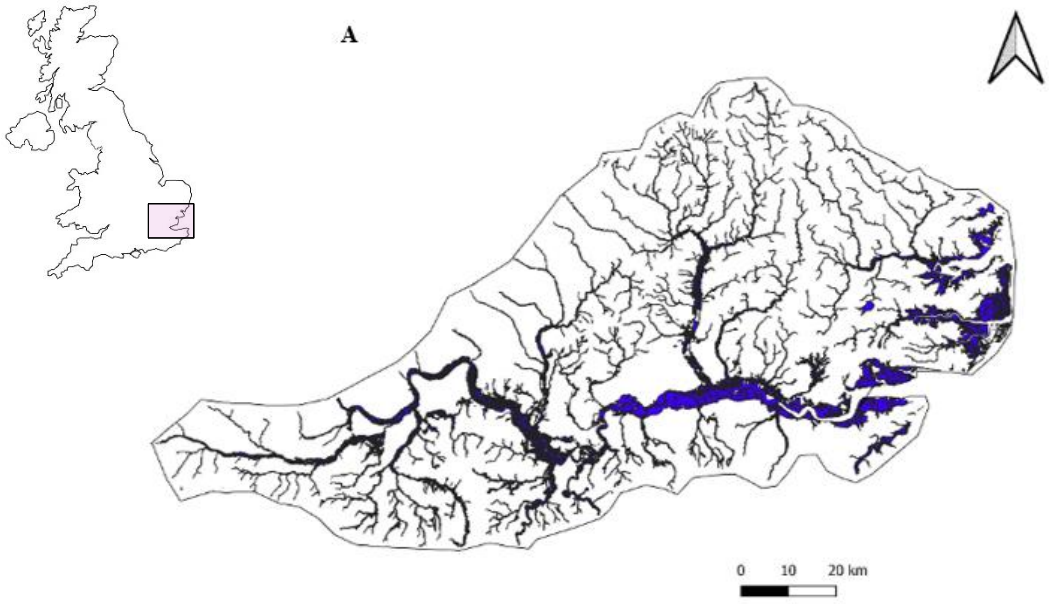

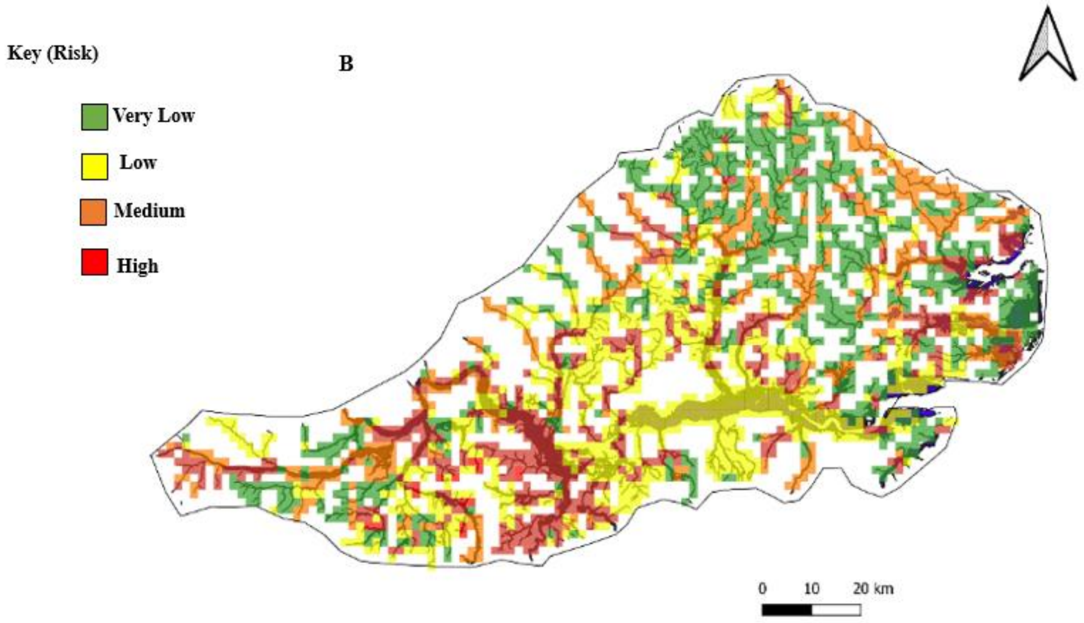

Figure 6.2. *Outlines lead's mobility within the Thames catchment boundary, and the different colours denote the risk. The figure 6.2 (A) summarises the river system within the Thames catchment. Figure 6.2 (B) indicates the risk of lead mobility. Figure 6.2 (B) begins with dividing the Thames catchment into 1 mile x 1 mile grids. Within such girds, soil physicochemical data (e.g., pH, iron, and aluminium) was collected and inputted into the random forest model to estimate lead porewater solubility.*

6.5 Discussion

This chapter explored the opportunities of combining geospatial analysis and random forest machine learning to predict lead porewater solubility across the Thames catchment. This approach developed a colour-coded map indicating locations of high, medium, and low lead solubility fraction changes during flooding; however, further validation is necessary. Data needs to be collected within several locations across the Thames catchment to confirm the map's predictions.

The data show the opportunities for the wide-scale application of random forest models to predict a PHE response during flooding. Many studies also demonstrate the opportunities of using these random forests for such flood modelling, by improving the feature selection, variable importance understanding and their ability to quickly process input features (Breiman 2001, Rodriguez-Galiano 2012).

The analysis outlines several PHE porewater solubility hotspots. The data indicate that risk assessment approaches towards addressing future PHE remobilisation should focus on a few locations within the Thames. However, it is important to address some limitations of this analysis. The Thames map generated is a risk assessment map based on the random forest training dataset. More specifically, the random forest model was trained on physicochemistry and PHE porewater solubility correlations within the Clyde catchment. These predictions are generated from the random forest training dataset and do not reflect reality. In other words, this risk map is a prediction estimate and not any indication of reality, emphasising the need for future research to conduct laboratory results across the Thames catchment, testing the reliability and validation of these predictions (Hengl et al 2017). However, by offering a balanced approach, the random forest model did account for several key parameters which influence PHE remobilisation (e.g., physicochemical changes) which may reflect some form of reality. This chapter aimed to illustrate the opportunities and applications machine learning and geospatial analysis have towards estimating PHE mobility.

Such findings also indicate the importance of accounting for the risk of flooding in such predictive estimates. For example, if a location has a hazard, based on a soil's physicochemical attributes, of creating a high chemically remobilised fraction of lead during a flood; however, has a very low probability of flooding, then the risk of soluble PHE is minimal. In other words, if the location is susceptible to soluble PHE; however, it has a very low flood risk, then the risk factor is low because flooding may never happen in the first place. Many studies support this, emphasising that floodplain dynamics significantly influence contaminant mobility, whereby hydrological changes have been shown to impact contaminant distributions (Saaristo et al., 2024; Gfeller et al., 2021). This highlights the necessity of integrating flood risk into predictive models for improved risk assessment." Such analysis must be appreciated for any predictive model. Moreover, the model could also account for type of population present, for example, are there schools nearby with vulnerable receptors, vulnerable wildlife zones etc.

The data also shows the high variability of lead porewater solubility. This high variability is attributed to the high variation in soil physicochemistry. For risk assessment purposes, predicting lead porewater solubility across large spatial scales must appreciate the local variability in physicochemical conditions. Applying a spatial scale grid of 5 miles, for example, may have a high chemically remobilised variation, emphasising the need for risk assessment purposes to predict lead porewater solubility within much smaller scales. These findings emphasise the importance of the data within this thesis to develop reliable predictive tools to aid rapidly testing locations susceptible to high fractions of PHE mobility. By identifying sites where there is PHE remobilisation risk, receptor risk and high flood probabilities, these factors can be overlaid to identify areas for monitoring where the risks are high. Essentially, this approach effectively aids rapidly testing these high-risk locations.

6.6 Conclusion

This chapter explored the opportunities of combining machine learning random forests with geospatial analysis to predict lead porewater solubility during flooding. The chapter investigated the opportunities of dividing the UK into sub-gird cells, incorporating physicochemical data into each cell, and then using the developed random forest model to simulate the chemically remobilised fraction of lead under a flood within each cell.

The results reveal several conclusions. Firstly, lead porewater solubility may be highly spatially variable, emphasising the need to develop rapid tools to estimate mobility variations. Predicting the chemically remobilised fraction of lead should be tailored to hotspot locations, which were apparent across the Thames catchment. However, this chapter reveals the limitations of these results, indicating that such mapping predictions are constrained to the reliability of the random forest models training dataset. Moreover, the information used to generate physicochemical data for these random forest models to formulate predictions may be unreliable and requires laboratory assessments to test the reliability of these online databases (e.g., from BGS GBASE).

This chapter calls for future research around testing the predictions of these random forest predictions across the Humber and assessing the reliability of such predictions. The chapter also calls for more research around exploring more reliable databases, which may provide an extensive array of geospatial data around a soil's physicochemistry.

Chapter 7 Thesis Conclusions

Several field and laboratory experiments were conducted to investigate the role of soil physicochemistry in predicting PHE porewater solubility, bioaccessibility, and speciation changes caused by flooding. These experiments aimed to examine the role of training AI modelling using laboratory and fieldwork data to reliably predict PHE dynamics during flooding (Chapter 4 aims). The laboratory work involved conducting multiple microcosm and mesocosm artificial flooding experiments. Soil porewater was collected throughout the flooding and drainage periods and was analysed for physicochemical parameters. PHE chemical speciation was determined using the chemometric CISED sequential extraction procedure. PHE bioaccessibility was established using the BARGE procedure. The soil porewater physicochemistry was determined using ICP-OES analysis.

These data were then used in various AI modelling approaches to evaluate the usefulness of predicting PHE porewater solubility, bioaccessibility, and solid-phase distribution during flooding using soil porewater physicochemistry. Specifically, different AI modelling was assessed, including machine learning random forests, XGBoost, and deep learning recurrent neural networks. This work is driven by the knowledge that exposure to such PHE may cause severe health implications, and with climate change increasing flooding frequency, emphasises the need for improved PHE monitoring (Goodland 2013). The data presented in this thesis have shown that:

- The soil's physicochemistry is reliable as a predictive proxy for estimating PHE porewater solubility, bioaccessibility, and solid phase distribution. These findings are significant because soil physicochemistry is well understood across the UK, meaning specific geographical locations with particular soil physicochemical characteristics could be prioritised for future research (Chapter 2; Section 2.3.4 and Chapter 3; Section 3.4.2).
- Machine and deep learning approaches using physicochemistry training data have significant opportunities for reliably estimating PHE changes during flooding (Chapter 4; Section 4.3.2).
- Random forest models are most reliable for estimating PHE porewater solubility, bioaccessibility, and solid phase distribution. These findings emphasise a significant conclusion showing that machine learning AI approaches outperform deep learning and conventional statistical models (Chapter 4; Section 4.3.2, 4.3.3, 4.3.4).
- Significant future opportunities exist for combining random forest modelling with geospatial analysis tools to predict PHE changes during flooding (Chapter 6; Section 6.4.1).

The following section outlines these findings in more detail:

7.1 The Role of Soil Physicochemistry Predicting PHE Dynamics

The data show that physicochemistry changes during flooding influence PHE porewater solubility, bioaccessibility, and solid phase distribution (Chapter 3). Physicochemical changes are highly interconnected, meaning that a straightforward relationship between the increase of one variable (e.g., pH) affecting another (e.g., iron concentrations) is simplified, and any predictive model must account for this interconnectedness.

Predicting PHE dynamics requires training predictive models on diverse physicochemical data from different groups (e.g., oxides, abiotic, microbial). The data also show that the flood length, which alters physicochemical conditions differently, particularly the redox conditions, must be appreciated in predictive modelling (Chapter 3; Section 3.4.4).

7.2 The Implications AI Predicting PHE Dynamics

The data show that deep-learning neural networks, machine-learning random forest models, and extreme gradient boosters can estimate PHE changes during flooding (Chapter 4). Such data reveal that all these models are better at predicting regression (i.e., porewater soluble and bioaccessibility fractions) than classification predictions (i.e., solid phase distribution).

However, the ability of random forest models for predictive purposes is not limited to the task being regression or classification but rather the complexity of the problem (Biau 2012). Training such models on physicochemistry data, which covers different groups (e.g., anaerobic, oxides and micronutrients), reliably predict porewater solubility and bioaccessibility. However, the results in Chapter 4, Section 4.3.2, reveal that different AI modelling types assign different variable importance rankings to specific physicochemical variables influencing PHE mobility. For example, random forest models assign soil iron concentrations higher importance in influencing PHE mobility than neural networks.

7.3 The Role of Random Forest Modelling

The results show decision tree learners, specifically random forests, have the highest prediction accuracy around estimating PHE porewater solubility, bioaccessibility, and solid phase distribution (Chapter 4; Sections 4.3.2, 4.3.3., 4.3.4, respectively). Such models exhibit the lowest training and testing RMSE. Incorporating mechanistic data from Visual MINTEQ and PHREEQC further improved the random forest predictive performance by increasing the model fit with the testing data and slightly lowering the training and testing RMSE (Chapter 4; Section 4.3.5). The data indicate that these random forests may outperform the models investigated because feature randomisation, replacement sampling, and out-of-bag data reduce the model bias and variance.

7.4 Random Forests and Geospatial Analysis

The data reveal the opportunities of dividing a location into geographical spatial grids (1 mile by 1 mile) and concatenating physicochemistry data to such grids, using the "concatenate by location function on QGIS (Chapter 6). After concatenating such data, the random forests show opportunities for predicting PHE porewater solubility across large spatial scales. Such data indicate that these random forests can predict the risk of PHE porewater solubility by incorporating information relating to the population of that location and the flood probability. These population and flood risk data should be treated as additional training features within the random forests.

7.5 Next Steps to be Done

The next steps required are as follows:

1. Investigate how soil microbes and fungi influence PHE porewater solubility, bioaccessibility, and solid phase distribution.

This research focused little on soil microbes and the complex interplay between microbial changes during flooding, which significantly influences PHE dynamics. Analysing the role soil microbes play in affecting bioaccessibility would significantly increase the predictive accuracy. This higher accuracy is due to microbes playing a central role in soil biogeochemical cycling, particularly in organic carbon degradation, which is important for influencing PHE dynamics.

More specifically, understanding the relationship between microbes and PHE dynamics would enhance understanding PHE interactions with the organic mineral phase. Soil microbes influence how PHE coprecipitate with organic mineral fractions, specifically humic substances and fulvic acids. Understanding the nexus between microbes, organic matter, and PHE dynamics improves the capability of monitoring PHE changes during flooding within locations with particularly high organic matter fractions.

2. The number of riverine catchments analysed.

Conducing microcosm experiments across more catchments would verify and validate the model predictions, testing the random forest model's generalisation ability. Different riverine catchments have different soil physicochemical properties, land gradients, vegetation coverages, bedrock geology and flood regimes. This difference tests these artificial intelligence models to predict PHE dynamics across heterogeneous conditions. Testing on these varying conditions reduces the likelihood of these artificial intelligence models overfitting and underfitting the data. Increasing data variations reduces the likelihood of these AI models overfitting or underfitting patterns in one data type, preventing the model from becoming overly specific with a low ability to generalise.

Moreover, different riverine catchments flood differently. Depending on the land gradient, land use type, soil texture, and riverine hydrological characteristics, some riverine catchments may flood for longer and shorter periods (Chapter 3, Section 3.4.5). Examining different riverine catchments also addresses the complexities surrounding how different rivers flood, hence improving the random forest generalisation performance. The land gradient, land use type, and soil texture all influence flood water's velocity, flow and infiltration, impacting soil physicochemistry (Ponting et al 2021). For example, steeper land gradients increase surface runoff, reducing soil water infiltration and saturation and impacting soil redox status. Understanding the relationship between differing land gradients, vegetation coverages, and land use types influencing soil physicochemistry during flooding may increase the performance of the random forest to predict PHE dynamics within multiple catchments with different physical characteristics indicated above.

3. Representing a real flooding scenario

The random forest was trained on laboratory data; however, training this model on data from actual flooding experiments would enhance the ability of the model to predict on larger scales. More specifically, the interactions between these physicochemical variables influencing PHE dynamics differ on larger scales. For example, larger-scale setups may encompass more variables influencing PHE dynamics, which laboratory work cannot capture. Such differing variables may include variability in soil texture and chemical properties across catchments. From a modelling perspective, using real flood measurements can help validate the modelling approaches by testing their predictions against the “real” data.

4. Microbial species influencing PHE dynamics during flooding

The data presented in this thesis analysed how soil microbial communities influence PHE porewater solubility under changing temperature gradients (20ºC, 30ºC and 40ºC) (Chapter 3, Section 3.3.5); however, the experiment did not analyse how microbial species types change under these temperature gradients. These changes in microbes under these temperature gradients could have been measured using eDNA sequencing. It was intended to use eDNA sequencing; however, given financial constraints and time implications, this research did not focus on using eDNA sequencing. Applying eDNA sequencing is important for future research. There are several fungal and microbial types, all of which respond differently during flooding, and investigating how different species influence PHE dynamics could serve as an important predictive parameter, similar to soil physicochemistry.

In future scenarios, the experiment should take soil samples under these changing temperature conditions and analyse how the microbial richness and diversity alter. This analysis of the soil’s bacterial and microbial composition may significantly enhance the ability of random forest modelling to predict how PHE remobilises during flooding by training on datasets that contain information about how biological communities respond to temperature change. Such analysis is observed in Nagler et al (2022) study, which uses eDNA sequencing of soil microbes to enhance biomonitoring.

7.6 Future Recommendations

There is scope for enhancing the research around predicting PHE porewater solubility, bioaccessibility, and solid phase distribution using physicochemistry data. The main recommendations for future research from this thesis are:

Predictive Modelling

- Understanding how incorporating physicochemical variables into random forest modelling can predict PHE risk from an inhalation exposure scenario. This is important because there are significant research limitations around airborne contamination. Moreover, the interactions between physicochemical parameters influencing airborne contamination are likely significantly different from those at the soil interface. This difference means that the AI models developed and trained within this research may have significant limitations around being restricted to predicting PHE dynamics within the soil interface rather than atmospheric.

- Validate such random forest predictions across catchments with differing physicochemical, mineralogical, and geological components. This recommendation may be the most important for this research because it finalises the conclusions around the role of AI and physicochemistry in predicting PHE dynamics during flooding. Validating these model predictions also establishes any underlying constraints or weaknesses within the initial modelling predictions.
- Investigate the vertical transport, fate, and behaviour of PHE and the role of random forests in monitoring such change during flooding. This serves interesting grounds around how PHE interacts in soil systems; however, it is less important for risk assessment purposes, focusing on PHE exposure within the upper soil layers.
- Determine novel ways physicochemical information can predict PHE solid phase distribution more than just determining the soil extractable mineral phase. The data presented in this thesis shows the profound opportunities of using AI and soil physicochemistry to predict PHE solid-phase distribution. By solid-phase distribution, this means the modelling could estimate which soil mineral phase, such as exchangeable, carbonate, and organic, PHE coprecipitate. However, these AI models had difficulties predicting the chemical speciation, for example, what specifically is PHE coprecipitating within the organic mineral phase. These predictive challenges are most likely attributed to data limitations, and future work should involve conducting several chemical speciation tests, correlating the physicochemical changes with PHE chemical speciation, and retraining these AI models on more chemical speciation data.
- Examine the accuracy of the GBASE model predictions as input data for the random forest model to predict over large macro scales, exploring sub-grid variability in predictions.

Policy and Governance

- Evaluate how such knowledge can improve environmental policy around flood management. A novel modelling approach was developed to assess PHE changes during flooding rapidly. It is important to investigate how this model compares with the existing approach to flood modelling, how this model may benefit environmental consultants, and how this model could be used for wide-scale risk assessments is important.

  The current approach to monitoring flooding influencing PHE dynamics is slow and requires intensive laboratory work. Future research should evaluate how this modelling approach could complement existing approaches for examining PHE dynamics during flooding. Inevitably, the role of AI has profound opportunities for significantly upscaling testing and identifying new locations of risk to PHE dynamic changes during flooding. Future work should also re-evaluate locations of more susceptible risk than others, essentially triaging locations of vulnerability.

Laboratory and Field Investigations

- Analyse PHE remobilisation and bioaccessibility under a real flood scenario, conducting fieldwork analysis rather than laboratory microcosm and mesocosm setups. This research aimed to simulate a flooding scenario by conducting larger-scale mesocosm experiments. However, these mesocosms are only partially representative of carrying out research during actual flooding periods. Conducting fieldwork flooding experiments may introduce variables not previously considered within the laboratory setups, which may influence PHE dynamics more or less than anticipated. Such variables include the influence of the riverine physicochemistry, ambient weather conditions, and vegetation coverage.

In conclusion, this research aimed to develop a fast, reliable, and novel methodology for analysing PHE porewater solubility, bioaccessibility and solid-phase distribution changes during flooding. This research has achieved these aims, uncovering the fundamental role of soil physicochemistry and the opportunities for training AI to predict PHE dynamics. The data within this thesis establishes the profound possibilities of combining soil physicochemical data with artificial intelligence to rapidly and reliably examine PHE dynamic changes during flooding.

This research emphasises the next steps around verifying and validating the developed random forest further, testing such predictions within different catchments, training this model on more data, and evaluating its role in complementing existing monitoring approaches.

References

Abdu, H. Robinson, A. Seyfried, M. Jones, S. (2008). Water Resources Research. *Geophysical imaging of watershed subsurface patterns and prediction of soil texture and water holding capacity,* 44(1), pp. 35-56.

Abdolrasol, M. G., Hussain, S. S., Ustun, T. S., Sarker, M. R., Hannan, M. A., Mohamed, R., Milad, A. (2021). Electronics. *Artificial neural networks based optimization techniques: A review*, 10(21), pp. 2689.

Antić-Mladenović, S., Frohne, T., Kresović, M., Stärk, H. J., Savić, D., Ličina, V., Rinklebe, J. (2017). Chemosphere. *Redox-controlled release dynamics of thallium in periodically flooded arable soil*, 178(1), pp. 268-276.

Anyanwu, E. D., Jonah, U. E., Adetunji, O. G., Nwoke, O. B. (2023). International Journal of Energy and Water Resources. *An appraisal of the physicochemical parameters of Ikwu River, Umuahia, Abia State in South-eastern, Nigeria for multiple uses*, 7(1), pp. 1-8.

Arnold, T. (2017). *Interface to the Keras Deep Learning Library*. Open Source Software, 2(14), pp. 296-300.

Arnqvist, G. (2020). Trends in Ecology and Evolution. *Mixed models offer no freedom from degrees of freedom,* 35(4), pp. 329-335.

Argumedo-Jimenez, C., Chaverra, D. E., Restrepo-Baena, O. J. (2023). Mining, Metallurgy & Exploration. *Nitric Acid Pretreatment Applied to a Refractory Gold-Tellurides Ore,* 40 (6), pp. 2051-2058.

Arth, I., Frenzel, P. (2000). Biology and Fertility of Soils. *Nitrification and denitrification in the rhizosphere of rice: the detection of processes by a new multi-channel electrode,* 31(1), pp. 427-435.

Asselman, K., Pellens, N., Radhakrishnan, S., Chandran, C. V., Martens, J. A., Taulelle, F., Kirschhock, C. E. (2021). Materials Horizons. *Super-ions of sodium cations with hydrated hydroxide anions: inorganic structure-directing agents in zeolite synthesis,* 8(9), pp. 2576-2583.

Assi, A. T., Blake, J., Mohtar, R. H., Braudeau, E. (2019). Irrigation Science. *Soil aggregates structure-based approach for quantifying the field capacity, permanent wilting point and available water capacity,* 37(1), pp. 511-522.

Banasiak, L. J., Schäfer, A. I. (2009). Journal of Membrane Science. *Removal of boron, fluoride and nitrate by electrodialysis in the presence of organic matter,* 334 (1-2), pp. 101-109.

Barré, P., Plante, A. F., Cécillon, L., Lutfalla, S., Baudin, F., Bernard, S., Chenu, C. (2016). Biogeochemistry. *The energetic and chemical signatures of persistent soil organic matter*, 130 (1), pp. 1-12.

Bashir, M. A., Rehim, A., Liu, J., Imran, M., Liu, H., Suleman, M., Naveed, S. (2019). Catena. *Soil survey techniques determine nutrient status in soil profile and metal retention by calcium carbonate,* 173 (1), pp. 141-149.

Basso, S., Merz, R., Tarasova, L., Miniussi, A. (2023). Nature Geoscience. *Extreme flooding controlled by stream network organization and flow regime,* 16 (4), pp. 339-343.

Belkin, M., Hsu, D., Ma, S., Mandal, S. (2019). Proceedings of the National Academy of Sciences. *Reconciling modern machine-learning practice and the classical bias–variance trade-off*, 116 (32), pp. 15849-15854.

Bengtsson, H. Bravo, H. Gentleman, R. Hossjer, O. Jaffee, H. Jiang, D. Langfelder, P. (2017). CRAN. *Package "matrixStats",* 1(1), pp. 1-34.

British Geological Survey (2024). *Geochemical Baseline Survey of the Environment (G-BASE).* https://www.bgs.ac.uk/geology-projects/applied-geochemistry/g-base/ [Accessed 3rd May 2024].

Biau, G. Scornet, E. (2016). Test. *A Random Forest Guided Tour,* 25(2), pp. 197-227.

Bidstrup, P. (1983). *Chromium: Metabolism and Toxicity.* 1st ed. Oxford: Oxford University Press.

Bindal, S. Singh, C. (2019). Water Research. *Predicting groundwater arsenic contamination: Regions at risk in highest populated state of India,* 159(1), pp. 65-76.

Biswas, N. K., Hossain, F., Bonnema, M., Aminul Haque, A. M., Biswas, R. K., Bhuyan, A., Hossain, A. (2020). Journal of Hydro informatics. *A computationally efficient flash flood early warning system for a mountainous and transboundary river basin in Bangladesh,* 22(6), pp. 1672-1692.

Blanco Camba, P., Rodríguez Pereiro, I., Fernández, V., Ramil Criado, M., Alonso Vega, F. (2024). *Physicochemical Properties and Microbiome of Vineyard Soils from DOP Ribeiro (NW Spain) Are Influenced by Agricultural Management,* 1(1), pp. 24-55.

Boateng, E. Y., Otoo, J., Abaye, D. A. (2020). Journal of Data Analysis and Information Processing. *Basic tenets of classification algorithms K-nearest-neighbor, support vector machine, random forest and neural network: a review,* 8(4), pp. 341-357.

Boer, T. E., Tas, N., Braster, M., Temminghoff, E. J., Roling, W. F., & Roelofs, D. (2012). Environmental Science and Technology. *The influence of long-term copper contaminated agricultural soil at different pH levels on microbial communities and springtail transcriptional regulation,* 46(1), pp. 60-68.

Brandão, M. S. B., Galembeck, F. (1990). Colloids and Surfaces. *Copper, lead and zinc adsorption on MnO2-impregnated cellulose acetate,* 48(1), pp. 351-362.

Breiman, L. (2001). Machine Learning. *Random Forests,* 45(1), pp. 5-32.

British Geological Survey. (2023). *G-Base for the UK: Geochemistry.* Available: https://www.bgs.ac.uk/datasets/g-base-for-the-uk/ [Accessed 18th February 2023].

Brugnara, Y., McCarthy, M. P., Willett, K. M., Rayner, N. A. (2023). International Journal of Climatology. *Homogenization of daily temperature and humidity series in the UK,* 43(4), pp. 1693-1709.

Buschmann, J., Kappeler, A., Lindauer, U., Kistler, D., Berg, M., Sigg, L. (2006). Environmental Science and Technology. *Arsenite and arsenate binding to dissolved humic acids: influence of pH, type of humic acid, and aluminum*, 40(19), pp. 6015-6020.

Byun, C., Nam, J. M., Kim, J. G. (2017). Plant Ecology. *Effects of flooding regime on wetland plant growth and species dominance in a mesocosm experiment*, 218(3), pp, 517-527.

Cabbar, H. C. (1999). Journal of Hazardous Materials. *Effects of humidity and soil organic matter on the sorption of chlorinated methanes in synthetic humic-clay complexes,* 68(3), pp. 217-226.

Calabia, A. Molina, I. Jin, S. (2020). Remote Sensing. *Soil Moisture Content from GNSS Reflectometry Using Dielectric Permittivity from Fresnel Reflection Coefficients,* 12(1), pp. 122-131.

Calderon, M. R., Almeida, C. A., Jofré, M. B., González, S. P., & Miserendino, M. L. (2023). Science of the Total Environment. *Flow regulation by dams impacts more than land use on water quality and benthic communities in high-gradient streams in a semi-arid region*, 881(1), pp.163468.

Cave, M., Wragg, J., Gowing, C., Gardner, A. (2015). Environmental Geochemistry and Health. *Measuring the solid-phase fractionation of lead in urban and rural soils using* *a combination of geochemical survey data and chemical extractions*, 37(1), pp. 779-790.

Cave, M. R., Milodowski, A. E., Friel, E. N. (2004). Geochemistry: Exploration, Environment, Analysis. *Evaluation of a method for identification of host physico-chemical phases for trace metals and measurement of their solid-phase partitioning in soil samples by nitric acid extraction and chemometric mixture resolution,* 4(1), pp. 71-86.

Chen, X. J., Ma, J. J., Yu, R. L., Hu, G. R., Yan, Y. (2022). Environmental Science and Pollution Research. *Bioaccessibility of microplastic-associated heavy metals using an in vitro digestion model and its implications for human health risk assessment,* 29(51), pp. 76983-76991.

Chen, Y., Hu, C., Deng, D., Li, Y., Luo, L. (2020). Ecotoxicology and Environmental Safety. *Factors affecting sorption behaviors of tetracycline to soils: Importance of soil organic carbon, pH and Cd contamination,* 197(1), pp. 110572.

Chianese, S. Fenti, A. Iovino, P. Musmarra, D. Salvestrini, S. (2020). Molecules. *Sorption of organic Pollutants by Humic Acids: A Review,* 25(4), pp. 918-922.

Ciszewski, D. Grygar, T. (2016). Water, Air and Soil Pollution. *A review of flood related storage and remobilisation of heavy meatal pollutants in river systems,* 239(7), pp. 1-19.

Gfeller, L., Amery, F., Voegelin, A., & Mestrot, A. (2021). Mercury mobility, colloid formation, and methylation in a polluted agricultural floodplain soil during flooding and draining cycles. *Biogeosciences, 18*(10), 3445–3463.

CLEA. (2023). *Soil Guideline Values*. https://www.claire.co.uk/ [Accessed 1st February 2023].

ClydeInfo. (2023). Weather Station. http://www.clydeinfo.co.uk/ [4th June 2023].

Cocerva, T., Robb, M., Wong, A., Doherty, R., Newell, J., Ofterdinger, U., Cox, S. F. (2024). Ecotoxicology and Environmental Safety. *Using oral bioaccessibility measurements to refine risk assessment of potentially toxic elements in topsoils across an urban area,* 276(1), pp. 116293.

Cohen, J. Fleiss, J. (1973). Educational and Psychological Measurement. *The Equivalence of Weighted Kappa and the Intraclass Correlation Coefficient as Measures of Reliability,* 33(3), pp. 14-24.

Comeau, L. P., Lai, D. Y., Cui, J. J., Hartill, J. (2018). MethodsX. *Soil heterotrophic respiration assessment using minimally disturbed soil microcosm cores,* 5(1), pp. 834-840.

Connolly, C. T., Stahl, M. O., DeYoung, B. A., Bostick, B. C. (2021). Environmental Science & Technology. *Surface flooding as a key driver of groundwater arsenic contamination in Southeast Asia,* 56(2), pp. 928-937.

Conrad, L. Perzanowski, M. (2019). Clinic Reviews in Allergy and Immunology. *The Role of Environmental Controls in Managing Asthma in Lower-Income Urban Communities,* 57(1), pp. 391-402.

Copplestone, D. Hirth, G. Cresswell, T. Johansen, M. (2020). Annals of ICRP. *Protection of the Environment,* 49(1), pp. 46-56.

Couch, S. Kuhn, M. (2022). The Journal of Open-Source Software. *Stacks: Stacked Ensemble Modelling with Tidy Data Principles,* 7(75), pp. 44-71.

Couronné, R., Probst, P., Boulesteix, A. L. (2018). BMC Bioinformatics. *Random forest versus logistic regression: a large-scale benchmark experiment,* 19(1), pp. 1-14.

Cundy, A. B., Hopkinson, L., Whitby, R. L. (2008). Science of the Total Environment. *Use of iron-based technologies in contaminated land and groundwater remediation: A review,* 400(1-3), pp. 42-51.

Cutler, D. R., Edwards Jr, T. C., Beard, K. H., Cutler, A., Hess, K. T., Gibson, J., Lawler, J. J. (2007). Ecology. *Random forests for classification in ecology,* 88(11), pp. 2783-2792.

Crispo, M., Dobson, M. C., Blevins, R. S., Meredith, W., Lake, J. A., Edmondson, J. L. (2021). Environmental Pollution. *Heavy metals and metalloids concentrations across UK urban horticultural soils and the factors influencing their bioavailability to food crops,* 288(1), pp. 117960.

Daramola, S. O., Demlie, M., Hingston, E. D. C. (2024). Journal of Environmental Management. *Mineralogical and sorption characterization of lateritic soils from Southwestern Nigeria for use as landfill liners,* 355(1), pp. 120511

Das, A. P., Sukla, L. B., Pradhan, N., Nayak, S. (2011). Bioresource Technology. *Manganese biomining: a review,* 102(16), pp. 7381-7387.

De Paolis, F., Kukkonen, J. (1997). Chemosphere. *Binding of organic pollutants to humic and fulvic acids: influence of pH and the structure of humic material,* 34(8), pp. 1693-1704.

De, B. Kuila, T. Kim, N. Lee, J. (2017). Carbon. *Carbon dot stabilized copper sulphide nanoparticles decorated graphene oxide hydrogel for high performance asymmetric supercapacitor,* 122(1), pp. 247-257.

Dec, K., Łukomska, A., Maciejewska, D., Jakubczyk, K., Baranowska-Bosiacka, I., Chlubek, D., Gutowska, I. (2017). Biological Trace Element Research. *The influence of fluorine on the disturbances of homeostasis in the central nervous system,* 177(1), pp. 224-234.

Dehnen, S., Schafer, L. L., Lectka, T., Togni, A. (2021). Inorganic Chemistry. *Fluorine: a very special element and its very special impacts on chemistry,* 60(23), pp. 17419-17425.

Della Puppa, L., Komárek, M., Bordas, F., Bollinger, J. C., Joussein, E. (2013). Journal of Colloid and Interface Science. *Adsorption of copper, cadmium, lead and zinc onto a synthetic manganese oxide,* 399(1), pp. 99-106.

Demir-Kavuk, O., Kamada, M., Akutsu, T., Knapp, E. W. (2011). BMC Bioinformatics. *Prediction using step-wise L1, L2 regularization and feature selection for small data sets with large number of features,* 12(1), pp.1-10.

Deonarine, A., Lau, B. L., Aiken, G. R., Ryan, J. N., Hsu-Kim, H. (2011). Environmental Science and Technology. *Effects of humic substances on precipitation and aggregation of zinc sulfide nanoparticles,* 45(8), pp. 3217-3223.

Devi, K. Khatua, K. (2017). Arabian Journal for Science and Engineering. *Depth-average velocity and boundary shear stress prediction in asymmetric compound channels,* 42(9), pp. 3849-3862.

Dexter, A. R., Richard, G. (2009). Soil Science Society of America Journal. *Water Potentials Produced by Oven-Drying of Soil Samples,* 73(5), pp. 1646-1651.

Ding, C., Du, S., Ma, Y., Li, X., Zhang, T., Wang, X. (2019). Geoderma. *Changes in the pH of paddy soils after flooding and drainage: modelling and validation*, 337(1), pp. 511-513.

Dixit, S., Hering, J. G. (2003). Environmental Science & Technology. *Comparison of arsenic (V) and arsenic (III) sorption onto iron oxide minerals: implications for arsenic mobility,* 37(18), pp. 4182-4189.

Doherty, S., Rueegsegger, I., Tighe, M. K., Milan, L. A., Wilson, S. C. (2022). Environmental pollution. *Antimony and arsenic particle size distribution in a mining contaminated freshwater river: Implications for sediment quality assessment and quantifying dispersion*, 305(1), pp.119-204.

Driver, J. Konz, J. Whitmyre, G. (1989). Bulletin of Environmental Contamination Toxicology. *Soil Adherence to Human Skin,* 43(1), pp. 814-820.

Dube, K., Chapungu, L., Fitchett, J. M. (2021). Foundational and Fundamental Topics. *Meteorological and climatic aspects of cyclone Idai and Kenneth*, 2(1), pp. 19-36.

Duplay, J. Semhi, K. Errais, E. Imfeld, G. Babcsanyi, I. Perrone, T. (2014). Geoderma. *Copper, Zinc, Lead and Cadmium bioavailability and retention in vineyard soils (Rouffach, France): The impact of cultural practices,* 230(1), pp. 318-328.

Eggleton, J., Thomas, K. V. (2004). Environment international. *A review of factors affecting the release and bioavailability of contaminants during sediment disturbance events*, 30(7), pp. 973-980.

El-Naggar, A., Ahmed, N., Mosa, A., Niazi, N. K., Yousaf, B., Sharma, A., Chang, S. X. (2021). Journal of hazardous materials. *Nickel in soil and water: Sources, biogeochemistry, and remediation using biochar*, 419(1), pp. 126-141.

Environment Agency. (2021). *Check if you can get flood warnings for your address.* https://www.fws.environment-agency.gov.uk/ [Accessed 2nd May 2021].

Fan, Q., Yamaguchi, N., Tanaka, M., Tsukada, H., Takahashi, Y. (2014). Journal of environmental radioactivity. *Relationship between the adsorption species of cesium and radiocesium interception potential in soils and minerals: an EXAFS study,* 138(1), pp. 92-100.

Feng, Q., Liu, J., & Gong, J. (2015). Water. *Urban flood mapping based on unmanned aerial vehicle remote sensing and random forest classifier - A case of Yuyao, China, 7*(4), pp. 1437-1455.

Filgueiras, A. V., Lavilla, I., Bendicho, C. (2004). Science of the Total Environment. *Evaluation of distribution, mobility and binding behaviour of heavy metals in surficial sediments of Louro River (Galicia, Spain) using chemometric analysis: a case study*, 330(1-3), pp. 115-129.

Fleming, P. Koletsi, D. Pandis, N. (2014). PLoS One. *Blinded by PRISMA: are systematic reviewers focusing on PRISMA and ignoring other guidelines?* 9(5), pp. 44-67.

Flynn, E. D., Catalano, J. G. (2019). Geochimica et Cosmochimica Acta. *Reductive transformations of layered manganese oxides by small organic acids and the fate of trace metals,* 250(1), pp.149-172.

Foroutan, R. Peighambardoust, S. Ahmadi, A. Akbari, A. Farjadfard, S. Ramavandi, B. (2021). Journal of Environmental Chemical Engineering. *Adsorption mercury, cobalt, and nickel with a reclaimable and magnetic composite of hydroxyapatite/Fe3O4/polydopamine,* 9(4), pp. 105-145.

Fu, C., Li, Y., Zeng, L., Zhang, H., Tu, C., Zhou, Q., Luo, Y. (2021). Global Change Biology. *Stocks and losses of soil organic carbon from Chinese vegetated coastal habitats,* 27(1), pp. 202-214.

Galiano, V. Mendes, M. Soldado, M. Olmo, M. Ribeiro, L. (2014). Science of the Total Environment. *Predictive modeling of groundwater nitrate pollution using Random Forest and multisource variables related to intrinsic and specific vulnerability: A case study in an agricultural setting (Southern Spain),* 476(1), pp. 189-206.

Gall, M. Ayrault, S. Evrard, O. Laceby, J. Gateuille, D. Lefevre, I. Mouchel, M. Meybeck, M. (2018). Environmental Pollution. *Investigating the metal contamination of sediment transported by the 2016 Seine River flood (Paris, France),* 240(1), pp. 125-139.

Gao, J. Q., Duan, M. Y., Zhang, X. Y., Li, Q. W., Yu, F. H. (2018). Catena. *Effects of frequency and intensity of drying-rewetting cycles on Hydrocotyle vulgaris growth and greenhouse gas emissions from wetland microcosms,* 164(1), pp. 44-49.

Genuer, R. Poggi, M. Malot, T. Pattern Recognit. (2010). Pattern Recognition Letters. *Variable selection using random forest,* 31(1), pp. 2225-2236.

Ghita, R. V., Negrila, C. C., Cotirlan, C., Logofatu, C. (2013). Digest Journal of Nanomaterials & Biostructures (DJNB). *On the Passivation of GaAs Surface by Sulfide Compounds,* 8(3), pp. 111-115

Giacomino, A., Abollino, O., Malandrino, M., Mentasti, E. (2011). Analytica Chimica Acta. *The role of chemometrics in single and sequential extraction assays: A Review. Part II. Cluster analysis, multiple linear regression, mixture resolution, experimental design and other techniques,* 688(2), pp.122-139.

Goodland, R. (2013). Nature Climate Change. *Lifting Livestock's Long Shadow,* 3(2), pp. 2-4.

Grabowska, M., Glińska-Lewczuk, K., Obolewski, K., Burandt, P., Kobus, S., Dunalska, J., Skrzypczak, A. (2014). Polish Journal of Environmental Studies. *Effects of hydrological and physicochemical factors on phytoplankton communities in floodplain lakes,* 23(3), pp. 713-725.

Gransee, A., Führs, H. (2013). Plant and Soil. *Magnesium mobility in soils as a challenge for soil and plant analysis, magnesium fertilization and root uptake under adverse growth conditions,* 368(1), pp. 5-21.

Graupner, N., Röhl, O., Jensen, M., Beisser, D., Begerow, D., Boenigk, J. (2017). Aquatic Microbial Ecology. *Effects of short-term flooding on aquatic and terrestrial microeukaryotic communities: a mesocosm approach,* 80(3), pp. 257-272.

Gu, X., Wong, J. W. (2004). Environmental Science and Technology. *Identification of inhibitory substances affecting bioleaching of heavy metals from anaerobically digested sewage sludge,* 38(10), pp. 2934-2939.

Guo, H., Xia, Y., Wu, F., Huang, F. (2021). Geochimica et Cosmochimica Acta. *Zinc isotopic fractionation between aqueous fluids and silicate magmas: An experimental study*, 311(1), pp. 226-237.

Gustafsson, J. (2011). Department of Land and Water Resources. *Visual MINTEQ 3.0 User Guide,* 1(1), 1-13.

Haites, E. (2018). Climate Policy. *Carbon taxes and greenhouse gas emissions trading systems: what have we learned?* 18(1), pp. 955-966.

Hamilton, E.M., Barlow, T.S., Gowing, C.J. Watts, M.J. (2015). Microchemical Journal. *Bioaccessibility performance data for fifty-seven elements in guidance material BGS 102,* 123(1), pp. 131-138.

Han, R., Zou, W., Zhang, Z., Shi, J., Yang, J. (2006). Journal of Hazardous Materials. *Removal of copper (II) and lead (II) from aqueous solution by manganese oxide coated sand: I. Characterization and kinetic study,* 137(1), pp. 384-395.

Hao, X., Han, X., Wang, C., Yan, J., Lu, X., Chen, X., Zou, W. (2023). Agriculture, Ecosystems and Environment. *Temporal dynamics of density separated soil organic carbon pools as revealed by δ13C changes under 17 years of straw return*, 356(1), pp.108656.

Hassink, J. (1996). Soil Science Society of America Journal. *Preservation of plant residue in soils differing in unsaturated protective capacity,* 60(2), pp. 487-491.
Hastie, T., Tibshirani, R., Friedman, J. H., Friedman, J. H. (2009). *The elements of statistical learning: data mining, inference, and prediction*. 1st ed. Springer: New York.

Hayat, K., Khan, A., Bibi, F., Murad, W., Fu, Y., Batiha, G. E. S., Al-Harrasi, A. (2021). Metabolites. *Effect of cadmium and copper exposure on growth, physio-Chemicals and medicinal properties of Cajanus cajan l.(Pigeon pea),* 11(11), pp. 769.

Hedges, L. Goderich, J. Curtis, P. (1999). Ecology. *The meta-analysis of response ratios in experimental ecology,* 80(4), pp. 1150-1156.

Hengl, T., de Jesus, J. M., Heuvelink, G. B. M., Gonzalez, M. R., Kilibarda, M., Blagotić, A., Shangguan, W., Wright, M. N., Geng, X., & Bauer-Marschallinger, B. (2017). SoilGrids250m: Global gridded soil information based on machine learning. *PLOS ONE, 12*(2), e0169748.

Hernandez-Coro, A., Sánchez-Hernández, B. E., Montes, S., Martinez-Lazcano, J. C., Gonzalez-Guevara, E., Perez-Severiano, F. Neuroscience and Behavioural Reviews. *Alterations in gene expression due to chronic lead exposure induce behavioural changes,* 126(1), pp. 361-367.

Hewins, D. B., Chuan, X., Bork, E. W., & Carlyle, C. N. (2016). Pedobiologia. *Measuring the effect of freezing on hydrolytic and oxidative extracellular enzyme activities associated with plant litter decomposition,* 59(5-6), pp. 253-256.

Heyden, B. Roychoudhury, A. (2015). Current Pollution Reports. *Application, Chemical Interaction and Fate of Iron Minerals in Polluted Sediment and Soils,* 1(4), pp. 265-279.

Higgins, J. P., Thompson, S. G., & Spiegelhalter, D. J. (2009). Statistics in Society. *A re-evaluation of random-effects meta-analysis. Journal of the Royal Statistical Society Series A:* 172 (1), 137-159.

Hockmann, K., Lenz, M., Tandy, S., Nachtegaal, M., Janousch, M., Schulin, R. (2014). Journal of Hazardous Materials. *Release of antimony from contaminated soil induced by redox changes,* 275(1), pp. 215-221.

Hong, D., Yokoya, N., Chanussot, J., Xu, J., Zhu, X. X. (2019). ISPRS journal of photogrammetry and remote sensing. *Learning to propagate labels on graphs: An iterative multitask regression framework for semi-supervised hyperspectral dimensionality reduction*, 158(1), pp. 35-49.

Hosaka, T., Fukabori, T., Kojima, H., Kubota, K., Komaba, S. (2021). ChemSusChem. *Effect of particle size and anion vacancy on electrochemical potassium ion insertion into potassium manganese hexacyanoferrates,* 14(4), pp. 1166-1175.

Houba, V. J. G., Temminghoff, E. J. M., Gaikhorst, G. A., Van Vark, W. (2000). Communications in soil science and plant analysis. *Soil analysis procedures using 0.01 M calcium chloride as extraction reagent,* 31(9-10) pp. 1299-1396.

Huang, J., Jones, A., Waite, T. D., Chen, Y., Huang, X., Rosso, K. M., Zhang, H. (2021). Chemical Reviews. *Fe (II) redox chemistry in the environment*,121(13), pp. 8161-8233.

Hui, N. Liu, X. Kurola, J. Mikola, J. Romantschuk, M. (2012). Boreal Environment Research. *Lead (Pb) contamination alters richness and diversity of the fungal, but not the bacterial community in pine forest soil,* 4(1), pp.18-43.

Husson, F. Josse, J. Le, S. Mazet, J. (2016). CRAN. *Package "Factominer",* 96(1), pp. 1-64.

Hu, P., Wu, L., Hollister, E. B., Wang, A. S., Somenahally, A. C., Hons, F. M., Gentry, T. J. (2019). Frontiers in Microbiology. *Fungal community structural and microbial functional pattern changes after soil amendments by oilseed meals of Jatropha curcas and Camelina sativa: a microcosm study,* 10(1), pp. 447022.

Iwuoha, P. O., Adiela, P. U., Nwannah, C. C., Okeke, O. C. (2016). International Journal of Engineering Science. *Sediment source and transport in river channels: implications for river structures*, 5(5), pp. 19-26

Izaditame, F., Siebecker, M. G., Sparks, D. L. (2022). Journal of Hazardous Materials. *Sea-level-rise-induced flooding drives arsenic release from coastal sediments*, 423(1), pp. 127-161.

James, G., Witten, D., Hastie, T., Tibshirani, R. (2013). *An introduction to statistical learning*. 1st ed. Springer: New York.

Jaruga, P., Coskun, E., Kimbrough, K., Jacob, A., Johnson, W. E., Dizdaroglu, M. (2017). Environmental Toxicology. *Biomarkers of oxidatively induced DNA damage in dreissenid mussels: A genotoxicity assessment tool for the Laurentian Great Lakes*, 32(9), 2144-2153.

Jiang, W., Haver, D., Rust, M., Gan, J. (2012). Water Research. *Runoff of pyrethroid insecticides from concrete surfaces following simulated and natural rainfalls*, 46(3), pp. 645-652.

Juhasz, A. L., Weber, J., Smith, E., Naidu, R., Rees, M., Rofe, A., Sansom, L. (2009). Environmental Science and Technology. *Assessment of four commonly employed in vitro arsenic bioaccessibility assays for predicting in vivo relative arsenic bioavailability in contaminated soils,* 43(24), pp. 9487-9494.

Kah, M. Navarro, D. Schenkeveld, W. Kookana, R. Kirby, J. Santra, S. Ozcan, A. (2022). Environmental Science: *Nano Fate of copper in soil: effect of agrochemical (nano)formulations and soil properties,* 9(2), pp. 653-662.

Kandel, I., Castelli, M. (2020). ICT Express. *The effect of batch size on the generalizability of the convolutional neural networks on a histopathology dataset,* 6(4), pp. 312-315.

Karmakar, A., Srivastava, S. K. (2017). ACS Applied Materials and Interfaces. *Interconnected copper cobaltite nanochains as efficient electrocatalysts for water oxidation in alkaline medium*, 9(27), pp. 22378-22387.

Kanevski, M., Pozdnoukhov, A., Timonin, V., Maignan, M. (2008). Soil pollution characterization using support vector machines: from monitoring network design to multiscale mapping.

Kanevski, M., Timonin, V., Pozdnoukhov, A. (2011). Automatic mapping and classification of spatial environmental data. *Geocomputation, Sustainability and Environmental Planning*, 205-223.

Kebede, G., Tafese, T., Abda, E. M., Kamaraj, M., Assefa, F. (2021). Journal of Chemistry. *Factors influencing the bacterial bioremediation of hydrocarbon contaminants in the soil: mechanisms and impacts,* 1(1), pp. 45-67.

Kelly, T. Hamilton, E. Watts, M. Ponting, J. Sizmur, T. (2020). Environmental Toxicology and Chemistry. *The Effect of Flooding and Drainage Duration on the Release of Trace Elements from Floodplain Soils,* 39(11), pp. 2124-2135.

Khaledian, Y., Kiani, F., Ebrahimi, S., Brevik, E. C., Aitkenhead-Peterson, J. (2017). Land Degradation and Development. *Assessment and monitoring of soil degradation during land use change using multivariate analysis,* 28(1), pp. 128-141.

Kiczenski, T. J., Stebbins, J. F. (2002). Journal of Non-Crystalline Solids. *Fluorine sites in calcium and barium oxyfluorides: F-19 NMR on crystalline model compounds and glasses*, 306(2), pp. 160-168.

Kile, D. Chiou, C. Zhou, H. Li, H. Xu, O. (1995). Environmental Science and Technology. *Partition on Nonpolar Organic Pollutants from Water to Soil and Sediment Organic Matters,* 29(5), pp. 1401-1406.

Kilunga, P.I., Sivalingam, P., Laffite, A., Grandjean, D., Mulaji, C.K., De Alencastro, L.F., Mpiana, P.T. and Poté, J. (2017). Chemosphere. *Accumulation of toxic metals and organic micro-pollutants in sediments from tropical urban rivers, Kinshasa, Democratic Republic of the Congo,* 179(1), pp. 37-48.

Kim, T. K. (2015). Korean journal of anesthesiology. *T test as a parametric statistic,* 68(6), pp. 540

Kirezci, E. Young, I. Ranasinghe, R. Muis, S. Nicholls, R. Lincke, D. Hinkel, J. (2020). Scientific Reports. *Projections of Global-Scale Sea Levels and Resulting Episodic Coastal Flooding Over the 21st Century*, 10(1), pp. 1-12.

Koh, D. Park, J. Lee, S. Kim, H. Jung, H. Kim, I. Choi, S. Park, D. (2021). Safety and Health at Work. *Estimate of Lead Exposure Intensity by Industry Using Nationwide Exposure Databases in Korea*, 1(1), pp. 14-19.

Kontopantelis, E., Reeves, D. (2012). Statistical Methods in Medical Research. *Performance of statistical methods for meta-analysis when true study effects are non-normally distributed: a simulation study,* 21(4), pp. 409-426.

Koricheva, J. Gurevitch, J. Nakagawa, S. Stewart, G. (2018). Nature. *Meta-analysis and the science of research synthesis*, 555(1), pp. 175-182.

Kossmeier, M. Tran, S. Voracek, M. (2020). Zeitschrift Fur Psychologie-Journal of Psychology. *Power-Enhanced Plots for Meta-Analysis: The Sunset Funnel Plot*, 228(1), pp. 43-49.

Kuhn, M. Johnson, K. (2013). *Applied Predictive Modelling.* 1st ed. New York: Springer-Verlag.

Kukumägi, M., Ostonen, I., Kupper, P., Truu, M., Tulva, I., Varik, M., Lõhmus, K. (2014). Agricultural and Forest Meteorology. *The effects of elevated atmospheric humidity on soil respiration components in a young silver birch forest,* 1(194), PP. 167-174.

Kulsum, P. G. P. S., Khanam, R., Das, S., Nayak, A. K., Tack, F. M., Meers, E., Biswas, J. K. (2023). Environmental Research. *A state-of-the-art review on cadmium uptake, toxicity, and tolerance in rice: From physiological response to remediation process,* 220(1), pp. 115098.

Kumar, V., Pandita, S., Sidhu, G. P. S., Sharma, A., Khanna, K., Kaur, P., Setia, R. (2021). Chemosphere. *Copper bioavailability, uptake, toxicity and tolerance in plants: A comprehensive review,* 262(1), pp. 127-134.

Kushwaha, A., Hans, N., Kumar, S., Rani, R. (2018). Ecotoxicology and Environmental Safety. *A critical review on speciation, mobilization and toxicity of lead in soil-microbe-plant system and bioremediation strategies,* 147(1), pp. 1035-1045.

Konsten, C. J., van Breemen, N., Suping, S., Aribawa, I. B., Groenenberg, J. E. (1994). Soil Science Society of America Journal. *Effects of Flooding on pH of Rice-Producing, Acid Sulfate Soils in Indonesia,* 58(3), pp. 871-883.

Laing, G. D., Van de Moortel, A., Lesage, E., Tack, F. M., Verloo, M. G. (2008). Wastewater treatment, plant dynamics and management in constructed and natural wetlands. *Factors affecting metal accumulation, mobility and availability in intertidal wetlands of the Scheldt estuary (Belgium),* 1(1), pp. 121-133.

Lair, G. J., Gerzabek, M. H., Haberhauer, G. (2007). Environmental Chemistry Letters. *Sorption of heavy metals on organic and inorganic soil constituents*, 5(1), pp. 23-27.

Lamberty, B., Thomson, A. (2010). Nature. *Temperature-associated increases in the global soil respiration record*, 464(7288), pp. 579-582.

Lee, S., Kim, J. C., Jung, H. S., Lee, M. J., Lee, S. (2017). Geomatics, Natural Hazards and Risk. *Spatial prediction of flood susceptibility using random-forest and boosted-tree models in Seoul metropolitan city, Korea*, 8(2), pp. 1185-1203.

Lepock, J. R., Frey, H. E., Inniss, W. E. (1990). Biochimica et Biophysica Acta (BBA)-Molecular Cell Research. *Thermal analysis of bacteria by differential scanning calorimetry: relationship of protein denaturation in situ to maximum growth temperature,* 1055(1), pp. 19-26.

Li, J. Q., Li, W. S., Zhang, W. T., Zhu, S., Luo, C. Y., Liu, W. S., Zhang, L. Y. (2023). Chinese Journal of Polymer Science. *Enhancing Molecular Chain Entanglement and π-π Stacking Toward the Improvement of Shape Memory Performance of Polyimide,* 1(1), pp. 1-8.

Li, X., Sun, Q., Yan, X., Li, P., & Lv, R. (2023). Resistivity responses of sodium sulfate and sodium chloride-type loess under different water and salinity conditions. *Environmental Science and Pollution Research*, 30(38), pp. 88734-88743.

Li, Z., Li, Q., Chen, T. (2024). Advances in Atmospheric Sciences. *Record-breaking high-temperature outlook for 2023: An assessment based on the China global merged temperature (cmst) dataset,* 41(2), pp. 369-376.

Liu, F. Liu, G. Zhu, Z. Wang, S. Zhao, F. (2019). Chemosphere. *Interactions between microplastics and phthalate esters as affected by microplastics characteristics and solution chemistry,* 214(1), pp. 688-694.

Liu, P. Zhang, Y. Tang, Q. Shi, S. (2021). Biochemical Engineering Journal. *Bioremediation of Metal Contaminated Soils by Microbially Induced Carbonate Precipitation and its Effects on Ecotoxicology and Long-Term Stability,* 166 (1), 107-116.

Lodygin, E., Abakumov, E. (2022). Agronomy. *The Impact of agricultural use of Retisols on the molecular structure of humic substances,* 12(1), pp.144-155.
Lu, P., Zhang, G., Apps, J., Zhu, C. (2022). Earth-Science Reviews. *Comparison of thermodynamic data files for PHREEQC*, 225(1), pp. 1-43.

Lytle, D. Tang, M. Francis, A. O'Donnell, A. Newton, J. (2020). Water Research. *The effect of chloride, sulfate and dissolved inorganic carbon on iron release from cast iron,* 183(1), pp. 116-123.

MacDonnell, C. J. (2020). Unpublished MSc, University of Otago. *An eye on coastal change: Characterising spatial-temporal coastal sensitivity at high-resolution-Okia Reserve, Otago Peninsula, New Zealand*, 1(1), pp. 1-14.

Malik, A. Puissant, J. Buckeridge, K. Goodall, Jehmlich, N. Chowdhury, S. Gweon, H. Peyton, J. Mason, K. Agtmaal, M. Blaud, A. Clark, I. Whitaker, J. Pywell, R. Ostle, N. Gleixner, Griffiths, R. (2018).

Mao, Y. Yu, S. Li, P. Liu, G. Ouyang, S. Zhu, Z. Zhang, P. (2021). Environmental Research. *A novel magnesium-rich tricalcium aluminate for simultaneous removal of ammonium and phosphorus: Response surface methodology and mechanism investigation,* 195(1), pp. 110-123.

Martin, M. Wattenbach, M. Smith, P. Meersmans, J. Jolivet, C. Boulonne, L. Arrouays, D. (2015). Biogeosciences. *Spatial distribution of soil organic carbon stocks in France*, 8(5), pp. 1053-1065.

Marr, J. G., Harff, P. A., Shanmugam, G., Parker, G. (2001). Geological Society of America Bulletin. *Experiments on subaqueous sandy gravity flows: the role of clay and water content in flow dynamics and depositional structures,* 113(11), pp. 1377-1386.

Matis, B. A., Mousa, H. N., Cochran, M. A., Eckert, G. J. (2000). Quintessence international. *Clinical evaluation of bleaching agents of different concentrations,* 31(5), pp.1-12.

McCauley, A. Jones, C. Jacobsen, J. (2009). Nutrient Management Module. *Soil pH and Organic Matter*, 8(2), pp. 1-12.

McLaren, D. (2019). Biological and Environmental Science Thesis. *Flooding induced changes in the mobility, bioaccessibility and solid phase distribution of potentially harmful elements,* 1(1), pp. 1-192.

McMahon, J. M., Olley, J. M., Brooks, A. P., Smart, J. C., Stewart-Koster, B., Venables, W. N., Stout, J. C. (2020). Science of the Total Environment. *Vegetation and longitudinal coarse sediment connectivity affect the ability of ecosystem restoration to reduce riverbank erosion and turbidity in drinking water,* 707(1), pp. 135-194.

Mehrotra, A. S., Sedlak, D. L. (2005). Water Environment Federation. *Iron Addition Decreases Net Mercury Methylation in Laboratory Wetland Microcosms*, 1(1), pp. 8074-8098.

Mehta, N., Cipullo, S., Cocerva, T., Coulon, F., Dino, G. A., Ajmone-Marsan, F., De Luca, D. A. (2020). Chemosphere. *Incorporating oral bioaccessibility into human health risk assessment due to potentially toxic elements in extractive waste and contaminated soils from an abandoned mine site,* 255(1), pp. 126927.

Mendez, B. Webster, R. Fiedler, S. Siebe, C. (2017). European Journal of Soil Science. *Changes in soil redox potential in response to flood irrigation with wastewater in central Mexico,* 68(1), pp. 886-896.

Mendes, P., Velazco, S. J. E., de Andrade, A. F. A., Júnior, P. D. M. (2020). Ecological Modelling. *Dealing with overprediction in species distribution models: How adding distance constraints can improve model accuracy,* 431(1), pp. 109180.

Meng, Y., Cave, M., Zhang, C. (2020). Chemosphere. *Identifying geogenic and anthropogenic controls on different spatial distribution patterns of aluminium, calcium and lead in urban topsoil of Greater London Authority area,* 238(1), pp. 124541.

Menger, F. Ferrero, P. Wiberg, K. Ahrens, L. (2020). Trends in Environmental Analytical and Chemistry. *Wide-scope screening of polar contaminants of concern in water: A critical review of liquid chromatography-high resolution mass spectrometry-based strategies,* 28(1), pp. 14-34.

Middleton, D. R., Watts, M. J., Beriro, D. J., Hamilton, E. M., Leonardi, G. S., Fletcher, T., Polya, D. A. (2017). Environmental Science: processes & impacts. *Arsenic in residential soil and household dust in Cornwall, south west England: potential human exposure and the influence of historical mining,* 19(4), pp. 517-527.

Moles, N. R., Kelly, M., Smyth, D. (2016). Journal of the Mining Heritage Trust of Ireland. *Environmental legacy of 19th century lead mining and mineral processing at the Newtownards Lead Mines,* 15(1), pp. 41-53.

Nunan, N., Schmidt, H. Raynaud, X. (2020). Philosophical Transactions of the Royal Society B. *The ecology of heterogeneity: soil bacterial communities and C dynamics,* 375(1798). pp. 20190249.

Pang, B., Nijkamp, E., Wu, Y. N. (2020). Journal of Educational and Behavioural Statistics. *Deep learning with tensorflow: A review*, 45(2), pp. 227-248.

Paz, A. M., Castanheira, N., Farzamian, M., Paz, M. C., Gonçalves, M. C., Santos, F. A. M., Triantafilis, J. (2020). Geoderma. *Prediction of soil salinity and sodicity using electromagnetic conductivity imaging,* 361(1), pp. 114086.

Peana, M., Pelucelli, A., Medici, S., Cappai, R., Nurchi, V. M., Zoroddu, M. A. (2021). Current Medicinal Chemistry. *Metal toxicity and speciation: a review,* 28(35), pp. 7190-7208.

Peck, L. S., Webb, K. E., Bailey, D. M. (2004). Functional Ecology. *Extreme sensitivity of biological function to temperature in Antarctic marine species,* 18(5), pp. 625-630.

Peng, X., Wu, J., Zhao, Z., Wang, X., Dai, H., Xu, L., Hu, F. (2022). Chemical Engineering Journal. *Activation of peroxymonosulfate by single-atom Fe-g-C3N4 catalysts for high efficiency degradation of tetracycline via nonradical pathways: Role of high-valent iron-oxo species and Fe–Nx sites,* 427(1), pp. 130803.

Petruzzelli, G. Pedron, F. Rosellini, I. (2019). Environmental Science. *Bioavailability and bioaccessibility in soil: a short review and a case study,* 7(2), pp. 208-225.

Pinheiro, J. P., Mota, A. M., Benedetti, M. F. (1999). Environmental Science and Technology. *Lead and calcium binding to fulvic acids: salt effect and competition,* 33(19), 3398-3404.

Pinto, M. D. C. E., da Silva, D. D., Gomes, A. L. A., dos Santos, R. M. M., de Couto, R. A. A., de Novais, R. F., Pinto, F. G. (2019). Journal of Cleaner Production. *Biochar from carrot residues chemically modified with magnesium for removing phosphorus from aqueous solution,* 222(1), pp. 36-46.

Pisanu, C. Franconi, F. Gessa, G. Mameli, S. Pisanu, G. Campesi, L. Leggio, L. Agabio, R. (2019). Pharmacological Research. *Sex differences in the response to opioids for pain relief: A systematic review and meta-analysis,* 148(1), pp. 104-133.

Prigent, A., Imbol Koungue, R. A., Lübbecke, J. F., Brandt, P., Harlaß, J., Latif, M. (2024). Climate Dynamics. *Future weakening of southeastern tropical Atlantic Ocean interannual sea surface temperature variability in a global climate model,* 62(3), pp. 1997-2016.

Ponting, J. Kelly, T. Verhoef, A. Watts, M. Sizmur, T. (2021). Science of the Total Environment. *The impact of increased flooding occurrence on the mobility of potentially toxic elements in floodplain soil - A review,* 754(1), pp. 1-9.

Probst, P. Wright, M. Boulesteix, A. (2019). Wiley Interdisciplinary Reviews: data mining and knowledge discovery. *Hyperparameters and tuning strategies for random forest,* 9(3), pp. 1301.

Poggere, G., Gasparin, A., Barbosa, J. Z., Melo, G. W., Corrêa, R. S., Motta, A. C. V. (2023). Journal of Trace Elements and Minerals. *Soil contamination by copper: Sources, ecological risks, and mitigation strategies in Brazil,* 4(1), pp.100059.

Rastegari Mehr, M., Shakeri, A., Amjadian, K., Khalilzadeh Poshtegal, M., Sharifi, R. (2021). Journal of Environmental Health Science and Engineering. *Bioavailability, distribution and health risk assessment of arsenic and heavy metals (HMs) in agricultural soils of Kermanshah Province, west of Iran,*19(1), pp. 107-120.

Richardson Jr, J. J. (2021). Environmental Science and Policy. *The national flood insurance program as an incentive to employ multiple regulatory approaches to manage floodplains: Lessons learned from Pennsylvania, Vermont and West Virginia*,115(1), pp.8-15.

Ritter, M. They, N. Konzen, E. (2019). RStudio. *Introdução ao software estatístico R,* 1(1), pp.1-12.

Rodriguez-Galiano, V. F., Ghimire, B., Rogan, J., Chica-Olmo, M., & Rigol-Sanchez, J. P. (2012). An assessment of the effectiveness of a random forest classifier for land-cover classification. *ISPRS Journal of Photogrammetry and Remote Sensing, 67*, 93–104.

Roe, G. H., Feldl, N., Armour, K. C., Hwang, Y. T., Frierson, D. M. (2015). Nature Geoscience. *The remote impacts of climate feedbacks on regional climate predictability*, 8(2), pp. 135-139.
Römkens, M. J., Helming, K., Prasad, S. N. (2002). Catena. *Soil erosion under different rainfall intensities, surface roughness, and soil water regimes,* 46(2-3), pp. 103-123.

Rosenberg, M. (2005). Evolution. *The file-drawer problem revisited: a general weighted method for calculating fail-safe numbers in meta-analysis*, 59(2), pp. 464-468.

Rossi, J., Govaerts, A., De Vos, B., Verbist, B., Vervoort, A., Poesen, J., Muys, B. and Deckers, J. (2009). Catena. *Spatial structures of soil organic carbon in tropical forests - a case study of Southeastern Tanzania*, 77(1), pp. 19-27.

Roussiez, V., Ludwig, W., Monaco, A., Probst, J. L., Bouloubassi, I., Buscail, R., Saragoni, G. (2006). Continental Shelf Research. *Sources and sinks of sediment-bound contaminants in the Gulf of Lions (NW Mediterranean Sea): a multi-tracer approach* 26(16), pp. 1843-1857.

Rowley, M. C., Grand, S., Verrecchia, É. P. (2018). Biogeochemistry. *Calcium-mediated stabilisation of soil organic carbon,* 137(1-2), pp. 27-49.

Saaristo, M., et al. (2024). Spatial and Temporal Dynamics of Chemical and Microbial Contaminants in Floodwaters: Implications for Environmental and Human Health. *Environmental Science & Technology*.

Saint-Laurent, D., Gervais-Beaulac, V., Paradis, R., Arsenault-Boucher, L., Demers, S. (2017). *Forests. Distribution of soil organic carbon in riparian forest soils affected by frequent floods (Southern Québec, Canada)*, 8(4), p.124.

Sandroni, V., Smith, C. M., Donovan, A. (2003). Talanta. *Microwave digestion of sediment, soils and urban particulate matter for trace metal analysis,* 60(4), pp. 715-723

Sanderson, P., Naidu, R., Bolan, N., Lim, J. E., Ok, Y. S. (2015). Journal of Hazardous Materials. Chemical stabilisation of lead in shooting range soils with phosphate and magnesium oxide: Synchrotron investigation, 299(1), pp. 395-403.

Sarhadi, A., Rousseau-Rizzi, R., Mandli, K., Neal, J., Wiper, M. P., Feldmann, M., Emanuel, K. (2024). Bulletin of the American Meteorological Society. *Climate change contributions to increasing compound flooding risk in New York City,* 105(2), pp. 337-356.

Schmidt, J., Krekeler, C., Dommert, F., Zhao, Y., Berger, R., Site, L. D., Holm, C. (2010). The Journal of Physical Chemistry B. *Ionic charge reduction and atomic partial charges from first-principles calculations of 1, 3-dimethylimidazolium chloride,* 114(18), pp. 6150-6155.

Schubach, M. Re, M. Robinson, P. Valetini, G. (2017). Overcoming Challenges in Rare Genetic Diseases. *Imbalance-Aware Machine Learning for Predicting Rare and Common Disease-Associated Non-Coding Variants,* No. 2951, pp. 1-12.

Schwartz, G. E., Rivera, N., Lee, S. W., Harrington, J. M., Hower, J. C., Levine, K. E., Hsu-Kim, H. (2016). Applied Geochemistry. *Leaching potential and redox* *transformations of arsenic and selenium in sediment microcosms with fly ash,* 67(1), pp. 177-185.

Seo, E. Cheong, Y. Yim, G. Min, K. Geroni, J. (2017). Catena. *Recovery of Fe, Al and Mn in acid coal mine drainage by sequential selective precipitation with control of pH,* 148(1), pp. 11-16.

Shaheen, A. Iqbal, J. (2018). Sustainability. *Spatial distribution and mobility assessment of carcinogenic heavy metals in soil profiles using geostatistics and random forest, boruta algorithm,* 10(3), pp. 799-802.

Sharma, N., Wang, Z., Catalano, J. G., Giammar, D. E. (2022). ACS Earth and Space Chemistry. *Dynamic responses of trace metal bioaccessibility to fluctuating redox conditions in wetland soils and stream sediments,* 6(5), pp. 1331-1344.

Shi, E. Xu, Z. Yang, X. Liu, Q. Zhang, H. Wimmer, A. Li, L. (2018). Environmental Pollution. *Re-evaluation of stability and toxicity of silver sulfide nanoparticle in environmental water: Oxidative dissolution by manganese oxide,* 243(1), pp. 1242-1251.

Shokunbi, O. S., Idowu, G. A., Aiyesanmi, A. F., Davidson, C. M. (2024). Environmental Management. *Assessment of Microplastics and Potentially Toxic Elements in Surface Sediments of the River Kelvin, Central Scotland, United Kingdom,* 1(1), pp. 1-14.

Siddique, M. A. B., Khan, M. M. R., Arif, R. B., Ashrafi, Z. (2018, September). Study and observation of the variations of accuracies for handwritten digits recognition with various hidden layers and epochs using neural network algorithm. In *2018 4th International Conference on Electrical Engineering and Information & Communication Technology (iCEEiCT)* (pp. 118-123).

Simmler, M., Bommer, J., Frischknecht, S., Christl, I., Kotsev, T., Kretzschmar, R. (2017). Environmental Pollution. *Reductive solubilization of arsenic in a mining-impacted river floodplain: Influence of soil properties and temperature,* 231(1), pp. 722-731.

Simmonds, M. (2015). Systematic Reviews. *Quantifying the risk of error when interpreting funnel plots,* 4(1), pp. 1-15.

Şimşek, S. (2016). Desalination and Water Treatment. *Adsorption properties of lignin containing bentonite–polyacrylamide composite for ions,* 57(50), pp. 23790-23799.

Sinha, P. Gaughan, A. Stevens, F. Nieves, J. (2019). Computers, Environment and Urban Systems. *Assessing the spatial sensitivity of a random forest model: Application in gridded population modelling,* 75(1), pp. 132-145.

Site, A. (2000). Journal of Physical and Chemical Reference Data. *Factors affecting sorption of organic compounds in natural sorbent/water systems and sorption coefficients for selected pollutants. A review,* 30(1), pp. 187-439.

Sorenson, P. McCormick, S. Dyck, M. (2019). Canadian Journal of Soil Science. *Soil contamination sampling intensity: determining accuracy and confidence using a Monte Carlo simulation,* 99(3), pp. 254-261.
Springel, V., & Hernquist, L. (2002). Monthly Notices of the Royal Astronomical Society. *Cosmological smoothed particle hydrodynamics simulations: the entropy equation,* 333(3), pp. 649-664.

Steely, S. Amarasiriwardena, D. Xing, B. (2007). Environmental Pollution. *An investigation of inorganic antimony species and antimony associated with soil humic acid molar mass fractions in contaminated soils,* 148(2), pp. 590-598.

Stewart, C. Paustian, K. Conant, R. Plante, A. Six, J. (2009). Soil Biology and Biochemistry. *Soil carbon saturation: Implications for measurable carbon pool dynamics in long-term incubations,* 41(1), pp. 13-24.

Stewart, J. M., Bhattacharya, S. K., Madura, R. L., Mason, S. H., Schonberg, J. C. (1995). Water Research. *Anaerobic treatability of selected organic toxicants in petrochemical wastes,* 29(12), pp. 2730-2738.

Suda, A., Makino, T. (2016). Geoderma. *Functional effects of manganese and iron oxides on the dynamics of trace elements in soils with a special focus on arsenic and cadmium: a review*, 270(1), pp. 68-75.

Sun, L., Chen, S., Chao, L., Sun, T. (2007). Bulletin of Environmental Contamination and Toxicology. *Effects of flooding on changes in Eh, pH and speciation of cadmium and lead in contaminated soil,* 79(1), pp. 514-518.

Sun, Y., Li, G., Zhang, J., Qian, D. (2019). Advances in Civil Engineering. *Prediction of the strength of rubberized concrete by an evolved random forest model,* 1(1), pp. 1-7.
Su, D.,

Stanimirović, P. S., Han, L. B., Jin, L. (2023). CAAI Transactions on Intelligence Technology. *Neural dynamics for improving optimiser in deep learning with noise considered,* 1(1), pp. 1-34.

Suzuki, T., Nakamura, A., Niinae, M., Nakata, H., Fujii, H., Tasaka, Y. (2013). Chemical engineering journal. *Lead immobilization in artificially contaminated kaolinite using magnesium oxide-based materials: Immobilization mechanisms and long-term evaluation,* 232(1), pp. 380-387.

Swartjes, F. A. (2010). *Introduction to contaminated site management, I*n *Dealing with Contaminated Sites: From Theory Towards Practical Application*, 1st ed. Dordrecht: Springer Netherlands.

Szuskiewicz, M. Petrovsky, E. Lukasik, A. Gruba, P. Grison, H. (2021). Geoderma. *Technogenic contamination or geogenic enrichment in Regosols and Leptosols? Magnetic and geochemical imprints on topsoil horizons,* 381(1), pp. 114-128.

Takegawa, Y., Takao, T., Sakaguchi, H., Nakai, T., Takeo, K., Morita, Y., Kodama, Y. (2022). Scientific Reports. *The importance of pH adjustment for preventing fibrin glue dissolution in the stomach: an in vitro study,* 12(1), pp. 6986.

Tanaka, A., Tadano, T. (1972). Potash Review. *Potassium in relation to iron toxicity of the rice plant,* 21(1), pp. 1-12.

Tang, H., Xu, M., Luo, J., Zhao, L., Ye, G., Shi, F., Li, Y. (2019). Environmental Sciences Europe. *Liver toxicity assessments in rats following sub-chronic oral exposure to copper nanoparticles,* 31(1), pp. 1-14.

Tessier, A. P. G. C., Campbell, P. G., Bisson, M. J. A. C. (1979). Analytical Chemistry. *Sequential extraction procedure for the speciation of particulate trace metals,* 51(7), pp. 844-851.

Thakur, N., Raigond, P., Singh, Y., Mishra, T., Singh, B., Lal, M. K., Dutt, S. (2020). Trends in Food Science & Technology. *Recent updates on bioaccessibility of phytonutrients*, 97(1), pp. 366-380.

Thapa, R., Gupta, S., Guin, S., Kaur, H. (2017). Applied Water Science. *Assessment of groundwater potential zones using multi-influencing factor (MIF) and GIS: a case study from Birbhum district, West Bengal,* 7(1), pp. 4117-4131.

Thompson, A. Goyne, K. (2012). Nature Education Knowledge. *Introduction to the sorption of chemical constituents in soils*, 4(4), pp. 7-14.

Tougui, I., Jilbab, A., El Mhamdi, J. (2021). Healthcare Informatics Research. *Impact of the choice of cross-validation techniques on the results of machine learning-based diagnostic applications,* 27(3), pp. 189-199.

Trukhina, M., Popov, K., Oshchepkov, M., Tkachenko, S., Vorob'eva, A., Rudakova, G. (2022). Int. J. Corros. Scale Inhib. *Impact of colloidal iron hydroxide and colloidal silicon dioxide on calcium sulfate crystallization in the presence of antiscalants,* 11(3), pp. 1147-1171.

Tyler, J. J., Jones, M., Arrowsmith, C., Allott, T., & Leng, M. J. (2016). Climate Dynamics. *Spatial patterns in the oxygen isotope composition of daily rainfall in the British Isles*, 47(1), 1971-1987.

Tyler, G. (2004). Science of the Total Environment. *Ionic charge, radius, and potential control root/soil concentration ratios of fifty cationic elements in the organic horizon of a beech (Fagus sylvatica) forest podzol,* 329(1-3), pp. 231-239.

Tyralis, H., Papacharalampous, G., Langousis, A. (2019). Water. *A brief review of random forests for water scientists and practitioners and their recent history in water resources,* 11(5), pp. 910-932.

UKCEH. (2022). *Environmental Science for a World where People and Nature Prosper.* https://www.ceh [Accessed 12th November 2022].

Uriarte, D. Andres, D. (2006). BMC Bioinform. *Gene selection and classification of microarray data using random forest,* 7(3), pp. 1-13.

USEPA. (2022). *Flooding.* https://www.epa.gov/ [Accessed 3rd October 2022]

USGS. (2022). *Hurricane Harvey Flooding.* https://www.usgs.gov/ [Accessed 4th May 2022].

Viji, R., Yi, Y., Song, J., Liu, H., Zhou, Y., Li, C. (2020). Journal of Environmental Management. *The changes in physicochemical and stable isotope compositions in the lower Yellow River of China due to artificial flooding*, 276(1), pp. 111-123.

Walling, D. E., Owens, P. N., Carter, J., Leeks, G. J. L., Lewis, S., Meharg, A. A., Wright, J. (2003). Applied Geochemistry. *Storage of sediment-associated nutrients and contaminants in river channel and floodplain systems*, 18(2), pp. 195-220.

Walton, C. R., Zak, D., Audet, J., Petersen, R. J., Lange, J., Oehmke, C., Hoffmann, C. C. (2020). Science of the Total Environment. *Wetland buffer zones for nitrogen and phosphorus retention: Impacts of soil type, hydrology and vegetation*, 727(1), pp .138709.

Wang, Q. Huang, Q. Guo, G. Qin, J. Luo, J. Zhu, Z. Hong, Y. Xu, Y. Hu, S. Hu, W. Yang, C. Wang, J. (2020). Chemosphere. *Reducing bioavailability of heavy metals in contaminated soil and uptake by maize using organic-inorganic mixed fertilizer,* 261(1), pp. 128-132.

Wang, M., Hou, J., Deng, R. (2023). Ecotoxicology and Environmental Safety. *Co-exposure of environmental contaminants with unfavorable temperature or humidity/moisture: Joint hazards and underlying mechanisms.* 264(1), pp .115432.

Wang, Z. Liu, S. Huang, C. Liu, Y. Bu, Z. (2017). Catena. *Impact of land use change on profile distributions of organic carbon fractions in peat and mineral soils in Northeast China,* 152(1), pp. 1-8.

Wang, Y., Hu, T., Zhang, W., Lin, J., Wang, Z., Lyu, S., Tong, H. (2023). Chemosphere. *Biodegradation of polylactic acid by a mesophilic bacteria Bacillus safensis,* 318(1), pp.137991.

Weeks, J. Hettiarachchi, G. (2020). Soil Science Society of American Journal. *Source and formulation matter: New insights into phosphorus fertilizer fate and transport in mildly calcareous soils,* 84(3), pp. 731-746.

Whitby, H. Berg, C. (2015). Marine Chemistry. *Evidence for copper-binding humic substances in seawater,* 173(1), pp. 282-299

Wilson, S. Lockwood, P. Ashley, P. Tighe, M. (2010). Environmental Pollution. *The chemistry and behaviour of antimony in the soil environment with comparisons to arsenic: A critical review,* 158(5), pp. 1169-1181.

Wisawapipat, W., Christl, I., Bouchet, S., Fang, X., Chareonpanich, M., Kretzschmar, R. (2024). Chemosphere. *Temporal development of arsenic speciation and extractability in acidified and non-acidified paddy soil amended with silicon-rich fly ash and manganese-or zinc-oxides under flooded and drainage conditions,* 351 (1), pp. 141140.

World Health Organisation. (2023). *Industrially Contaminated Sites.* https://www.who.int/ [Accessed 1st November 2021].

Wragg, J. Cave, M. Basta, N. Brandon, E. Casteel, S. Denys, S. Gron, C. Oomen, A. Reimer, K. Tack, K. Wiele, T. (2011). Science of the Total Environment. *An inter-laboratory trial of the unified BARGE bioaccessibility method for arsenic, cadmium, and lead in soil,* 409(19), pp. 4016-4030.

Wragg, J (2009). Certificate of Analysis: BGS Guidance Material 102 Ironstone Soil.

Wu, M., Qi, C., Derrible, S., Choi, Y., Fourie, A., Ok, Y. S. (2024). Communications Earth & Environment. *Regional and global hotspots of arsenic contamination of topsoil identified by deep learning,* 5(1), pp. 10.

Wyke, S., Peña-Fernández, A., Brooke, N., Duarte-Davidson, R. (2014). Environment International. *The importance of evaluating the physicochemical and toxicological properties of a contaminant for remediating environments affected by chemical incidents*, 72(1), pp. 109-118.

Xia, Q. Peng, C. Lamb, D. Mallavarapu, M. Naidu, R. Ng, J. (2016). Chemosphere. *Bioaccessibility of arsenic and cadmium assessed for in vitro bioaccessibility in spiked soils and their interaction during the Unified BARGE Method (UBM) extraction,* 147(1), pp. 444-450.

Xiao, W., Ye, X., Zhu, Z., Zhang, Q., Zhao, S., Chen, D., Hu, J. (2021). Science of the Total Environment. *Continuous flooding stimulates root iron plaque formation and reduces chromium accumulation in rice (Oryza sativa L.),* 788(1), pp. 147786.

Xie, L., Jiao, Z., Zhang, H., Wang, T., Qin, J., Zhang, S., Luo, M., Lu, M., Yao, B., Wang, H. and Xu, D. (2022). Toxicology Letters. *Altered hippocampal GR/KCC2 signaling mediates susceptibility to convulsion in male offspring following dexamethasone exposure during pregnancy in rats,* 364(1), pp. 12-23.

Xie, Q., Sari, A., Pu, W., Chen, Y., Brady, P. V., Al Maskari, N., Saeedi, A. (2018). Journal of Petroleum Science and Engineering. *pH effect on wettability of oil/brine/carbonate system: Implications for low salinity water flooding,* 168(1), pp. 419-425.

Xiong, X. U., Harville, E. W., Buekens, P., Mattison, D. R., Elkind-Hirsch, K., Pridjian, G. (2008). The American Journal of the Medical Sciences. *Exposure to Hurricane Katrina, post-traumatic stress disorder and birth outcomes*, 336(2), pp.111-115.

Xu, D., Gao, B., Wan, X., Peng, W., Zhang, B. (2022). Water Research. *Influence of catastrophic flood on microplastics organization in surface water of the Three Gorges Reservoir, China*, 211(1), pp. 118-129.

Xu, J., Zhang, R., Xie, X., Ma, Z., Liu, J., Wang, X. (2023). Plant and Soil. *Copper accumulation process and rhizosphere mechanism under different water conditions in riparian wetland of Poyang Lake, China,* 484(1), pp. 363-378.

Yang, F. Zhang, S. Fu, Q. Antonietti, M. (2020). Land Degradation and Development. *Conjugation of artificial humic acids with inorganic soil matter to restore land for improved conservation of water and nutrients*, 31(7), pp. 884-893.

Yoonah, J. Andreas, S. Kilian, S. (2018). Science of the Total Environment. *Comparison of the sampling rates and partitioning behaviour of polar and non-polar contaminants in the polar organic chemical integrative sampler and a monophasic mixed polymer sampler for application as an equilibrium passive sampler*, 627(1), pp. 11-34.

Yorkshire Dales River Trust. (2021). *Working together to ensure our rivers thrive*. https://www.ydrt.org.uk/ [Accessed 1st January 2021].

Zhang, J., Li, J., Zhang, J., Xie, R., Yang, W. (2010). The Journal of Physical Chemistry. *Aqueous synthesis of ZnSe nanocrystals by using glutathione as ligand: the pH-mediated coordination of Zn2+ with glutathione*, 114(25), pp. 11087-11091.

Zhang, W. Lin, M. (2020). Science of the Total Environment. *Influence of redox potential on leaching behaviour of a solidified chromium contaminated soil*, 733(1), pp. 139-140.

Zhang, W. Singh, P. Parling, E. Delides, S. (2004). Minerals Engineering. *Arsenic removal from contaminated water by natural iron ores*, 17(4), pp. 517-524.

Zhao, L. C., Xu, L. (2024). Construction and Building Materials. *Experimental investigation on mechanical response of soil reinforced by carbon nanotubes and silica dioxide nanoparticles*, 415(1), pp. 134203.

Zhang, H., Wang, J. J. (2014). Loss on ignition method. *Soil test methods from the southeastern United States*, 1(1), pp. 155-157.

Zingaretti, D., Baciocchi, R. (2021). Applied Sciences. *Different approaches for incorporating bioaccessibility of inorganics in human health risk assessment of contaminated soils,* 11(7), pp. 3005.

Zou, Z., Habraken, W. J., Matveeva, G., Jensen, A. C., Bertinetti, L., Hood, M. A., Fratzl, P. (2019). Science. *A hydrated crystalline calcium carbonate phase: Calcium carbonate hemihydrate*, 363(6425), pp. 396-400.